Doctoral theses at NTNU, 2020:147

Mirco Peron

Relating stress corrosion cracking behavior to microstructural and surface properties of biocompatible AZ31 alloy

Doctoral thesis

NTNU
Norwegian University of Science and Technology
Thesis for the Degree of Philosophiae Doctor
Faculty of Engineering
Department of Mechanical and Industrial Engineering

NTNU
Norwegian University of Science and Technology

Mirco Peron

Relating stress corrosion cracking behavior to microstructural and surface properties of biocompatible AZ31 alloy

Thesis for the Degree of Philosophiae Doctor

Trondheim, May 2020

Norwegian University of Science and Technology
Faculty of Engineering
Department of Mechanical and Industrial Engineering

NTNU
Norwegian University of
Science and Technology

NTNU
Norwegian University of Science and Technology

Thesis for the Degree of Philosophiae Doctor

Faculty of Engineering
Department of Mechanical and Industrial Engineering

ISBN 978-82-326-4642-5 (printed ver.)
ISBN 978-82-326-4643-2 (electronic ver.)
ISSN 1503-8181

Doctoral theses at NTNU, 2020:147

Printed by NTNU Grafisk senter

"*You can't climb the ladder of success with your hands in your pockets"*

Arnold Schwarzenegger

Preface

This PhD thesis is submitted to the Norwegian University of Science and Technology (NTNU) for partial fulfilment of the requirements for the degree of philosophiae doctor. This doctoral work has been performed at the Department of Mechanical and Industrial Engineering, NTNU, with Professor Jan Torgersen as main supervisor and Professor Filippo Berto as co-supervisor. This work was conducted as a part of a fellowship awarded gratefully by the Department of Mechanical and Industrial Engineering at NTNU.

Acknowledgements

I owe my deepest gratitude to my supervisor Professor Jan Torgersen for giving me the opportunity to perform this Ph.D. and for his great support and encouragement and fruitful discussions during the Ph.D. studies. He provided me the intellectual freedom to work on challenging and exciting topics with a wholehearted support and I cannot thank him enough for what he has done for me so far! I sincerely thank Professor Paul Heinz Mayrhofer and Professor Matteo Benedetti for accepting to examine this thesis and providing constructive comments to enhance it.

I would like to thank my co-supervisor Professor Filippo Berto for his support and help during my doctoral period. He knows how hard it can be for an Italian living far from the loved ones and he was always ready to provide me words of support during the hard times and to spur me to be committed and consistent to hard work. I am also very grateful to Professor Fabio Sgarbossa who gave me the opportunity to work in a field that has always interested me. He was always prone to provide me all the support I needed and his passion for research was of great stimulus for me in the hard times.

Doing experimental research means spending a lot of time in the lab to prepare and perform the tests. Therefore, I would also like to express my sincere gratitude to Carl Magnus Midtbø, Børge Holen, Pål Christian Skaret and Cristian Torres Rodriguez who were continuously backing me up and helping me in the technical practices. I extend my gratitude to my colleague and friend Seyed Mohammad Javad Razavi from whom I have learned a lot of research life lessons, and to all the other colleagues and friends: Lise Sandnes, Luigi Mario Viespoli, Marco Simonetto, Giuseppe Fragapane, Abdulla Bin Afif, Dr. Anup Dadlani, Håkon Johnsen, Kristin Ødegaard, Markus Lid, Emanuele Solfiti, Klas Solberg and Marco Maurizi.

Special thanks to my dear friends Francesco Leoni and Pietro Foti. Samuel Taylor Coleridge said that “friendship is a sheltering tree”. Only God knows how many times you have been my shelter and my strength, and for this I would never be thankful enough!

I want to thank also the “AIA Castelfranco Veneto” group in Italy, particularly Luca Bizzotto and Aiax Ramon Ignatovici. Luca, thanks for believing in me when it was hard to do it and everyone else was suggesting you to give up. One of the most famous Les Brown’s quote is “shoot for the moon. Even if you miss it, you will land among the stars”. You taught me not only to dream big, but also to work hard to achieve it, and this is one of the biggest life lessons I have ever learned. Ramon, iubirea mea, your support in all the aspects of my life has been constant since the first time we met. A Japanese proverb says “fall down seven times, stand up eight”, and this is what I have learned from you, to never give up, to always believe in what I am doing that the results will arrive.

Thanks to all my friends in Italy, especially Filippo Dandolo, Giacomo Buson, Davide Tramarin, Pierpaolo Saccon and Francesco De Gaspari. A special mention goes to Leonardo Rosso, my dearest friend, who has never let the distance stop him from supporting me. More than 2000 kilometers separate us but I have always felt you by my side, you have always been there to support me, to suggest me and also to scold me when necessary. No matter where life will bring us, we both know that we can always count on each other.

Last but definitely not least, I would like to express all my gratitude and love to all my cousins, uncles and aunts, and especially to my parents, my brother and his family for the never-ending love and the unconditional support. Many thanks to my parents who have made me the man I am today, letting me free to take my decisions and to learn from my mistakes. Thanks to my brother who constantly supports me and still treats me as his "little brother". Michele, you were my idol and my best friend when I was a kid, despite the age difference, and now I look at you with admiration for the person you are.

Trondheim, February 2020

Mirco Peron

Abstract

Magnesium (Mg) and its alloys have attracted significant attention as temporary implant materials due to their excellent biocompatibility with human physiology. In fact, Mg is essential to the human metabolism as a cofactor for many enzymes and Mg ions are well-known to facilitate tissue-healing. In addition, the mechanical properties (density, elastic modulus, yield strength and ultimate tensile strength) of Mg and its alloys resemble those of natural bone reducing the risk of the stress-shielding-related problems observed with other metallic implant materials such as stainless steel, titanium and Co-Cr alloys. However, despite their high potential, Mg and its alloys are not yet utilized in biomedical applications. This is due to the (1) rapid corrosion and degradation in the human body that leads to a loss of mechanical integrity before tissues have sufficient time to heal, (2) the evolution of hydrogen as corrosion product accompanied by hydrogen pocket formation that hampers healing or even cause the death of patients through the blockage of the blood stream and (3) the sudden fracture of implants due to the simultaneous action of the corrosive human-body-fluid and mechanical loads through corrosion-assisted cracking phenomena (stress corrosion cracking (SCC) and corrosion fatigue (CF)).

In the past years, several approaches have been developed to improve the corrosion resistance of Mg and its alloys. These approaches can be divided into two main groups, one characterized by the modification of the bulk and the other by the modification of the surface. Among the former, Severe Plastic Deformation (SPD) techniques, such as Equal Channel Angular Pressing (ECAP), have attracted attention as possibility for inducing a very fine and homogeneous microstructure throughout all the samples. The latter group relies on surface modifications obtained by mechanical processing (e.g. cryogenic machining) or by the protection through coatings deposited by various techniques (e.g. sputter and Atomic Layer Deposition (ALD)). However, the assessment of the effectiveness of the different approaches in improving the resistance of Mg and its alloys to corrosion-assisted cracking phenomena is still underexplored.

In an attempt to understand the fundamental mechanisms linking the microstructural and surface properties to the SCC susceptibility, this thesis investigates how selected procedures initially intended for improving the corrosion resistance of Mg and its alloys impact the SCC susceptibility of AZ31 alloys in Simulated Body Fluid (SBF) at 37 °C. The procedures selected from an extensive literature review investigating the different procedures used to improve the corrosion behavior and the mechanisms regulating the SCC phenomenon were ECAP, cryogenic machining and coatings obtained by means of ALD.

1, 2 and 4 passes of ECAP were carried out on an AZ31 alloy and samples subjected to one pass of ECAP have been shown to be less susceptible to SCC compared to the material in the as-received condition (the elongation to failure was increased by 150%) due to the improved corrosion resistance as a consequence of a reduced grain size. The reduced SCC susceptibility after one pass of ECAP was also confirmed by the morphology of the fracture surfaces that reveals an increased ductility compared to the

as-received material. However further ECAP processing (2 and 4 passes) are reported to worsen the SCC susceptibility due to an increased brittleness of the material as a consequence of an increased amount of hydrogen evolved. This is due to the unfavorable texture evolution, as confirmed by the mechanical characterization (tensile tests and hardness measurements).

AZ31 samples were machined under cryogenic cooling and afterwards subjected to Slow Strain Rate Tests (SSRTs) at a strain rate of $3.5 \cdot 10^{-6}$ s^{-1} to evaluate the SCC susceptibility. Cryogenic machined samples were characterized by lower SCC susceptibility than dry cut samples (the elongation to failure was increased by 28%) as a consequence of their improved corrosion performances due to the presence of a wider nanocrystalline layer, resulting in a faster formation of passivating surface oxides, and to the presence of compressive residual stresses instead of tensile.

Being ALD a recently developed technique still underexplored in terms of corrosion and biological properties, it was compared to sputter technique in terms of corrosion protectiveness and the induced biocompatibility of three different coatings were evaluated. The ALD technique has been shown to provide the better corrosion protection (assessed by means of potentiodynamic polarization curves and hydrogen evolution experiments) both in case of smooth and rough surfaces due to an increased surface integrity (observed by SEM and XPS analyses). In addition, in the case of 3D porous structures, the improvements provided by the ALD technique were even higher as a consequence of the line-of-sight limitation of sputtering (confirmed by means of SEM analyses). In addition, the biocompatibility of TiO_2, ZrO_2 and HfO_2 coatings obtained by means of ALD have been investigated by means of MTS assay on L929 cells and the HfO_2 coatings were shown to provide the best biocompatibility due to the highest corrosion resistance. This can be reasoned by their lower wettability and their higher electrochemical stability and surface integrity (in terms of cracks and pores). TiO_2, though generally considered a biocompatible coating, was found to provide the lowest improvements in terms of corrosion resistance and cell viability. Interestingly, TiO_2 coatings are characterized by grade 3 cytotoxicity after 5 days of culture due to their high corrosion rate, which does not meet the demands for cellular applications. These results indicate the strong link between biocompatibility and corrosion protection and signify the need of considering the latter when choosing a biocompatible coating to protect temporary Mg based alloys before implantation.

Finally, the SCC susceptibility of TiO_2 and ZrO_2 ALDed coated AZ31 alloys have been evaluated and the ZrO_2 coated samples were reported to have the lowest SCC susceptibility. In fact, the elongation to failure of the TiO_2 coated samples were increased by 125% and that of ZrO_2 coated samples by 220%. The different SCC susceptibility was attributed to the improved corrosion of the ZrO_2 coated samples compared to the TiO_2 coated samples as a consequence of four main aspects, i.e. different cohesive energies, different wettability, different defect densities and sizes and different mechanical properties.

Contents

List of Figures

List of Tables

Table 2.2.7: Summary of the biocompatibility of pure Mg. All samples are cast, unless otherwise specified. Additional information can be found in Appendix 2.2.C

Table 2.2.8: Summary of AZ alloys mechanical properties. All the AZ samples are cast, unless otherwise specified. Additional information can be found in Appendix 2.2.C

Table 2.2.9: Summary of the DC polarization curve results for AZ series Mg alloys. All the AZ samples are cast, unless otherwise specified. *=measured after 7 days of immersion. Additional information can be found in Appendix 2.2.C.

Table 2.2.10: Summary of the corrosion rates for AZ series Mg alloys. All AZ samples are cast, unless otherwise specified. Additional information can be found in Appendix 2.2.C.

Table 2.2.11: Summary of the biocompatibility of AZ31 and AZ91 alloys. All the samples are cast, unless otherwise specified. Additional information can be found in Appendix 2.2.C.

Table 2.2.12: Summary of AM alloys mechanical properties. All the AM samples are cast, unless otherwise specified. Additional information can be found in Appendix 2.2.C.

Table 2.2.13: Corrosion rate for different AM and AZ alloys obtained with two different manufacturing processes.

Table 2.2.14: Summary of Mg–Al–RE alloys mechanical properties. All the Mg–Al–RE samples are cast, unless otherwise specified. Additional information can be found in Appendix 2.2.C.

Table 2.2.15: Summary of Mg–Zn alloys mechanical properties. All the Mg–Zn samples are cast, unless otherwise specified. Additional information can be found in Appendix 2.2.C.

Table 2.2.16: Summary of the DC polarization curve results for Mg–Zn binary alloys. All the Mg–Zn samples are cast, unless otherwise specified. Additional information can be found in Appendix 2.2.C.

Table 2.2.17: Summary of the corrosion rates for Mg–Zn binary alloys. All the Mg–Zn samples are cast, unless otherwise specified. Additional information can be found in Appendix 2.2.C.

Table 2.2.18: HUVEC adhesion density results for different Mg–Zn–Sr alloys and their comparison with pure Mg and AZ31 alloy. For two different culture times, either direct or indirect cell cultures are used.

Table 2.2.19: Summary of the mechanical properties of Mg–Zn–Zr alloys. All the Mg–Zn–Zr samples are cast, unless otherwise specified. Additional information can be

Abbreviations

AE	Mg alloy with main alloying elements Aluminium and Rare Earth
Ag	Silver
Al	Aluminium
AM	Mg alloy with main alloying elements Aluminium and Manganese
APD	Accumulative plastic deformed
ARB	Accumulative roll-bonded
ARR	Asymmetric reduction rolling
AU	Artificial urine
AZ	Mg alloy with main alloying elements Aluminium and Zinc
B	Boron
BDF	Bi-directional forged
BE	Backward extruded
Bi	Bismuth
BMGs	Bulk metallic glasses
BP	Back pressure
Ca	Calcium
Ce	Cerium
CEC	Cyclic extrusion and compression
CEE	Cyclic expansion extrusion
CF	Corrosion fatigue
CP	Commercial pure Mg
CR	Cross rolling
Cr	Chromium
Cu	Copper
DC	direct contact
DCC	direct chilling cast
DCE	Double continuous extrusion
DCT	Deep cryogenically treated
DMD	Disintegrated Melt Deposition
DMEM	Dulbecco's modified Eagle's medium
DSR	Differential speed rolled
DSST	Double step solution treated
EBSD	Electron Backscatter Diffraction
EBSS	Earle's balanced salt solution
ECAE	Equal channel angular extruded
ECAP	Equal channel angular pressed
ECAP-BP	Equal-channel angular pressed with applied back pressure
ECM	Endothelial cell medium
Ecorr	Corrosion potential
EPT	Electropulsing treatment
ESR	Equal speed rolling
FBS	Fetal bovine serum
Fe	Iron
FSP	Friction stir processed

Gd	Gadolinium
GPMC	Gravity permanent mold casted
Hank's	Hank's solution
HBF	Human body fluid
HBSS	Hank's balanced salt solution
HCl	Hydrochloric acid
HE	Hydrostatic extruded
HEMA	High energy mechanical alloyed
HP	High pure Mg
HPDC	High pressure die casted
HPT	High pressure torsion
HRDSR	high-ratio differential speed rolling
HSRMF	High strain rate multiple forging
HSRR	High strain rate rolled
HTP	H-Tube pressed
IC	indirect contact
Icorr	Corrosion current
icorr	Corrosion current density
IR	Isothermal rolling
KBM	Kirkland's biocorrosion medium
La	Lanthanum
LAE	Mg alloy with main alloying elements Lithium, Aluminium and Rare Earth
LAM	Laser additive manufacturing
LB	Lysogeny broth
LENS	Laser engineered net shaping
Li	Lithium
LPDC	Low pressure die casted
LSP	Laser shock peening
LSRMF	Low strain rate multiple forging
LTUSSE	Low temperature ultra-slow-speed extruded
MAD	multiaxial deformation
MAF	Multidirectional forged
MC-HPDC	High pressure die casted with melt conditioning
MDF	Multi-direction forged
MEM	Minimum essential medium
MEMp	MEM containing 40 g/L bovine serum albumin
MIF	Multiaxial isothermal forged
MM	Misch Metal
Mn	Manganese
MPF	Multi electrolyte physiological fluid
MPHR	Multi-pass hot rolled
MTE	Microtube extrusion
Nb	Niobium
Nd	Neodymium
Ni	Nickel
PBS	Phosphate-buffered saline

PEO	Plasma electrolytic oxidation
PM	Powder metallurgy
PMF	Pulse magnetic field
Pr	Praseodymium
PVD	Physical vapor deposition
RAP	Recrystallization and partial melting
RB	Reverse bending
RDC	Rheo-die casted
RE	Rare Earth
REE	Rare Earth elements
RHT	Recrystallization heat treatment
Ringer's	Ringer's solution
RS	Rapid solidified
RSC	Rheo-squeeze casting
RS P/M	Rapid solidification powder metallurgy
RTE	Room temperature extruded
RU	Repeated upsetting
Sb	Antimony
SBF	Simulation body fluid
Sc	Scandium
SCC	Stress corrosion cracking
SHT	Solution heat treated
Si	Silicon
SLM	Selective laser melted
SMAT	Surface mechanical attrition treated
SMCM	Smooth muscle cell medium
SMF	Steady magnetic field
Sn	Tin
SPD	Severe plastic deformation
SR	Symmetrical rolled
Sr	Strontium
S-RS P/M	Simplified rapid solidification powder metallurgy
SSP	Severe shot peening
SSST	Single step solution treated
SSTT	Semi-solid thermal transformation
SVDC	Super vacuum die casted
Ti	Titanium
TRC	Twin roll casted
TSB	Tryptic Soy Broth
UHP	Ultra high pure Mg
UR	Unidirectional rolling
UTS	Ultimate tensile strength
UV	Ultrasonic vibration
V	Vanadium
VFUT	Variable frequency ultrasonic treatment
WE	Mg alloy with main alloying elements Yttrium and Rare Earth element
XHP	Ultra-high purity

Y	Yttrium
ZE	Mg alloy with main alloying elements Zinc and Rare Earth element
ZK	Mg alloy with main alloying elements Zinc and Zirconium
ZM	Mg alloy with main alloying elements Zinc and Manganese
Zn	Zinc
ZW	Mg alloy with main alloying elements Zinc and Yttrium
ZX	Mg alloy with main alloying elements Zinc and Calcium
αMEM	alpha minimum essential medium

Chapter 1

Introduction and Methods

1.1. Motivation

Biomedical implants have played a fundamental role in the improvement of the worldwide population's health. They are used in applications such as orthopaedics, cardiovascular stent and neural prosthetics, where the need to replace or repair the fractured or diseased parts of the human body is highly needed [1–4]. Among these, orthopaedic surgery is characterized by the highest annual growth rate [3]. According to Long and Rach [5], almost 90% of the population over 40 years is affected by degenerative joint diseases. Total hip replacements are predicted to represent half of the estimated total number of operations in 2030 [6]. The surgical implantation of artificial biomaterials of specific size and shape is an effective solution in restoring the load-bearing capacity of damaged bone tissue. In fact, although bones are characterized by outstanding mechanical and structural properties, they can fracture because of three main reasons [7–9]:

- Failure due to stresses arising from the daily activities
- Fracture caused by a sudden injury
- Pathological fractures resulting from bone infections and tumors

Depending on their applications, implant devices can be classified into permanent or temporary. The former are required in applications such as joint replacements, where a long term existence in the human body is required, while the latter are utilized in the fields of engineering scaffolds and bone fixators such as bone plates, screws, pins and stents, where biomaterials are required to stay inside the human body only for a restricted period, i.e. as long as bone heals (3-4 months [10,11]).
The materials currently used for temporary applications are permanent metallic materials, such as stainless steel, titanium, and cobalt-chromium alloys [12]. Because of their high strength and good corrosion resistance, they have been widely used as load-bearing implants for bone healing and repair of damaged tissues [13–15]. The key problems with these permanent implants are however two-fold. Firstly, their elastic modulus highly differs from that of bone: for both stainless steel and cobalt-chrome alloys it is ten times higher, while for Ti-6Al-4V five times higher than bone (Table 1.1).

Properties	Natural Bone	Stainless Steel	Ti Alloy	Co-Cr Alloy	Magnesium
Density (g/cm^3)	1.7–2.0	7.9–8.1	4.4–4.5	8.3–9.2	1.74–2.0
Elastic modulus (MPa)	3–20	189–205	110–117	230	41–45
Tensile strength (MPa)	80–150	480–620	930–1140	900–1540	170–270
Compressive yield strength (MPa)	130–180	170–310	758–1117	450–1000	65–100
Elongation at failure (%)	1–7	30–40	8–15	30–45	6–20
Fracture toughness (MPa $m^{1/2}$)	3–6	50–200	55–115	100	15–40

Table 1.1. Comparison of the mechanical properties of natural bone with various implant materials [13,16–21].

This results in the occurrence of the stress-shielding phenomenon, which is a consequence of stress distribution changes between the bone and the implant [22–28]: bones adapt to the reduced stress field according to the Wolff's law [29] resulting in the bone either becoming more porous (internal remodelling) or thinner (external remodelling) increasing the possibility of implant failure. Secondly, due to the potential rise of long-term complications [30–34], the permanent implant must be removed when the healing process is completed. However, the additional surgeries necessary to remove the implant cause an increase in costs to the health care system, as well as emotional stress to the patient.

In order to solve these drawbacks, biodegradable materials, i.e. materials that ideally degrade in the same manner and speed as the natural bone heals, have been studied [35–37]. Both natural and synthetic polymers have been studied extensively as biodegradable materials. In fact, natural polymers such as polysaccharides and collagen have all produced favourable outcomes in tissue engineering applications [38–44], while synthetic polymers such as polyglycolic acid (PGA), poly-L-lactic acid (PLA), poly-DL-lactic acid and poly-capro lactone have been used as biodegradable sutures, drug delivery systems, fixation devices and low load-bearing applications [45–52]. However, due to their low mechanical strength compared to metals, polymers have been mostly used in soft tissue reconstruction and low load-bearing applications. Moreover, they may also absorb liquids and swell, leach undesirable products such as monomers, fillers and antioxidants. Furthermore, the sterilization process may affect their properties [7]. The combination of high strength and biocompatibility can be found in biodegradable metal alloys. Several of them, such as iron-based metals, Zn-based metals and tungsten have been studied [53]. Most of the scientific efforts, however, focus on Magnesium (Mg) and its alloys [53–55]. Among metallic engineering materials, Mg possesses, in fact, one of the best bio-compatibilities with human physiology and the best mechanical compatibility with human bone [56]. The density of magnesium and its alloys (1.74-2 g/cm^3) is in fact very similar to that of cortical bone (1.7-2 g/cm^3). In addition, the similarities of the elastic moduli of Mg and its alloys with those of natural bone (Table 1.1) potentially reduces the possibilities of stress shielding in hard tissue applications [57,58]. Moreover, Mg is the fourth most abundant element in the human body: the human body usually contains 35 g of Mg per 70 kg of body weight and it is recommended that an adult receives 240–420 mg daily [21]. It is a cofactor for many enzymes (it is involved in more than 300 enzymatic reactions), it plays a role in protein and nucleic acid synthesis, mitochondrial activity and integrity and in many other cellular functions [59–62]. Finally, Mg^{2+} ions, resulting from the degradation process are reported to aid the healing and growth of tissue. Any excess of these ions is harmlessly excreted in the urine [18,63]. However, despite its many advantages, Mg has some disadvantages. First the strength of cast pure magnesium is too low compared to that of human bone [64,65]. Another disadvantage of Mg and its alloys is their high corrosion rate in the body that may lead to a loss of mechanical integrity before tissues have enough time to heal. Moreover, Mg and its alloys are reactive metals and they corrode in aqueous environments according to the reactions [66,67]:

$$Mg + 2H_2O \rightarrow Mg(OH)_2 + H_2 \quad (1.1)$$

H_2 as a corrosion product together with the generation of respective H_2 pockets can influence the healing process or, if the pockets are large, they may cause the death of patients through blocking the blood stream [68]. Finally, the simultaneous action of the corrosive human-body-fluid and the mechanical loading can cause further complications through sudden fracture of implants due to corrosion-assisted cracking, such as stress corrosion cracking (SCC) and corrosion fatigue (CF) [69,70]. SCC is particularly dangerous as it leads to a sudden and catastrophic failure under mechanical loading normally considered safe, and Mg and its alloys are particularly susceptible [71–73]. Therefore, it is important to develop Mg-based implants granting both strength and corrosion resistance in the human body without causing corrosion-assisted cracking phenomena.
Most studies focused on improving the strength of cast pure Mg materials and their electrochemical properties, whereas the effects of these strategies on the resistance of Mg and its alloys to corrosion-assisted cracking is overlooked. It is thus of great importance to understand such strategies affect the SCC susceptibility in order to develop Mg-based implants that can guarantee an adequate resistance to the combined effect of the corrosive human body fluid and the mechanical loading characteristics of the human body.

1.2. Overcoming the drawbacks of Mg and its alloys in the biomedical sector

The application of Mg in the biomedical sector is hampered by two main drawbacks, i.e. the low strength of as-cast Mg and its high corrosion rate in the physiologic environments. Several approaches have been investigated to overcome those limitations, which can be classified into two main categories:

1) Alloying
2) Grain refinement

In addition, surface treatments have also been investigated to reduce the corrosion susceptibility.
In Section 1.2.1., the approaches to improve the corrosion resistance of as-cast Mg will be revised, while those to improve the mechanical strength will be reported in Section 1.2.2.

1.2.1. Corrosion mitigation strategies

The exceedingly high corrosion rate of as-cast Mg represents a severe limitation in its deployment as biomedical material. The corrosion rate of pristine Mg will lead to the desorption of the implant before the healing process is complete. In addition, the continuous desorption of the material can lead to an untimely failure of the implant. Furthermore, H_2 gas evolves from the corrosion process leading to the twofold problem of embrittlement due to the hydrogen embrittlement phenomenon [74] and to biocompatibility issues induced by hydrogen pockets that are harmful to the

surrounding tissue. Song et al. reported that the maximum tolerable H_2 evolution rate is 0.01 ml/(cm^2 day), which corresponds to a corrosion rate of 0.02 mm/year.

1.2.1.1. Alloying

One of the main causes of corrosion is the presence of second phases and impurities (in particular iron, copper and nickel) that are known to accelerate the corrosion of the Mg matrix due to the establishment of galvanic cells. Impurities and second phases deposited in the grain boundary region during the solidification are more cathodic with respect to the Mg matrix, which leads to the occurrence of inter-granular corrosion (Figure 1.1).

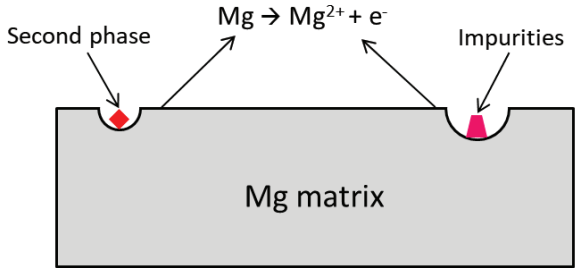

Figure 1.1: Schematic representation of inter-granular corrosion [58]

Song compared the amount of evolved hydrogen in Hank's solution for commercially pure and high pure Mg stating that purification reduces the H_2 evolution rate from 26 to 0.008 ml/cm^2/day [75]. This is in accordance with Hofstetter et al. [76], who reported an ultrahigh purity ZX50 Mg alloy to show greater corrosion resistance compared to high purity alloys (almost three times) and to standard purity alloy (over an order of magnitude). The main difference in these alloys is their impurity level, reported in Table 1.2.

Alloy	Fe (ppm)	Cu (ppm)	Ni (ppm)
standard purity ZX50	42	9	8
high purity ZX50	31	8	7
ultrahigh purity ZX50	0.5	0.09	0.05

Table 1.2. Impurity content of ZX50 alloys studied in Ref. [76]

Alloying elements have opposing effects: on the one hand, they improve the corrosion resistance through the "scavenger effect" and their passivation properties, while, on the other hand, they deteriorate the corrosion resistance via the formation of second phases if their solid solubility limit is exceeded (defined as the extent to which an element will dissolve in base materials without forming a different phase [77]). Zn and Mn, for example, help to overcome the harmful corrosive effect of Fe and Ni impurities as well as other heavy-metal elements ("scavenger effect"). In addition, the formation of dense passive films on the surface can inhibit the Cl^- permeation thereby controlling matrix

dissolution. However, most of the elements are characterized by a very low solubility (see Figure 1.2) and thus the insolubility of elements in Mg represents a problematic scenario from a corrosion perspective.

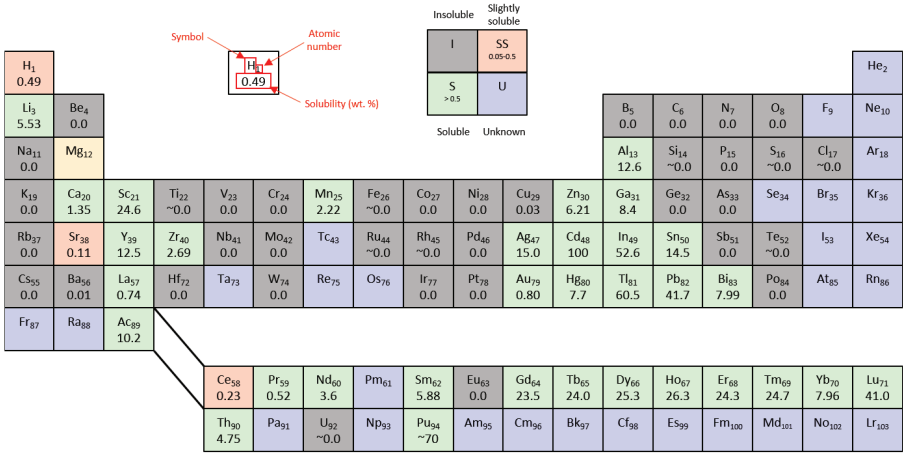

Figure 1.2: The maximum solubility of elements in magnesium (at any temperature) given in wt.% [78]

1.2.1.2. Grain size

Grain refinement has been reported to improve the corrosion resistance of Mg alloys. Grain boundaries are characterized by higher imperfection and higher internal energy compared to the Mg matrix, any corrosive attack acts preferentially on grain boundaries. Segregation of alloying elements and second phases occur on these boundaries leading to an accelerated cathodic activity of the surrounding Mg matrix. This would normally favour coarse grains, however, such segregations are continuously distributed in Mg alloys with finer grains leading to a more homogeneous corrosion behaviour acting as a corrosion barrier due to their passivation behaviour [56,79]. In addition, there are high compressive stresses within the oxide layer due to lattice mismatches with respect to the hexagonal Mg lattice, which cause cracks in the oxide and introducing a large volume fraction of grain boundaries has been shown to compensate this effect, leading to improved corrosion responses [80]. Furthermore, since grain boundaries provide nucleation sites for the growth of passivating oxide films (MgO), the smaller the grain size, the faster the formation of the MgO layer. Finally, the interfacial adherence of the MgO layer is higher at grain boundaries compared with the bulk [80,81]. Recently, in fact, Kim and Kim observed the formation of many isolated MgO nanocrystals in the fine-grained Mg substrate below the MgO layer, which may have been formed as oxygen atoms diffused from the surface into the grain boundaries of the matrix [82]. They proposed that the formation of the layer containing a mixture of MgO and Mg phases between the MgO layer and the Mg substrate is beneficial in decreasing the susceptibility of cracking of the MgO layer or the interface between MgO and the Mg substrate by acting as a buffer layer that decreases the sharpness of the tensile stress gradient across the boundary between the MgO layer and the Mg substrate. Finally, fine

grain sizes improve the corrosion assisted cracking resistance since they inhibit crack initiation and dislocation motion and lead to an increase in the number of barriers to crack propagation. In fact, high dislocation density has been found to decrease the electrochemical potential of the Mg matrix increasing the anodic dissolution [83]. Ben Hamu et al. reported the corrosion rate of AZ31 Mg alloys to be reduced by almost 17% when decreasing the grain size from a range of 2935 μm to a range of 9-14 μm [84]. This is in accordance with Liu et al. that reported finer grain sizes to lower weight losses (Figure 1.3) [85].

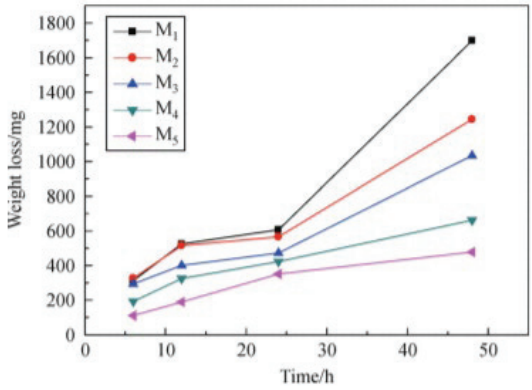

Figure 1.3: Weight loss of the pure Mg with different grain sizes immersed in the SBF. M1 data are characterized by the highest grain size (500 μm), whereas M5 by the lowest (233 μm). Reprinted with permission from Springer [85].

Grain refinement can be mainly obtained in two different ways. First, one can leverage the grain refinement effect of certain alloying elements. For example, the addition of Zr, Si, and Ca to pure magnesium is widely known to result in efficient grain refinement due to their growth restriction effects, i.e., constitutional undercooling, during solidification, but the effect of nucleant particles, either introduced with the alloying additions or as secondary phases formed as a result of these additions, may enhance the grain refinement [86]. Another, quite effective option, is to act on the manufacturing process and on the cooling strategies [84,85,87–89]. In fact, inducing high plastic deformations within the material is known to lead to the nucleation and growth of new finer grains as a consequence of the dynamic recrystallization phenomenon.

1.2.1.3. Surface Treatments

Corrosion is a surface phenomenon, and thus several ways have been studied to tune the surface in a way to reduce the corrosion on Mg and its alloys. Although the main way to reduce the corrosion rate was that of creating a barrier between Mg and the corrosive environment through the application of coatings (see Section 1.2.3.), microstructural and topological aspects can also be tuned for its reduction. Dealing with the former, the crystallographic orientations have been reported to affect the corrosion behavior of both pure Mg [90] and Mg alloys [91]. Experimental and theoretical studies showed that the

(0001) basal plane of AZ31 Mg alloy is more corrosion resistant than the other planes due to its higher atomic coordination and hence lower surface energy [91]. Xin et al. prepared AZ31 Mg samples with different crystallographic orientations by cutting the sample at different angles of 0°, 30°, 60°, and 90° from the rolled sheet, as shown in Figure 1.4a [92]. A rolled sheet of Mg alloy was reported frequently to have a strong basal texture on the rolled surface [93]. Therefore, the intensity of the basal texture on the Mg samples decreased with the larger angles, as shown in Figure 1.4b.

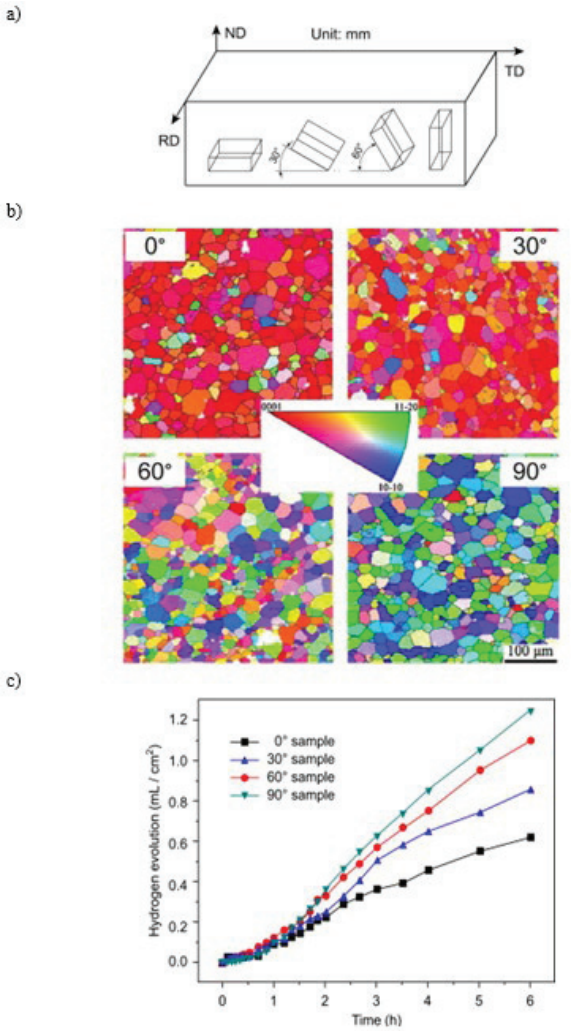

Figure 1.4: (a) Schematic illustration of sample preparation. (b) Inverse pole figure maps of 0°, 30°, 60°, and 90° samples. (c) Hydrogen evolution rates of the AZ31 Mg samples immersed in 3.5 wt% NaCl. Reprinted with permission from Elsevier [92].

As shown in Figure 1.4c, a clear relationship between the corrosion resistance and the crystallographic orientation exists, and this is in agreement with earlier data from the literature indicating that the corrosion resistance of Mg alloys increases with increased intensity of basal texture. Therefore, manufacturing Mg and its alloys with techniques able to induce a strong basal texture on the surface, or, even better, on the whole material, would reduce the corrosion rate.
Dealing with the topology of an implant, it is widely reported that rough and porous surfaces enhance the ingrowth of cells and tissue at the patient specific site of interest [94,95]. However, increasing the surface roughness is reported to increase the corrosion rate. In fact, Nguyen et al. evaluated the effect of different surfaces roughness on the corrosion rate of Mg after 6 hours of soaking in Hank's balanced salt solution at 37 °C [96] and reported a higher surface roughness leads to a higher corrosion rate (Figure 1.5), agreeing with the results obtained in Ref. [97].

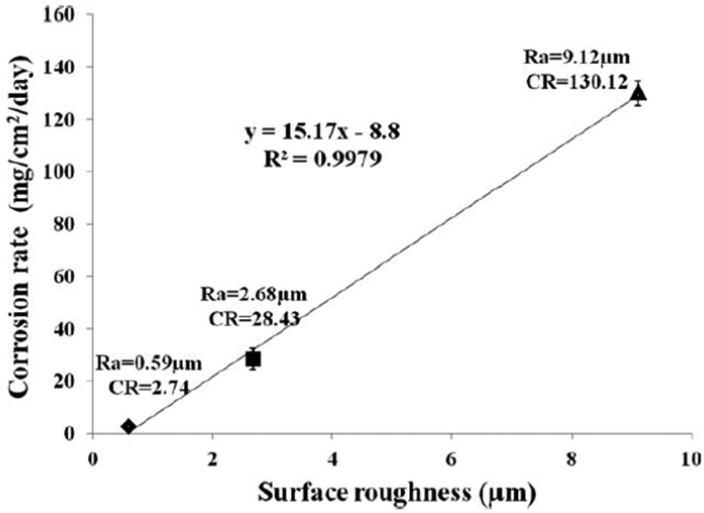

Figure 1.5: Corrosion rate as a function of the surface roughness. Reprinted with permission from Wiley [96].

Thus, aiming to reduce the corrosion rate, techniques providing smooth surfaces must be preferred.

1.2.2. Mechanical properties tuning

As already mentioned, the poor mechanical properties of cast pure Mg is a concern for their use in biomedical applications. In fact, many researchers studied the mechanical properties of a 99.99 wt.% pure Mg both under tensile, bending and compressive loads [98–101], but the properties reported are far lower compared to those of human bone (Table 1.3). It is worth mentioning that in the following, the fatigue properties have not been considered.

Material	Yield stress (MPa)	Ultimate tensile strength (MPa)	Elongation to failure (%)	Compressive yield strength (MPa)	Ultimate compressive strength (MPa)
Pure magnesium	20.4	84.5	13	99	157.7
Cortical bone	110	175	-	-	200

Table 1.3. Mechanical properties of cast 99.99 wt.% Magnesium (Ref. [98]) and of cortical bones (Ref. [99]).

To overcome this drawback of cast pure Mg, researchers started to investigate the improvement of the mechanical properties by means of different manufacturing processes, leveraging on the grain refinement effect. In fact, according to the famous Hall-Petch equation, the lower the grain size, the higher the yield strength. In addition, alloying elements are also known to improve the strength of the material due to the solid solution strengthening and precipitation hardening effect. Finally, the surface treatments used to improve the corrosion resistance might also influence the mechanical properties if they affect the crystallographic orientation.

1.2.2.1. Alloying

Depending on their concentration with respect to their solid solubility limits (see Figure 1.2.), the added alloying elements can strengthen the base material by means of two different ways:

1) *Solid solution strengthening*, if the concentration is lower than the solid solubility limit
2) *Precipitation hardening*, if the concentration is higher than the solid solubility limit

In case (1), the lattice is distorted either because the atoms of the alloying elements substitute atoms of the base metal in the crystalline lattice (substitutional solid solution) or because they interpose themselves between the atoms of the lattice (interstitial solid solution) (Figure 1.6). A distortion of the lattice strengthens the material delaying the movement of the dislocations.

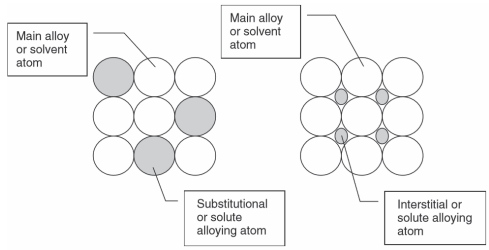

Figure 1.6: Schematic illustration of substitutional and interstitial alloying

In case (2), instead, the movement of the dislocations is limited by an appropriate distribution of particles at the grain boundaries and inside the grains. The difference with solid solution strengthening is that the latter is a single-phase system while the former has at least two phases, where the precipitate(s) are the reinforcing phase. It is preferable to obtain a homogeneous distribution of particles, since a non-homogeneous concentration of the precipitates leads to non-homogeneous mechanical properties. The size of the particles is very important: small size particles give better mechanical properties. The hardening effect is due to an increase in the difficulty of the dislocation motion and to an increase in the concentration of dislocations through the mechanism known as Orowan looping [102].

1.2.2.2. Grain Refinement

A metal is not usually made up of a single large crystal, but of many small crystals called grains, consisting in lattices with different orientation from the adjacent one. The formation of the grains begins during the solidification of the material: this last phase influences the characteristics of the grains, in terms of size and quantity. The interfaces between the different crystalline lattices are called grain boundary (Figure 1.7). The size and the orientation of the grains determine some mechanical properties of the material: the grain boundaries obstruct the plastic deformation, since the dislocations are hindered in movement near interfaces. This effect gets larger with increasing difference in crystalline lattice orientation from one grain to the other. It is thus easy to understand that a material with fine grains has a higher mechanical strength than one with coarse grains; the reduction of the grain size is an important hardening mechanism of the metal that can be obtained by means of heat treatments, such as quenching, different manufacturing process (extrusion, rolling), and/or severe plastic deformation techniques (Equal Channel Angular Pressing (ECAP)). For example, Gu et al. [103] compared the yield strength and the ultimate tensile strength (UTS) of as-cast and rolled 99.95 wt.% pure Mg reporting the rolling procedure to increase the yield strength and UTS of 460% and 97%, respectively, due to a reduction in the grain size of almost 90%.

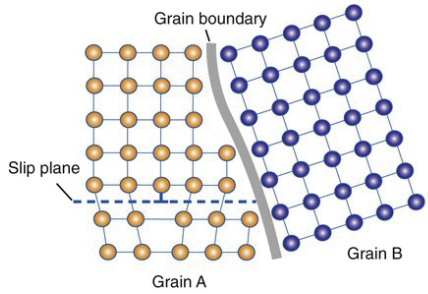

Figure 1.7: Effect of the grain boundary on the dislocation movement. Modified from Ref. [104].

The mathematical model representing this mechanism can be described with the Hall-Petch equation which shows how, at temperatures lower than recrystallization, a fine-grained metal is stronger than a coarse-grained one:

$$\sigma_S = \sigma_0 + \frac{k}{\sqrt{d}} \quad (1.2)$$

σ_s: yield strength
σ_0, k: constants characteristic of the material
d: average size of the crystalline grains

1.2.2.3. Crystallographic orientation

Mg has a variety of potential deformation mechanisms, such as basal slip, prismatic slip, pyramidal slip and twinning. Studies on the deformation of a single crystal showed that the critical resolved shear stress (τ_{CRSS}) for prismatic and pyramidal slips is ~100 times higher than for the basal slip at the room temperature [105]. From the geometric point of view, the activation of a particular slip system is given by the Schmid's law (Equation 1.3)

$$\sigma_s = \left(\frac{1}{m}\right)\tau_{CRSS} \quad (1.3)$$

$$m = \cos(\chi)\cos(\lambda) \quad (1.4)$$

Schmid factor (m) is given in Equation 1.4, where χ represents the angle between the direction of applied force and slip plane and λ represents the angle between applied force and slip direction, see Figure 1.8.

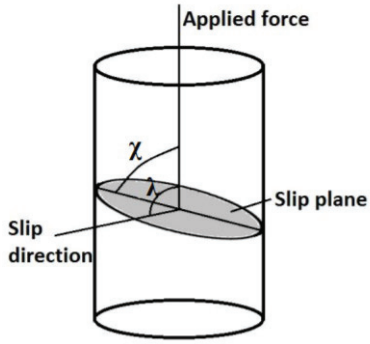

Figure 1.8: Slip plane and slip direction [106]

Figure 1.9 provides the results of tests carried out to determine the influence of the orientation on the yield point of the Mg basal plane. The theoretical curve was calculated according to Equation 1.3. The angle differences are very significant, with "soft orientation" with a slip plane of 45° to the tensile axis and "hard orientation" with a slip plane ~90 ° to the tensile axis [106].

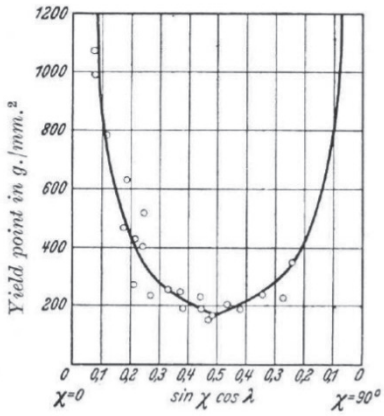

Figure 1.9: The yield point of magnesium basal plane as a function of orientation [106]

In a polycrystalline material, the orientation of individual grains could be random, and anisotropy of the single crystal deformation is suppressed. However, when non-random texture is present in the material, the anisotropy of mechanical properties of the single crystal is passed to the polycrystalline material. The degree of anisotropy is given by how strong the texture is. Therefore, in the Mg polycrystal, the crystallographic texture plays an important role for plastic deformation. A typical texture is formed when Mg and Mg alloys are thermomechanically processed. The formation of a strong basal texture during rolling and extrusion is observed with basal planes oriented parallel to the rolling and extrusion direction. With the strong basal texture developed by means of rolling and extrusion, both the yield and ultimate tensile strength were improved, while the ductility decreased [107–109]. To increase the ductility, the basal poles should be rotated by 45° with respect to the loading directions. However, this would lead to a reduction of the yield strength since lower applied stresses are then needed to produce yielding on the basal planes [110] and thus a trade-off is needed.

1.2.3. Coatings

The current literature reveals that a wide range of coating materials and coating formation techniques are employed to enhance the corrosion resistance of Mg-based alloys. Preventing the fluid to enter the Mg substrate, it is in fact possible to hinder the corrosion. For biomedical applications, there are several requirements for a coating. Most importantly, it must be (1) non-toxic to not cause any harm to the surrounding environment [111]. As the surface of the implant is where cells and new tissue will form, the coating must be (2) biocompatible for these to adhere and grow. This is in regards to both surface morphology and coating composition. Additionally, as Mg is biodegradable, the coating shall be (3) biodegradable as well. The aim in corrosion protection of Mg implants is to slow down the initial degradation rate so tissues have time to heal, hence a coating will need to have a (4) slower degradation rate than the Mg material itself. To be able to control and predict the degradation rate, uniform corrosion is desired, and it is therefore also advantageous if the coating has a (5) uniform

thickness. Uniformity also entails a (6) cracks-free and (7) pore-free nature of the protecting film. Although pores may induce osseointegration [28], they are known to reduce the protectiveness of the coating since they provide a path for fluids to reach the substrate. Moreover, pores enhance the possibility of localized corrosion which further can introduce corrosion induced cracking phenomena. Finally, (8) high adhesion and bonding strength between the coating and the substrate is fundamental to provide an effective barrier to the corrosive environment and to impede the delamination of the coating. The coating materials influence the first four requirements, while the coating techniques govern the remaining. In this Section, we will focus on the different coating techniques, describing them and evaluating their performances with respect to the requirements from 5 to 8.

1.2.3.1. Chemical conversion treatments

When preparing conversion coatings, the substrate is immersed in an electrolyte where chemical reactions between the substrate and the content in the electrolyte form an insoluble film on the substrate surface [112]. The most common conversion coatings used to improve the corrosion resistance of Mg for biomedical uses are fluoride- and phosphate-based coatings. The process is relatively short, varying from a few seconds to tens of seconds. Conversion coatings can have thicknesses ranging from a few nanometers to several micrometers, with the immersion time determining the thickness [111]. However, the film growth takes place at the metal/solution interface and thus, after the surface is completely covered by the coating layer, the conversion coating process stops, not allowing a full control of the coating thickness [113]. In addition, conversion coatings offer great adhesion to the substrate due to chemical bonds and forming a strong adhesion layer between the substrate and the coating [114]. However, Ref. [113], for example, reported the poor long-term protection of this class of coatings due to the presence of cracks and pores.

1.2.3.2. Anodizing

When an external voltage is applied during conversion coating, the process is called anodizing [112]. Plasma anodizing, namely micro-arc oxidation (MAO) [115] or plasma electrolytic oxidation (PEO) [116] treatment, is a relatively new anodizing process to provide protection to Mg alloys. In this anodizing process, an oxide film with a thickness of range from 5–200 μm develops on the substrate material at the Mg or Mg alloy surface. This occurs usually at high voltages driven by an electrical source in an alkaline electrolyte containing phosphate, silicate, borate, and organic substances. The MAO and PEO coatings were found to be mainly composed of MgO, with some other electrolyte-borne elements (Mg_2SiO_4, $Mg_3(PO_4)_2$ or $MgAl_2O_4$, etc.) [117–119]. The anodizing performance of Mg and its alloys generally depends on a range of key parameters of the process, such as electrolytic composition, applied constant voltage or current and substrate types [120]. However, cracks and micropores are generally produced in MAO or PEO coating films due to the sparking phenomenon at high voltage in the anodizing process, thus reducing the corrosion resistance of oxide films.

1.2.3.3. Chemical solution deposition

Among chemical solution deposition (CSD) techniques, the sol-gel process represents one of the most common techniques. The sol-gel process is a wet chemical method where the film is formed by colloidal suspension of either inorganic or metal organic precursors [121]. The process is simple, and defects as phase transformations and changes in microstructures are avoided because the process temperature is low. Sol-gel processing also results in fairly good adhesion between the coating and the substrate [122]. However, the process often tends to form dots or heaps on the surface rather than a uniform coating [123], which is a disadvantage for corrosion protection. In addition, the sol-gel coatings also tend to crack upon drying [121].
The sol-gel process can be carried out with different methods as for instance dip-coating, spin-coating, spray-coating and roll-coating. In dip-coating, one simply dips the specimen in the solution to then apply the coating. The thickness of the coating depends on the number of dips, the viscosity of the solution, and the dipping rate [124]. The method is suited for thicker coatings, as it is hard to control its thickness. With spin-coating and roll-coating, better thickness control is achieved [121]. In spin coating, the solution is applied at the middle of the specimen, and the specimen is then spun to evenly distribute the solution on the surface. In roll-coating, the solution is fed to a wheel, which rolls over the surface, and hence distributes the solution. The drawback of these two methods is that they are limited to flat specimens. Spray-coating can be applied to various shapes and is similar to dip-coating, with the difference that the coating is sprayed onto the substrate. Spray-coating can also provide a more uniform thickness than spin-coating.

1.2.3.4. Physical Vapor Deposition (PVD) techniques

In its most basic form, physical vapor deposition involves the evaporation of a condensable material and its subsequent condensation on a substrate surface. The coating material, often referred to as condensable material, is vaporized from a source (slug or target). The source material is situated a short distance away from the object to be coated, i.e. the substrate. The vapor is obtained by exposing the source (solid or liquid) to very high temperatures/kinetic energies [125,126]. The condensable material enters the vapor state and travels in vacuum in straight lines (flux) until it collides with a cold surface. As soon as the condensable vapor reaches a cool surface, the small agglomerate of atoms/single atoms start to impinge the surface rapidly losing their kinetic energy through lateral diffusion or surface diffusion. These eventually cool and condense on the surface to form a solid film. Depending on the condensable material to be deposited, a deposition temperature ranging from 380-550 °C or even higher is needed to obtain a dense coating [127]. If the substrate material is sensitive to heat, it is still possible to deposit material at lower temperatures, even at room temperature. At low substrate temperatures, however, the ability of the atoms of the coating material to impinge the substrate surface with enough kinetic energy to reach an active site for attachment is greatly reduced. The inability to diffuse into the surface makes the condensable material pack loosely [128]. As the first agglomerate of atoms form on the surface, they obstruct the path for the rest of the straight-moving flux resulting in the shadowing of a large number of spots on the substrate surface. In addition, the inability of atoms to diffuse into the surface of the substrate results in a loosely bound film [127].

These limitations are encountered in Mg and its alloys due to their low melting temperatures. The stability of the structure and exterior dimensions during processing cannot be guaranteed if Mg and its alloys are exposed to temperatures above 250 °C [129,130]. In most cases, the optimal deposition temperature to prevent solid-state reactions inside Mg alloy substrates is even lower [131]. To provide good adhesions when the substrate temperature is low, the only PVD processes that can be employed are those in which the energy required for the mobility of the atoms of the coating material is mostly supplied by a plasma or another high-energy flux (condensable flux, ion beam). These include plasma-enhanced PVD (PEPVD), sputter deposition, ion beam sputter deposition (IBSD), ion plating, ion beam-assisted deposition (IBAD), reactive ion beam-assisted deposition (RIBAD) and plasma immersed ion implantation and deposition (PIIID) [128,132–134]. The main difference between the ion-assisted deposition techniques and plasma enhanced techniques is that in the first class of techniques, the energetic ion source and the condensable material flux is separated, allowing more control of each deposition parameter. This, in turn, improves the coating properties compared to plasma enhanced techniques, where the ion flux and condensable material flux comes from the same plasma source [127]. However, the protectiveness of the PVD coatings is reduced by the formation of cracks due to the difference in the thermal expansion coefficient between the coating and the substrate that induces residual stresses on the coating leading to the formation of cracks [135,136]. In addition, the effectiveness of these coatings are also limited due to the fact that PVD techniques are line-of-sight deposition processes with limited applicability to 3D geometries, particularly undercuts [127].

1.2.3.5. Chemical Vapor Deposition (CVD) techniques

Chemical vapor deposition (CVD) is the collective name for a number of processes where a thin film is formed by chemical reactions between the substrate surface and the vapor. The coating is in fact deposited from the exposition of the substrate surface to one or more volatile precursors, which react and/or decompose on the substrate surface to produce the desired deposit. A characteristic feature of the CVD technique is its ability to distribute species evenly across the substrate surface, enabling the production of coatings of uniform thickness with a low porosity even on substrates of complicated geometric shapes [137,138]. Among the CVD techniques, Atomic Layer Deposition (ALD) stands out in terms of conformality, film density and the possibility for compositional control because of its self-limiting surface-gas phase reactions that have recently found application in corrosion protection [139,140]. The ALD-process can be divided into four steps [141,142]:

1) The main precursor is vaporized and fed into the reactor chamber, where a sufficient impact time leads to the complete coverage of available surface reactive sites on the specimen's surface. The precursor is often a coordination compound (a metal center with ligands).
2) The excess precursor (unreacted compounds) and the reaction products are thereafter purged (by an inert gas, usually N_2 or Ar) and pumped of the reactor chamber. This is an important step when the cycle is repeated to make sure that the precursor and co-reactant do not react with each other in the gas phase.

3) The second precursor, often a small molecule, is introduced when the system is cleared, which reacts with the molecules on the surface resulting from the reaction with the first precursor.
4) The system is then again purged and pumped.

This process, or cycle, deposits (ideally) a monolayer on the substrate surface at a time. To increase the thickness of the film, the cycle is repeated. For the process to work, it is crucial that the precursor and the co-reactant do not react with themselves nor with the reaction products. This is to make sure that the reactions happens on the substrate surface only, and that the process will be self-limiting in the sense that when the surface is saturated, the deposition stops [141]. ALD can be carried out at low processing temperatures in order to avoid temperature defects such as phase transformations. It provides good adhesion and reduces the cracks formation due to the limited processing temperature. However, ALD is time-demanding compared to other techniques due to slow growth rates.

1.3. Research objectives

Although some Mg alloys have been approved for the clinical protocol (K-MET™ Bioresorbable Bone screw obtained the approval from MFDS in Korea [143] for example), their deployment as materials for biomedical applications is still hampered by various limitations. In addition to the low strength of pure magnesium, the high corrosion rates of Mg and its alloys represent the main drawback. In fact, H_2 as a corrosion product has several harmful effects. First, the H_2 released from the corrosion process can influence the healing process increasing the pH: a pH higher than 8.5 is reported to inhibit the proliferation of hBMSCs [144]. In addition, if the H_2 forms large pockets, they may cause the death of patients through the blockage of the blood stream [145]. Moreover, an exceedingly high corrosion rate will lead to the desorption and/or the failure of the implant before the healing process is complete (three months according to [146]). In particular, the H_2 evolved from the corrosion process can embrittle the implant through the hydrogen embrittlement phenomenon (HE) [147], that, in combination with the anodic dissolution of Mg and its alloys, causes SCC. SCC is particularly dangerous as it leads to a sudden and catastrophic failure under mechanical loads that are otherwise considered safe. Yet the development of Mg-based implants granting both strength and corrosion resistance in the human body without causing SCC failure is still overlooked. In fact, several studies focused on different strategies to improve the strength of cast pure Mg and its electrochemical properties, but very few focused on the respective effect on the SCC susceptibility. This thesis aims thus to understand how some of the different procedures used to improve the strength and the corrosion resistance of Mg influence the SCC susceptibility. This was studied in seven papers, which are later presented in the thesis. This work can be divided into 5 parts:

1) The main mechanisms governing the SCC phenomenon and the different techniques used to improve the mechanical strength and the corrosion resistance of Mg has been reviewed in Paper I and in the Book. In Paper I, a deep discussion of the SCC phenomenon is provided together with a brief overview of some procedures used to improve the corrosion resistance. These procedures were further elaborated in the Book, and were confronted with procedures to

improve the mechanical strength. The interplay between these procedures is discussed. Several thermo-mechanical processes and severe plastic deformation techniques have been assessed, providing a benchmark of the more effective strategies to improve corrosion resistance, i.e. severe plastic deformation technique and surface treatments obtained by means of mechanical processing and coatings.

2) In Paper II, the effect of Equal Channel Angular Pressing (ECAP), an SPD technique, on the SCC susceptibility has been investigated. Slow strain rate tests (SSRT) have been carried out in simulated body fluid (SBF) to evaluate the effect of several ECAP passes on the SCC susceptibility of AZ31 alloy. The evaluation of the corrosion resistance together with the fracture surface analyses have been carried out to understand the different SCC susceptibility provided by the different ECAP treatments.
3) In Paper III, the effect of surface treatments obtained by means of mechanical processing on the SCC susceptibility of AZ31 alloy has been evaluated. In particular, cryogenic machining has been considered. The effect of the cryogenic machining on the SCC susceptibility has been assessed by means of SSRT in SBF and a full characterization of the machined surface integrity, including microstructural observations, residual stress, nano-hardness measurements and surface texture analyses were carried out together with the assessment of the corrosion properties to explain the observed results.
4) In Papers IV and V, the applicability of a new coating technique, i.e. Atomic Layer Deposition (ALD), for biomedical applications has been assessed. In particular, Paper IV compares the corrosion resistance provided by a TiO_2 coating obtained by ALD with that obtained by sputtering. Two different surface roughness and topologies have been considered in order to resemble the biological conditions. In Paper V, the biocompatibility provided by three different coating materials, i.e. TiO_2, ZrO_2 and HfO_2, has been assessed by means of MTS colorimetric assay using L929 cells and the results were discussed with respect to the corresponding corrosion performances.
5) Finally, Paper VI assesses the effects of TiO_2 and ZrO_2 ALD coatings on the SCC susceptibility of AZ31 alloy. SSRTs have been carried out in SBF. The evaluation of the corrosion resistance by means of potentiodynamic polarization curves and hydrogen evolution experiments together with the fracture surface analyses have been carried out to understand the different SCC susceptibilities provided by the two coating materials.

1.4. Experimental Procedures

The details of the experimental procedures are presented in the respective articles. However, a general overview of the methodology and the used equipment is provided in this section.

1.4.1. Material and metallography

The material used in this PhD work is AZ31 Mg alloy. Although Al alloys are not suitable for biomedical implants due to the toxicity deriving from the long-term effects

of exposure to Al such as reduced reproductive ability [148], dementia [149] and Alzheimer's disease [150,151], as emerged from Paper I and Paper II, AZ alloys, in particular AZ31, are the most studied. AZ31 has thus been chosen, allowing a comparison of the results obtained in this thesis with those reported in the literature. The AZ31 magnesium alloy used in this work was supplied in form of commercially available bars from Dynamic Metals Ltd (Dynamic Metals Ltd, Bedfordshire, UK) and the microstructure was assessed by means of Leica DMRETM Optical Microscope (Leica microsystems, Wetzlar, Germany). To do so, the samples were cut and prepared for microstructural analysis using SiC papers for grinding and colloidal silica for final polishing. The grain structure was revealed by etching using a solution of alcohol (95 ml), picric acid (5 g), and acetic acid (10 ml) for 10 s.
Corrosion experiments (Section 1.4.2.) and Stress Corrosion Cracking susceptibility (Section 1.4.3.) have been carried out using simulated body fluid (SBF) solution, preparing according to Ref. [152] and with the composition reported in Table 1.4.

Reagents	Amount
NaCl	8.035 g
$NaHCO_3$	0.355 g
KCl	0.225 g
$K_2HPO_4 \cdot 3H_2O$	0.231 g
$MgCl_2 \cdot 6H_2O$	0.311 g
1.0M-HCl	39 ml
$CaCl_2$	0.292 g
Na_2SO_4	0.072 g
Tris	6.118 g

Table 1.4: Reagents and their quantities for preparation of 1000 ml of the SBF solution according to [152].

1.4.2. Corrosion experiments

The corrosion performances of the AZ31 alloy was measured by means of potentiodynamic polarization curves and hydrogen evolution experiments. Samples of different shapes, sizes and surface conditions were used, and they are described in the according papers. However, the equipment used are the same for all the works and they are here described.

1.4.2.1. Potentiodynamic polarization curves

Potentiodynamic polarization tests were carried out on a Gamry Interface1000 potentiostat (Gamry Instruments, PA, USA), except in paper IV where an Amel^{TM} 2549 potentiostat (Amel Electrochemistry, Milano, Italy) was used. The electrochemical tests used three-electrode equipment with the AZ31 samples as a working electrode, a Hg/Hg_2SO_4 electrode as a reference electrode (except in paper IV where a saturated Calomel electrode was used). The samples were immersed in SBF solution. The temperature was set to 37±1°C to reproduce human body conditions. The potentiodynamic polarization curves were obtained applying a potential from ±1 V with

respect to the open circuit potential (OCP), obtained after a stabilization period of 30 min. The scan rate of the potentiodynamic polarization test was 0.5 mV/s. The area of the samples exposed to SBF was 1 cm^2 and corrosion current density was determined using the Tafel extrapolation method, according to the ASTM G5-14 standard [153]. The tests were repeated three times for each condition.

1.4.2.2. Hydrogen evolution experiments

The corrosion of one mole of Mg leads to the evolution of one mole of hydrogen gas (see Equation 1.1). This allows the measurement of Mg's corrosion rate through the collection of evolving hydrogen gas bubbles. This method allows to overcome the drawback of the mass loss rate, i.e. the fact that un-corroded areas of the metallic substrate underneath the corrosion products are also removed when complete removal of the corrosion products is achieved. Hence, hydrogen evolution tests were used. AZ31 Mg alloy was immersed individually in SBF at 37 °C for more than 72 hours. From each sample, the hydrogen bubbles were collected in a burette (Figure 1.10), according to an established protocol published elsewhere [154].

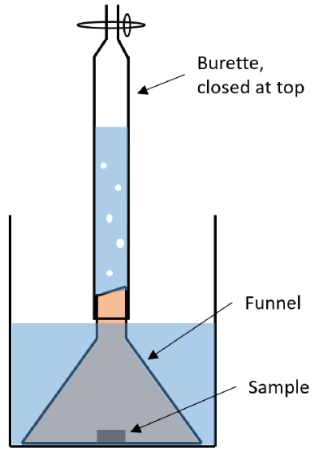

Figure 1.10: Schematic illustration of the set-up for the measurement of the evolved hydrogen volume.

1.4.3. Stress Corrosion Cracking (SCC) susceptibility

Slow strain rate tests are a common technique used for studying the combined effect of stress and corrosion/degradation process on the mechanical properties of a material, and they have been used in this PhD work to assess the SCC susceptibility. The SSRT experiments were carried out on dog-bone samples (the dimensions vary for each technique and they are reported in the respective papers) at a strain rate of $3.5 \cdot 10^{-6}$ s^{-1} in SBF solution at body temperature (37 ± 1°C). The strain rate value was chosen according to [155] to render the AZ31 alloy susceptible to SCC. A schematic representation of the experimental set-up is shown in Figure 1.11. The sample was immersed for the whole duration of the test and the SBF solution was constantly

changed by a pumping system. The SBF solution container was immersed in a water bath, which's temperature was constantly monitored with a thermometer. When the temperature was below its set value, a commercial resistance heating element placed inside the water bath automatically turned on until the desired temperature was reached again. In addition, while carrying out the SSRTs, the area of the specimen exposed to SBF was restricted to its gauge length using Teflon tapes wrapping the rest of the specimen, thus maintaining a constant area of exposure to the corrosive solution as well as avoiding the possibility of galvanic effects with other components of the testing set-up. For the sake of comparison, SSRTs were also carried out in air. SSRTs were repeated three times for reproducibility.

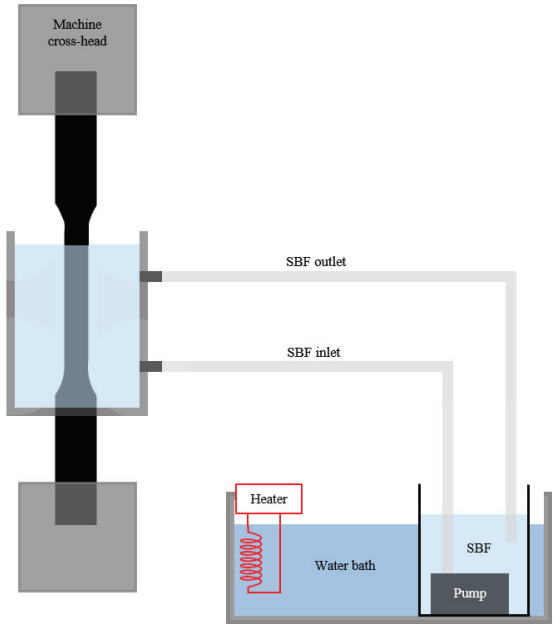

Figure 1.11: Schematic representation of the SSRT set-up.

In order to quantify the AZ31 SCC sensitivity, the susceptibility indices I_{UTS} and I_{ε} were calculated according to Eq. (1.5) and Eq. (1.6) [156]:

$$I_{UTS} = \frac{UTS_{air} - UTS_{SBF}}{UTS_{air}} \tag{1.5}$$

And

$$I_{\varepsilon} = \frac{\varepsilon_{air} - \varepsilon_{SBF}}{\varepsilon_{air}} \tag{1.6}$$

where UTS is the Ultimate Tensile Strength and ε the elongation at failure, both evaluated during tests conducted in SBF solution and air. When the value of the susceptibility index approaches zero, the material is considered to be highly resistant to SCC, namely the greater the index the greater the susceptibility to SCC.

1.4.4. Fractography

The specimen fracture surfaces of the samples tested were observed by means of a FEI Quanta 450 Scanning Electron Microscope (Thermo Fisher Scientific Inc., USA). Prior to fractographic evaluations, the samples tested in the corrosive environment were cleaned from the corrosion products by immersion for one minute in a solution prepared using 50 g chromium trioxide (CrO_3), 2.5 g silver nitrate ($AgNO_3$) and 5 g barium nitrate ($Ba(NO_3)_2$) in 250 ml distilled water, as suggested elsewhere [157]. Both the samples tested in air and in SBF were washed with distilled water and finally ultrasonically cleaned in acetone for 10 min before the fractographic evaluations.

1.5. List of publications and contributions

This thesis contains a general introductory part (Chapter 1) , a book and six journal papers on the topic of this research, which are included in chapters two to six. The book is presented in its short version and supplementary information can be found in Appendix 2.2.C.

Paper I:

Mg and Its Alloys for Biomedical Applications: Exploring Corrosion and Its Interplay with Mechanical Failure

Authors: Mirco Peron, Jan Torgersen, Filippo Berto

Metals 2017, 7(7), 252

DOI: *10.3390/met7070252*

Contribution: M.P. wrote the entire manuscript. J.T. and F.B. provided scientific guidance, proof reading and suggestions.

Graphical Abstract:

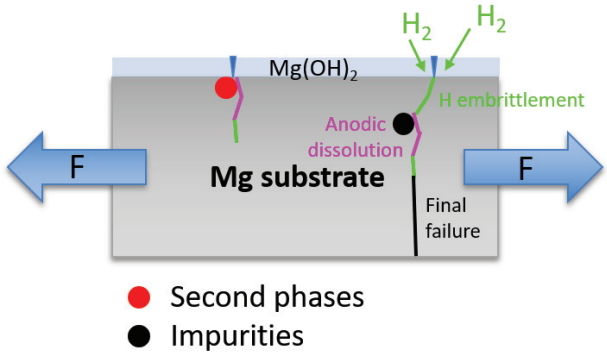

Figure 1.12: SCC failure mechanism consisting of the combination of the anodic dissolution and the cleavage-like fracture due to hydrogen embrittlement

Book:

Magnesium and Its Alloys as Implant Materials: Corrosion, Mechanical and Biological Performances

Authors: Mirco Peron, Filippo Berto, Jan Torgersen

CRC Press, Taylor & Francis Group, Boca Raton, Florida, United States, forthcoming April 2020

DOI: *10.1201/9781003000327*

Contribution: M.P. wrote the entire manuscript. F.B and J.T. provided scientific guidance, proof reading and suggestions.

Graphical Abstract:

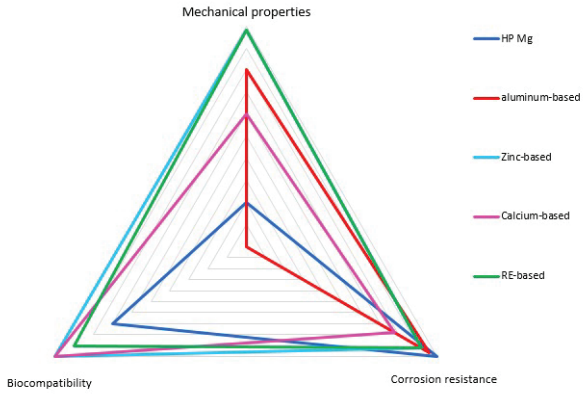

Figure 1.13: Radar chart of the main alloying families with respect to the mechanical properties, corrosion resistance and biocompatibility.

Paper II:

The effect of Equal Channel Angular Pressing on the Stress Corrosion Cracking susceptibility of AZ31 alloy in simulated body fluid

Authors: Mirco Peron, Pål Christian Skaret, Alberto Fabrizi, Roberto Montanari, Hans Jørgen Roven, Paolo Ferro, Filippo Berto, Jan Torgersen

Journal of the Mechanical Behavior of Biomedical Materials (resubmitted after minor revision, the reported version is that before revision)

Contribution: M.P. designed the study and wrote the manuscript. M.P. performed the Slow Strain Rate Tests, the corrosion experiments and the failure analyses. P.C.S. performed the ECAP treatment. A.F. performed the microstructural analyses. R.M. performed the hardness measurements. H.J.R., P.F., F.B. and J.T. provided scientific guidance, proof reading and suggestions.

Graphical Abstract:

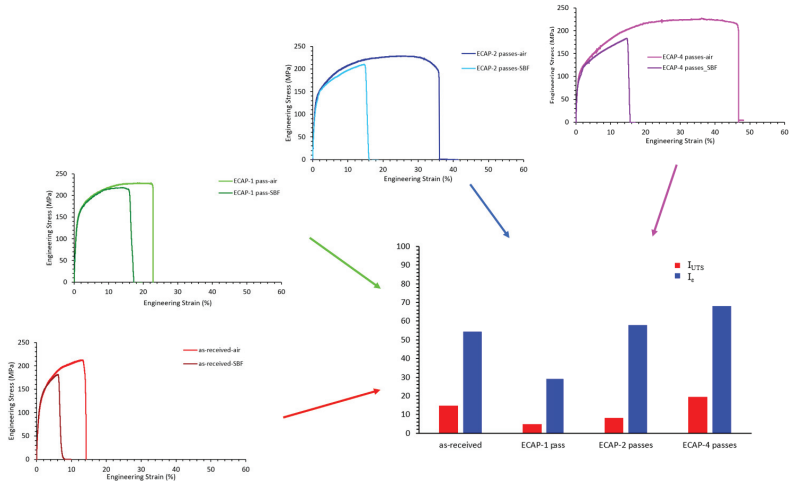

Figure 1.14: SCC susceptibility indexes of AZ31 sample in the as-received conditions and after 1, 2 and 4 passes of ECAP

Paper III:

Enhancement of stress corrosion cracking of AZ31 magnesium alloy in simulated body fluid thanks to cryogenic machining

Authors: Mirco Peron, Rachele Bertolini, Andrea Ghiotti, Jan Torgersen, Stefania Brushi, Filippo Berto

Journal of the Mechanical Behavior of Biomedical Materials 101 (2020) 103429

DOI: 10.1016/j.jmbbm.2019.103429

Contribution: M.P. and R.B. wrote the manuscript. M.P. designed the study and performed the Slow Strain Rate Tests. R.B. manufactured the samples and performed the microstructural analyses, the corrosion experiments and the failure analyses. A.G., J.T., S.B. and F.B. provided scientific guidance, proof reading and suggestions.

Graphical Abstract:

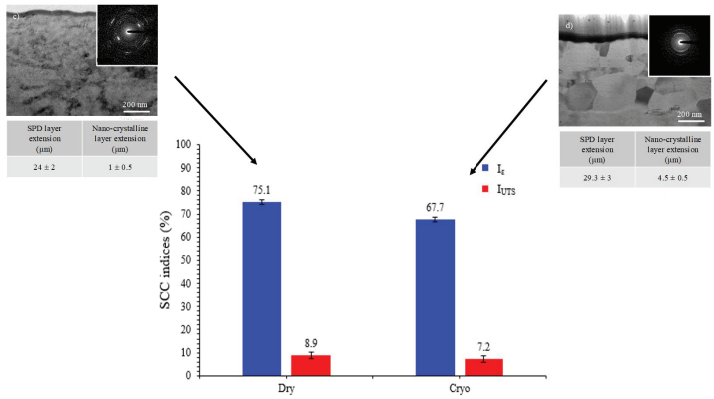

Figure 1.15: SCC susceptibility of dry and cryogenic machined AZ31 samples as a consequence of the different extension of the nano-crystalline layer

Paper IV:

On the comparison between the corrosion performances of sputtered and ALDed TiO_2 thin layer with different substrate roughness and topology

Authors: Mirco Peron, Abdulla Bin Afif, Anup Dadlani, Filippo Berto, Jan Torgersen

Surface and Coatings Technology (submitted paper)

Contribution: M.P. designed the study and wrote the manuscript. M.P. performed the corrosion experiments and the micro- and macro-morphological observation. A.B.A. coated the samples, performed the XPS analyses and, together with A.D., interpreted the XPS results. F.B. and J.T. provided scientific guidance, proof reading and suggestions.

Graphical Abstract:

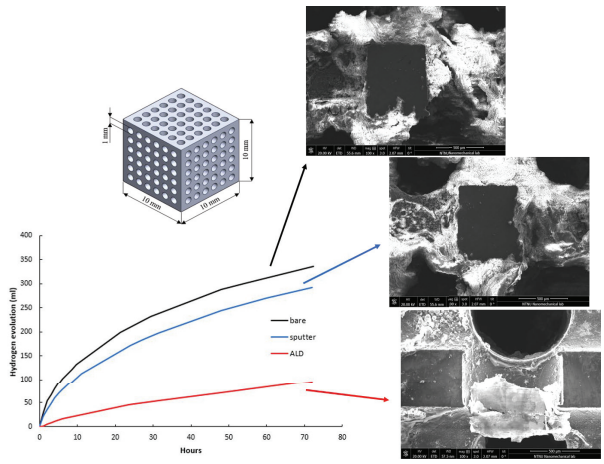

Figure 1.16: Hydrogen evolution of 3D porous structures with micro-morphologies of the undercuts and shadowed areas of the sliced 3D structures reporting the line-of-sight limitation of the sputter technique

Paper V:

On the evaluation of ALD TiO_2, ZrO_2 and HfO_2 coatings on corrosion and cytotoxicity performances

Authors: Mirco Peron, Susanna Cogo, Maria Bjelland, Abdulla Bin Afif, Anup Dadlani, Elisa Greggio, Filippo Berto, Jan Torgersen

Acta Biomaterialia (submitted paper)

Contribution: M.P. designed the study and wrote the manuscript. M.P. performed the micro- and macro-morphological observation and, together with M.B., the corrosion experiments. S.C. carried out the cytotoxicity tests and interpreted the results. A.B.A. coated the samples, performed the XPS analyses and, together with A.D., interpreted the XPS results. E.G., F.B. and J.T. provided scientific guidance, proof reading and suggestions.

Graphical Abstract:

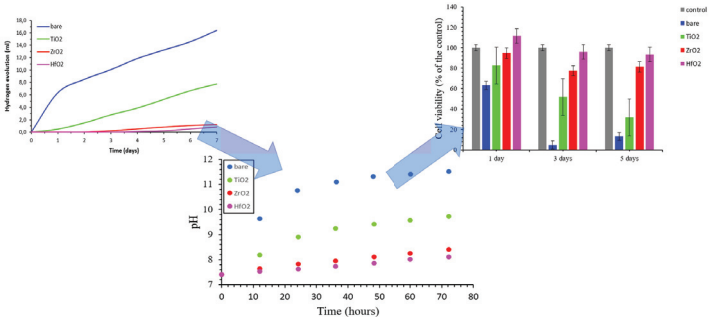

Figure 1.17: Link between corrosion behavior and cell viability of TiO_2, ZrO_2 and HfO_2 ALDed coated AZ31 samples

Paper VI:

Effect of titania and zirconia ALD coating on stress corrosion cracking susceptibility of AZ31 alloy in simulated body fluid

Authors: Mirco Peron, Abdulla Bin Afif, Anup Dadlani, Filippo Berto, Jan Torgersen

Materials & Design (submitted paper)

Contribution: M.P. designed the study and wrote the manuscript. M.P. performed the Slow Strain Rate Tests, the corrosion experiments and the failure analyses. A.B.A. coated the samples, performed the XPS analyses and, together with A.D., interpreted the XPS results. F.B. and J.T. provided scientific guidance, proof reading and suggestions.

Graphical Abstract:

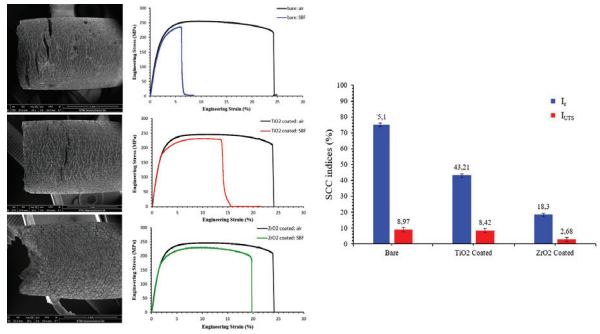

Figure 1.18: Effects of TiO_2 and ZrO_2 ALD coatings on the SCC susceptibility and on the ductility of AZ31 alloys tested in SBF

1.6. Thesis outline

The thesis is composed of an introductory chapter (Chapter 1), a collection of six journal papers and a book presented as Chapter 2 to 6, and the final chapter on conclusion and recommendation. A brief summary of the chapters is given below:

Chapter 1 summarizes the challenges of using Mg and its alloys as biomedical materials with a focus on the drawbacks related to corrosion and mechanical properties. A short description of the experimental procedures has been also provided in this chapter.

Chapter 2 contains the first paper and the book reviewing the different strategies employed to overcome the drawbacks of Mg and its alloys and the mechanisms controlling the corrosion-assisted cracking phenomena

Chapter 3 includes the second paper, which is about the effect of ECAP on the SCC susceptibility of AZ31 alloy. By modifying the bulk of the material with different passes of ECAP, the SCC susceptibility has been evaluated.

Chapter 4 of the thesis contains the third paper. The effect of cryogenic machining on the SCC behavior of AZ31 alloy has been assessed, carrying out a full characterization of the machined surface integrity to explain the observed results.

Chapter 5 of the thesis comprises the fourth and fifth papers on the introduction of the newly developed ALD technique in the biomedical field. Its corrosion performances were compared with those obtained by the commonplace sputter technique and the biocompatibility of three different ALDed coatings were investigated by means of MTS assay on L929 cells.

Chapter 6 includes the sixth paper on the effect of two different ALDed coatings on the SCC susceptibility of an AZ31 alloy.

Chapter 7 presents the concluding remarks of the performed researches during the course of PhD and recommendations for the future studies on the topic.

Bibliography chapter 1

[1] E. Regar, G. Sianos, P.W. Serruys, Stent development and local drug delivery., Br. Med. Bull. 59 (2001) 227–48. http://www.ncbi.nlm.nih.gov/pubmed/11756213 (accessed April 2, 2017).

[2] W. Greatbatch, C.F. Holmes, History of implantable devices, IEEE Eng. Med. Biol. Mag. 10 (1991) 38–41. https://doi.org/10.1109/51.84185.

[3] P.H. Long, Medical Devices in Orthopedic Applications, Toxicol. Pathol. 36 (2008) 85–91. https://doi.org/10.1177/0192623307310951.

[4] W. Khan, E. Muntimadugu, M. Jaffe, A.J. Domb, Implantable Medical Devices,

in: Springer US, 2014: pp. 33–59. https://doi.org/10.1007/978-1-4614-9434-8_2.
[5] M. Long, H.. Rack, Titanium alloys in total joint replacement—a materials science perspective, Biomaterials. 19 (1998) 1621–1639. https://doi.org/10.1016/S0142-9612(97)00146-4.
[6] E. Gultepe, D. Nagesha, S. Sridhar, M. Amiji, Nanoporous inorganic membranes or coatings for sustained drug delivery in implantable devices, Adv. Drug Deliv. Rev. 62 (2010) 305–315. https://doi.org/10.1016/j.addr.2009.11.003.
[7] S. Ramakrishna, J. Mayer, E. Wintermantel, K.W. Leong, Biomedical applications of polymer-composite materials: A review, Compos. Sci. Technol. 61 (2001) 1189–1224. https://doi.org/10.1016/S0266-3538(00)00241-4.
[8] J. Black, Biological performance of materials : fundamentals of biocompatibility, CRC Taylor & Francis, 2006.
[9] D.L. Hamblen, A.H.R.W. Simpson, J.C. Adams, J.C. Adams, Adams's outline of fractures, including joint injuries., Churchill Livingstone Elsevier, 2007.
[10] N. Li, Y. Zheng, Novel Magnesium Alloys Developed for Biomedical Application: A Review, J. Mater. Sci. Technol. 29 (2013) 489–502. https://doi.org/10.1016/J.JMST.2013.02.005.
[11] F. Witte, V. Kaese, H. Haferkamp, E. Switzer, A. Meyer-Lindenberg, C.J. Wirth, H. Windhagen, In vivo corrosion of four magnesium alloys and the associated bone response, Biomaterials. 26 (2005) 3557–3563. https://doi.org/10.1016/j.biomaterials.2004.09.049.
[12] Q. Chen, G.A. Thouas, Metallic implant biomaterials, Mater. Sci. Eng. R Reports. 87 (2015) 1–57. https://doi.org/10.1016/J.MSER.2014.10.001.
[13] T. Hanawa, Overview of metals and applications, in: Met. Biomed. Devices, Elsevier, 2010: pp. 3–24. https://doi.org/10.1533/9781845699246.1.3.
[14] T. Albrektsson, P.-I. Brånemark, H.-A. Hansson, J. Lindström, Osseointegrated Titanium Implants: *Requirements for Ensuring a Long-Lasting, Direct Bone-to-Implant Anchorage in Man*, Acta Orthop. Scand. 52 (1981) 155–170. https://doi.org/10.3109/17453678108991776.
[15] F. Rossi, N.P. Lang, E. De Santis, F. Morelli, G. Favero, D. Botticelli, Bone-healing pattern at the surface of titanium implants: an experimental study in the dog, Clin. Oral Implants Res. 25 (2014) 124–131. https://doi.org/10.1111/clr.12097.
[16] L.-N. Zhang, Z.-T. Hou, X. Ye, Z.-B. Xu, X.-L. Bai, P. Shang, The effect of selected alloying element additions on properties of Mg-based alloy as bioimplants: A literature review, Front. Mater. Sci. 7 (2013) 227–236. https://doi.org/10.1007/s11706-013-0210-z.
[17] M. Wang, BIOACTIVE CERAMIC-POLYMER COMPOSITES FOR TISSUE REPLACEMENT, in: 2004: pp. 8-1-8–29. https://doi.org/10.1142/9789812562227_0008.
[18] M.P. Staiger, A.M. Pietak, J. Huadmai, G. Dias, Magnesium and its alloys as orthopedic biomaterials: A review, Biomaterials. 27 (2006) 1728–1734. https://doi.org/10.1016/j.biomaterials.2005.10.003.
[19] E.P. DeGarmo, J.T. Black, R. a. Kohser, DeGarmo's Materials and Processes in Manufacturing, (2011) 1184. https://doi.org/10.1017/CBO9781107415324.004.
[20] L.J. Gibson, M.F. Ashby, Cellular solids : structure & properties, Pergamon Press, 1988.

https://books.google.co.uk/books/about/Cellular_solids.html?id=X6xVAAAAMAAJ (accessed March 31, 2017).
[21] A.C. Hänzi, A.S. Sologubenko, P.J. Uggowitzer, Design strategy for new biodegradable Mg–Y–Zn alloys for medical applications, Int. J. Mater. Res. 100 (2009) 1127–1136. https://doi.org/10.3139/146.110157.
[22] T.W. Bauer, J. Schils, The pathology of total joint arthroplasty.II. Mechanisms of implant failure., Skeletal Radiol. 28 (1999) 483–97. http://www.ncbi.nlm.nih.gov/pubmed/10525792 (accessed March 31, 2017).
[23] A.R. Dujovne, J.D. Bobyn, J.J. Krygier, J.E. Miller, C.E. Brooks, Mechanical compatibility of noncemented hip prostheses with the human femur, J. Arthroplasty. 8 (1993) 7–22. https://doi.org/10.1016/S0883-5403(06)80102-6.
[24] C.A. Engh, J.D. Bobyn, The influence of stem size and extent of porous coating on femoral bone resorption after primary cementless hip arthroplasty., Clin. Orthop. Relat. Res. (1988) 7–28. http://www.ncbi.nlm.nih.gov/pubmed/3370887 (accessed March 31, 2017).
[25] J. Kerner, R. Huiskes, G.H. van Lenthe, H. Weinans, B. van Rietbergen, C.A. Engh, A.A. Amis, Correlation between pre-operative periprosthetic bone density and post-operative bone loss in THA can be explained by strain-adaptive remodelling., J. Biomech. 32 (1999) 695–703. https://doi.org/10.1016/S0021-9290(99)00041-X.
[26] D.R. Sumner, J.O. Galante, Determinants of stress shielding: design versus materials versus interface., Clin. Orthop. Relat. Res. (1992) 202–12. http://www.ncbi.nlm.nih.gov/pubmed/1729005 (accessed March 31, 2017).
[27] T.M. Turner, D.R. Sumner, R.M. Urban, R. Igloria, J.O. Galante, Maintenance of proximal cortical bone with use of a less stiff femoral component in hemiarthroplasty of the hip without cement. An investigation in a canine model at six months and two years., J. Bone Joint Surg. Am. 79 (1997) 1381–90. http://www.ncbi.nlm.nih.gov/pubmed/9314401 (accessed March 31, 2017).
[28] B. Van Rietbergen, R. Huiskes, H. Weinans, D.R. Sumner, T.M. Turner, J.O. Galante, The mechanism of bone remodeling and resorption around press-fitted THA stems, J. Biomech. 26 (1993) 369–382. https://doi.org/10.1016/0021-9290(93)90001-U.
[29] J. Wolff, The Law of Bone Remodelling, Springer Berlin Heidelberg, Berlin, Heidelberg, 1986. https://doi.org/10.1007/978-3-642-71031-5.
[30] B.G. Pound, Corrosion behavior of metallic materials in biomedical applications . I . Ti and its alloys, 32 (2014) 1–20. https://doi.org/10.1515/corrrev-2014-0007.
[31] B.G. Pound, Corrosion behavior of metallic materials in biomedical applications . II . Stainless steels and Co-Cr alloys, 32 (2014) 21–41. https://doi.org/10.1515/corrrev-2014-0008.
[32] J.J. Jacobs, J.L. Gilbert, R.M. Urban, Corrosion of metal orthopaedic implants., J. Bone Joint Surg. Am. 80 (1998) 268–82. http://www.ncbi.nlm.nih.gov/pubmed/9486734 (accessed March 31, 2017).
[33] J.J. Jacobs, N.J. Hallab, A.K. Skipor, R.M. Urban, Metal degradation products: a cause for concern in metal-metal bearings?, Clin. Orthop. Relat. Res. (2003) 139–47. https://doi.org/10.1097/01.blo.0000096810.78689.62.
[34] I.B. Beech, J.A. Sunner, C.R. Arciola, P. Cristiani, Microbially-influenced corrosion: damage to prostheses, delight for bacteria., Int. J. Artif. Organs. 29

(2006) 443–52. http://www.ncbi.nlm.nih.gov/pubmed/16705614 (accessed June 20, 2017).
[35] M. Schinhammer, A.C. Hänzi, J.F. Löffler, P.J. Uggowitzer, Design strategy for biodegradable Fe-based alloys for medical applications, Acta Biomater. 6 (2010) 1705–1713. https://doi.org/10.1016/j.actbio.2009.07.039.
[36] D. Vojtěch, J. Kubásek, J. Šerák, P. Novák, Mechanical and corrosion properties of newly developed biodegradable Zn-based alloys for bone fixation, Acta Biomater. 7 (2011) 3515–3522. https://doi.org/10.1016/j.actbio.2011.05.008.
[37] R.J. Kroeze, M.N. Helder, L.E. Govaert, T.H. Smit, Biodegradable Polymers in Bone Tissue Engineering, Materials (Basel). 2 (2009) 833–856. https://doi.org/10.3390/ma2030833.
[38] L. Yang, L.-M. Zhang, Chemical structural and chain conformational characterization of some bioactive polysaccharides isolated from natural sources, Carbohydr. Polym. 76 (2009) 349–361. https://doi.org/10.1016/J.CARBPOL.2008.12.015.
[39] V.R. Sinha, R. Kumria, Polysaccharides in colon-specific drug delivery, Int. J. Pharm. 224 (2001) 19–38. https://doi.org/10.1016/S0378-5173(01)00720-7.
[40] R. Sun, J. M. Fang, A. Goodwin, J. M. Lawther, A. J. Bolton, Fractionation and characterization of polysaccharides from abaca fibre, Carbohydr. Polym. 37 (1998) 351–359. https://doi.org/10.1016/S0144-8617(98)00046-0.
[41] G. Crini, Recent developments in polysaccharide-based materials used as adsorbents in wastewater treatment, Prog. Polym. Sci. 30 (2005) 38–70. https://doi.org/10.1016/J.PROGPOLYMSCI.2004.11.002.
[42] T. Sato, G. Chen, T. Ushida, T. Ishii, N. Ochiai, T. Tateishi, J. Tanaka, Evaluation of PLLA–collagen hybrid sponge as a scaffold for cartilage tissue engineering, Mater. Sci. Eng. C. 24 (2004) 365–372. https://doi.org/10.1016/J.MSEC.2003.12.010.
[43] N.-T. Dai, M.R. Williamson, N. Khammo, E.F. Adams, A.G.A. Coombes, Composite cell support membranes based on collagen and polycaprolactone for tissue engineering of skin, Biomaterials. 25 (2004) 4263–4271. https://doi.org/10.1016/J.BIOMATERIALS.2003.11.022.
[44] T.-H. Chun, K.B. Hotary, F. Sabeh, A.R. Saltiel, E.D. Allen, S.J. Weiss, A Pericellular Collagenase Directs the 3-Dimensional Development of White Adipose Tissue, Cell. 125 (2006) 577–591. https://doi.org/10.1016/j.cell.2006.02.050.
[45] X. Zheng, B. Kan, M. Gou, S. Fu, J. Zhang, K. Men, L. Chen, F. Luo, Y. Zhao, X. Zhao, Y. Wei, Z. Qian, Preparation of MPEG–PLA nanoparticle for honokiol delivery in vitro, Int. J. Pharm. 386 (2010) 262–267. https://doi.org/10.1016/J.IJPHARM.2009.11.014.
[46] Y. Dong, S.-S. Feng, Methoxy poly(ethylene glycol)-poly(lactide) (MPEG-PLA) nanoparticles for controlled delivery of anticancer drugs, Biomaterials. 25 (2004) 2843–2849. https://doi.org/10.1016/j.biomaterials.2003.09.055.
[47] J.M. Kanczler, P.J. Ginty, J.J.A. Barry, N.M.P. Clarke, S.M. Howdle, K.M. Shakesheff, R.O.C. Oreffo, The effect of mesenchymal populations and vascular endothelial growth factor delivered from biodegradable polymer scaffolds on bone formation, Biomaterials. 29 (2008) 1892–1900. https://doi.org/10.1016/j.biomaterials.2007.12.031.

[48] L. Rimondini, N. Nicoli-Aldini, M. Fini, G. Guzzardella, M. Tschon, R. Giardino, In vivo experimental study on bone regeneration in critical bone defects using an injectable biodegradable PLA/PGA copolymer, Oral Surgery, Oral Med. Oral Pathol. Oral Radiol. Endodontology. 99 (2005) 148–154. https://doi.org/10.1016/J.TRIPLEO.2004.05.010.
[49] F. Rezgui, M. Swistek, J.M. Hiver, C. G'Sell, T. Sadoun, Deformation and damage upon stretching of degradable polymers (PLA and PCL), Polymer (Guildf). 46 (2005) 7370–7385. https://doi.org/10.1016/J.POLYMER.2005.03.116.
[50] Y. Li, C. Volland, T. Kissel, Biodegradable brush-like graft polymers from poly(D,L-lactide) or poly(D,L-lactide-coglycolide) and charge-modified, hydrophilic dextrans as backbone—in-vitro degradation and controlled releases of hydrophilic macromolecules, Polymer (Guildf). 39 (1998) 3087–3097. https://doi.org/10.1016/S0032-3861(97)10048-9.
[51] Y.-C. Wang, M.-C. Lin, D.-M. Wang, H.-J. Hsieh, Fabrication of a novel porous PGA-chitosan hybrid matrix for tissue engineering, Biomaterials. 24 (2003) 1047–1057. https://doi.org/10.1016/S0142-9612(02)00434-9.
[52] C.-Y. Hsieh, S.-P. Tsai, D.-M. Wang, Y.-N. Chang, H.-J. Hsieh, Preparation of γ-PGA/chitosan composite tissue engineering matrices, Biomaterials. 26 (2005) 5617–5623. https://doi.org/10.1016/j.biomaterials.2005.02.012.
[53] Y.F. Zheng, X.N. Gu, F. Witte, Biodegradable metals, Mater. Sci. Eng. R Reports. 77 (2014) 1–34. https://doi.org/10.1016/j.mser.2014.01.001.
[54] E. Aghion, Biodegradable Metals, Metals (Basel). 8 (2018) 804. https://doi.org/10.3390/met8100804.
[55] H. Hermawan, Biodegradable Metals: State of the Art, in: Springer, Berlin, Heidelberg, 2012: pp. 13–22. https://doi.org/10.1007/978-3-642-31170-3_2.
[56] R.K. Singh Raman, S. Jafari, S.E. Harandi, Corrosion fatigue fracture of magnesium alloys in bioimplant applications: A review, Eng. Fract. Mech. 137 (2015) 97–108. https://doi.org/10.1016/j.engfracmech.2014.08.009.
[57] G.E.J. Poinern, S. Brundavanam, D. Fawcett, Biomedical Magnesium Alloys: A Review of Material Properties, Surface Modifications and Potential as a Biodegradable Orthopaedic Implant, Am. J. Biomed. Eng. 2 (2012) 218–240. http://article.sapub.org/10.5923.j.ajbe.20120206.02.html#Ref (accessed April 19, 2018).
[58] M. Peron, J. Torgersen, F. Berto, Mg and Its Alloys for Biomedical Applications: Exploring Corrosion and Its Interplay with Mechanical Failure, Metals (Basel). 7 (2017) 252. https://doi.org/10.3390/met7070252.
[59] M.E. Maguire, J.A. Cowan, Magnesium chemistry and biochemistry, BioMetals. 15 (2002) 203–210. https://link.springer.com/content/pdf/10.1023/A:1016058229972.pdf (accessed April 19, 2018).
[60] R.M. Touyz, Magnesium in clinical medicine., Front. Biosci. 9 (2004) 1278–93. http://www.ncbi.nlm.nih.gov/pubmed/14977544 (accessed April 19, 2018).
[61] N.E. Saris, E. Mervaala, H. Karppanen, J.A. Khawaja, A. Lewenstam, Magnesium. An update on physiological, clinical and analytical aspects., Clin. Chim. Acta. 294 (2000) 1–26. http://www.ncbi.nlm.nih.gov/pubmed/10727669 (accessed April 19, 2018).

[62] J.G. Gums, Magnesium in cardiovascular and other disorders., Am. J. Health. Syst. Pharm. 61 (2004) 1569–76. http://www.ncbi.nlm.nih.gov/pubmed/15372830 (accessed April 19, 2018).
[63] J. Walker, S. Shadanbaz, T.B.F. Woodfield, M.P. Staiger, G.J. Dias, Magnesium biomaterials for orthopedic application: a review from a biological perspective., J. Biomed. Mater. Res. B. Appl. Biomater. 102 (2014) 1316–31. https://doi.org/10.1002/jbm.b.33113.
[64] D. Liu, D. Yang, X. Li, S. Hu, Mechanical properties, corrosion resistance and biocompatibilities of degradable Mg-RE alloys: A review, J. Mater. Res. Technol. (2018). https://doi.org/10.1016/J.JMRT.2018.08.003.
[65] X.N. Gu, W.R. Zhou, Y.F. Zheng, Y. Cheng, S.C. Wei, S.P. Zhong, T.F. Xi, L.J. Chen, Corrosion fatigue behaviors of two biomedical Mg alloys - AZ91D and WE43 - In simulated body fluid, Acta Biomater. 6 (2010) 4605–4613. https://doi.org/10.1016/j.actbio.2010.07.026.
[66] W.-D. Mueller, M. Lucia Nascimento, M.F. Lorenzo de Mele, Critical discussion of the results from different corrosion studies of Mg and Mg alloys for biomaterial applications☆, Acta Biomater. 6 (2010) 1749–1755. https://doi.org/10.1016/j.actbio.2009.12.048.
[67] K. Chen, J. Dai, X. Zhang, Improvement of corrosion resistance of magnesium alloys for biomedical applications, Corros. Rev. 33 (2015) 101–117. https://doi.org/10.1515/corrrev-2015-0007.
[68] C.P. Mccord, J.J. Prendergast, S.F. Meek, G.C. Harrold, Chemical gas gangrene from metallic magnesium, Indust Med [Beloit]. 11 (1942) 71–76. https://eurekamag.com/research/024/316/024316820.php (accessed April 19, 2018).
[69] H.L. Logan, Mechanism of Stress-Corrosion Cracking in the AZ31B Magnesium Alloy, J. Res. Natl. Bur. Stand. (1934). 61 (1958) 503–508.
[70] M.S. Bhuiyan, Y. Mutoh, T. Murai, S. Iwakami, Corrosion fatigue behavior of extruded magnesium alloy AZ61 under three different corrosive environments, Int. J. Fatigue. 30 (2008) 1756–1765. https://doi.org/10.1016/j.ijfatigue.2008.02.012.
[71] S. Jafari, R.K.S. Raman, C.H.J. Davies, J. Hofstetter, P.J. Uggowitzer, J.F. Löffler, Stress corrosion cracking and corrosion fatigue characterisation of MgZn1Ca0.3 (ZX10) in a simulated physiological environment, J. Mech. Behav. Biomed. Mater. 65 (2017) 634–643. https://doi.org/10.1016/J.JMBBM.2016.09.033.
[72] M.B. Kannan, R.K.S. Raman, In vitro degradation and mechanical integrity of calcium-containing magnesium alloys in modified-simulated body fluid, Biomaterials. 29 (2008) 2306–2314. https://doi.org/10.1016/J.BIOMATERIALS.2008.02.003.
[73] S. Jafari, R.K.S. Raman, C.H.J. Davies, Stress corrosion cracking of an extruded magnesium alloy (ZK21) in a simulated body fluid, Eng. Fract. Mech. 201 (2018) 47–55. https://doi.org/10.1016/J.ENGFRACMECH.2018.09.002.
[74] M. Kappes, M. Iannuzzi, R.M. Carranza, Hydrogen Embrittlement of Magnesium and Magnesium Alloys: A Review, J. Electrochem. Soc. 160 (2013) C168–C178. https://doi.org/10.1149/2.023304jes.
[75] G. Song, Control of biodegradation of biocompatable magnesium alloys, Corros.

Sci. 49 (2007) 1696–1701. https://doi.org/10.1016/J.CORSCI.2007.01.001.
[76] J. Hofstetter, M. Becker, E. Martinelli, A.M. Weinberg, B. Mingler, H. Kilian, S. Pogatscher, P.J. Uggowitzer, J.F. Löffler, High-Strength Low-Alloy (HSLA) Mg–Zn–Ca Alloys with Excellent Biodegradation Performance, JOM. 66 (2014) 566–572. https://doi.org/10.1007/s11837-014-0875-5.
[77] D. Persaud-Sharma, A. McGoron, Biodegradable Magnesium Alloys: A Review of Material Development and Applications, J. Biomim. Biomater. Tissue Eng. 12 (2012) 25–39. https://doi.org/10.4028/www.scientific.net/JBBTE.12.25.
[78] M. Peron, J. Torgersen, F. Berto, Magnesium and its alloys as implant materials : corrosion, mechanical and biological performances, n.d.
[79] F. Witte, N. Hort, C. Vogt, S. Cohen, K.U. Kainer, R. Willumeit, F. Feyerabend, Degradable biomaterials based on magnesium corrosion, Curr. Opin. Solid State Mater. Sci. 12 (2008) 63–72. https://doi.org/10.1016/j.cossms.2009.04.001.
[80] N. Birbilis, K.D. Ralston, S. Virtanen, H.L. Fraser, C.H.J. Davies, Grain character influences on corrosion of ECAPed pure magnesium, Corros. Eng. Sci. Technol. 45 (2010) 224–230. https://doi.org/10.1179/147842209X12559428167805.
[81] K.D. Ralston, N. Birbilis, C.H.J. Davies, Revealing the relationship between grain size and corrosion rate of metals, Scr. Mater. 63 (2010) 1201–1204. https://doi.org/10.1016/J.SCRIPTAMAT.2010.08.035.
[82] H.S. Kim, W.J. Kim, Enhanced corrosion resistance of ultrafine-grained AZ61 alloy containing very fine particles of Mg17Al12 phase, Corros. Sci. 75 (2013) 228–238. https://doi.org/10.1016/J.CORSCI.2013.05.032.
[83] G. Ben-Hamu, A. Eliezer, E.M. Gutman, RETRACTED: Electrochemical behavior of magnesium alloys strained in buffer solutions, Electrochim. Acta. 52 (2006) 304–313. https://doi.org/10.1016/J.ELECTACTA.2006.05.009.
[84] G. Ben Hamu, D. Eliezer, L. Wagner, The relation between severe plastic deformation microstructure and corrosion behavior of AZ31 magnesium alloy, J. Alloys Compd. 468 (2009) 222–229. https://doi.org/10.1016/J.JALLCOM.2008.01.084.
[85] Y. Liu, D. Liu, C. You, M. Chen, Effects of grain size on the corrosion resistance of pure magnesium by cooling rate-controlled solidification, Front. Mater. Sci. 9 (2015) 247–253. https://doi.org/10.1007/s11706-015-0299-3.
[86] Y.C. Lee, A.K. Dahle, D.H. Stjohn, The role of solute in grain refinement of magnesium, Metall. Mater. Trans. A Phys. Metall. Mater. Sci. 31 (2000) 2895–2906. https://doi.org/10.1007/BF02830349.
[87] G.R. Argade, S.K. Panigrahi, R.S. Mishra, Effects of grain size on the corrosion resistance of wrought magnesium alloys containing neodymium, Corros. Sci. 58 (2012) 145–151. https://doi.org/10.1016/J.CORSCI.2012.01.021.
[88] Y.-C. Zhao, G.-S. Huang, G.-G. Wang, T.-Z. Han, F.-S. Pan, Influence of Grain Orientation on the Corrosion Behavior of Rolled AZ31 Magnesium Alloy, Acta Metall. Sin. (English Lett. 28 (n.d.). https://doi.org/10.1007/s40195-015-0337-2.
[89] R. Bertolini, S. Bruschi, A. Ghiotti, L. Pezzato, M. Dabalà, The Effect of Cooling Strategies and Machining Feed Rate on the Corrosion Behavior and Wettability of AZ31 Alloy for Biomedical Applications, Procedia CIRP. 65 (2017) 7–12. https://doi.org/10.1016/J.PROCIR.2017.03.168.
[90] M. Liu, D. Qiu, M.C. Zhao, G. Song, A. Atrens, The effect of crystallographic

orientation on the active corrosion of pure magnesium, Scr. Mater. 58 (2008) 421–424. https://doi.org/10.1016/j.scriptamat.2007.10.027.
[91] G.L. Song, R. Mishra, Z. Xu, Crystallographic orientation and electrochemical activity of AZ31 Mg alloy, Electrochem. Commun. 12 (2010) 1009–1012. https://doi.org/10.1016/j.elecom.2010.05.011.
[92] R. Xin, B. Li, L. Li, Q. Liu, Influence of texture on corrosion rate of AZ31 Mg alloy in 3.5wt.% NaCl, Mater. Des. 32 (2011) 4548–4552. https://doi.org/10.1016/j.matdes.2011.04.031.
[93] T.C. Chang, J.Y. Wang, C.M. O, S. Lee, Grain refining of magnesium alloy AZ31 by rolling, in: J. Mater. Process. Technol., 2003: pp. 588–591. https://doi.org/10.1016/S0924-0136(03)00797-0.
[94] R. Smeets, B. Stadlinger, F. Schwarz, B. Beck-Broichsitter, O. Jung, C. Precht, F. Kloss, A. Gröbe, M. Heiland, T. Ebker, T. Ebker, Impact of Dental Implant Surface Modifications on Osseointegration, Biomed Res. Int. 2016 (2016) 1–16. https://doi.org/10.1155/2016/6285620.
[95] T. Albrektsson, A. Wennerberg, Oral implant surfaces: Part 1--review focusing on topographic and chemical properties of different surfaces and in vivo responses to them., Int. J. Prosthodont. 17 (n.d.) 536–43. http://www.ncbi.nlm.nih.gov/pubmed/15543910 (accessed October 30, 2017).
[96] T.L. Nguyen, A. Blanquet, M.P. Staiger, G.J. Dias, T.B.F. Woodfield, On the role of surface roughness in the corrosion of pure magnesium in vitro, J. Biomed. Mater. Res. Part B Appl. Biomater. 100B (2012) 1310–1318. https://doi.org/10.1002/jbm.b.32697.
[97] T. Nguyen, J. Waterman, M. Staiger, T. Woodfield, Controlling *in vitro* corrosion rate of pure Mg with rough surface texture via biomimetic coating systems, Corros. Eng. Sci. Technol. 47 (2012) 358–364. https://doi.org/10.1179/1743278212Y.0000000023.
[98] Y.-L. Zhou, Y. Li, D.-M. Luo, Y. Ding, P. Hodgson, Microstructures, mechanical and corrosion properties and biocompatibility of as extruded Mg–Mn–Zn–Nd alloys for biomedical applications, Mater. Sci. Eng. C. 49 (2015) 93–100. https://doi.org/10.1016/j.msec.2014.12.057.
[99] P. Trivedi, K.C. Nune, R.D.K. Misra, Degradation behaviour of magnesium-rare earth biomedical alloys, Mater. Technol. 31 (2016) 726–731. https://doi.org/10.1080/10667857.2016.1213550.
[100] Y. Pan, S. He, D. Wang, D. Huang, T. Zheng, S. Wang, P. Dong, C. Chen, In vitro degradation and electrochemical corrosion evaluations of microarc oxidized pure Mg, Mg–Ca and Mg–Ca–Zn alloys for biomedical applications, Mater. Sci. Eng. C. 47 (2015) 85–96. https://doi.org/10.1016/J.MSEC.2014.11.048.
[101] Y. Wan, G. Xiong, H. Luo, F. He, Y. Huang, X. Zhou, Preparation and characterization of a new biomedical magnesium–calcium alloy, Mater. Des. 29 (2008) 2034–2037. https://doi.org/10.1016/J.MATDES.2008.04.017.
[102] F. Sun, Y.F. Gu, J.B. Yan, Z.H. Zhong, M. Yuyama, Phenomenological and microstructural analysis of intermediate temperatures creep in a Ni–Fe-based alloy for advanced ultra-supercritical fossil power plants, Acta Mater. 102 (2016) 70–78. https://doi.org/10.1016/J.ACTAMAT.2015.09.006.
[103] X. Gu, Y. Zheng, Y. Cheng, S. Zhong, T. Xi, In vitro corrosion and biocompatibility of binary magnesium alloys, Biomaterials. 30 (2009) 484–498.

https://doi.org/10.1016/J.BIOMATERIALS.2008.10.021.
[104] 17: Wrought Metals | Pocket Dentistry, (n.d.). https://pocketdentistry.com/17-wrought-metals/ (accessed February 19, 2020).
[105] J. Koike, T. Kobayashi, T. Mukai, H. Watanabe, M. Suzuki, K. Maruyama, K. Higashi, The activity of non-basal slip systems and dynamic recovery at room temperature in fine-grained AZ31B magnesium alloys, Acta Mater. 51 (2003) 2055–2065. https://doi.org/10.1016/S1359-6454(03)00005-3.
[106] E. Schmid, W. Boas, PLASTICITY OF CRYSTALS WITH SPECIAL REFERENCE TO METALS, n.d.
[107] J. Peng, Z. Zhang, Z. Liu, Y. Li, P. Guo, W. Zhou, Y. Wu, The effect of texture and grain size on improving the mechanical properties of Mg-Al-Zn alloys by friction stir processing, Sci. Rep. 8 (2018). https://doi.org/10.1038/s41598-018-22344-3.
[108] X. Zhao, S. Li, Y. Xue, Z. Zhang, An investigation on microstructure, texture and mechanical properties of AZ80 Mg alloy processed by annular channel angular extrusion, Materials (Basel). 12 (2019). https://doi.org/10.3390/ma12061001.
[109] S. Huang, M. Li, J.E. Allison, S. Zhang, D. Li, Y. Peng, Effects of direct extrusion process on microstructure, texture evolution and yield strength of magnesium alloy AZ31, in: Magnes. Technol., 2012: pp. 349–354. https://doi.org/10.1007/978-3-319-48203-3_64.
[110] A. Yamashita, Z. Horita, T.G. Langdon, Improving the mechanical properties of magnesium and a magnesium alloy through severe plastic deformation, Mater. Sci. Eng. A. 300 (2001) 142–147. https://doi.org/10.1016/S0921-5093(00)01660-9.
[111] E. Zhang, Phosphate treatment of magnesium alloy implants for biomedical applications, in: Surf. Modif. Magnes. Its Alloy. Biomed. Appl., Elsevier Inc., 2015: pp. 23–57. https://doi.org/10.1016/B978-1-78242-078-1.00002-5.
[112] L.F.M. da Silva, A. Öchsner, R.D. Adams, Handbook of Adhesion Technology: Second Edition, Springer International Publishing, 2018. https://doi.org/10.1007/978-3-319-55411-2.
[113] T.F. da Conceição, N. Scharnagl, Fluoride conversion coatings for magnesium and its alloys for the biological environment, in: Surf. Modif. Magnes. Its Alloy. Biomed. Appl., Elsevier Inc., 2015: pp. 3–21. https://doi.org/10.1016/B978-1-78242-078-1.00001-3.
[114] X.B. Chen, K. Chong, T.B. Abbott, N. Birbilis, M.A. Easton, Biocompatible strontium-phosphate and manganese-phosphate conversion coatings for magnesium and its alloys, in: Surf. Modif. Magnes. Its Alloy. Biomed. Appl., Elsevier Inc., 2015: pp. 407–432. https://doi.org/10.1016/B978-1-78242-078-1.00015-3.
[115] Y.M. Wang, F.H. Wang, M.J. Xu, B. Zhao, L.X. Guo, J.H. Ouyang, Microstructure and corrosion behavior of coated AZ91 alloy by microarc oxidation for biomedical application, Appl. Surf. Sci. 255 (2009) 9124–9131. https://doi.org/10.1016/j.apsusc.2009.06.116.
[116] P. Gupta, G. Tenhundfeld, E.O. Daigle, D. Ryabkov, Electrolytic plasma technology: Science and engineering-An overview, Surf. Coatings Technol. 201 (2007) 8746–8760. https://doi.org/10.1016/j.surfcoat.2006.11.023.
[117] R. Arrabal, E. Matykina, P. Skeldon, G.E. Thompson, A. Pardo, Transport of

species during plasma electrolytic oxidation of WE43-T6 magnesium alloy, J. Electrochem. Soc. 155 (2008). https://doi.org/10.1149/1.2823374.
[118] C.E. Barchiche, E. Rocca, C. Juers, J. Hazan, J. Steinmetz, Corrosion resistance of plasma-anodized AZ91D magnesium alloy by electrochemical methods, Electrochim. Acta. 53 (2007) 417–425. https://doi.org/10.1016/j.electacta.2007.04.030.
[119] Q. Cai, L. Wang, B. Wei, Q. Liu, Electrochemical performance of microarc oxidation films formed on AZ91D magnesium alloy in silicate and phosphate electrolytes, Surf. Coatings Technol. 200 (2006) 3727–3733. https://doi.org/10.1016/j.surfcoat.2005.05.039.
[120] N. Nassif, I. Ghayad, Corrosion protection and surface treatment of magnesium alloys used for orthopedic applications, Adv. Mater. Sci. Eng. 2013 (2013). https://doi.org/10.1155/2013/532896.
[121] R.M. Pilliar, Sol-gel surface modification of biomaterials, in: Surf. Coat. Modif. Met. Biomater., Elsevier Inc., 2015: pp. 185–217. https://doi.org/10.1016/B978-1-78242-303-4.00006-5.
[122] R.I.M. Asri, W.S.W. Harun, M.A. Hassan, S.A.C. Ghani, Z. Buyong, A review of hydroxyapatite-based coating techniques: Sol-gel and electrochemical depositions on biocompatible metals, J. Mech. Behav. Biomed. Mater. 57 (2016) 95–108. https://doi.org/10.1016/j.jmbbm.2015.11.031.
[123] S. Hiromoto, Chemical solution deposition of hydroxyapatite and octacalcium phosphate coatings for magnesium and its alloys to improve biocompatibility, in: Surf. Modif. Magnes. Its Alloy. Biomed. Appl., Elsevier Inc., 2015: pp. 60–80. https://doi.org/10.1016/B978-1-78242-078-1.00003-7.
[124] C. Augello, H. Liu, Surface modification of magnesium by functional polymer coatings for neural applications, in: Surf. Modif. Magnes. Its Alloy. Biomed. Appl., Elsevier Inc., 2015: pp. 335–353. https://doi.org/10.1016/B978-1-78242-078-1.00012-8.
[125] J.E. Mahan, Physical Vapor Deposition of Thin Films, Phys. Vap. Depos. Thin Film. by John E. Mahan, Pp. 336. ISBN 0-471-33001-9. Wiley-VCH , January 2000. (2000) 336.
[126] D.M. Mattox, Handbook of Physical Vapor Deposition (PVD) Processing, Elsevier Inc., 2007. https://doi.org/10.1016/c2009-0-18800-1.
[127] I.S. Abela, Physical vapour deposition on Mg alloys for biomedical applications, in: Surf. Modif. Magnes. Its Alloy. Biomed. Appl., Elsevier Inc., 2015: pp. 81–100. https://doi.org/10.1016/B978-1-78242-078-1.00004-9.
[128] T. Itoh, Ion Beam Assisted Film Growth, Elsevier, 1989. https://doi.org/10.1016/c2009-0-08798-4.
[129] M.M. Avedesian, H. Baker, ASM International. Handbook Committee., Magnesium and magnesium alloys, ASM International, 1999.
[130] I. Polmear, D. St. John, J.F. Nie, M. Qian, Light Alloys: Metallurgy of the Light Metals: Fifth Ed., Elsevier Inc., 2017.
[131] K. Meshinchi, Improving the Properties of Magnesium Alloys for High Temperature Applications, in: Magnes. Alloy. - Des. Process. Prop., InTech, 2011. https://doi.org/10.5772/13022.
[132] A. Anders, Handbook of plasma immersion ion implantation and deposition, Wiley, 2000.

[133] A.H. Deutchman, R.J. Partyka, Ion Beam Enhanced Deposited (IBED) Tribological Coatings for Non-Ferrous Alloys, n.d. www.beamalloytechnologies.com (accessed January 16, 2020).
[134] M. Klingenberg, J. Arps, R. Wei, J. Demaree, J. Hirvonen, Practical applications of ion beam and plasma processing for improving corrosion and wear protection, Surf. Coatings Technol. 158–159 (2002) 164–169. https://doi.org/10.1016/S0257-8972(02)00194-9.
[135] S. Il Pyun, Y.G. Yoon, E. Lugscheider, R. Mathesius, Relationship between interfacial reaction and adhesion at PVD TiO2 film-metal (Ti or Al) interfaces, Surf. Coatings Technol. 61 (1993) 233–237. https://doi.org/10.1016/0257-8972(93)90231-C.
[136] C. (Christoph) Leyens, M. (Manfred) Peters, John Wiley & Sons., Wiley InterScience (Online service), Titanium and titanium alloys : fundamentals and applications, Wiley-VCH, 2003.
[137] P.M. Martin, Handbook of Deposition Technologies for Films and Coatings : Science, Applications and Technology., Elsevier Science, 2009.
[138] O. Graniel, M. Weber, S. Balme, P. Miele, M. Bechelany, Atomic layer deposition for biosensing applications, Biosens. Bioelectron. 122 (2018) 147–159. https://doi.org/10.1016/J.BIOS.2018.09.038.
[139] X. Liu, Q. Yang, Z. Li, W. Yuan, Y. Zheng, Z. Cui, X. Yang, K.W.K. Yeung, S. Wu, A combined coating strategy based on atomic layer deposition for enhancement of corrosion resistance of AZ31 magnesium alloy, Appl. Surf. Sci. 434 (2018) 1101–1111. https://doi.org/10.1016/J.APSUSC.2017.11.032.
[140] E. Marin, A. Lanzutti, L. Guzman, L. Fedrizzi, Chemical and electrochemical characterization of TiO2/Al2O3 atomic layer depositions on AZ-31 magnesium alloy, J. Coatings Technol. Res. 9 (2012) 347–355. https://doi.org/10.1007/s11998-011-9372-8.
[141] H.C.M. Knoops, S.E. Potts, A.A. Bol, W.M.M. Kessels, Atomic Layer Deposition, in: Handb. Cryst. Growth, Elsevier, 2015: pp. 1101–1134. https://doi.org/10.1016/B978-0-444-63304-0.00027-5.
[142] P.R. Chalker, Photochemical atomic layer deposition and etching, Surf. Coatings Technol. 291 (2016) 258–263. https://doi.org/10.1016/j.surfcoat.2016.02.046.
[143] The Efficacy and Safety of Magnesium Alloy Screw as a Novel Bioabsorbable Material in Patients Due to Hand Fractures - Tabular View - ClinicalTrials.gov, (n.d.). https://clinicaltrials.gov/ct2/show/record/NCT02456415 (accessed October 11, 2018).
[144] L.-E. Monfoulet, P. Becquart, D. Marchat, K. Vandamme, M. Bourguignon, E. Pacard, V. Viateau, H. Petite, D. Logeart-Avramoglou, The pH in the Microenvironment of Human Mesenchymal Stem Cells Is a Critical Factor for Optimal Osteogenesis in Tissue-Engineered Constructs, Tissue Eng. Part A. 20 (2014) 1827–1840. https://doi.org/10.1089/ten.tea.2013.0500.
[145] C.. Wen, M. Mabuchi, Y. Yamada, K. Shimojima, Y. Chino, T. Asahina, Processing of biocompatible porous Ti and Mg, Scr. Mater. 45 (2001) 1147–1153. https://doi.org/10.1016/S1359-6462(01)01132-0.
[146] I. Adekanmbi, C.Z. Mosher, H.H. Lu, M. Riehle, H. Kubba, K.E. Tanner, Mechanical behaviour of biodegradable AZ31 magnesium alloy after long term in vitro degradation, Mater. Sci. Eng. C. 77 (2017) 1135–1144.

https://doi.org/10.1016/j.msec.2017.03.216.
[147] R.G. Song, C. Blawert, W. Dietzel, A. Atrens, A study on stress corrosion cracking and hydrogen embrittlement of AZ31 magnesium alloy, Mater. Sci. Eng. A. 399 (2005) 308–317. https://doi.org/10.1016/j.msea.2005.04.003.
[148] J.L. Domingo, Reproductive and developmental toxicity of aluminum: A review, Neurotoxicol. Teratol. 17 (1995) 515–521. https://doi.org/10.1016/0892-0362(95)00002-9.
[149] B. Venugopal, T.D. Luckey, Metal toxicity in mammals. Volume 2. Chemical toxicity of metals and metalloids., Met. Toxic. Mammals. Vol. 2. Chem. Toxic. Met. Met. (1978). https://www.cabdirect.org/cabdirect/abstract/19781476480 (accessed May 16, 2017).
[150] T.P. Flaten, Aluminium as a risk factor in Alzheimer's disease, with emphasis on drinking water., Brain Res. Bull. 55 (2001) 187–96. http://www.ncbi.nlm.nih.gov/pubmed/11470314 (accessed May 16, 2017).
[151] S.S.A. El-Rahman, Neuropathology of aluminum toxicity in rats (glutamate and GABA impairment)., Pharmacol. Res. 47 (2003) 189–94. http://www.ncbi.nlm.nih.gov/pubmed/12591013 (accessed May 16, 2017).
[152] T. Kokubo, H. Takadama, How useful is SBF in predicting in vivo bone bioactivity?, Biomaterials. 27 (2006) 2907–2915. https://doi.org/10.1016/J.BIOMATERIALS.2006.01.017.
[153] ASTM G5 - 14 Standard Reference Test Method for Making Potentiodynamic Anodic Polarization Measurements, (n.d.). https://compass.astm.org/Standards/HISTORICAL/G5-14.htm (accessed December 3, 2019).
[154] G. Song, A. Atrens, D. StJohn, An Hydrogen Evolution Method for the Estimation of the Corrosion Rate of Magnesium Alloys, in: Magnes. Technol. 2001, John Wiley & Sons, Inc., Hoboken, NJ, USA, 2013: pp. 254–262. https://doi.org/10.1002/9781118805497.ch44.
[155] M. Bobby Kannan, W. Dietzel, C. Blawert, A. Atrens, P. Lyon, Stress corrosion cracking of rare-earth containing magnesium alloys ZE41, QE22 and Elektron 21 (EV31A) compared with AZ80, Mater. Sci. Eng. A. 480 (2008) 529–539. https://doi.org/10.1016/J.MSEA.2007.07.070.
[156] L. Choudhary, R.K. Singh Raman, J. Hofstetter, P.J. Uggowitzer, In-vitro characterization of stress corrosion cracking of aluminium-free magnesium alloys for temporary bio-implant applications, Mater. Sci. Eng. C. 42 (2014) 629–636. https://doi.org/10.1016/J.MSEC.2014.06.018.
[157] D. Thirumalaikumarasamy, K. Shanmugam, V. Balasubramanian, Comparison of the corrosion behaviour of AZ31B magnesium alloy under immersion test and potentiodynamic polarization test in NaCl solution, J. Magnes. Alloy. 2 (2014) 36–49. https://doi.org/10.1016/J.JMA.2014.01.004.

Chapter 2

Understanding the corrosion, mechanical and biological performances of Mg and its alloys and their interplay with SCC

2.1. Paper I: Mg and Its Alloys for Biomedical Applications: Exploring Corrosion and Its Interplay with Mechanical Failure

M. Peron[1], J. Torgersen, F. Berto

Department of Mechanical and Industrial Engineering, Norwegian University of Science and Technology (NTNU), Richard Birkelands vei 2b, 7034, Trondheim

Abstract[2]

The future of biomaterial design will rely on temporary implant materials that degrade while tissues grow, releasing no toxic species during degradation and no residue after full regeneration of the targeted anatomic site. In this aspect, Mg and its alloys are receiving increasing attention because they allow both mechanical strength and biodegradability. Yet their use as biomedical implants is limited due to their poor corrosion resistance and the consequential mechanical integrity problems leading to corrosion assisted cracking. This review provides the reader with an overview of current biomaterials, their stringent mechanical and chemical requirements and the potential of Mg alloys to fulfil them. We provide insight into corrosion mechanisms of Mg and its alloys, the fundamentals and established models behind stress corrosion cracking and corrosion fatigue. We explain Mgs unique negative differential effect and approaches to describe it. Finally, we go into depth on corrosion improvements, reviewing literature on high purity Mg, on the effect of alloying elements and their tolerance levels, as well as research on surface treatments that allow to tune degradation kinetics. Bridging fundamentals aspects with current research activities in the field, this review intends to give a substantial overview for all interested readers; potential and current researchers and practitioners of the future not yet familiar with this promising material.

Keywords: Mg alloys; biocompatible; corrosion; crack growth; corrosion assisted cracking

2.1.1. Introduction

In the last decades, concurrent with the increased lifetime in today's world population, the amount of people undergoing surgical procedures involving the implantation of medical devices is continuously growing [1]. These implants are generally used for applications that ensure a substantial improvement in patients' quality of life, such as orthopaedics, pacemakers, cardiovascular stents, defibrillators, neural prosthetics and drug delivery systems [2–5]. Among these, orthopaedic surgery is the most important

[1] Corresponding author
[2] *Metals* 2017, 7(7), 252

[4], characterized by the highest annual growth rate. Indeed, according to Long and Rach [6], almost 90% of the population over 40 years is affected by degenerative joint diseases. Total hip replacements are predicted to represent half of the estimated total number of operations in 2030 [7]. For this reason, the research has centred on new biocompatible materials and on improving their performances [8–10]. Especially strength and corrosion resistance in human body fluid (HBF) has been a major issue of research [11].

Tailoring biomaterials to their specific use, many important properties must be considered. First, they must be bioinert or bioactive [12]; the former means that the organism has a coexistence with the material without noticeable change in the organism and/or exogenous material, whereas the latter implies that there is an interaction with and/or a response from living tissue, e.g., the formation of direct biochemical bonds with the surface of the material in bioceramics. Further, they must not evoke a sustained inflammatory response once implanted in the human body, have appropriate mechanical properties for their use and include appropriate permeability and processability for designed applications [13].

Several materials provide these properties and they can be divided into four main classes [4,14]: metals [15], polymers [16,17], ceramics [12,18] and composite materials [14,19]. It is worth to note that implant design, and therefore material choice, depends on the application of the devices and on the environment in which they are employed (Table 2.1.1).

Table 2.1.1: Biomedical applications of biocompatible materials [4,12,14,15,17,19–21].

Application	**Material**
Spinal fixation	stainless steel; Ti, Ti alloys
Bone fixation (bone plate, screw, wire, bone nail, etc.)	stainless steel; Ti, Ti alloys; PMMA; PS; CF/PEEK; CF/Epoxy; CF/PS; Bio-Glass/PU; Bio-Glass/PS; PET/SR; PET/Hydrogel; CF/LCP; GF/PEEK; Bone particles/PMMA; Ti/PMMA; UHMWPE/PMMA; UHMWPE; GF/PMMA; CF/PMMA; KF/PMMA; PMMA/PMMA; Bio-Glass/Bis-GMA; CF/PP; CF/PS; CF/PLLA; CF/PLA; KF/PC; HA/PE; PLLA/PLDLA; PGA/PGA; Alumina; Zirconia; Tricalcium phosphate; Bio-Glass-Metal fiber composite; Bio-Glass
Artificial joint	Co-Cr-Mo alloy; Ti alloys; Alumina; Zirconia; PET/SR;CF/UHMWPE; PET/Hydrogel; CF/Epoxy; CF/C; CF/PS; CF/PEEK; CF/PTFE; CF/UHMWPE; CF/PE; UHMWPE/UHMWPE; HA/HDPE; Metal Bio-Glass coatings
Spinal spacer	stainless steel; Ti alloys
Dental implant and bridge	Ti; Ti alloys; Au; CF/C; SiC/C; Alumina; Bio-Glass; HA;

	Bio-Glass coated alumina; Bio-Glass coated vitallium; Au-Cu-Ag; Au-Cu-Ag-Pt-Pd; UHMWPE/PMMA; CF/PMMA; GF/PMMA; KF/PMMA;
Tendon/Ligament/Cartilage Replacement	PET/PU; PTFE/PU; CF/PTFE; CF/C; PET/PHEMA; KF/PMA; KF/PE; CF/PTFE; CF/PLLA; GF/PU; PP; ePTFE; PET/PET; PA; PU; PLGA

Despite the recent technological evolution of polymeric and ceramic materials, metals, such as stainless steel, cobalt-chromium , and titanium alloys, are still the most used materials in biomedical applications, covering 70% of the total production volume [15,22,23].
What makes these materials irreplaceable are their high:

(1) Strength
(2) Fracture toughness
(3) Ductility
(4) Fatigue life
(5) Wear resistance and
(6) Corrosion resistance

It is widely reported [14,24] that bones are subjected to a stress of about 4 MPa on a daily basis and hip joints may experience a load as high as 10 times of the body weight in some cases, these implantable devices require high properties in terms of (1) and (2). Moreover, a high percentage of elongation at fracture (3) is needed in order to prevent brittle failure leading to the predominant choice of metallic implants as bioimplant materials. The human body also experiences dynamic loads: Ramakrishna et al. [14] reported that hip joints are subjected to loads applied for 1×10^6 cycles per year making (4) a requirement. This kind of joints are also affected by sliding issues potentially leading to the formation of wear debris if (5) is not high enough. This again causes acute immune response resulting in inflammation and/or fibrosis [4]. Finally, implanting materials in the human body necessitates great biocompatibility implying that they do not release any toxic substances into the body (6).
However, since the mechanical properties of metals highly differ from those of human bone, they are not always suitable for medical devices (see Table 2.1.2.): the bigger the difference in elastic modulus, the higher the occurrence of stress-shielding, which is a phenomenological consequence of stress distribution changes [25–33]. Bones adapt to the changed stress field according to the Wolff's law [34], resulting in the bone either becoming more porous (internal remodelling) or thinner (external remodelling), leading to a higher risk of implant failure. Considering a hip joint, for example, upon the implantation of a respective prosthesis, the entire bone-biomaterial system can be abstracted as two springs in parallel (Figure 2.1.1).

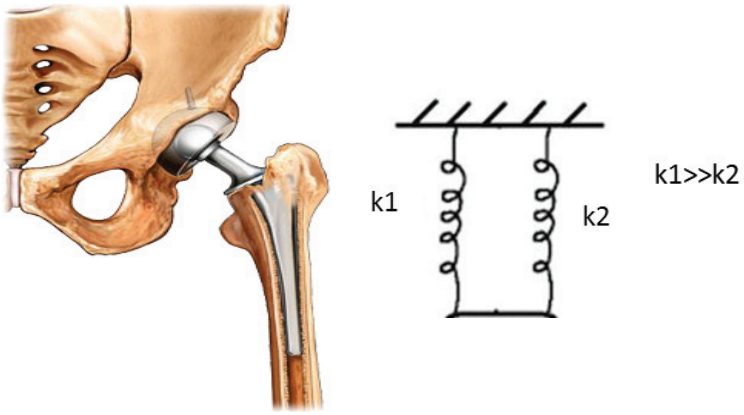

(**a**) (**b**)

Figure 2.1.1: (**a**) Total hip joint representation and (**b**) schematic view of two springs in parallel, where *k*1 and *k*2 are implant and bone stiffness, respectively. (From [35]).

The load redistribution phenomenon is strictly related to the stiffness ratio according to:

$$\frac{\sigma_1}{\sigma_2} = \frac{E_1}{E_2} \qquad (2.1.1)$$

where σ and *E* is applied stress and material stiffness, respectively. Subscripts 1 and 2 refer to implant and bone, respectively. As the load on the bone decreases with the implant, the bone will become less dense and thinner due to the insufficient stimuli for continued remodelling (Figure 2.1.2.).

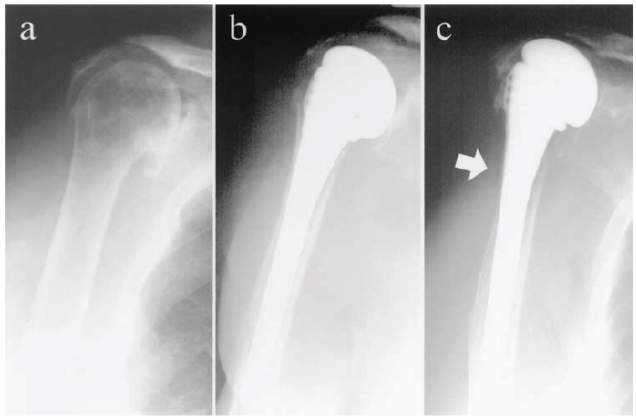

Figure 2.1.2: Stress-shielding example in shoulder replacement surgery; (**a**) preoperative image; (**b**) image immediately after the surgery; (**c**) image after 7 years

from the surgery; arrow indicates the region of bone resorption. Reproduced with permission from [36], Copyright Elsevier, 2003.

Stress induced bone remodelling is widely described in literature [31,32,37] and several models have been proposed to explain this phenomenon. Van Rietbergen et al. [33] stated that the bone mass is regulated by the remodelling signal S, which is the strain energy (U) per unit of mass:

$$S = \frac{U}{\rho} \tag{2.1.2}$$

where ρ is the bone density. Bone remodelling as described in Equation (3) corresponds to the rate of net bone-mass turnover $\frac{dM}{dt}$ and happens when S differs from the characteristic reference value S_{ref} describing the remodelling signal in non-operated conditions:

$$\frac{dM}{dt} = S - S_{ref} \tag{2.1.3}$$

The theory further assumes that no remodeling takes place when $S - S_{ref}$ does not exceed a threshold. Huiskes et al. [38] agreed that local strain perturbation governs the remodelling process by means of an interaction with osteocytes, since they are widely reported to be transductor of mechanical signals [39–42]. They suggested that increased (or decreased) strain signals the osteocyte to transmit stimuli to the bone surface, where bone is formed (or removed) until the strain normalizes.

Table 2.1.2: Comparison of the mechanical properties of natural bone with various implant materials [11,15,19,43–46].

Properties	Natural Bone	Stainless Steel	Ti Alloy	Co-Cr Alloy	Magnesium
Density (g/cm^3)	1.7–2.0	7.9–8.1	4.4–4.5	8.3–9.2	1.74–2.0
Elastic modulus (MPa)	3–20	189–205	110–117	230	41–45
Tensile strength (MPa)	80–150	480–620	930–1140	900–1540	170–270
Compressive yield strength (MPa)	130–180	170–310	758–1117	450–1000	65–100
Elongation at failure (%)	1–7	30–40	8–15	30–45	6–20
Fracture toughness (MPa m$^{1/2}$)	3–6	50–200	55–115	100	15–40

In certain biomedical applications, especially fixators such as bone plates, screws, pins and stents, biomedical devices are required to stay inside the human body only for a restricted period, i.e. as long as bones heal. Thus, materials that ideally degrade in the same manner and speed as natural bone heals [10,47,48] are widely required to be utilized for these temporary devices. Biodegradable materials allow circumventing

cumbersome second surgeries involving the removal of the old implant. Besides complications and distress for the patient, this also increases insurance costs [49–55]. However, classic metallic materials as those above are not biodegradable and, if not removed, lead to long-term complications, as local inflammations due to the potential release of cytotoxic ions as a consequence of corrosion or wear processes [22,23,56–58]. It is therefore very attractive to identify materials that degrade in the same way as bone heals, dissolving entirely after complete healing. In this process, these materials must not cause any toxic, allergic, inflammatory or cancerous effects.

In recent years, researchers and clinicians have employed a variety of compositions, properties and forms in which polymers are available to best match the specifications of the materials' desired biomedical function [4,13,16,20,59]. However, they tend to be too flexible and too weak for load-bearing applications required in orthopaedic surgery. Moreover, they may also absorb liquids and swell, leach undesirable products such as monomers, fillers and antioxidants, and, furthermore, the sterilization process may affect their properties [14].

Thus, to overcome this drawback of polymeric materials, researchers' and clinicians' attention focused on metallic biodegradable materials. Several of them have been studied but most of the scientific efforts focus on Magnesium (Mg) and its alloys. Among metallic engineering materials, Mg possesses one of the best bio-compatibilities with human physiology and the best mechanical compatibility with human bone [60]. Its low density and elastic modulus best mimic the properties of natural bones (Table 2). Moreover, Mg is the fourth most abundant element in the human body (it is recommended that an adult receives 240–420 mg daily) and it is essential for the metabolism in many biological mechanisms (Mg is a cofactor for many enzymes [46]). Finally, Mg^{2+} ions, resulting from the degradation process (see Section 2.1.2), are reported to aid the healing and growth of tissue. Any excess of these ions is harmlessly excreted in the urine [43].

Despite the advantageous properties of bioactive Mg and its alloys, there are some limitations for their use in temporary implants. The major drawback is the high corrosion rate in the physiological environment that may lead to a loss of mechanical integrity before tissues have sufficient time to heal. Moreover, hydrogen as a corrosion product together with the generation of respective hydrogen pockets can influence the healing process or, if the pockets are large, they may cause death of patients through blocking of the blood stream. Finally, the simultaneous action of the corrosive human-body-fluid and the mechanical loading can cause the further complication of sudden fracture of implants due to corrosion-assisted cracking, such as stress corrosion cracking (SCC) and corrosion fatigue (CF) [61–63].

The aim of this work is to describe the state of the art regarding corrosion behaviour assessment and the developed methods for improving the corrosion resistance of Mg. First a short summary of the degradation mechanism of magnesium in human body fluid will be provided, and then a focus on the corrosion-assisted cracking phenomena (SCC and CF). Finally, an overview of how to improve corrosion properties will be given.

2.1.2. Corrosion

The main drawback in the use of magnesium in orthopaedic implants is its high corrosion rate in the electrolytic physiological environment. Mg and its alloys are

reactive metals and they corrode in aqueous environments according to the reactions given below [64,65]:

$$\mathrm{Mg} + 2\mathrm{H_2O} \rightarrow \mathrm{Mg(OH)_2} + \mathrm{H_2} \tag{2.1.4}$$

The corrosion reaction can be divided into the anodic and cathodic partial reaction, (2.1.5) and (2.1.6), respectively [66]:

$$Mg \rightarrow \mathrm{Mg^{2+}} + 2e^- \tag{2.1.5}$$

$$2H_2O + 2e^- \rightarrow H_2 + 2(OH^-) \tag{2.1.6}$$

According to Equation (2.1.4), a film of $Mg(OH)_2$ forms on the surface of Mg and its alloys, preventing further corrosion in water since it is slightly soluble there.

$$Mg^{2+} + 2(OH^-) \rightarrow Mg(OH)_2 \tag{2.1.7}$$

However, if the corrosive medium contains any chlorides with concentration above 30 mmol/L [67], the magnesium hydroxide will be converted to magnesium chloride $MgCl_2$ according to [43]:

$$Mg(OH)_2 + 2Cl^- \rightarrow MgCl_2 + 2(OH^-) \tag{2.1.8}$$

Magnesium chloride is highly soluble in aqueous solution, determining the further corrosion development of Mg and its alloys in the human body, where the chloride content is about 150 mmol/L [68–71].

It is worth to note that the chemistry involved in the corrosion, i.e., magnesium chloride solubility and hydrogen evolution, highly influences the in vivo performances of magnesium devices. Starting from the solubility of $MgCl_2$ film, it is reported that it can affect the mechanical behaviour in two different ways. According to Ghali et al. [72], two different corrosion modes are possible, uniform and localized. Mg alloys with slow and constant degradation rate (lower than 0.5 mm/year [65]) are required to facilitate sufficient time to heal for the bone. Further, a uniform degradation mode is key as localized corrosion can lead to toxicity and early failure of the implant. However, uniform corrosion is not the main corrosion mode. Kirkland et al. [73] reported that 29 of 31 Mg alloys suffer of localized corrosion, i.e., pitting. The difference discriminating uniform from localized corrosion is mainly linked to the presence of second phases, precipitates or impurities on the surface of the Mg alloys, inhomogeneities generally widely present in Mg and its alloys. The most common impurities are Fe, Ni and Cu. They are most harmful in terms of corrosion resistance due to their very negative corrosion potential [65,74–76]. They are cathodic with respect to the Mg matrix, resulting in a faster corrosion rate and determining a higher and more severe susceptibility to pitting that quickly destroys the $Mg(OH)_2$ protective film [60]. Once this film is removed, the surrounding corrosive fluid will have contact with the Mg matrix, causing further corrosion according to the just mentioned mechanism. If the

inhomogeneities are not uniformly distributed [65] or above a tolerance limit [77], the material will corrode in a localized manner, acting as precursor for stress corrosion cracking (SCC) and corrosion fatigue (CF). These mechanisms highly affect the corrosion resistance of Mg and its alloys, hampering their application for biomedical implants and they will be described in detail in the next section.
Hydrogen evolution due to the corrosion mechanism involved in Equation (4) influences the in vivo performances of Mg alloys in two ways [22,78–82]. First, when the corrosion rate is too high, human body cannot absorb the entire amount of developed hydrogen, thus generating gas pockets and bubbles. Though Witte et al. [70] found 0.068 mL/cm^2/day leading to no subcutaneous bubbles after 2–3 weeks on guinea pig, and even if Song [79] set 0.01 mL/cm^2/day as tolerated value in his work, no scientific evidence has been reported that these values can be used as a threshold for acceptable hydrogen amounts in the human body. In orthopaedic applications, where blood transport mechanisms are poor, these gas pockets are harmful since they occur around the device, causing risk of implant failure, tissue separation or, in the worst case, death of the patient due to blood clotting [79–82]. Second, hydrogen evolution is strictly connected to the corrosion-assisted cracking, i.e. SCC and CF, since their propagation is highly influenced by the hydrogen embrittlement (HE) phenomenon [22,78], which will be discussed in the next section.

2.1.3. Corrosion Assisted Cracking Phenomena

From the middle of the 20th century, several metallic materials have been reported susceptible to the synergistic effect of mechanical loads and corrosive medium, leading to corrosion assisted cracking phenomena, i.e. SCC and CF [61–63]. These mechanisms result from a simultaneous combination of three factors, susceptible material, corrosive environment and tensile stress. Mg and its alloys have gained interest as materials for biomedical devices due to their degradation properties upon exposure to the human body fluid, and hence researchers and clinicians have started to investigate the susceptibility of these materials to corrosion assisted cracking mechanisms. This involves the consideration of whether the mechanical property reduction results from the combination of applied stresses and corrosive environment, i.e. SCC, or simply is a consequence of the reduction of implant cross-section because of corrosion mechanisms. Choudhary and Raman [83] performed slow strain rate tensile (SSRT) tests on AZ91D alloy in modified simulated body fluid (m-SBF) at different conditions: (a) strained in air; (b) strained in m-SBF; (c) strained in air after a pre-immersion in m-SBF solution for a time as long as the time to failure of case (a); (d) continuously cathodically charged and simultaneously pulled in m-SBF. Comparing the results (Figure 2.1.3), they found a considerable reduction in mechanical properties of specimens stressed in m-SBF, leading to the conclusion that the synergistic effect of corrosive environment and mechanical loads, rather than the corrosive environment itself, mostly affects the corrosion resistance of Mg and its alloys.

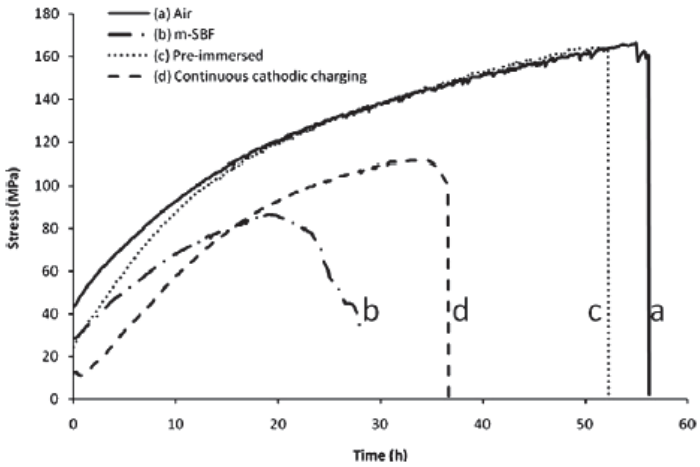

Figure 2.1.3: Stress-time plot of AZ91D alloy tested ate strain rate of 2.2×10^{-7} s^{-1} under different environmental conditions. Reproduced with permission from [83], Copyright Elsevier, 2012.

Since orthopaedic devices are subjected to different acute loadings during their use, i.e., tension, compression, bending and torsion depending on human activities and skeletal location [78] and since these loadings are repetitive (just thinking to the daily activities of walking), SCC and CF are of great concern for the use of Mg and its alloys as material for biomedical devices. Moreover, Mg and its alloys suffer pitting in human body fluid, due to the presence of chlorides and impurities [43,60,67,68,77,78,84–88], making these phenomena main limitations. Chemical induced pits and implants' sharp contours provide the required stress concentration for the onset of such phenomena, which are described below [60,89]. Their most detrimental effect is implant failure at stresses considerably below the yield and design stresses [83], i.e. at mechanical conditions otherwise considered to be safe [75]. Such sudden failure produces serious issues to the patient, such as the need of a complicated and harmful removal of the failed implant and subsequential inflammatory responses, as well as the necessity of a new device implantation.
This section provides the reader with a description of these phenomena. It should be noted that the mechanistic understanding of SCC and CF mostly derives from knowledge obtained on Mg-Al alloys. As Al is toxic to the human body, the mechanisms might not be entirely representative of biocompatible alloys, but it still provides a meaningful framework to describe the theory (see Section 2.1.5.2.1).

2.1.3.1. Stress Corrosion Cracking (SCC)

When static tensile stresses and corrosive environments act together on susceptible materials, they lead to the SCC. This mechanism is characterized by the onset and propagation of cracks, resulting in the embrittlement of ductile Mg in the corrosive medium leading to a considerable elongation reduction [60,83].

The onset of SCC requires a localized corrosion site, where the conditions for crack initiation are met. It is widely reported that these cracks initiate at high stress locations, such as roots of a corrosion pit or pre-existing microscopic flaws (surfaces defects) [60,75,78,83,90]. Localized corrosion sites take place after the fracture of the magnesium hydroxide protective film as a consequence of the chemical reaction with chloride ions according to Equation (2.1.8). This proceeds locally because second phases and/or impurities of the alloy underneath affect the protective film resistance. Moreover, it is widely reported [76] that the breakdown of the protective film also follows the applied stresses. Failure can derive from stress enhancing elements such as inclusions or notches in the implant geometries enhancing stresses from daily activities or residual ones introduced during device fabrication. Moreover, the presence of dynamic loading, i.e. CF, may lead to the formation of fatigue cracking providing a preferential site for SCC [60,75,91].
Once localized corrosion takes place, the cracks propagate until failure. However, the propagation phase is not well understood and literature distinguishes between several mechanisms. In their review, Winzer et al. [75] divided them into two groups of mechanisms:

1. Anodic dissolution mechanisms categorized in the: (a) galvanic attack by film rupture model; (b) tunnelling model; (c) preferential attack model.
2. Mechanical fracture mechanisms or cleavage-like fracture as described in the hydrogen embrittlement model

The development of 1a started from the observation that SCC propagation in AZ31 alloys is halted once a cathodic current is applied. Logan [92,93] proposed an electrochemical model for the crack propagation phase under corrosive media. He theorized that once an applied strain is sufficient to produce a breakdown of the $Mg(OH)_2$ protective film, an electrochemical cell occurs between the anodic film-free surface and the cathodic protective layer (Figure 4).

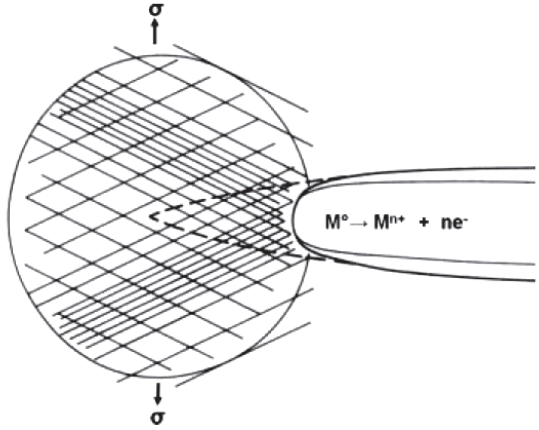

Figure 2.1.4: Continuous crack propagation according to the film rupture model. Reproduced with permission from [75], Copyright John Wiley and Sons, 2005.

Moreover, he suggested that this electrochemical cell determines a localized corrosion that, acting as a notch, leads to a region of stress concentration. Thus the protective film does not reform, allowing a continuous crack propagation. However, some authors refuted this model for different reasons. Ebtehaj et al. [94] as well as Wearmouth et al. [95], for example, found a discontinuous crack growth taking place by an alternating sequence of film rupture and repassivation. A continuous propagation mode is possible only when repassivation is limited. Logan proposed this electrochemical model since he observed an improvement of corrosion resistance applying a cathodic current. However, he neglected that also hydrogen embrittlement models (which will be described later in this section) require a film-free surface that can be influenced by a cathodic charge. Furthermore, he observed a crack growth rate of 10^{-6} m/s and calculated a current density of 14 A/cm^2 needed to ensure such crack velocities. Pugh et al. [96] considered this value too high for a dissolution model. Thus Winzer et al. [75] considered the observations made by Logan being more closely described by another model, the preferential attack model, which will be described later.

The tunnelling model was proposed by Pickering and Swan [97] and is characterized by the formation of tubular pits due to the rupture of the surface film at emerging slip steps (Figure 2.1.5a). At the beginning, the direction of these pits is considered to be governed by the electrochemical potential difference between the Mg matrix and the second phase that they assumed to be $Mg_{17}Al_{12}$. After the establishment of a local galvanic cell able to prevent re-passivation, crack propagation is governed by a ductile tearing of metal between narrow tunnels (Figure 2.1.5b).

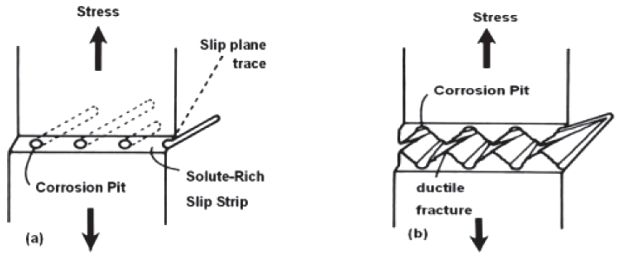

Figure 2.1.5: (**a**) Tubular pits form due to film rupture on slip steps; (**b**) crack propagation occurs by ductile tearing of remaining ligaments. Reproduced with permission from [75], Copyright John Wiley and Sons, 2005.

However, Winzer et al. [75] refuted this model observing that Pickering and Swan proposed it for a material (Mg-1Al) completely unlikely to form a second phase since the amount of aluminium is lower than its solid solubility limit (a better understanding of this concept will be provided in Section 2.1.5).

The preferential attack model has been proposed by Fairman and Bray [98] and it is commonly believed to be the main dissolution mechanism. As a consequence of alloying operation, it is widely reported [99] that second phases can precipitate on grain boundaries. Their presence enhances stresses as a consequence of different elastic properties with respect to the matrix leading to a surface film rupture. Once the anodic Mg matrix and the cathodic second phases ($Mg_{17}Al_{12}$ in Fairman and Bray's work) are

in contact with the human body fluid (HBF), which acts as electrolyte, an electrochemical cell develops, leading to an accelerated dissolution (Figure 2.1.6).

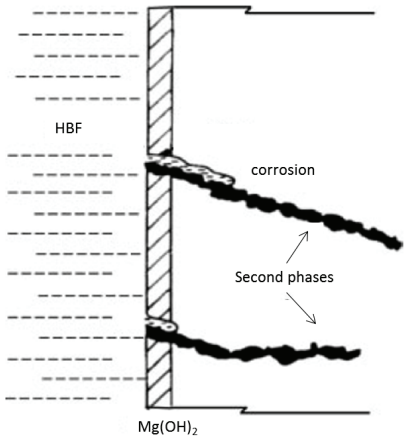

Figure 2.1.6: Preferential corrosion of Mg matrix along the precipitates. Modified from [75]

Depending on the distribution of second phases, crack propagation is reported continuous [100], if there are continuous grain boundary precipitates, or discontinuous [77,78,83,98,101,102], if second phases are non-uniformly distributed or unfavourably oriented. The discontinuous crack propagation is affected by a slower galvanic dissolution, providing enough time for the formation of the surface protective film, and hence rendering film rupture and repassivation competing processes.

Concerning the other main group of propagation mechanisms, the mechanical fracture mechanisms or cleavage-like fracture, the model describing hydrogen embrittlement (HE) is reported to be the most descriptive. Several models describing cleavage fracture without HE are available [75], but not satisfactory. Studying SCC of a single-phase Mg-7.6 wt % Al alloy, Pugh et al. [96] suggested that the propagation phase is discontinuous, alternating between crack propagation, due to the embrittlement of a thin oxide surface layer ahead of the crack tip, and crack arrest, due to the ductile region ahead of the embrittled layer. However, Fairman and Bray [98] argued against Pugh et al.'s model as they either do not detect oxide layers on the fracture surfaces or do not observe brittle fracture on Mg-Al alloys in chloride solutions. Several authors [77,78,83,86,101,102] agreed that cleavage fracture is a consequence of hydrogen induced Mg matrix embrittlement. Presence of hydrogen is a consequence of the Mg corrosion mechanism in aqueous solutions (see Section 2.1.2); according to the cathodic partial reaction, one molecule of hydrogen gas is produced for each atom of Mg dissolved in the human body, but hydrogen is also produced at an anodic potential due to the negative difference effect (NDE, detailed in Section 2.1.4). Chakrapani and Pugh [103] suggested that H_2 is involved in brittle fracture since it can be related to the formation of brittle hydrides (MgH_2) or in decohesion phenomena. Some authors [104] also proposed an adsorption model in order to explain the HE mechanism, where hydrogen is adsorbed from the solution at the crack tip or transported to the cracked

region by dislocation motion. However, Bursle and Pugh [105] argued against the adsorption model. They stated that, according to dislocation motion, the adsorbed hydrogen would embrittle only a few atomic layers ahead of the crack tip, which is smaller than the observed crack arrest markings of the fractography. Furthermore, they observed a 1 μm layer of MgH_2 on the fracture surface of their specimens further disproving the model. Bursle and other authors [106] stated that embrittlement occurs due to the formation of brittle hydrides ahead of the crack tip favouring crack propagation while suppressing plasticization around the crack region.
Figure 2.1.7 briefly describes the mechanical fracture based/cleavage like fracture mechanism: after the formation of the brittle region ahead of the crack tip, the applied stresses determine the propagation of this crack inside the brittle area. The following ductile area prevents further crack propagation. Repassivation occurs ahead of the crack tip leading to hydrogen embrittlement.

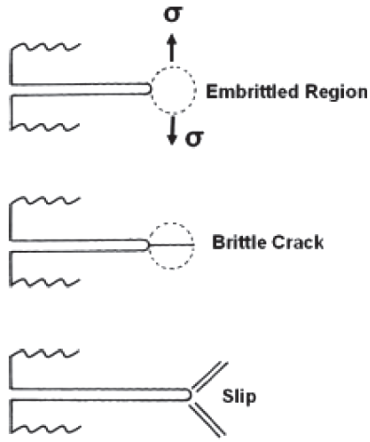

Figure 2.1.7: Model for mechanical induced cracking. Reproduced with permission from [75], Copyright John Wiley and Sons, 2005.

Finding a solid mechanism for SCC propagation phase (anodic dissolution mechanisms or cleavage-like fracture) is subject to intensive research. However, the anodic dissolution described by the preferential attack model sufficiently describes the specific inter-granular stress corrosion cracking (IGSCC). Trans-granular stress corrosion cracking (TGSCC) follows cleavage-like fracture due to HE. Thus, in order to obtain a more detailed understanding of the problem, fracture surface micrographs relate anodic dissolution and cleavage-like fracture to inter-granular (IG) and trans-granular (TG) crack growth, respectively. Since anodic dissolution requires the presence of second phases, the propagation mode is strongly influenced by microstructure. In fact, Fairman and West [107] tested single phase Mg-7Al-1Zn and observing a TG propagation mode since no $Mg_{17}Al_{12}$ has been found from their microstructural observations, whereas Farman and Bray [98] reported that the Mg-Al alloys with Al content higher than 6 wt % fail in a IG mode due to the large presence of second phases. Moreover, also grain size influences the propagation phase. In fact, increasing the grain size leads to a transition to TGSCC. Priest et al. [100] reported the maximum grain size for prevailing

IG to be 28 μm, regardless of the presence of second phases. Fairman and Bray [98] reported that Mg-Al-Zn and Mg-Al alloys with fine grains (at about 5 μm) fail in a IG manner; Pardue et al. [100] observed a TG crack propagation in their Mg-6Al-1Zn alloy with a coarse grain size (about 80 μm). Similarily, Pugh et al. [96] reported a TG crack propagation mode in their high purity binary magnesium alloy with 7.6 wt % Al content with grain size of 70 μm. All results have been obtained on thermally treated specimens. Without heat treatment, a combined IG and TG mechanism (anodic dissolution and cleavage-like fracture) is underlying SCC propagation [83,101]. In Choudhary and Raman's work [83], fractographic analyses of AZ91D alloy tested under m-SBF reveal both trans- and inter-granular cracking. Moreover, specimens were also tested in m-SBF under a continuous cathodic charge, showing an improvement in corrosion resistance compared to the ones tested without any charge (Figure 2.1.3). From micrographic analyses, the authors suggested that a cathodic charge prevents the anodic dissolution mechanism, leading to TGSCC only (indicated by arrows in Figure 2.1.8).

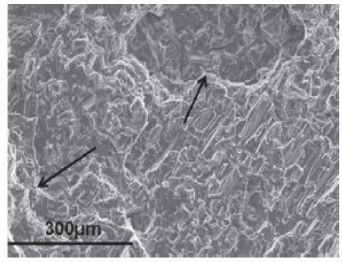

Figure 2.1.8: Fractographic analyses of AZ91D alloy sample continuously cathodically charged and simultaneously tested in modified simulated body fluid (m-SBF). Reproduced with permission from [83], Copyright Elsevier, 2012.

Until now, the influence of applied stresses was not considered, it was simply mentioned that stresses derive from daily activities or are remaining as residuals after fabrication. The susceptibility of SCC to the applied stress levels was not yet detailed. It is widely known that the occurrence of SCC is linked to a stress above a certain threshold, called σ_{SCC}. Thus, in the design phase, a stress below σ_{SCC} should be targeted to avoid the onset of SCC. However, production processes can introduce flaws or defects, such as cracks inside the material negatively affecting its strength. Since these process limitations are difficult to overcome, a damage-tolerant approach has to be taken into account. It is hence important to characterize the conditions for onset and propagation of cracks on defects to predict the lifetime of a device in a corrosive medium. Since cracks propagate in a brittle manner in SCC, the linear elastic fracture mechanics approach (LEFM) is widely used in literature [75,83,94,95], providing a design tool for predicting the time to failure of an implant.

LEFM is an important, widely studied and accepted failure prediction criterion. A point criterion insufficiently describes the stress field in the presence of a singularity; a proper description requires a field based criterion. In the proximity of the crack tip, the stress intensity factor in mode I (K_I) can be described according to Gross and Mendelson [108]:

$$K_I = \alpha \cdot \sigma_g \sqrt{\pi a} \qquad (2.1.9)$$

where "a" is the length of the initial defect, "α" is a geometric parameter and "σ_g" is the applied stress. One of the main underlying assumptions of LEFM is the Paris curve (see Figure 2.1.9, red line) that describes the fatigue crack propagation rate (da/dN) as a function of the applied stress intensity factor range (ΔK_I).

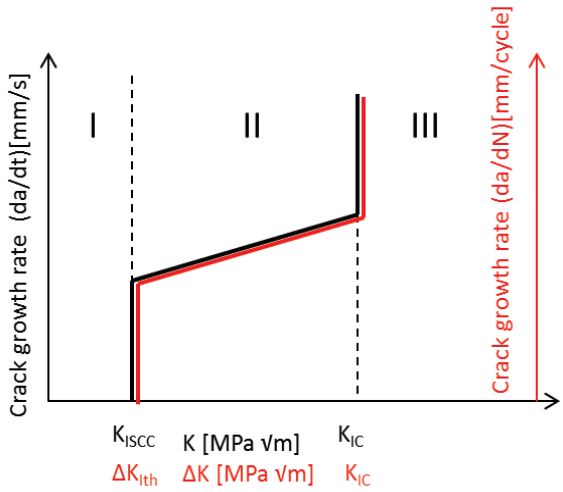

Figure 2.1.9: Paris curve (red line); Paris-like curve for Stress Corrosion Cracking (SCC) (black line).

The Paris curve is characterized by three different regions: region I has no crack growth and stress intensity factors below ΔK_{Ith} (threshold stress intensity factor for fatigue crack growth), region III results in sudden failure with loads exceeding the fracture toughness (K_{IC}). The region labelled II describes a linearly increasing growth rate with the stress intensity factor.
With respect to biomedical implant research and application, a Paris-like curve may also describe SCC (Figure 2.1.9, black line). ΔK_{Ith} becomes K_{ISCC} (threshold stress intensity factor for SCC crack growth) and the crack growth rate is now based on time. To prevent failure due to SCC, stresses below K_{ISCC} are targeted, which represents a main parameter for Mg alloy based implant design. Its calculation is inspired by fracture mechanics, testing fatigue air pre-cracked and circumferential notched specimens. Circumferential notched tensile (CNT) tests are carried out at different stress levels in corrosive environments aiming at best representing body-like environments [94]. K_I is calculated at each applied load from Equation (2.1.9) and then the corresponding time to failure is extracted. Finally, experimental data are plotted in a time to failure (t_f)-K_I graph (Figure 2.1.10). Time to failure increases exponentially decreasing the applied stress, i.e., the stress intensity factor, and the K_{ISCC} can be defined as the horizontal asymptote in the t_f-K_I plot (Figure 2.1.10).

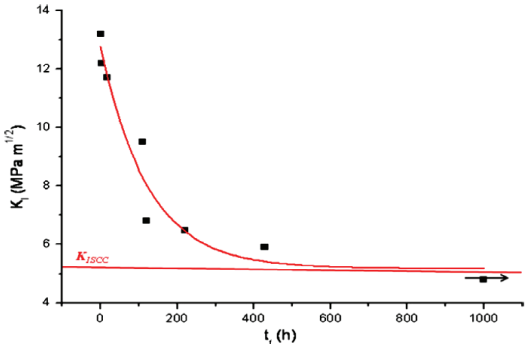

Figure 2.1.10: t_f-K_I plot for determination of K_{ISCC}. Reproduced with permission from [83], Copyright Elsevier, 2012.

Several works have been performed on evaluating the Mg threshold stress intensity factor for SCC crack growth in corrosive environment, as reported by Winzer in his review [75]. Since the use of Mg and its alloys in biomedical field is a relative new issue, very few consider a corrosive medium replicating human body conditions. Choudhary and Raman [83] studied the corrosion behaviour of AZ91D alloy in m-SBF and they report a K_{ISCC} value of 5.18 MPa m$^{1/2}$. Testing specimens at different stress intensity factors, they reported no failure after 1000 h CNT testing at a K_I value of 4.8 MPa m$^{1/2}$, below the threshold limit that they propose.

However, in some circumstances the threshold value K_{ISCC} loses its meaning. For small cracks or flaws, LEFM is not applicable as it becomes underrating (for $a \rightarrow 0$, $K_I \rightarrow \infty$, see Figure 2.1.11). The SCC threshold σ_{SCC} (mentioned above) determined like K_{ISCC} but on smooth specimens, replaces K_{ISCC}.

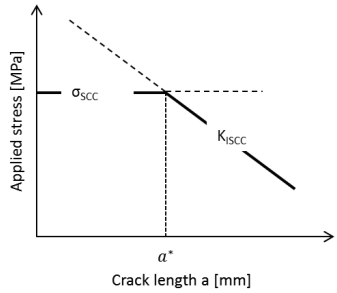

Figure 2.1.11: Definition of a^*.

The minimum crack length for LEFM can be calculated from the crack length "a^*" implying $K_I = K_{ISCC}$ with an applied stress equal to σ_{SCC}:

$$K_{ISCC} = \alpha \cdot \sigma_{SCC} \cdot \sqrt{\pi a^*} \qquad (2.1.10)$$

obtaining:

$$a^* = \frac{K_{ISCC}^2}{\pi \alpha^2 \sigma_{SCC}^2} \quad (2.1.11)$$

At the best of the authors' knowledge, there is limited information on the upper threshold size of a^* that may lead to stress corrosion cracking according to LEFM. In the field of Mg and its alloys as biomedical implant materials, it is a potential topic of interest as it provides a powerful design tool for implant compliance prediction, determining whether the implant shall be designed employing a solid mechanics approach or fracture mechanistic considerations.
Taking into account σ_{SCC} and K_{ISCC} depending on the length of the flaws, a safe region can be defined with respect to SCC (Figure 2.1.12) [75]: for stresses belonging to region I, no SCC will occur, whereas region II is affected by continuous crack growth due to stress and corrosion. The upper limit of this region is defined by K_{IC} and by the material's fracture tensile stress for small cracks. For applied stresses above the threshold (region III), sudden failure will occur with loads exceeding material strength. Region I is desired in temporary biomedical applications as implant failure is only characterized by homogeneous corrosion, avoiding an accelerated failure due to SCC.

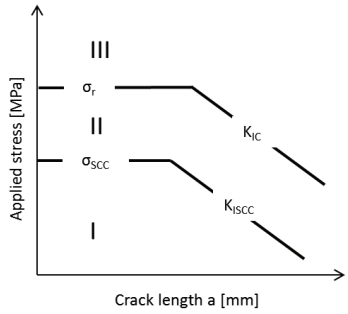

Figure 2.1.12: Influence of applied stress on the material behaviour in corrosive environment.

2.1.3.2. Corrosion Fatigue (CF)

Orthopaedic implants experience severe dynamic loads due to walking, running and other body movements. Taylor [109] reported a mean of 2×10^6 walking cycles per year. The simultaneous effect of cyclic loading and corrosive environment leads to a reduced stresses resistance. Gu et al. [91] found that the fatigue limit for Mg high strength extruded alloy WE43, i.e., fatigue strength at 10^7 cycles, is much lower for specimens tested in simulated body fluid (SBF) than for those tested in air (40 MPa vs. 110 MPa) and that the fatigue strength for die-cast AZ91D tested in air is 50 MPa at 10^7 cycles, whereas 20 MPa at 10^6 cycles for specimens tested in SBF. They defined the reduction rate of fatigue strength (RRFS) for evaluating effects of the corrosive

environment. RRFS is the extension of another index proposed by Bhuiyan [110] and it is defined as:

$$RRFS = \frac{\sigma_{air} - \sigma_{SBF}}{\sigma_{air}} \quad (2.1.12)$$

where σ_{air} is the fatigue strength for specimens tested in air and σ_{SBF} is the fatigue strength in SBF at the same number of cycles. For different Mg alloys, RRFS may range from 30 to 70%, showing the significant impact of the corrosive medium on the fatigue resistance of Mg and its alloys [86,91].

Failure due to dynamic loading in a corrosive environment is related to corrosion fatigue (CF) and relations can be drawn from SCC. Although CF is considered among the major concerns in biomedical applications causing device failure [111,112], it is still vastly unexplored. Current knowledge relates the reduction in fatigue strength to the nucleation of corrosion pits (as for SCC) acting as preferential sites for fatigue crack initiation. Jafari et al. [86] investigated as-cast AZ91D specimens in modified SBF under different electrochemical conditions, open circuit potential (OCP), cathodic and anodic charging condition, reporting that reducing pitting size increases fatigue strength (Figure 2.1.13).

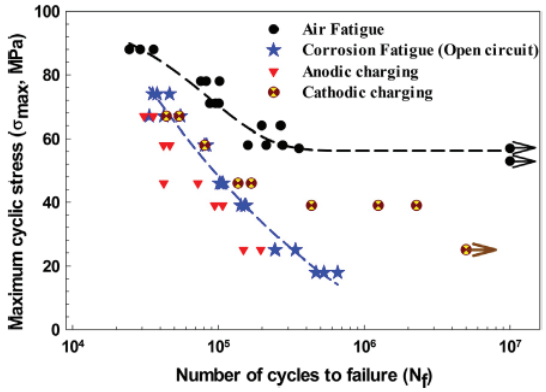

Figure 2.1.13: S-N curve for AZ91D magnesium alloy under different electrochemical conditions. Reproduced with permission from [86], Copyright Elsevier, 2015.

The pitting of Mg and its alloys under cathodic potential is lower than under anodic potential. This lower sensitivity mainly affects fatigue behaviour at low stress amplitudes, where pit depths are not enough for fatigue crack initiation improving fatigue resistance.

As for SCC, researchers argue between anodic dissolution and hydrogen embrittlement as the main propagation mechanism for CF. Zeng et al. [113] reported that AZ61 alloys mainly suffer of HE in wet air, whereas VMD10 and IMV7-1 show a crack-tip dissolution propagation phenomenon [114]. Yet, Uematsu [102] referred to HE as primary and anodic dissolution as the secondary mechanism for CF crack propagation [86]. Figure 2.1.13 shows that specimens tested under an applied anodic potential are

characterized by lower fatigue strength, due to the concurrent action of anodic dissolution and hydrogen embrittlement.
Moreover, crack growth rate can be further increased by a simultaneous SCC [60]. Vasudevan and Sadanada [115] distinguished three different combined roles of SCC and CF in crack propagation, depending on the applied stress intensity factor (K_{max}) compared to K_{ISCC} (Figure 2.1.14).
Figure 2.1.14a describes what is considered as true CF behaviour since the environment plays a harmful role for all the stress intensity factor values: the corrosive environment reduces the maximum stress intensity factor value for fatigue crack propagation $K_{max,th}$, leading to a higher crack growth rate until K_{max} approaches the fracture toughness K_{IC}, where the crack growth rate curve for corrosive environment merges with the one for the inert fluid. In the second case (Figure 2.1.14b), there is no environmental contribution until K_{max} reaches K_{ISCC}, after which superposition of SCC and CF occurs implying a stress dependant process. The last scenario (Figure 2.1.14c) is characterized by the combination of the two previously described processes.
Since corrosion assisted cracking phenomena, i.e., SCC and CF, are time-dependent, frequency of loading (that range from 1 Hz to 3 Hz, see Table 2.1.3) strongly affects fatigue strength.

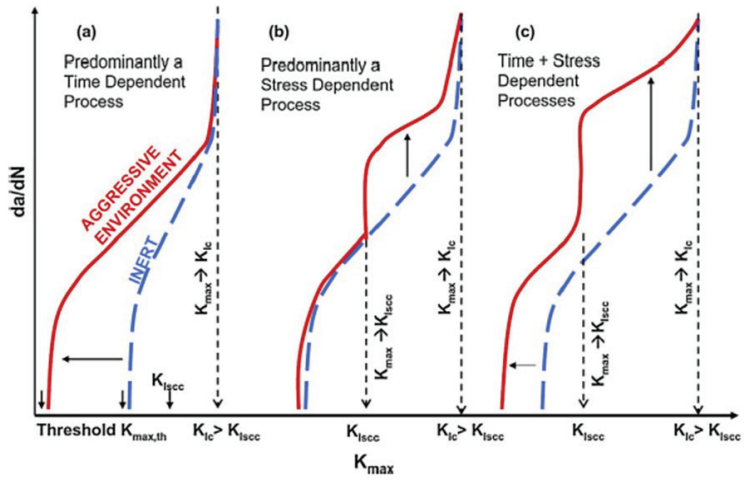

Figure 2.1.14: Schematic representation of crack growth rate under different combinations of static and dynamic loading in inert and corrosive environments. Crack growth rate depending on stress intensity factor in (**a**) pure corrosion fatigue (CF), (**b**) stress and (**c**) time-stress dependent SCC and CF combinations. Reproduced with permission from [115], Copyright Elsevier, 2009.

Table 2.1.3: Frequency range for orthopaedic applications. Modified from [60].

Implants	Frequency (Hz)	Activity
Orthopaedic	1–3	Normal walking (vertical direction)
Orthopaedic	0.5–1.5	Normal walking (lateral direction)

Low frequencies increase the fatigue crack growth rate, providing enough time for corrosion and allowing localized dissolution and/or H to embrittle the matrix. Moreover, the effect of frequency depends on the applied stress, being more pronounced in the low stress regime. The fatigue crack growth rate decreases with frequency due to the crack closure effect [116]. Several studies on strain rate effects on SCC show that intermediate strain rates provide maximum susceptibility for corrosion assisted cracking [75,87,94,95,117]. At low strain rate, film integrity is preserved, avoiding hydrogen to enter and embrittle the Mg matrix. Increasing strain rate, the repassivation effect is limited, allowing the hydrogen to facilitate the crack propagation. At higher strain rates there is insufficient time for hydrogen embrittlement minimizing this synergistic influence rendering strain determined cracking dominating.

2.1.4. Negative Difference Effect (NDE)

The NDE is an unusual phenomenon affecting especially magnesium dissolution. From an electrochemical point of view, corrosion reactions can be either cathodic or anodic, and they are inversely related. For traditional metals (i.e., copper and steel) an increase in applied anodic/cathodic potential leads to an increase in the anodic/cathodic reaction rate, increasing/decreasing hydrogen evolution.
Looking at Figure 2.1.15, the solid lines labelled as I_a and I_c represent the normal anodic and the cathodic partial reaction, respectively, both assumed to follow Tafel kinetics. Increasing the applied potential from E_{corr} to E_{appl} leads to a decrease in cathodic reaction rate (from I_0 to $I_{H,e}$) and an increase in anodic reaction rate (from I_0 to $I_{Mg,e}$). However, Mg and its alloys behave in a different manner, anodic polarisation increases the amount of hydrogen evolution, i.e., an increase in cathodic reaction rate according to I_H curve. Increasing the applied potential from E_{corr} to E_{appl}, the actual cathodic corrosion rate corresponds to $I_{H,m}$, which is greater than the expected current $I_{H,e}$. Moreover, also the Mg corrosion rate is increased. According to the I_{Mg} curve, anodic corrosion corresponds to $I_{Mg,m}$, greater than $I_{Mg,e}$.

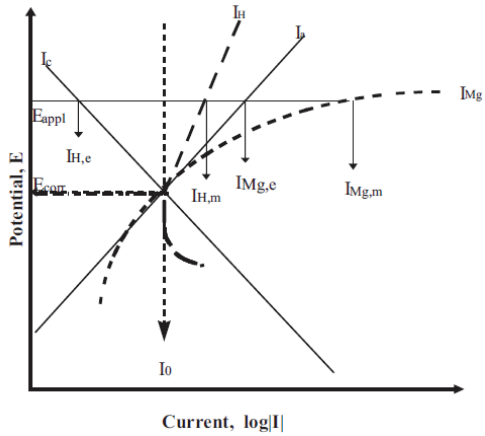

Figure 2.1.15: Schematic representation of negative different effect. Reproduced with permission from [118], Copyright Elsevier, 1997.

Several authors have tried to explain the NDE phenomenon, developing four different models shortly described here:

i. Partially protective surface film
ii. Monovalent magnesium ion model
iii. Particle undermining model
iv. Magnesium hydride (MgH_2) model

For a deeper insight, the readers are referred to [77].

2.1.4.1. Partially Protective Surface Film

It is well known that a passivating film forms naturally on the surface of Mg, preventing further corrosion. This model suggests that NDE is attributed to the rupture of the protective layer when current is flowing through the interfacial electrical double layer formed between the magnesium surface and the electrolytic medium. Once the protective film is broken, divalent magnesium ions dissolve and undergo hydrolysis lowering the pH of the solution and increasing the parasitic corrosion rate. The higher the current density or potential is, the greater the removal of protective layer will be (Figure 2.1.16).

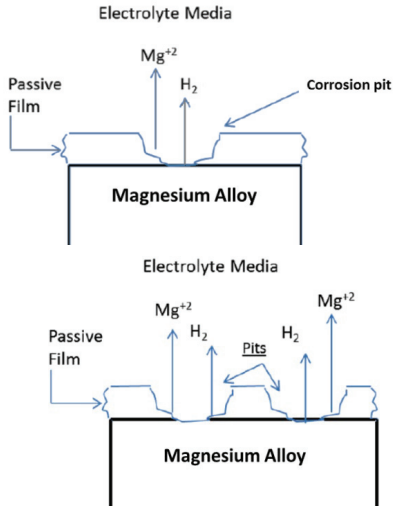

(**a**) (**b**)

Figure 2.1.16: Model of partially protective surface film at low (**a**) and high (**b**) applied potential (*E*) or current (*I*). Modified from [85].

2.1.4.2. Monovalent Magnesium Ion Model

This model proposes that a transient Mg^+ monovalent ion may be involved in the NDE as illustrated in Figure 2.1.17.

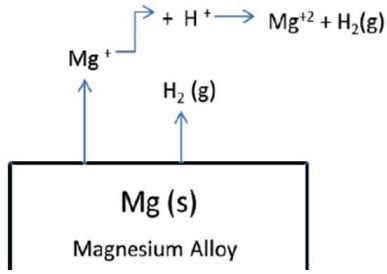

Figure 2.1.17: Monovalent magnesium ion model. Modified from [85].

Mg^+ monovalent ion is produced electrochemically according to:

$$Mg \rightarrow Mg^+ + e^- \tag{2.1.13}$$

then chemically reacting with two protons to yield hydrogen gas via:

$$2Mg^+ + 2H^+ \rightarrow 2Mg^{2+} + H_2 \tag{2.1.14}$$

providing a chemical rather than electrochemical explanation of hydrogen production.

2.1.4.3. Particle Undermining Model

This model suggests the NDE to be explained by the development of second phases or impurities, especially at high anodic current densities or potentials. Second phases and impurities are more cathodic with respect to the Mg matrix, resulting in high localized galvanic corrosion at their boundaries. The phases fall out due to an increased mass loss weakening the material. This phenomenon increases with higher current densities (Figure 2.1.18).

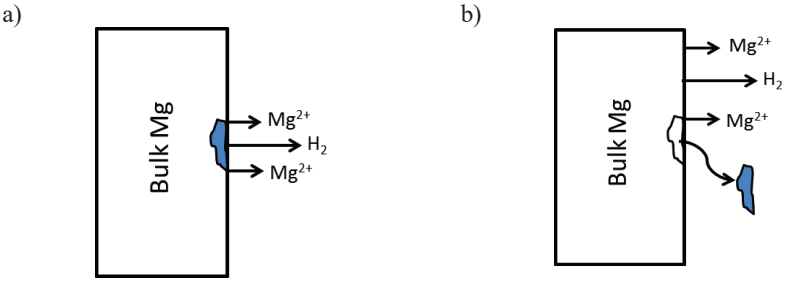

Figure 2.1.18: Particle undermining model, at low **(a)** and high **(b)** current density or potential. Modified from [77].

2.1.4.4. Magnesium Hydride (MgH_2) Model

This model builds on the formation of a MgH_2 layer on the specimens' surface [119], which reacts with H_2O to produce H_2:

$$MgH_2 + 2H_2O \rightarrow Mg^{2+} + 2OH^- + 2H_2 \quad (2.1.15)$$

This can be significant in an anodic condition (Figure 2.1.19).

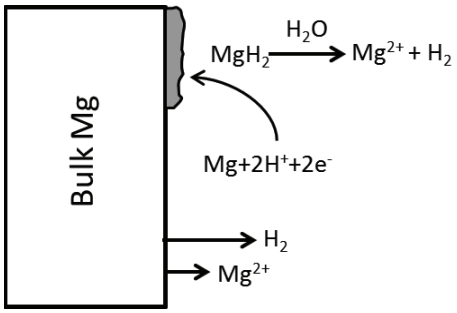

Figure 2.1.19: Magnesium hydride MgH_2 model, modified from [77]

Song et al. [77] combined model 1 and 2, providing one of the most applicable models. Increasing applied potential or current density, a larger surface area of the material becomes film free, Mg produces monovalent Mg^+ (Equation (2.1.13)), which in turn leads to hydrogen generation via:

$$Mg^+ + H_2O \rightarrow Mg^+ + OH^- + \frac{1}{2}H_2 \quad (2.1.16)$$

For strong negative values of applied potential/high current densities, the model considers the film surface intact, leading to low anodic dissolution, whereas cathodic hydrogen evolution is still allowed but decreasing with increased potential. Once the pitting potential is reached, the surface film breaks down, favouring hydrogen evolution and Mg ions dissolution, which, of course, increases with applied potential/current density.

2.1.5. Corrosion Improvements

The importance of temporary biomedical devices is continuously increasing. Mg-based materials are emerging as attractive metallic materials in this field, because of bone like mechanical properties and chemical compatibility (Mg is a trace element of the human body). The main limitation is their low corrosion resistance leading to implant failure before bone healing is sufficient. Researcher efforts start to grow in this field, aiming to improve Mg and its alloys' corrosion behaviour. In the last years, some methods have been developed, acting either on the bulk material or on the surface. These will be discussed in detail below.

2.1.5.1. High-Purity Mg and Mg alloys

Because of poor molten metal handling processes and as a consequence of the natural composition of the raw Mg, some undesirable impurities, such as iron (Fe), nickel (Ni) and copper (Cu), are incorporated into the material. Moreover, the amount of impurities is inversely related to the efficiency of the refining process. The effect of impurities on Mg based materials' corrosion behaviour has thus gained great interest. Inclusions are the main issue affecting corrosion and thus have been intensively investigated in recent years [120,121], especially in conjunction with the leaching of potential toxic (Ni) elements into the surrounding causing inflammations [68,85,122,123]. The corrosion rate is reported to increase 10–100 times if the concentration of impurities rises beyond the solid solubility determined tolerance maximum [124]. This solid solubility limit is defined as the extent to which an element will dissolve in base materials (Mg in this case) without forming a different phase [85]. Thus, a higher solid solubility limit leads to more homogenously dispersed elements, whereas a lower one increases the amount of separate phases within the Mg-matrix. The tolerance limits are usually low and the limit at which segregation in pure metal (Fe) or Mg-intermetallic phases (Ni, Cu) occurs, can be as low as 35–50 ppm for Fe, 100–300 ppm for Cu, and 20–50 ppm for Ni [68].

In these segregations, a galvanic corrosion is higher as the standard reduction potential is greater than that of Mg. The formation of this corrosion cell induces a preferential dissolution of Mg acting as anodic material, while the mass of the cathodic material will remain. Moreover, the galvanic corrosion is a localized phenomenon also increasing pitting formation and thus enhancing the SCC and CF sensitivity. Several authors reported that SCC susceptibility increases with Fe concentration due to emerging corrosion cells between the anodic matrix and cathodic impurities [100,125].

It is fundamental to keep these elements under their tolerance levels, or to moderate their activity utilizing alloying element (discussed later). Achieving higher corrosion resistance is linked to an amount of impurities (Fe, Ni and Cu) under the tolerance limits. Shi et al. [126] discovered better corrosion resistance of high purity Mg and its alloys comparing low and high purity Mg and Mg1Al alloys (Figure 2.1.20) in salt immersion test (SIT) and salt spray test (SST). Hofstetter et al. [127] stated that an ultrahigh purity ZX50 Mg alloy shows greater corrosion resistance compared to high purity alloys (almost three times) and to standard purity alloy (over an order of magnitude). Li et al. [128] reported that specimens made from 99.99 wt % pure Mg have no mass loss even after 180 days of immersion in SBF.

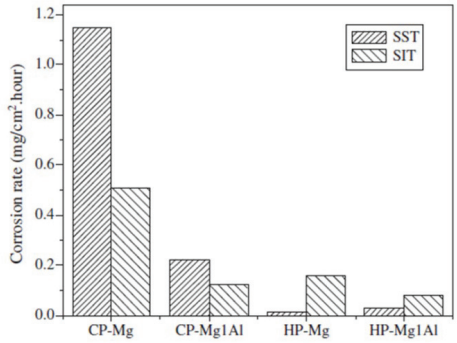

Figure 2.1.20: Comparison of the corrosion rates of the high purity (HP) with low purity Mg (CP) in the salt immersion test (3% NaCl SIT) and salt spray test (SST). Reproduced with permission from [126], Copyright Elsevier, 2006.

2.1.5.1.1. Tolerance level

The tolerance level represents a threshold value, below which the corrosion rate is limited, and once the amount of impurities exceeds this threshold, the corrosion rapidly increases. Obviously, each element has its own solid solubility determined tolerance limit. At the same concentration, the detrimental effect of impurities decreases as follows: Ni > Fe > Cu. However, a typical Mg alloy incorporates several alloying elements, all of which cross-influence their tolerance levels. An element specific impurity threshold level is thus not possible to define. To the best of the authors' knowledge, the first study on the critical level of impurities has been performed by Hanawalt et al. [129]. They have carried out corrosion tests on Mg alloys immersed in 3% NaCl solution and compared it to pure Mg. For pure Mg, they reported the tolerance level for Fe, Ni and Cu to be 0.017 wt %, 0.0005 wt % and 0.1 wt %, respectively. Increasing the amount of Manganese (Mn) from 0.2 to 2 wt %, the Ni tolerance limit grows from 0.001 to 0.015 wt % (Figure 2.1.21).

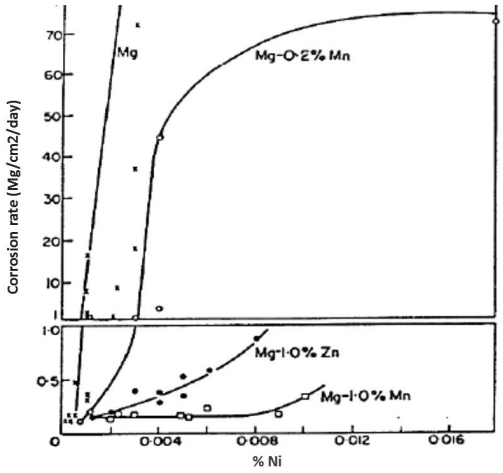

Figure 2.1.21: Tolerance limits for Nickel in pure Mg and Mg-Zn and Mg-Mn alloys. Modified from [129].

Others have studied Ni tolerance levels, revealing that not only third elements but also the casting method has influences on the solubility [77,130]. Sand and permanent mould casted have a significantly lower nickel solid solubility (10 ppm) as high pressure die casted AZ91 alloys (50 ppm) [77].

Hanawalt et al. [129] studied the solid solubility limits of the three main impurities on binary alloys, especially on Mg-Al alloys. They reported a significant influence of Al content on Fe tolerance level, in contrast to none observed on Cu and Ni. 7 wt % of Al in the alloy drops the tolerance level of Fe from 0.017 wt % to 0.0005 wt %. The reason is the formation of Fe-Al phases ($FeAl_3$) being even more cathodic than iron particles.

Furthermore, they studied also ternary alloys, such as Mg-Al-Mn, reporting that an amount of 0.2 wt % of Mn rendering Fe tolerance levels not to drop below 0.002 wt %, meaning that they are stable over a wide range of Al contents.

Adding Mn as alloying element to Mg-Al improves corrosion resistance by increasing the Fe tolerance level [77,130,131]. A weight ratio Fe/Mn of 0.032 is widely defined to be the threshold above which the corrosion rate highly increases [77,130,131]. Mercer and Hillis [132] found that the Fe tolerance levels for AE42 and AM60 alloys are different, but comparable when considering the Fe/Mn ratio.

The copper tolerance level is also influenced by other alloying elements. A small amount of Cu is beneficial for creep strength, but strongly affects corrosion. For example, the addition of Cu in Mg-Al-Zn alloys has a detrimental effect due to the incorporation of Cu in the eutectic phase as Mg(Cu, Zn) [106]. The Cu tolerance level is highly influenced by Zn. Song and Atrens [77] reported a higher Cu tolerance if Zn is above 0.4 wt %. These results agree with Hanawalt [129] reporting that the addition of 3 wt % Zn increases Cu corrosion tolerance in a Mg-Al-Mn (0.2 wt %) system, whereas no changes are observed at 0.5 wt % Zn (Figure 2.1.22).

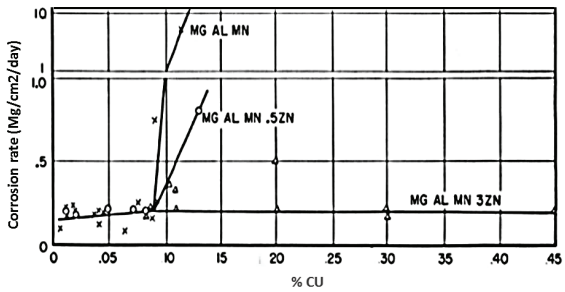

Figure 2.1.22: Effect of Cu in a Mg-Al-Mn-Zn alloy. Modified from [129].

2.1.5.2. Alloying

No alloying strategy outperforms the corrosion resistance of ultra-high purity Mg [133]. Increasing alloying elements content increases second phases, promoting the establishment of a local galvanic cell at interfaces. For example, Shi et al. [126] compared the corrosion rate of high purity Mg with high a purity alloy containing 5 wt% Al. They found a higher corrosion rate for the latter due to the microgalvanic corrosion acceleration of the Mg matrix by the adjacent $Mg_{17}Al_{12}$ cathodic phases. However, pure Mg cannot provide the mechanical properties required for biomedical devices. Therefore, the use of alloying elements has also gained interest for increasing mechanical properties (strength, elastic modulus, elongation at fracture, etc.). Moreover, the addition of certain alloying elements is reported to improve the corrosion resistance of unalloyed Mg with conventional purity. The improvement in the corrosion behaviour can be achieved by three different ways:

- Refining the grain size through alloying. Since grain boundaries are characterized by higher imperfection and higher internal energy compared to the Mg matrix, any corrosive attack acts preferentially on grain boundaries. Segregation of alloying elements and second phases occur on these boundaries leading to an accelerated cathodic activity of the surrounding Mg matrix. This would normally favour coarse grains, however, such segregations are continuously distributed in Mg alloys with finer grains leading to a more homogeneous corrosion behaviour acting as a corrosion barrier [60,68]. Furthermore, fine grain sizes improve the corrosion assisted cracking resistance since they inhibit crack initiation and dislocation motion and lead to an increase in the number of barriers to crack propagation.
- Surrounding the Mg matrix continuously with passivating second phases allows the development of an oxidative film protecting the Mg matrix and acts as barrier to hamper corrosion.
- Adding elements reduces precipitation of second phases at grain boundaries or balances the potential difference between matrix and second phases to decrease microgalvanic corrosion.

Several alloying strategies allow achieving these improvements, it is however necessary to identify nontoxic ones. In this section, we provide a list of most used alloying

elements and their effects. It has to be noted that the effects of alloying elements are strictly related to the system where they are added.

2.1.5.2.1. Aluminium

Al is the most common addition to Mg, it is relatively cheap, light, soluble, and improves strength considerably (i.e., from 170 to 250 MPa considering AZ91) [134]. Furthermore, it is passivating and improves corrosion resistance. Corrosion behaviour studies of Mg alloys are almost exclusively on Mg-Al alloys, especially AZ91. Song et al. [99] tested pure Mg and different Mg-Al alloys in chloride solution finding that pure Mg has a higher anodic dissolution rate than AZ21. The surface film of specimens in this study consists of three different layers: an Al_2O_3 inner layer, a MgO middle layer and a $Mg(OH)_2$ outer layer (Figure 2.1.23). The higher corrosion resistance of AZ21 is related to the emergence of passivating Al_2O_3.

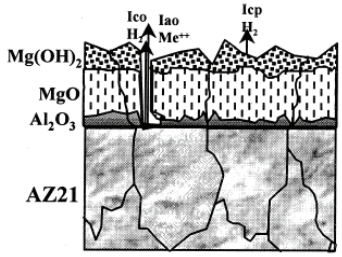

Figure 2.1.23: Corrosion interface of AZ21 alloy. Reproduced with permission from [99], Copyright Elsevier, 1998.

Compared to AZ21, AZ91 alloys have higher corrosion rates due to increased cathodic second phases along grain boundaries. Al is soluble to almost 12 wt % in Mg, depending on the temperature (Figure 2.1.24).

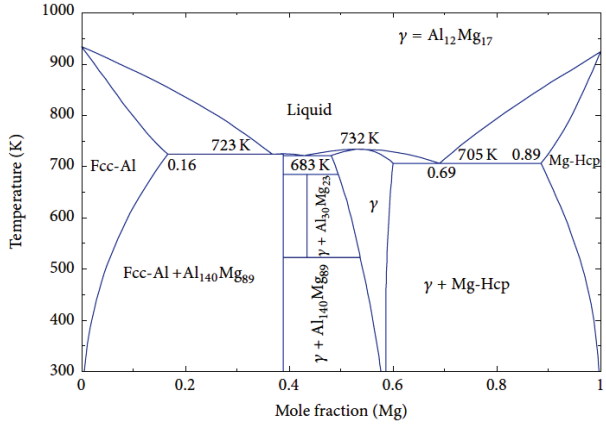

Figure 2.1.24: Mg-Al phase diagram. Reprinted with permission from [135].

Gusieva et al. [136] reported alloys of higher Al content than AZ31 to have second phases ($Mg_{17}Al_{12}$) implying that an amount of Al above 3 wt % lowers the corrosion resistance. Some authors contradicted this hypothesis stating that an increase in Al steadily rises corrosion resistance [137,138]. Lunder et al. [138], for example, proposed the anodic dissolution to be further decreased with Al above 10 wt %. Winzer et al. [75] finally resumed these studies observing two influences of $Mg_{17}Al_{12}$ phases on corrosion, they are a (1) barrier and (2) galvanic cathode influences, depending on the amount of second phases and on their distribution. $Mg_{17}Al_{12}$ acts as a galvanic cathode and accelerates corrosion at low volume fractions, whereas when forming an interconnected network at high fractions, reduce corrosion acting as a barrier through the passivating properties of Al (Figure 2.1.25).

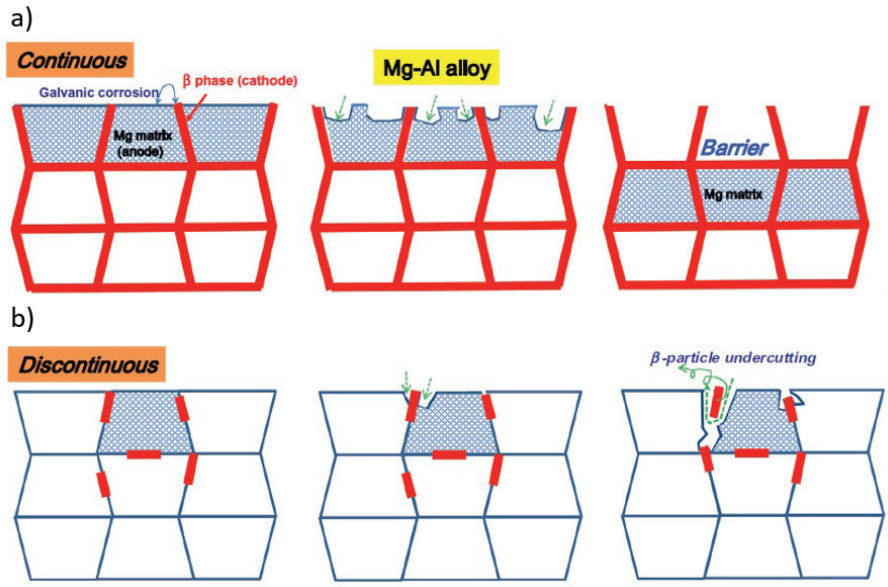

Figure 2.1.25: Schematic illustration of the role of $Mg_{17}Al_{12}$ phases in the Mg matrix whether their distribution is continuous **(a)** or discontinuous **(b)**. Reproduced with permission from [139], Copyright Elsevier, 2014.

These findings are interesting from a mechanistic perspective and might be generalizable for alloying elements with similar electronegativity (I_n). Yet the extensive knowledge obtained with Al alloys is not directly applicable for biomedical implants. Long term effects of exposure to Al reveals Al to be toxic, affecting the reproductive ability [140], inducing dementia [141] and leading to Alzheimer's disease [142,143].

2.1.5.2.2. Manganese

As a binary addition to Mg, Mn shows no significant increase on corrosion for concentrations of up to 5 wt % [129]. It increases the Fe tolerance level in Mg-Al alloys when keeping the Fe/Mn ratio at 0.032. The most likely mechanism explaining the moderation of Fe is that Fe is incorporated in an intermetallic AlMnFe compound, which is less active as local cathode, and thus reduces microgalvanic coupling [136,144]. However, Mn in concentrations higher than 10 μmol/L in the blood, has been shown to induce "Manganism", a neurological disorder similar to Parkinson's disease [145].

2.1.5.2.3. Zinc

Zn causes solid solution strengthening increasing the strength of Mg up to 280 MPa adding 6 wt % of zinc [11]. Moreover, Zn is an essential trace mineral to hundreds of biological enzymes, being required by human body at 15 mg/day [146,147]. The main drawback regarding Zn's biocompatibility is the reaction of Zn^{2+} with hydrochloric acid (HCl). Zn^{2+} evolves from the oxidation reaction of Zn used as alloying material,

$$Zn \rightarrow Zn^{2+} + 2e^{-} \tag{2.1.17}$$

and HCl reduced according to:

$$2HCl + 2e^{-} \rightarrow H_2 + 2Cl^{-} \tag{2.1.18}$$

leading then to the formation of $ZnCl_2$, known to damage stomach parietal cells [148]. In Mg alloys, Zn enhances the tolerance limit and reduces effects of the three main impurities (Fe, Cu, Ni) when their solid solubility limits have been exceeded. 1 wt % of Zn in Mg raises the tolerance limit for Ni [129]. Song and Atrens [77] reported the Ni tolerance limit to be increased up to 20 ppm in Mg-Al-Mn alloys with an addition of 3 wt % Zn, and it can further reduce the corrosion rate of ternary alloys when Ni and Fe tolerance levels are reached. At Zn concentration above 3 wt %, second phases form and the corrosion resistance lowers [67] leading to localized corrosion [149]. Another advantage of Zn alloying is the decrease in hydrogen evolution along with the decrease in solubility of the Mg matrix. Both, Mg^{2+} ions and Zn^{2+} ions bind with free OH^{-} anions forming $Zn(OH)_2$ and reducing the amounts of free H_2 [85]. However, in crystalline Mg, the solubility of alloying elements is limited, hydrogen evolution can hence only be slightly reduced. Mg-based glasses, in contrast, offer increased solubility for alloying elements, allowing to significantly lower corrosion. Zberg et al. [80] investigated glassy $Mg_{60+x}Zn_{35-x}Ca_5$ alloys (x = 0, 3, 6, 7, 9, 12, 14, 15) in SBF. They found that an increase in Zn reduces hydrogen evolution, with a distinct drop in hydrogen release at a Zn content of 28 wt % (Figure 2.1.26).

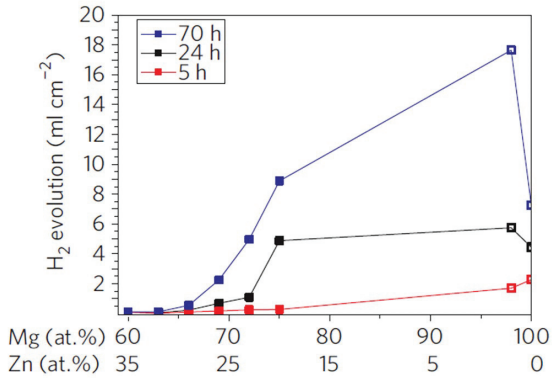

Figure 2.1.26: Hydrogen evolution measurement for MgZnCa alloys with different content of Zn. Reproduced with permission from [80], Copyright Nature Publishing Group, 2009.

2.1.5.2.4. Zirconium

Zirconium (Zr) can refine the grain size. Li et al. reported the microstructure of Mg-Zr binary alloys to be finer than pure Mg [150]. The grain size can be reduced to 50 μm. Zr alloys also have good corrosion resistance due to improved castability. Zr reacts with the impurities of molten Mg lowering their levels through precipitations. For example, Fe combines with Zr to form Fe_2Zr, which, by gravity, settles to the bottom of the melt improving the purity of the cast [77]. Song and St. John [151] compared the corrosion resistance of rare earth (RE)-containing alloys (Mg-REZn-Zr) with and without Zr addition, labelled with MEZ_r and MEZ_u, respectively (Figure 2.1.27).

They related the higher corrosion resistance of MEZ_r to the dissolution of iron impurities. From composition analysis of the two alloys, they found MEZ_u alloys (0.005 wt % Zr) to contain 0.0013 wt % Fe, whereas alloys characterized by 0.6 wt % Zr have lower Fe (0.004 wt %). However, purification cannot explain the difference in corrosion resistance between centres and edges of MEZ_R grains (Figure 2.1.28).

Song and St. John provided three possible explanations of these observations. First, they attributed the higher corrosion resistance of the grain centre to a higher amount of Zr with respect to the grain boundaries. Comparing MEZ_U and MEZ_R, they found the onset and propagation of corrosion to be slower in the latter suggesting that Zr in solid solution improves the resistance via solubility reduction of Mg in the same media. Second, they observed a decreased number of precipitated particles producing hydrogen in MEZ_R than in MEZ_u suggesting a reduction of the cathodic activity of intermetallic precipitates containing Zr. Third, the authors stated that the grain refinement effect of Zr provides more continuous layers of corrosion resistant intermetallic RE phases around grain boundaries, decelerating corrosion between grains.

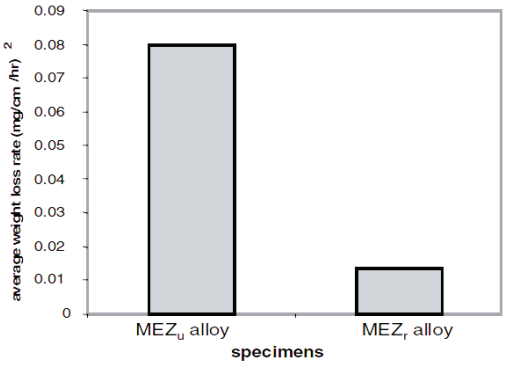

Figure 2.1.27: Weight loss rate for MEZ_u and MEZ_r specimens. Modified from [151].

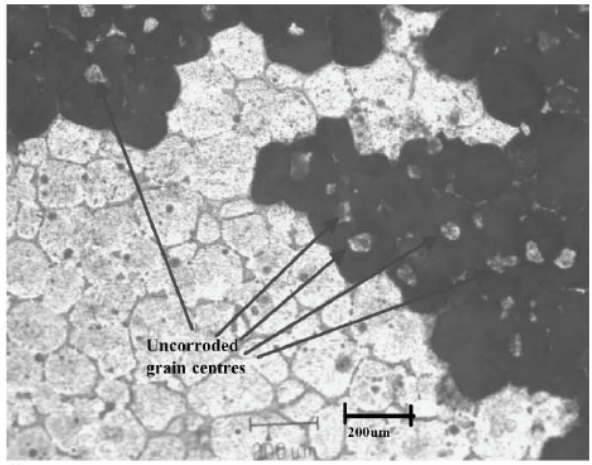

Figure 2.1.28: Optical micrographs of MEZ_R surface after immersion in chloride solution for 3 h. Reproduced with permission from [151], Copyright Elsevier, 2002.

2.1.5.2.5. Calcium

Ca is a major component in human bones and is beneficial for bone healing and growth [127,139,152]. It is widely utilized as alloying element for biodegradable Mg alloys. When Ca is present, Mg alloys develop a hydroxyapatite (HA) surface layer, improving its biocompatibility. Ca is also a grain refiner [153] improving mechanical properties. Zhang and Yang [154] reported a decrease in grain size from 175 to 51 μm in Mg-Zn-Mn alloys increasing the amount of Ca from 0.3 to 1 wt %. The solubility limit of Ca is however only 1 wt %, after which the corrosion resistance drops due to the development of Mg_2Ca second phases [155]. Yet Bornapour et al. [156] assumed the presence of a second phase as being desirable. Comparing the corrosion behaviour of pure Mg to that of different types of alloys with Ca and Sr (Mg-0.5Sr, Mg-0.6Ca, Mg-0.5Sr-0.6Ca, Mg-

0.3Sr-0.3Ca), they found that Mg-0.3Sr-0.3Ca alloys have the highest corrosion resistance, despite the presence of Ca/Sr-rich second phases (Figure 2.1.29).

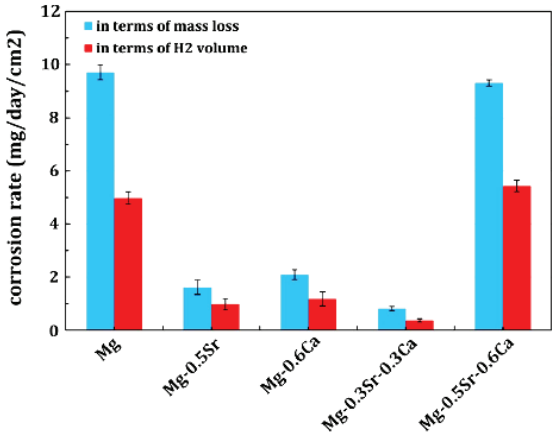

Figure 2.1.29. Corrosion rate of pure Mg, binary and ternary alloys in SBF at 37 °C. Reproduced with permission from [156], Copyright Elsevier, 2014.

They related the improvement in the corrosion behaviour to the presence of these phases in both the grain boundaries and in the interior aligning the corrosion potential of the matrix and the grain boundaries and hence lowering dissolution. Moreover they state that small amounts of Sr and Ca result in stable HA surface layers, whereas large amounts may result in a non-adherent HA surface layer that can easily detach losing its electrochemical barrier function.

2.1.5.2.6. Rare Earth (RE) Elements

RE are mostly present as additions to Zr containing alloys to improve their mechanical properties [75]. Rokhlin [157] reported a higher resistance against SCC with the addition of Cd and Nd to Mg-Zn-Zr alloys. A lower sensitivity to SCC using Nd has been obtained by Kannan et al. [158]. In their study, EV31A, composed by 2.35 wt % Nd and 1.3 wt % Gd, has a higher SCC susceptibility index (I_{SCC}) than AZ80 in chloride solution when tested at strain rates of 10^{-6} s^{-1} and 10^{-7} s^{-1}, respectively (Table 2.1.4). The SCC susceptibility index is calculated based on particular mechanical properties, e.g. ultimate tensile strength (UTS) and elongation to failure (ε_f), measured in a SSRT test in corrosive environments and compared to its corresponding value in air. A low I_{SCC} index corresponds to high SCC susceptibility. When this index approaches unity, the alloy is meant to be highly resistant to SCC in that particular medium.

Table 2.1.4: I_{SCC} indices for different alloys at different strain rate. Modified from [158].

Alloy	10^{-6} s^{-1} Strain Rate		10^{-7} s^{-1} Strain Rate	
	I_{SCC}		I_{SCC}	
	ε_f	UTS	ε_f	UTS
AZ80	0.35	0.83	0.09	0.62

ZE41	0.35	0.80	0.17	0.66
QE22	0.12	0.82	0.05	0.65
EV31A	0.70	0.85	0.67	0.85

The improved corrosion behaviour of EV31A is due to the development of a film of mixed oxides of Nd and Gd, which is more stable than the surface film of RE free alloys. However, despite that both ZE41 and QE22 contain RE elements, they have low corrosion resistance. Kannan et al. [158] attributed their lower corrosion properties to other elements, such as high Zn content (ZE41), and Ag with higher noble potential than Mg (QE22).

Nd is also reported to improve the corrosion resistance of Mg-Al. Zhang et al. [159] studied the effect of Nd on the corrosion behaviour of AZ91 finding a drop in corrosion rate when 1.5 wt % of Nd is added (Figure 2.1.30). They related this improvement to a modification of the alloy's microstructure, since Al-Mn phases are replaced by Al-Nd minimizing the effect of galvanic coupling.

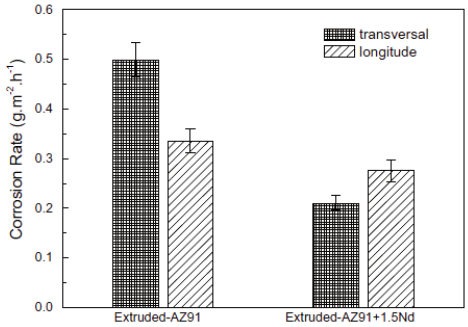

Figure 2.1.30: Corrosion rate of AZ91 with and without Nd. Reproduced with permission from [159], Copyright Elsevier, 2011.

When combined with Al, RE reduce ductility and strength due to the formation of Al_xRE_y , which is however connected to an improvement in corrosion resistance. For example, binary addition of La is detrimental for the corrosion resistance since it forms $Mg_{12}La$ cathodic phases above the solid solubility limit. As elemental addition to Mg-Al, however, it improves corrosion resistance. Liu et al. [160] reported a drop in corrosion rate when 0.5 wt % La is added to AZ91 (Figure 2.1.31), which they related to a modification of the alloy's microstructure. The formation of needle-like Al-La compounds and the alteration of $Mg_{17}Al_{12}$ from discontinuous to continuous is observed.

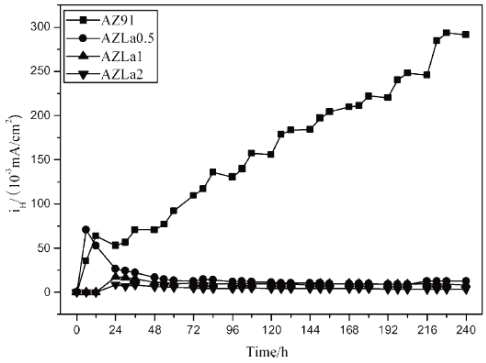

Figure 2.1.31: Corrosion current densities (i_H) of AZ91 alloy varied with different immersion time. Reproduced with permission from [160], Copyright John Wiley and Sons, 2009.

Zhou et al. [161] studied the effect of adding 0.24 wt % Ho and 0.44 wt % Ho to AZ91D alloys, which also significantly decreases the rate (Figure 2.1.32).

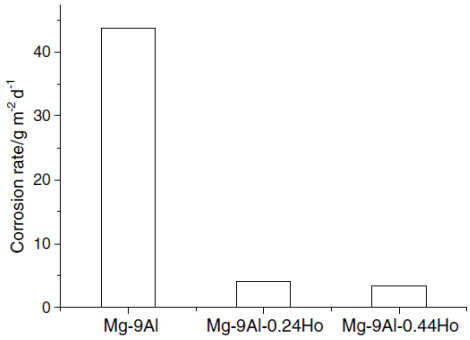

Figure 2.1.32: Corrosion rate of AZ91D with and without Ho. Reproduced with permission from [161], Copyright Elsevier, 2006.

Both Fe and Mg17Al12 volume fractions are reduced by Ho due to the formation of Al-Ho intermetallic phases inducing a lower microgalvanic corrosion through a lower difference in potential. The corrosive film of Ho containing alloys is more protective due to a higher Al concentration. Finally, Yao et al. [162] reported the Sc addition to AZ91E alloys, which refines the microstructure by means of Al_3Sc formation suppressing $Mg_{17}Al_{12}$ phases and reducing the corrosion rate from 8 to 2 μA cm^{-2} with a 0.1 wt % Sc addition. This shows that the addition of RE is beneficial to reduce corrosion and related mechanical failures, however, the synthesis of RE elements is expensive leading to high production costs, which limits their use.

2.1.5.3. Surface Treatment

There are two possible ways to improve the corrosion resistance of Mg and its alloys:

(1) Tailor composition and microstructure;
(2) Treat the surface/apply coatings.

(1) can be achieved through alloying. Here we therefore focus on (2) via biomedical coatings and their influence on corrosion. Due to Mg's high chemical reactivity, coating is a viable strategy for both increased biocompatibility and corrosion protection, allowing a wide range of possible non-toxic and fully degradable surface modifications. Mg alloys tend to passivate naturally forming a protective layer stack of an inner MgO (2.5 nm) and an outer $Mg(OH)_2$ layer (2.2 nm) [163]. This layer is not stable in chloride solution. Increasing the thickness of the passivating layer through thermal treatments is reported to be an effective method to improve the corrosion behaviour. Hanzi et al. [164] evaluated the hydrogen evolution rate of WE43 alloy under different surface conditions, obtained by means of various heat treatments (Figure 2.1.33):

- Samples were first heat-treated at 525 °C for 6 h and then they were grinded and polished (labelled as SHT);
- Samples were first heat-treated at 525 °C for 6 h and then they were artificially aged at 250 °C for 16 h before being grinded and polished (T6);
- Specimens were first polished, then annealed at 500 °C, being covered by an oxide layer during the annealing. The oxidation in air during the heat treatment was carried out for various times, i.e., 1 (ox1), 8 (ox8), 24 (ox24), 48 (ox48), 168 h (ox168).

After the third procedure, an oxide layer, made by MgO and Y_2O_3, covers the surface because of the heat treatment, and the latter growths with increasing oxidation duration, from 500 nm after 1 h to 2700 nm after 168 h. They reported that the higher the thickness of the protective film is, the slower and more homogeneous the degradation will be.

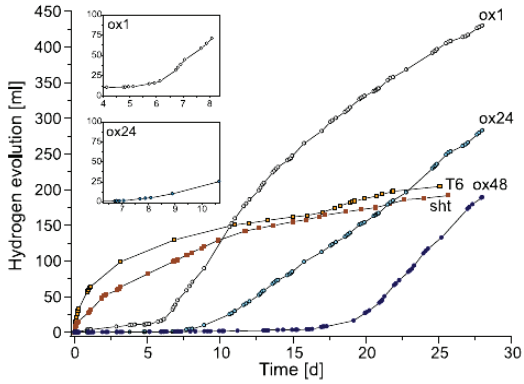

Figure 2.1.33: Hydrogen evolution of WE43 specimens in SBF at 37 °C after various heat treatment. Reproduced with permission from [164], Copyright Elsevier, 2009.

Interestingly, the degradation rate highly increases once the protective surface layer is penetrated or removed, (Figure 2.1.34), compared to heat treated and polished (SHT) and heat treated, aged and polished (T6) samples.

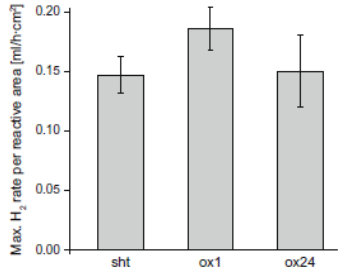

Figure 2.1.34: Maximum hydrogen evolution rate for different WE43 samples. Reproduced with permission from [164]., Copyright Elsevier, 2009

The reason can be found in a composition change due to the oxidation. Short oxidation results in Y-depletion underneath the oxide layer, thus lowering the amount of Y in Mg. However, an effective coating strategy must preserve the desired properties of the material underneath. Thus Calcium Phosphate (Ca-P such as dicalcium phosphate (DCPD) and hydroxyapatite (HA)) have been studied. They have gained large interest in biomedical applications due to their intrinsic biocompatibility related to their analogy to the inorganic component of natural bones that aid the bone growth [165]. Ca-P coatings can be obtained by means of several coating methods, either using conversion or deposition methods (for a review and a detailed description of these methods the readers are referred to [166]) and improve corrosion resistance and biocompatibility. Song et al. [167] fabricated three different kinds of Ca-P coatings on Mg-Zn alloys, i.e., DCPD, HA and fluoridated hydroxyapatite (FHA) via electrodeposition and compared their effects on the degradation behaviour in m-SBF (Figure 2.1.35).

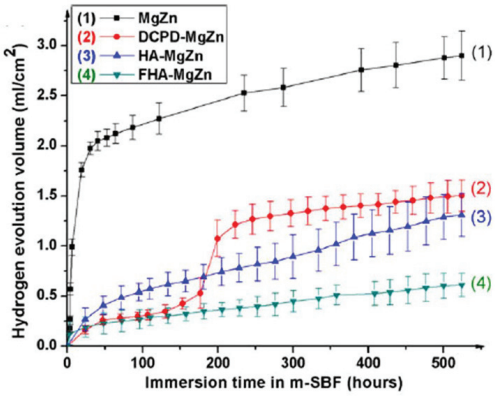

Figure 2.1.35: Hydrogen evolution of Mg-Zn alloys with and without Ca-P coatings in m-SBF. Reproduced with permission from [167], Copyright Elsevier, 2010.

The results show that coatings can significantly decrease the degradation rate of Mg-Zn alloys acting as an electrochemical barrier delaying the Mg alloys' corrosion. Wang et al. [168] compared the effect of a Ca-deficient hydroxyapatite coating on the degradation behaviour of Mg-Zn-Ca alloys in SBF. Performing slow strain rate tensile (SSRT) tests at 2.16×10^{-5} mm/s, a beneficial effect of the coating on SCC resistance has been shown, increasing the ultimate tensile strength (UTS) and time of fracture (TOF) by 5.6% and 16.6%, respectively. Zhu et al. [169] studied the corrosion resistance of a hydroxyapatite/aminated hydroxyethyl cellulose (HA/AHEC) coated AZ31 alloy in SBF. Uncoated and coated samples were immersed for seven days and hydrogen evolution was monitored. They reported that the coating greatly improves the corrosion resistance of AZ31 alloys, leading to a reduction in the average hydrogen release rate of about 65%, i.e., from 0.92 to 0.31 mL/cm^2/day. Moreover, they also studied the cytocompatibility of the coating, investigating the MC3T3-E1 cellular response, reporting the coated alloy to present no cytotoxic reaction to MC3T3-E1 cells and to significantly enhance their proliferation rate. Yang et al. [170] chemically coated AZ31 rods with Ca-P implanting them into the thighbone of rabbits to assess the changes in biocompatibility and biodegradation provided by the coating. After 8 weeks of implantation, coated samples show a slower biodegradation than uncoated while inducing a fast formation of new bone around the implants.
Chiu et al. [171] studied the effect of fluoride containing (MgF_2) coatings on pure Mg (99.96 wt %) immersed in Hank's balanced salt solution, which mimics ph values of the human body. By means of a conversion treatment, they cover the Mg samples surface with a 1.5 μm thick MgF_2 protective layer. After 18 days of immersion, they reported an average corrosion rate of 1.01 mm/year for coated specimens, and 3.70 mm/year for uncoated Mg, respectively. Witte et al. [172] confirmed this studying implants from LAE442 with and without MgF_2 coatings, implanted into the medial femur condyle of rabbits. The coating reduces mass loss (Figure 2.1.36) and, until it disappears, the release of alloying elements.

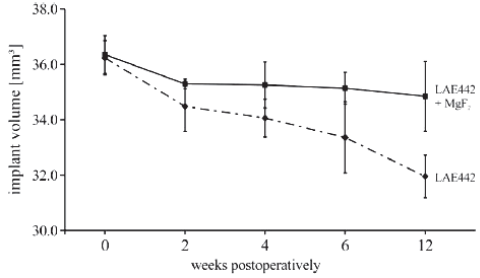

Figure 2.1.36: Implant volume of LAE442 and MgF_2-coated LAE442 at different postoperative intervals. Reproduced with permission from [172], Copyright Elsevier, 2010.

All reported implants are affected by localized corrosion leading to pitting once the protective layer breaks down. Further, the fluoride-containing coatings seem to irritate the local synovial tissue during their dissolution. Organic coatings, especially organic biopolymers, provide a viable alternative offering functionalization possibilities with

organic biomolecules. Polylactic-co-glycolic acid (PLGA) demonstrates great cell adhesion and proliferation properties [13]. Li et al. [173] performed cell attachment tests utilizing mouse osteoblast-like cells MC3T3-E1 on Mg-6Zn alloys with and without PLGA coating. The coated Mg alloys possess a significantly enhanced ability for cell attachment compared to the uncoated one (Figure 2.1.37).

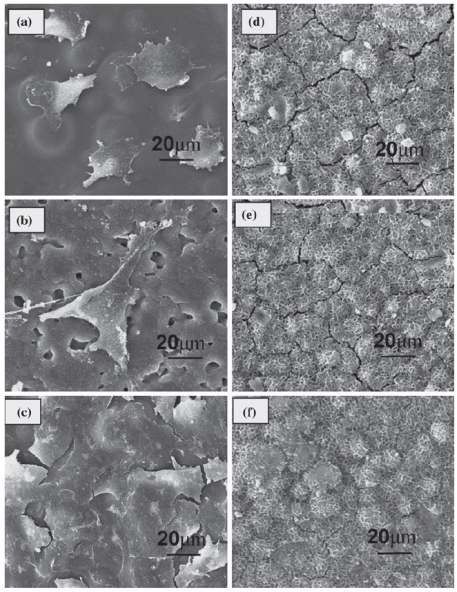

Figure 2.1.37: SEM micrographs of cell morphology after various culture times on polylactic-co-glycolic acid (PLGA) coated Mg alloys after (**a**) 1 day; (**b**) 2 days and (**c**) 3 days culture and uncoated PLGA after (**d**) 1 day; (**e**) 2 days and (**f**) 3 days culture. Reprinted with permission from [173], Copyright Springer, 2010.

Moreover, they also reported the PLGA coating to offer protection against corrosion since it significantly reduces the degradation rate of the Mg alloy (Table 2.1.5).

Table 2.1.5: Average degradation rate of naked and coated Mg6Zn alloys after 72 h and 144 h of immersion in 0.9% NaCl solution at 37 °C [173].

Immersion Time (h)	Average Degradation Rate (mg/cm^2/h)	
	Uncoated	Coated
72	0.063	2.44×10^{-4}
144	0.161	3.23×10^{-4}

2.1.6. Conclusions and Outlook

In some biomedical applications, such as plates, screws and wires, temporary devices have continuously gained interest in the last years to render cumbersome second surgeries after bone healing unnecessary. Among all biodegradable materials, Mg has attracted great research interest as material for temporary implants since it possesses one

of the best mechanical compatibilities with human bone. Its degradation products (Mg^{2+} ions) are essential to the human metabolism. However, the mechanical properties of Mg are too low to make it suitable for implants and hence researchers and clinicians focus on Mg alloys, although related clinical applications are still limited due to several factors. One of the main limitations is the low corrosion resistance inducing a loss of mechanical integrity in human body fluid before bone and surrounding tissues have sufficient time to heal. Moreover, since implants are subjected to different acute loadings during their use, Mg alloys must possess adequate resistance to cracking under the simultaneous action of the corrosive human body fluid and the tensile or cyclic test, i.e., resistance to stress corrosion cracking and corrosion fatigue. Few biomedical relevant studies of corrosion assisted cracking resistance are available since almost all results were obtained studying Mg-Al alloys, not suitable for biomedical devices due to the harmful effects of Al during long term exposure. To push Mg and its alloys to clinics, we will require proper evaluation on their corrosion assisted cracking. Finally, Mg dissolution in aqueous solutions results in hydrogen evolution that has a detrimental effect on biocompatibility. If the corrosion rate is too high, the amount of hydrogen produced cannot be absorbed by the human body leading to toxic gas bubbles and ultimate implant failures. Moreover, the formation of hydroxide ions (OH^-) involved in the corrosion of Mg alloys in aqueous solutions leads to an increase in the pH of the surrounding solution, resulting in a detrimental effect on cell proliferation.

Improvements for the corrosion resistance of Mg alloys have been widely studied recently. Researchers can tune the morphology of the metal, reducing impurities or utilize alloying elements that benefit mechanical and chemical properties. Further, they can employ surface modification strategies, coating Mg alloys with a corrosion resistant yet bioactive material, favouring also bone formation (e.g., Ca-P coatings). However, few reports exist on such coatings. The most employed, Ca-P, respectively HA, has poor mechanical properties and low adhesion to the Mg alloy leading to delamination [174].

This highlights the need for biocompatible surfaces and new coating methods in the future. The authors envision that key research will centre around the investigation of Mg and its alloys' corrosion behaviour and corrosion assisted cracking resistance coated with new biocompatible coatings such as TiO_2, TiC and TiN [175]. Further, extensive research will centre on device production processes and their effect on corrosion resistance. Grain refinement might be such a strategy. Song and Atrens [77] showed that finer grains allow a nearly continuous distribution of second phases, leading to a corrosion delay as corrosion products remain near the Mg matrix, and act as barrier. Furthermore, fine grains improve the corrosion assisted cracking resistance inhibiting crack initiation and dislocations motion leading to an increase in the number of barriers to crack propagation [91]. Related production processes that lead to finer grains are hot deformation and rapid solidification. The authors expect that these will be investigated in detail, exploring also the property of rapid solidification processes to increase the solubility of the alloying elements.

Acknowledgements

All authors acknowledge funding from the Faculty of Engineering at the Norwegian University of Science and Technology.

Conflict of interest

The authors declare no conflict of interest.

Bibliography Paper I

1. Ginebra, M.P.; Traykova, T.; Planell, J.A. Calcium phosphate cements as bone drug delivery systems: A review. *J. Control. Release* **2006**, *113*, 102–110.
2. Regar, E.; Sianos, G.; Serruys, P.W. Stent development and local drug delivery. *Br. Med. Bull.* **2001**, *59*, 227–248.
3. Greatbatch, W.; Holmes, C.F. History of implantable devices. *IEEE Eng. Med. Biol. Mag.* **1991**, *10*, 38–41.
4. Long, P.H. Medical Devices in Orthopedic Applications. *Toxicol. Pathol.* **2008**, *36*, 85–91.
5. Khan, W.; Muntimadugu, E.; Jaffe, M.; Domb, A.J. Implantable Medical Devices. *Focal Controlled Drug Delivery*; 2014; pp. 33–59.
6. Long, M.; Rack, H. Titanium alloys in total joint replacement—A materials science perspective. *Biomaterials* **1998**, *19*, 1621–1639.
7. Gultepe, E.; Nagesha, D.; Sridhar, S.; Amiji, M. Nanoporous inorganic membranes or coatings for sustained drug delivery in implantable devices. *Adv. Drug Deliv. Rev.* **2010**, *62*, 305–315.
8. Andrade, A.P. Towards New Biocompatible Materials: From Biological Polyesters to Synthetic Copoly (ester-urethanes) for Biomedical Applications. Ph.D. Thesis, University of Bern, Bern, Switzerland, January 2003.
9. Lutz, J.-F. Polymerization of oligo(ethylene glycol) (meth)acrylates: Toward new generations of smart biocompatible materials. *J. Polym. Sci. Part A Polym. Chem.* **2008**, *46*, 3459–3470.
10. Schinhammer, M.; Hänzi, A.C.; Löffler, J.F.; Uggowitzer, P.J. Design strategy for biodegradable Fe-based alloys for medical applications. *Acta Biomater.* **2010**, *6*, 1705–1713.
11. Zhang, L.-N.; Hou, Z.-T.; Ye, X.; Xu, Z.-B.; Bai, X.-L.; Shang, P. The effect of selected alloying element additions on properties of Mg-based alloy as bioimplants: A literature review. *Front. Mater. Sci.* **2013**, *7*, 227–236.
12. Dubok, V.A. Bioceramics—Yesterday, Today, Tomorrow. *Powder Metall. Met. Ceram.* **2000**, *39*, 381–394.
13. Ulery, B.D.; Nair, L.S.; Laurencin, C.T. Biomedical Applications of Biodegradable Polymers. *J. Polym. Sci. B. Polym. Phys.* **2011**, *49*, 832–864.
14. Ramakrishna, S.; Mayer, J.; Wintermantel, E.; Leong, K.W. Biomedical applications of polymer-composite materials: A review. *Compos. Sci. Technol.* **2001**, *61*, 1189–1224.
15. Hanawa, T. Overview of metals and applications. *Metals for Biomedical Devices*;, 2010; pp. 3–24.

16. Lendlein, A.; Rehahn, M.; Buchmeiser, M.R.; Haag, R. Polymers in Biomedicine and Electronics. *Macromol. Rapid Commun.* **2010**, *31*, 1487–1491.
17. Pruitt, L.; Furmanski, J. Polymeric biomaterials for load-bearing medical devices. *JOM J. Miner. Met. Mater. Soc.* **2009**, *61*, 14–20.
18. Hench, L.L. Bioceramics: From Concept to Clinic. *J. Am. Ceram. Soc.* **1991**, *74*, 1487–1510.
19. Wang, M. Bioactive ceramic-polymer composites for tissue replacement. *Engineering Materials for Biomedical Applications*, 2004; pp. 8-1–8-29.
20. Maitz, M.F. Applications of synthetic polymers in clinical medicine. *Biosurf. Biotribol.* **2015**, *1*, 161–176.
21. Thamaraiselvi, T.V.; Rajeswari, S. Biological evaluation of bioceramic materials—a review. *Carbon* **2004**, *24*, 172.
22. Pound, B.G. Corrosion behavior of metallic materials in biomedical applications. II. Stainless steels and Co-Cr alloys. *Corros. Rev.* **2014**, *32*, 21–41.
23. Pound, B.G. Corrosion behavior of metallic materials in biomedical applications. I. Ti and its alloys. *Corros. Rev.* **2014**, *32*, 1–20.
24. Black, J. *Biological Performance of Materials: Fundamentals of Biocompatibility*; CRC Press: Boca Raton, FL, USA, 2006.
25. Bauer, T.W.; Schils, J. The pathology of total joint arthroplasty. II. Mechanisms of implant failure. *Skelet. Radiol.* **1999**, *28*, 483–497.
26. Dujovne, A.R.; Bobyn, J.D.; Krygier, J.J.; Miller, J.E.; Brooks, C.E. Mechanical compatibility of noncemented hip prostheses with the human femur. *J. Arthroplast.* **1993**, *8*, 7–22.
27. Engh, C.; Bobyn, J.; Glassman, A. Porous-coated hip replacement. The factors governing bone ingrowth, stress shielding, and clinical results. *Bone Jt. J.* **1987**, *69*, 45–55.
28. Engh, C.A.; Bobyn, J.D. The influence of stem size and extent of porous coating on femoral bone resorption after primary cementless hip arthroplasty. *Clin. Orthop. Relat. Res.* **1988**, *231*, 7–28,.
29. Kerner, J.; Huiskes, R.; van Lenthe, G.H.; Weinans, H.; van Rietbergen, B.; Engh, C.A.; Amis, A.A. Correlation between pre-operative periprosthetic bone density and post-operative bone loss in THA can be explained by strain-adaptive remodelling. *J. Biomech.* **1999**, *32*, 695–703.
30. Sumner, D.R.; Galante, J.O. Determinants of stress shielding: Design versus materials versus interface. *Clin. Orthop. Relat. Res.* **1992**, *274*, 202–212.
31. Sumner, D.R.; Turner, T.M.; Igloria, R.; Urban, R.M.; Galante, J.O. Functional adaptation and ingrowth of bone vary as a function of hip implant stiffness. *J. Biomech.* **1998**, *31*, 909–917.
32. Turner, T.M.; Sumner, D.R.; Urban, R.M.; Igloria, R.; Galante, J.O. Maintenance of proximal cortical bone with use of a less stiff femoral component in hemiarthroplasty of the hip without cement. An investigation in a canine model at six months and two years. *J. Bone Jt. Surg. Am.* **1997**, *79*, 1381–1390.
33. Van Rietbergen, B.; Huiskes, R.; Weinans, H.; Sumner, D.R.; Turner, T.M.; Galante, J.O. The mechanism of bone remodeling and resorption around press-fitted THA stems. *J. Biomech.* **1993**, *26*, 369–382.

34. Wolff, J. *The Law of Bone Remodelling*; Springer: Berlin/Heidelberg, Germany, 1986.
35. Joint-IMplant-Surgeons-Hip-Replacement-Imgae.png (215 × 360). Available Online:http://www.jointimplantsurgeons.com/wp-ontent/uploads/2015/09/Joint-IMplant-Surgeons-Hip-replacement-imgae.png (accessed on 5 May 2017).
36. Nagels, J.; Stokdijk, M.; Rozing, P.M. Stress shielding and bone resorption in shoulder arthroplasty. *J. Shoulder Elb. Surg.* **2003**, *12*, 35–39.
37. Huiskes, R.; Weinans, H.; van Rietbergen, B. The relationship between stress shielding and bone resorption around total hip stems and the effects of flexible materials. *Clin. Orthop. Relat. Res.* **1992**, *274*, 124–134.
38. Huiskes, R.; Ruimerman, R.; van Lenthe, G.H.; Janssen, J.D. Effects of mechanical forces on maintenance and adaptation of form in trabecular bone. *Nature* **2000**, *405*, 704–706.
39. Mullender, M.G.; Huiskes, R. Proposal for the regulatory mechanism of Wolff's law. *J. Orthop. Res.* **1995**, *13*, 503–512.
40. Lanyon, L.E. Using functional loading to influence bone mass and architecture: Objectives, mechanisms, and relationship with estrogen of the mechanically adaptive process in bone. *Bone* **1996**, *18*, S37–S43.
41. Burger, E.H.; Klein-Nulend, J. Mechanotransduction in bone—Role of the lacuno-canalicular network. *FASEB J.* **1999**, *13*, S101–S112.
42. Noble, B.S.; Stevens, H.; Loveridge, N.; Reeve, J. Identification of apoptotic changes in osteocytes in normal and pathological human bone. *Bone* **1997**, *20*, 273–282.
43. Staiger, M.P.; Pietak, A.M.; Huadmai, J.; Dias, G. Magnesium and its alloys as orthopedic biomaterials: A review. *Biomaterials* **2006**, *27*, 1728–1734.
44. DeGarmo, E.P.; Black, J.T.; Kohser, R.A. *DeGarmo's Materials and Processes in Manufacturing*; John Wiley & Sons, 2011; p. 1184.
45. Gibson, L.J.; Ashby, M.F. *Cellular Solids: Structure & Amp; Properties*; Pergamon Press, 1988.
46. Hänzi, A.C.; Sologubenko, A.S.; Uggowitzer, P.J. Design strategy for new biodegradable Mg–Y–Zn alloys for medical applications. *Int. J. Mater. Res.* **2009**, *100*, 1127–1136.
47. Vojtěch, D.; Kubásek, J.; Šerák, J.; Novák, P. Mechanical and corrosion properties of newly developed biodegradable Zn-based alloys for bone fixation. *Acta Biomater.* **2011**, *7*, 3515–3522.
48. Kroeze, R.J.; Helder, M.N.; Govaert, L.E.; Smit, T.H. Biodegradable Polymers in Bone Tissue Engineering. *Materials* **2009**, *2*, 833–856.
49. Gunde, P.; Hänzi, A.C.; Sologubenko, A.S.; Uggowitzer, P.J. High-strength magnesium alloys for degradable implant applications. *Mater. Sci. Eng. A* **2011**, *528*, 1047–1054.
50. Granchi, D.; Ciapetti, G.; Stea, S.; Savarino, L.; Filippini, F.; Sudanese, A.; Zinghi, G.; Montanaro, L. Cytokine release in mononuclear cells of patients with Co}Cr hip prosthesis. *Biomaterials* **1999**, *20*, 1079–1086.
51. Niki, Y.; Matsumoto, H.; Suda, Y.; Otani, T.; Fujikawa, K.; Toyama, Y.; Hisamori, N.; Nozue, A. Metal ions induce bone-resorbing cytokine production through the redox pathway in synoviocytes and bone marrow macrophages. *Biomaterials* **2003**, *24*, 1447–1457.

52. Haynes, D.R.; Boyle, S.J.; Rogers, S.D.; Howie, D.W.; Vernon-Roberts, B. Variation in cytokines induced by particles from different prosthetic materials. *Clin. Orthop. Relat. Res.* **1998**, *352*, 223–230.
53. Wang, J.Y.; Wicklund, B.H.; Gustilo, R.B.; Tsukayarna, D.T. Titaniurn, chromium and cobalt ions modulate the release of bone-associated cytokines by human monocytes/macrophages in vitro. *Biomoterials* **1996**, *17*, 2233–2240.
54. Bi, Y.; van de Motter, R.R.; Ragab, A.A.; Goldberg, V.M.; Anderson, J.M.; Greenfield, E.M. Titanium particles stimulate bone resorption by inducing differentiation of murine osteoclasts. *J. Bone Jt. Surg. Am.* **2001**, *83*, 501–508.
55. Allen, M.J.; Myer, B.J.; Millett, P.J.; Rushton, N. The effects of particulate cobalt, chromium and cobalt-chromium alloy on human osteoblast-like cells in vitro. *J. Bone Jt. Surg. Br.* **1997**, *79*, 475–482.
56. Jacobs, J.J.; Gilbert, J.L.; Urban, R.M. Corrosion of metal orthopaedic implants. *J. Bone Jt. Surg. Am.* **1998**, *80*, 268–282.
57. Jacobs, J.J.; Hallab, N.J.; Skipor, A.K.; Urban, R.M. Metal degradation products: A cause for concern in metal-metal bearings? *Clin. Orthop. Relat. Res.* **2003**, *417*, 139–147.
58. Beech, I.B.; Sunner, J.A.; Arciola, C.R.; Cristiani, P. Microbially-influenced corrosion: Damage to prostheses, delight for bacteria. *Int. J. Artif. Organs* **2006**, *29*, 443–452.
59. Williams, D.F. On the nature of biomaterials. *Biomaterials* **2009**, *30*, 5897–5909.
60. Raman, R.K.S.; Jafari, S.; Harandi, S.E. Corrosion fatigue fracture of magnesium alloys in bioimplant applications: A review. *Eng. Fract. Mech.* **2015**, *137*, 97–108.
61. Sanderson, G.; Scully, J.C. Room Temperature Stress Corrosion Cracking of Titanium Alloys. *Nature* **1966**, *211*, 179.
62. Mori, K.; Takamura, A.; Shimose, T. Stress Corrosion Cracking off Ti and Zr in HCl-Methanol Solutions. *Corrosion* **1966**, *22*, 29–31.
63. Sutcliffe, J.M.; Fessler, R.R.; Boyd, W.K.; Parkins, R.N. Stress Corrosion Cracking of Carbon Steel in Carbonate Solutions. *Corrosion* **1972**, *28*, 313–320.
64. Mueller, W.-D.; Nascimento, M.L.; de Mele, M.F.L. Critical discussion of the results from different corrosion studies of Mg and Mg alloys for biomaterial applications. *Acta Biomater.* **2010**, *6*, 1749–1755.
65. Chen, K.; Dai, J.; Zhang, X. Improvement of corrosion resistance of magnesium alloys for biomedical applications. *Corros. Rev.* **2015**, *33*, 101–117.
66. Atrens, A.; Liu, M.; Abidin, N.I.Z. Corrosion mechanism applicable to biodegradable magnesium implants. *Mater. Sci. Eng. B* **2011**, *176*, 1609–1636.
67. Shaw, B.A. Corrosion Resistance of Magnesium Alloys. In *ASM Handbook*; Vol 13A Corrosion: Fundamentals, Testing, and Protection. ASM International Handbook Committee: Metals Park, OH, USA, 2003.
68. Witte, F.; Hort, N.; Vogt, C.; Cohen, S.; Kainer, K.U.; Willumeit, R.; Feyerabend, F. Degradable biomaterials based on magnesium corrosion. *Curr. Opin. Solid State Mater. Sci.* **2008**, *12*, 63–72.
69. Xu, L.; Yu, G.; Zhang, E.; Pan, F.; Yang, K. In vivo corrosion behavior of Mg-Mn-Zn alloy for bone implant application. *J. Biomed. Mater. Res. Part A* **2007**, *83*, 703–711.

70. Witte, F.; Kaese, V.; Haferkamp, H.; Switzer, E.; Meyer-Lindenberg, A.; Wirth, C.J.; Windhagen, H. In vivo corrosion of four magnesium alloys and the associated bone response. *Biomaterials* **2005**, *26*, 3557–3563.
71. Hänzi, A.C.; Gerber, I.; Schinhammer, M.; Löffler, J.F.; Uggowitzer, P.J. On the in vitro and in vivo degradation performance and biological response of new biodegradable Mg-Y-Zn alloys. *Acta Biomater.* **2010**, *6*, 1824–1833.
72. Ghali, E.; Dietzel, W.; Kainer, K.-U. General and Localized Corrosion of Magnesium Alloys: A Critical Review. *J. Mater. Eng. Perform.* **2004**, *13*, 7–23.
73. Kirkland, N.T.; Lespagnol, J.; Birbilis, N.; Staiger, M.P. A survey of bio-corrosion rates of magnesium alloys. *Corros. Sci.* **2010**, *52*, 287–291.
74. Manivasagam, G.; Suwas, S. Biodegradable Mg and Mg based alloys for biomedical implants. *Mater. Sci. Technol.* **2014**, *30*, 515–520.
75. Winzer, N.; Atrens, A.; Song, G.; Ghali, E.; Dietzel, W.; Kainer, K.U.; Hort, N.; Blawert, C. A critical review of the Stress Corrosion Cracking (SCC) of magnesium alloys. *Adv. Eng. Mater.* **2005**, *7*, 659–693.
76. Song, G.; Atrens, A.; Dargusch, M. Influence of microstructure on the corrosion of diecast AZ91D. *Corros. Sci.* **1998**, *41*, 249–273.
77. Song, G.-L.; Atrens, A. Corrosion Mechanisms of Magnesium Alloys. *Adv. Eng. Mater.* **1999**, *1*, 11–33.
78. Jafari, S.; Harandi, S.E.; Raman, R.K.S. A review of stress-corrosion cracking and corrosion fatigue of magnesium alloys for biodegradable implant applications. *JOM* **2015**, *67*, 1143–1153.
79. Song, G. Control of biodegradation of biocompatable magnesium alloys. *Corros. Sci.* **2007**, *49*, 1696–1701.
80. Zberg, B.; Uggowitzer, P.J.; Löffler, J.F. MgZnCa glasses without clinically observable hydrogen evolution for biodegradable implants. *Nat. Mater.* **2009**, *8*, 887–891.
81. Matias, T.B.; Asato, G.H.; Ramasco, B.T.; Botta, W.J.; Kiminami, C.S.; Bolfarini, C. Processing and characterization of amorphous magnesium based alloy for application in biomedical implants. *J. Mater. Res. Technol.* **2014**, *3*, 203–209.
82. Kirkland, N.T. Magnesium biomaterials: Past, present and future. *Corros. Eng. Sci. Technol.* **2012**, *47*, 322–328.
83. Choudhary, L.; Raman, R.K.S. Acta Biomaterialia Magnesium alloys as body implants : Fracture mechanism under dynamic and static loadings in a physiological environment. *Acta Biomater.* **2012**, *8*, 916–923.
84. Hofstetter, J.; Martinelli, E.; Weinberg, A.M.; Becker, M.; Mingler, B.; Uggowitzer, P.J.; Löffler, J.F. Assessing the degradation performance of ultrahigh-purity magnesium in vitro and in vivo. *Corros. Sci.* **2015**, *91*, 29–36.
85. Persaud-Sharma, D.; McGoron, A. Biodegradable Magnesium Alloys: A Review of Material Development and Applications. *J. Biomim. Biomater. Tissue Eng.* **2012**, *12*, 25–39.
86. Jafari, S.; Raman, R.K.S.; Davies, C.H.J. Corrosion fatigue of a magnesium alloy in modified simulated body fluid. *Eng. Fract. Mech.* **2015**, *137*, 2–11.
87. Song, G.; Atrens, A. Understanding Magnesium Corrosion—A Framework for Improved Alloy Performance. *Adv. Eng. Mater.* **2003**, *5*, 837–858.

88. Potzies, C.; Kainer, K.U. Fatigue of magnesium alloys. *Adv. Eng. Mater.* **2004**, *6*, 281–289.
89. Zheng, Y.F.; Gu, X.N.; Witte, F. Biodegradable metals. *Mater. Sci. Eng. R Rep.* **2014**, *77*, 1–34.
90. Maragoni, L.; Carraro, P.A.; Peron, M.; Quaresimin, M. Fatigue behaviour of glass/epoxy laminates in the presence of voids. *Int. J. Fatigue* **2017**, *95*, 18–28.
91. Gu, X.N.; Zhou, W.R.; Zheng, Y.F.; Cheng, Y.; Wei, S.C.; Zhong, S.P.; Xi, T.F.; Chen, L.J. Corrosion fatigue behaviors of two biomedical Mg alloys - AZ91D and WE43—In simulated body fluid. *Acta Biomater.* **2010**, *6*, 4605–4613.
92. Logan, H.L. Mechanism of Stress-Corrosion Cracking in the AZ31B Magnesium Alloy. *J. Res. Natl. Bur. Stand. (1934)* **1958**, *61*, 503–508.
93. Logan, H.L. Film-Rupture Mechanism of Stress Corrosion. *J. Res. Natl. Bur. Stand. (1934)* **1952**, *48*, 99–105.
94. Ebtehaj, K.; Hardie, D.; Parkins, R.N. The influence of chloride-chromate solution composition on the stress corrosion cracking of a Mg-Al alloy. *Corros. Sci.* **1988**, *28*, 811–821.
95. Wearmouth, W.R.; Dean, G.P.; Parkins, R.N. Role of Stress in the Stress Corrosion Cracking of a Mg-Al Alloy. *Corrosion* **1973**, *29*, 251–260.
96. Pugh, E.N.; Green, J.A.S.; Slattery, P.W. On the propagation of stress-corrosion cracks in magnesium-aluminum alloy. In the Proceedings of the 2nd International Conference on Fracture, London, UK, April 1969; Chapman & Hall Limited: London, UK, 1969.
97. Pickering, H.W.; Swann, P.R. Electron Metallography of Chemical Attack Upon Some Alloys Susceptible to Stress Corrosion Cracking. *Corrosion* **1963**, *19*, 373t–389t.
98. Fairman, L.; Bray, H.J. Intergranular Stress-Corrosion Crack Propagation in Magnesium Aluminium Alloys. *Br. Corros. J.* **1971**, *6*, 170–174.
99. Song, G.; Atrens, A.; Wu, X.; Zhang, B. Corrosion behaviour of AZ21, AZ501 and AZ91 in sodium chloride. *Corros. Sci.* **1998**, *40*, 1769–1791.
100. Pardue, W.M.; Beck, F.H.; Fontana, M.G. Propagation of stress-corrosion cracking in a magnesium-base alloy as determined by several techniques. *Trans. Am. Soc. Met.* **1961**, *54*, 539–548.
101. Raman, R.K.S.; Harandi, S.E. Understanding Corrosion-Assisted Cracking of Magnesium Alloys for Bioimplant Applications. *Magnesium Technology, 2016*;; pp. 343–346.
102. Uematsu, Y.; Kakiuchi, T.; Nakajima, M.; Nakamura, Y.; Miyazaki, S.; Makino, H. Fatigue crack propagation of AZ61 magnesium alloy under controlled humidity and visualization of hydrogen diffusion along the crack wake. *Int. J. Fatigue* **2014**, *59*, 234–243.
103. Chakrapani, D.G.; Pugh, E.N. The transgranular SCC of a Mg-Al alloy: Crystallographic, fractographic and acoustic-emission studies. *Metall. Trans. A* **1975**, *6*, 1155–1163.
104. Lynch, S.P.; Trevena, P. Stress Corrosion Cracking and Liquid Metal Embrittlement in Pure Magnesium. *Corrosion* **1988**, *44*, 113–124.
105. Bursle, A.; Pugh, E. On the Mechanism of Transgranular Stress-Corrosion Cracking. *Mechanisms of Environment Sensitive Cracking of*

Materials, Mechanisms of Environment Sensitive Cracking of Materials; Materials Society: London, UK, 1977.
106. Makar, G.L.; Kruger, J. Corrosion of magnesium. *Int. Mater. Rev.* **1993**, *38*, 138–153.
107. Fairman, L.; West, J.M. Stress corrosion cracking of a magnesium aluminium alloy. *Corros. Sci.* **1965**, *5*, 711–716.
108. Gross, B.; Mendelson, A. Plane elastostatic analysis of V-notched plates. *Int. J. Fract. Mech.* **1972**, *8*, 267–276.
109. Taylor, D. Fatigue of bone and bones: An analysis based on stressed volume. *J. Orthop. Res.* **1998**, *16*, 163–169.
110. Bhuiyan, M.S.; Mutoh, Y.; Murai, T.; Iwakami, S. Corrosion fatigue behavior of extruded magnesium alloy AZ61 under three different corrosive environments. *Int. J. Fatigue* **2008**, *30*, 1756–1765.
111. Sivakumar, M.; Rajeswari, S. Investigation of failures in stainless steel orthopaedic implant devices: Pit-induced stress corrosion cracking. *J. Mater. Sci. Lett.* **1992**, *11*, 1039–1042.
112. Antunes, R.A.; de Oliveira, M.C.L. Corrosion fatigue of biomedical metallic alloys: Mechanisms and mitigation. *Acta Biomater.* **2012**, *8*, 937–962.
113. Zeng, R.C.; Han, E.H.; Ke, W. Effect of Temperature and Relative Humidity on Fatigue Crack Propagation Behavior of AZ61 Magnesium Alloy. *Mater. Sci. Forum* **2007**, *546–549*, 409–412.
114. Shiplov, S.A. Mechanisms for corrosion fatigue crack propagation. *Fatigue Fract. Eng. Mater. Struct.* **2002**, *25*, 243–259.
115. Vasudevan, A.K.; Sadananda, K. Classification of environmentally assisted fatigue crack growth behavior. *Int. J. Fatigue* **2009**, *31*, 1696–1708.
116. Rozali, S.; Mutoh, Y.; Nagata, K. Effect of frequency on fatigue crack growth behavior of magnesium alloy AZ61 under immersed 3.5 mass% NaCl environment. *Mater. Sci. Eng. A* **2010**, *528*, 2509–2516.
117. Chakrapani, D.G.; Pugh, E.N. Hydrogen Embrittlement in a Mg-Al Alloy. *Metall. Trans. A* **1976**, *7*, 173–178.
118. Song, G.; Atrens, A.; Stjohn, D.; Nairn, J.; Li, Y. The electrochemical corrosion of pure magnesium in 1 N NaCl. *Corros. Sci.* **1997**, *39*, 855–875.
119. Perrault, G.G. Potentiostatic study of the magnesium electrode in aqueous solution. *J. Electroanal. Chem. Interfacial Electrochem.* **1970**, *27*, 47–58.
120. Murray, R.W.; Hillis, J.E. Magnesium Finishing: Chemical Treatment and Coating Practices. In *SAE Technical Paper 900791*; 1990.
121. Hillis, J.E. The Effects of Heavy Metal Contamination on Magnesium Corrosion Performance. In *SAE Technical Paper 830523*; :1983.
122. Ahamed, M. Toxic response of nickel nanoparticles in human lung epithelial A549 cells. *Toxicol. In Vitro* **2011**, *25*, 930–936.
123. Milavec-Puretić, V.; Orlić, D.; Marusić, A. Sensitivity to metals in 40 patients with failed hip endoprosthesis. *Arch. Orthop. Trauma Surg.* **1998**, *117*, 383–386.
124. Hillis, J.; Murray, R. Finishing alternatives for high purity magnesium alloys. SDCE 14th International Die Casting Congress and Exposition, Toronto, 1987.

125. Pelensky, M.A.; Gallaccio, A. Stress Corrosion of Magnesium Alloys—Environmental Factors. *Stress Corrosion Testing, ASTM STP425*; 1967.
126. Shi, Z.; Song, G.; Atrens, A. Corrosion resistance of anodised single-phase Mg alloys. *Surf. Coat. Technol.* **2006**, *201*, 492–503.
127. Hofstetter, J.; Becker, M.; Martinelli, E.; Weinberg, A.M.; Mingler, B.; Kilian, H.; Pogatscher, S.; Uggowitzer, P.J.; Löffler, J.F. High-strength low-alloy (HSLA) Mg-Zn-Ca alloys with excellent biodegradation performance. *JOM* **2014**, *66*, 566–572.
128. Li, L.; Gao, J.; Wang, Y. Evaluation of cyto-toxicity and corrosion behavior of alkali-heat-treated magnesium in simulated body fluid. *Surf. Coat. Technol.* **2004**, *185*, 92–98.
129. Hanawalt, J.D.; Nelson, C.E.; Peloubet, J.A. Corrosion studies of magnesium and its alloys. *Trans AIME* **1942**, *47*, 273–299.
130. Reichek, K.N.; Clark, K.J.; Hillis, J.E. Controlling the Salt Water Corrosion Performance of Magnesium AZ91 Alloy. *SAE Technical Paper 850417*, 1985.
131. Lunder, O.; Aune, T.K.; Nisancioglu, K. Effect of Mn Additions on the Corrosion Behavior of Mould-Cast Magnesium ASTM AZ91.*Corrosion* **1987**, *43*, 291–295.
132. Mercer, W.E.; Hillis, J.E. The Critical Contaminant Limits and Salt Water Corrosion Performance of Magnesium AE42 Alloy. *SAE Technical Paper 920073*, 1992.
133. Avedesian, M.M.; Baker, H. *Magnesium and Magnesium Alloys*; ASM International Handbook Committee, 1999.
134. Kainer, K.U.; Srinivasan, P.B.; Blawert, C.; Dietzel, W. Corrosion of magnesium and its alloys. *Shreir's Corros.* **2010**; *3*, 2011–2041.
135. Mezbahul-Islam, M.; Mostafa, A.O.; Medraj, M. Essential Magnesium Alloys Binary Phase Diagrams and Their Thermochemical Data. *J. Mater.* **2014**, *2014*, 1–33.
136. Gusieva, K.; Davies, C.H.J.; Scully, J.R.; Birbilis, N. Corrosion of magnesium alloys: The role of alloying. *Int. Mater. Rev.* **2015**, *60*, 169–194.
137. Hermann, F.; Sommer, F.; Jones, H.; Edyvean, R.G.J. Corrosion inhibition in magnesium-aluminium-based alloys induced by rapid solidification processing. *J. Mater. Sci.* **1989**, *24*, 2369–2379.
138. Lunder, O.; Lein, J.E.; Aune, T.K.; Nisancioglu, K. The Role of $Mg_{17}Al_{12}$ Phase in the Corrosion of Mg Alloy AZ91. *Corrosion* **1989**, *45*, 741–748.
139. Jeong, Y.S.; Kim, W.J. Enhancement of mechanical properties and corrosion resistance of Mg–Ca alloys through microstructural refinement by indirect extrusion. *Corros. Sci.* **2014**, *82*, 392–403.
140. Domingo, J.L. Reproductive and developmental toxicity of aluminum: A review. *Neurotoxicol. Teratol.* **1995**, *17*, 515–521.
141. Venugopal, B.; Luckey, T.D. *Metal Toxicity in Mammals. Volume 2. Chemical Toxicity of Metals and Metalloids*;, 1978.
142. Flaten, T.P. Aluminium as a risk factor in Alzheimer's disease, with emphasis on drinking water. *Brain Res. Bull.* **2001**, *55*, 187–196.
143. El-Rahman, S.S.A. Neuropathology of aluminum toxicity in rats (glutamate and GABA impairment). *Pharmacol. Res.* **2003**, *47*, 189–194.

144. Robinson, H.A.; George, P.F. Effect of Alloying and Impurity Elements In Magnesium Alloy Cast Anodes. *Corrosion* **1954**, *10*, 182–188.
145. Culotta, V.C.; Yang, M.; Hall, M.D. Manganese Transport and Trafficking: Lessons Learned from Saccharomyces cerevisiae. *Eukaryot. Cell* **2005**, *4*, 1159–1165.
146. Brandt, E.G.; Hellgren, M.; Brinck, T.; Bergman, T.; Edholm, O. Molecular dynamics study of zinc binding to cysteines in a peptide mimic of the alcohol dehydrogenase structural zinc site. *Phys. Chem. Chem. Phys.* **2009**, *11*, 975–983.
147. Prasad, A.S. Zinc in human health: Effect of zinc on immune cells. *Mol. Med.* **2008**, *14*, 353–357.
148. Bothwell, D.N.; Mair, E.A.; Cable, B.B. Chronic ingestion of a zinc-based penny. *Pediatrics* **2003**, *111*, 689–691.
149. Zhang, S.; Zhang, X.; Zhao, C.; Li, J.; Song, Y.; Xie, C.; Tao, H.; Zhang, Y.; He, Y.; Jiang, Y.; et al. Research on an Mg–Zn alloy as a degradable biomaterial. *Acta Biomater.* **2010**, *6*, 626–640.
150. Li, Y.; Wen, C.; Mushahary, D.; Sravanthi, R.; Harishankar, N.; Pande, G.; Hodgson, P. Mg–Zr–Sr alloys as biodegradable implant materials. *Acta Biomater.* **2012**, *8*, 3177–3188.
151. Song, G.; StJohn, D. The effect of zirconium grain refinement on the corrosion behaviour of magnesium-rare earth alloy MEZ. *J. Light Met.* **2002**, *2*, 1–16.
152. Jiao, W.; Li, H.F.; Zhao, K.; Bai, H.Y.; Whang, Y.B.; Zheng, Y.F.; Wang, W.H. Development of CaZn based glassy alloys as potential biodegradable bone graft substitute. *J. Non-Cryst. Solids* **2011**, *357*, 3830–3840.
153. Rad, H.R.B.; Idris, M.H.; Kadir, M.R.A.; Farahany, S. Microstructure analysis and corrosion behavior of biodegradable Mg–Ca implant alloys. *Mater. Des.* **2012**, *33*, 88–97.
154. Zhang, E.; Yang, L. Microstructure, mechanical properties and bio-corrosion properties of Mg–Zn–Mn–Ca alloy for biomedical application. *Mater. Sci. Eng. A* **2008**, *497*, 111–118.
155. Kirkland, N.T.; Birbilis, N.; Walker, J.; Woodfield, T.; Dias, G.J.; Staiger, M.P. In-vitro dissolution of magnesium-calcium binary alloys: Clarifying the unique role of calcium additions in bioresorbable magnesium implant alloys. *J. Biomed. Mater. Res. Part B Appl. Biomater.* **2010**, *95*, 91–100.
156. Bornapour, M.; Celikin, M.; Cerruti, M.; Pekguleryuz, M. Magnesium implant alloy with low levels of strontium and calcium: The third element effect and phase selection improve bio-corrosion resistance and mechanical performance. *Mater. Sci. Eng. C* **2014**, *35*, 267–282.
157. Lazar, L.L.; Rokhlin, L. *Magnesium Alloys Containing Rare Earth Metals: Structure and Properties*; Taylor & Francis, 2003.
158. Kannan, M.B.; Dietzel, W.; Blawert, C.; Atrens, A.; Lyon, P. Stress corrosion cracking of rare-earth containing magnesium alloys ZE41, QE22 and Elektron 21 (EV31A) compared with AZ80. *Mater. Sci. Eng. A* **2008**, *480*, 529–539.
159. Zhang, T.; Meng, G.; Shao, Y.; Cui, Z.; Wang, F. Corrosion of hot extrusion AZ91 magnesium alloy. Part II: Effect of rare earth element

neodymium (Nd) on the corrosion behavior of extruded alloy. *Corros. Sci.* **2011**, *53*, 2934–2942.
160. Li, W.; Cao, F.; Zhong, L.; Zheng, L.; Jia, B.; Zhang, Z.; Zhang, J. Influence of rare earth element Ce and La addition on corrosion behavior of AZ91 magnesium alloy. *Mater. Corros.* **2009**, *60*, 795–803.
161. Zhou, X.; Huang, Y.; Wei, Z.; Chen, Q.; Gan, F. Improvement of corrosion resistance of AZ91D magnesium alloy by holmium addition. *Corros. Sci.* **2006**, *48*, 4223–4233.
162. Yao, S.J.; Yi, D.Q.; Yang, S.; Cang, X.H.; Li, W.X. Effect of Sc on Microstructures and Corrosion Properties of AZ91. *Mater. Sci. Forum* **2007**, *546–549*, 139–142.
163. Santamaria, M.; di Quarto, F.; Zanna, S.; Marcus, P. Initial surface film on magnesium metal: A characterization by X-ray photoelectron spectroscopy (XPS) and photocurrent spectroscopy (PCS). *Electrochim. Acta* **2007**, *53*, 1314–1324.
164. Hänzi, A.C.; Gunde, P.; Schinhammer, M.; Uggowitzer, P.J. On the biodegradation performance of an Mg–Y–RE alloy with various surface conditions in simulated body fluid. *Acta Biomater.* **2009**, *5*, 162–171.
165. Best, S.M.; Porter, A.E.; Thian, E.S.; Huang, J. Bioceramics: Past, present and for the future. *J. Eur. Ceram. Soc.* **2008**, *28*, 1319–1327.
166. Hornberger, H.; Virtanen, S.; Boccaccini, A.R. Biomedical coatings on magnesium alloys—A review. *Acta Biomater.* **2012**, *8*, 2442–2455.
167. Song, Y.; Zhang, S.; Li, J.; Zhao, C.; Zhang, X. Electrodeposition of Ca–P coatings on biodegradable Mg alloy: In vitro biomineralization behavior. *Acta Biomater.* **2010**, *6*, 1736–1742.
168. Wang, H.X.; Guan, S.K.; Wang, X.; Ren, C.X.; Wang, L.G. In vitro degradation and mechanical integrity of Mg–Zn–Ca alloy coated with Ca-deficient hydroxyapatite by the pulse electrodeposition process. *Acta Biomater.* **2010**, *6*, 1743–1748.
169. Zhu, B.; Xu, Y.; Sun, J.; Yang, L.; Guo, C.; Liang, J.; Cao, B. Preparation and Characterization of Aminated Hydroxyethyl Cellulose-Induced Biomimetic Hydroxyapatite Coatings on the AZ31 Magnesium Alloy. *Metals* **2017**, *7*, 214.
170. Yang, J.; Cui, F.Z.; Lee, I.; Zhang, Y.; Yin, Q.S.; Xia, H.; Yang, S.X. In vivo biocompatibility and degradation behavior of Mg alloy coated by calcium phosphate in a rabbit model. *J. Biomater. Appl.* **2012**, *27*, 153–164.
171. Chiu, K.Y.; Wong, M.H.; Cheng, F.T.; Man, H.C. Characterization and corrosion studies of fluoride conversion coating on degradable Mg implants. *Surf. Coat. Technol.* **2007**, *202*, 590–598.
172. Witte, F.; Fischer, J.; Nellesen, J.; Vogt, C.; Vogt, J.; Donath, T.; Beckmann, F. In vivo corrosion and corrosion protection of magnesium alloy LAE442. *Acta Biomater.* **2010**, *6*, 1792–1799.
173. Li, J.N.; Cao, P.; Zhang, X.N.; Zhang, S.X.; He, Y.H. In vitro degradation and cell attachment of a PLGA coated biodegradable Mg–6Zn based alloy. *J. Mater. Sci.* **2010**, *45*, 6038–6045.
174. Albayrak, O.; El-Atwani, O.; Altintas, S. Hydroxyapatite coating on titanium substrate by electrophoretic deposition method: Effects of titanium

dioxide inner layer on adhesion strength and hydroxyapatite decomposition. *Surf. Coat. Technol.* **2008**, *202*, 2482–2487.
175. Glocker, D.A.; Ranade, S.V. *Medical Coatings and Deposition Technologies*; John Wiley & Sons, 2016.

2.2. Book: Magnesium and Its Alloys as Implant Materials: Corrosion, Mechanical and Biological Performances

M. Peron[1], F. Berto, J. Torgersen

Department of Mechanical and Industrial Engineering, Norwegian University of Science and Technology (NTNU), Richard Birkelands vei 2b, 7034, Trondheim

Summary[2]

Despite their tremendous potential, Mg and its alloys are not yet used in biomedical applications. This book aims to provide scientific insights into the challenges of the materials, and give an overview of the research regarding their mechanical properties, corrosion behaviour and biological performances. The authors intend to put the reader into the position to accurate discern the proper Mg-based material for his/her applications and to choose the proper improvement strategy to his/her cause. To this aim, the manuscript is structured as follow: in Section 2.2.2., the main challenges hampering the use of magnesium in biomedical applications and the common improvement strategies are listed. In Section 2.2.3., the most investigated Mg alloys are reported in separate sub-sections, detailing their mechanical properties, corrosion behaviour and biotoxicity. High-pure and ultra-high-pure Mg, Al-based Mg alloys, Zn-based Mg alloys, Ca-based alloys and RE-based Mg alloys have been considered. In Section 2.2.4., the alloys' performances with respect to the challenges is summarized providing the reader with useful information and suggestions on the potentially most suited choice. Finally, in Section 2.2.5., an outlook portraying the authors' opinion of the future development of the field will be provided. This book will allow biomedical engineers, surface scientists, material scientists, implant manufacturers and companies working on implant approval an overview of the state-of-the-art technologies adopted so far to overcome the drawbacks of Mg for biomedical applications. Particular emphasis is put on explaining the link between mechanical, corrosion and biocompatible properties of Mg and its alloys as well as their pros and cons. In doing so, the authors intend to put the reader into the position to accurate discern the proper Mg-based material for his/her applications and to choose the proper improvement strategy to his/her cause.

2.2.1. Chapter 1: Introduction

2.2.1.1. Introduction

[1] Corresponding author

[2] CRC Press, Taylor & Francis Group, Boca Raton, Florida, United States, forthcoming April 2020

Chapter 3

On the effect of the microstructure on the SCC susceptibility of AZ31 alloy

Paper II: The effect of Equal Channel Angular Pressing on the Stress Corrosion Cracking susceptibility of AZ31 alloy in simulated body fluid

M. Peron[a,1], P. C. Skaret[b], A. Fabrizi[c], R. Montanari[d], H. J. Roven[b], P. Ferro[c], F. Berto[a], J. Torgersen[a]

[a] *Department of Industrial and Mechanical Engineering, Norwegian University of Science and Technology, Richard Birkelands vei, 2b, 7034 Trondheim, Norway*
[b] *Department of Materials Science and Engineering, Norwegian University of Science and Technology, Alfred Getz vei, 2, 7491 Trondheim, Norway*
[c] *Department of Management and Engineering, Padova University, Stradella San Nicola, 3, 36100 Vicenza, Italy*
[d] *Department of Industrial Engineering, University of Rome "Tor Vergata", Via del Politecnico, 1, 00133, Rome, Italy*

Abstract[2]

Despite the great potential of Mg and its alloys as material for biodegradable implants, their low resistance to the simultaneous action of corrosion and mechanical stresses in the human body have hampered their use. Stress Corrosion Cracking has been reported as one of the most critical failure modes to overcome to allow such materials to be clinically applied. Thus, in this paper we investigate the effect of Equal Channel Angular Pressing (ECAP) on the Stress Corrosion Cracking (SCC) susceptibility of the AZ31 Mg alloy. To do so, AZ31 alloy has been subjected to 1, 2 and 4 passes of ECAP, and the samples so obtained have then been tested by means Slow Strain Rate Tests (SSRTs) in Simulated Body Fluid (SBF) at 37 °C. Samples subjected to one pass of ECAP are shown to be less susceptible to SCC compared to the material in the as-received condition due to the improved corrosion resistance (the corrosion current density was almost three times lower and the evolved hydrogen reduced by half) as a consequence of a reduced grain size (from 27.5 μm to 8.3 μm). The reduced SCC susceptibility after one pass of ECAP was also confirmed by the morphology of the fracture surfaces after SSRTs analyzed by means of Scanning Electron Microscopy (SEM), that reveals an increased ductility compared to the as-received material. However further ECAP processing (2 and 4 passes) are reported to worsen the SCC susceptibility due to an increased brittleness of the material as a consequence of an increased amount of hydrogen evolved. This is due to the unfavorable texture evolution, as confirmed by the mechanical characterization (tensile tests and hardness measurements). In conclusion, this study proved, for the first time to the best of the authors' knowledge, that the SCC susceptibility of AZ31 alloy can be improved by

[1] Corresponding author
[2] *Journal of the Mechanical Behavior of Biomedical Materials* (resubmitted after minor revision, the reported version is that before revision)

ECAP processing. The number of passes however needs to be optimized to avoid any undesired effect of the texture evolution.

Keywords: ECAP; Stress Corrosion Cracking; AZ31 alloy; Slow Strain Rate Tests; Simulated Body Fluid

3.1. Introduction

In the past years, the amount of people undergoing surgical procedures involving the implantation of medical devices is continuously growing [1]. In particular, orthopaedic surgery is the most important, with the associated healthcare system costs estimated to increase by 26% in 2030 compared to 2019 in Europe [2]. The materials currently used in orthopaedic surgery are permanent metallic materials, such as stainless steel, titanium, and cobalt-chromium alloys [3]. In particular, these inert materials are used as load-bearing implants for replacement of diseased or damaged tissues [4–6]. However, two main disadvantages are linked to the implementation of these materials. Firstly, the great difference in elastic modulus of these materials compared to that of human bone results in the occurrence of the stress-shielding phenomenon. This is a consequence of stress distribution changes between the bone and the implant [7–13]: bones adapt to the reduced stress field according to the Wolff's law [14], resulting in the bone either becoming more porous (internal remodelling) or thinner (external remodelling), leading to a higher risk of implant failure. Secondly, after the bone has healed, permanent metals must be removed from the body by using a secondary surgical intervention since they can lead to long-term complications, such as local inflammations due to the potential release of cytotoxic ions as a consequence of corrosion or wear processes [15–19]. To solve these drawbacks, biodegradable materials like magnesium and iron alloys have been proposed in medical science as a novel class of highly bioactive materials. That is, these materials are supposed to temporarily aid the healing process of a diseased tissue or organ and then they can progressively disappear by virtue of body fluids corrosion after a certain length of functional use, leading to simultaneous implant replacement through the surrounding tissue [20]. Magnesium is one of the most promising candidates for biodegradable applications due to its excellent bio-compatibilities with human physiology and the best mechanical compatibility with human bone [21]. Its low density and elastic modulus best mimic the properties of natural bones, reducing the risk of the stress shielding phenomenon [20]. Moreover, Mg is the fourth most abundant element in the human body (it is recommended that an adult receives 240–420 mg daily and any excess can be harmlessly excreted in the urine [22]). Finally, it is essential for the metabolism in many biological mechanisms, being a cofactor for many enzymes [23], and Mg^{2+} ions resulting from the degradation process are reported to aid the healing and growth of tissue. However, the greatest limitation of Mg consists of its fast corrosion rate, especially in human body fluid containing chloride, giving rise to immature drop in mechanical integrity of the device before accomplishing its defined mission [24]. Over and above corrosion rate, critical hydrogen gas bubbles and alkalization resulting from corrosion of Mg in body fluid are also other problematic subjects in fast corrosion-rate processes, leading to accumulation of evolved hydrogen bubbles in gas pockets next to the implant and consequently, causing necrosis of tissues. However, if the corrosion rate of Mg implant can be suitably

controlled, hydrogen evolution will not be rapid enough to cause critical subcutaneous bubbles, and the alkalization effect could be easily balanced by metabolic mechanisms in the human body. A further challenging issue to be faced concerns the fact that the implant must possess adequate resistance to cracking under the simultaneous action of the corrosive human body fluid and the mechanical loading characteristics of the human body. Corrosion-assisted cracking phenomena, such as stress corrosion cracking (SCC) and corrosion fatigue (CF), were in fact reported to cause the failure of several traditional implants [25–28]. In particular, SCC is particularly dangerous because it leads to a sudden and catastrophic fast failure under mechanical loading conditions otherwise considered to be safe, and magnesium and its alloys have been reported to be susceptible to it in simulated physiological conditions [29–31]. Therefore, it is important to develop Mg-based implants that confer a combination of strength and corrosion resistance in human body fluid without causing corrosion-assisted cracking phenomena. However, most studies have focused on improving the electrochemical properties of Mg and its alloys, whereas the literature on improving their resistance to corrosion-assisted cracking phenomena is very limited. In fact, while different procedures have been applied in the recent years to improve their corrosion resistance, from alloying to surface modification techniques, only few of them have been assessed regarding their effects on the susceptibility to corrosion-assisted cracking phenomena. Mohajernia et al. [32] reported that hydroxyapatite coating containing multi-walled carbon nanotubes reduced the corrosion current density of AZ31 alloy of three order of magnitude. In addition, they reported the elongation to failure of AZ31 samples subjected to slow strain rate tests (SSRT) in simulated body fluid (SBF) at 37 °C to be increased about 70% with the application of the coating. These results agree with those obtained by Chen et al. [33]. They coated Mg-4Zn-0.6Zr-0.4Sr with a composite coating consisting of a poly (lactic-co-glycolic acid) (PLGA) superimposed to a micro-arc oxidation (MAO) layer and they reported this composite coating to increase the elongation to failure of the bare alloy subjected to SSRT in modified simulated body fluid (m-SBF) at 37 °C from 5% to 11%. Again, the corrosion rate was reduced of three order of magnitude. However, when repetitive loadings are applied, the presence of coatings might result to be detrimental for the fatigue life of the implants due to the formation of cracks in the coating (due to elastic modulus mismatch) that act as stress concentrators and also due to the generally higher surface roughness of the coated samples compared to the polished uncoated counterparts [34]. Alternatively, alloying has been reported as a valuable solution to improve the corrosion resistance of Mg and the effect of different alloying elements on the corrosion-assisted cracking phenomena. For instance, Kannan et al. [35], compared the SCC susceptibility of three different rare earth (RE)-containing alloys, namely ZE41, QE22 and EV31A, with that of AZ80 alloy. They suggested that rare-earth elements in magnesium alloys can improve the SCC resistance significantly, being EV31A alloy the most resistant to SCC compared to the other alloy. The beneficial effect of RE was found also by Choudhary et al. [36]. According to their findings, a lower SCC susceptibility was observed for RE-containing alloys, i.e. WZ21 and WE43 compared to Mg-Zn-Ca alloy (ZX50). However, some RE elements were reported to be toxic for the human body [37], and in general alloying may introduce elements that lead to adverse biological reactions. In recent years, mechanical processing inducing severe plastic deformation (SPD) have been investigated as an alternative to alloying and coating techniques. Again, broad attention

was given to the effect of SPD techniques on the corrosion properties, whereas very few on the SCC susceptibility. Machining has been studied as method to reduce the corrosion rate. In particular, cryogenic machining has attracted researcher's attention on its effect on the corrosion behaviour of Mg alloys. Bertolini et al. reported dry machined AZ31 samples to be characterized by an hydrogen evolution rate twice that of the cryogenic machined counterparts [38]. In addition, Peron et al. [39] reported the elongation to failure of AZ31 samples subjected to slow strain rate tests (SSRT) in simulated body fluid (SBF) at 37 °C to be increased only about 30% with the cryogenic machining. These improvements were associated with the formation of a nano-crystalline and compressed surface layer. However, once the nano-crystalline surface layer dissolves, the machining induced corrosion resistance disappears. Recently, Equal Channel Angular Pressing (ECAP) has been proved to induce a very fine and homogeneous microstructure throughout all the samples. Broad attention was given to the effects of ECAP on the corrosion properties, whereas very few on the SCC susceptibility. Dealing with the corrosion behavior, the effects of ECAP still remain uncertain. In fact, some researchers reported that ultrafine-grained Mg alloy produced by ECAP deteriorated the corrosion resistance [40–42], whereas other works observed improved performances after ECAP [43–45]. This work aims thus to provide further insight into the effects of ECAP on the corrosion resistance. One, two and four passes of ECAP have thus been applied on AZ31 alloy and the corrosion behaviour has been assessed. To this aim, both potentiodynamic polarization curves and hydrogen evolution tests were used. The as-received material has also been tested as reference. In addition, for the first time to the best of the authors' knowledge, the effect of ECAP on the SCC susceptibility has been investigated. Slow strain rate tests (SSRT) at a strain rate of $3.5 \cdot 10^{-6}$ s^{-1} have been carried out on one, two and four ECAPed AZ31 samples. The samples were immersed for the whole duration of the tests in SBF at 37 °C. Fracture surfaces were analyzed by means of scanning electron microscopy (SEM) to provide a better understanding of the different failure mechanisms shown by the different ECAP-treated samples.

3.2. Materials and methods

3.2.1. Material and ECAP processing

In this study, ECAP was performed on AZ31 magnesium alloy. The commercially available bars (Dynamic Metals Ltd, Bedfordshire, UK) were machined into square billets with 19.7 mm side and 100 mm length. ECAP pressing was conducted through a die with an internal angle (Φ) of 90° between the vertical and the horizontal channels and a curvature angle (ψ) of 20° (Figure 3.1).

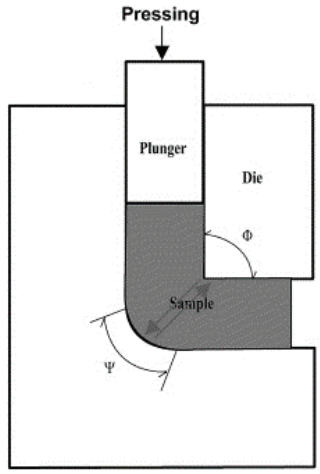

Figure 3.1: Schematic illustration of die configuration for ECAP processing.

The ECAP temperature was set as 250 °C to avoid the formation of extensive cracking that otherwise would have formed due to a lack of adequate ductility [46]. The die was homogeneously heated by 4 electrical resistance heaters placed along the vertical channel and at the intersection point of the channels. The temperature was monitored throughout the process using a thermocouple inserted in the die in the proximity of the sample. Repetitive pressings of the same sample were performed up to a maximum of 4 passes by rotating in the same direction the sample along their longitudinal axis by 90° before each new pass (route B_c according to established designation given in the literature [47]. The billets were pressed into the ECAP die with a speed of 1 mm/min using molybdenum disulphide (MoS_2) as lubricant. The tensile testing machine used for this operation was an MTS 311 (1000kN) (MTS, MN, USA).

3.2.2. Microstructural observation

Microstructural characterizations were performed on the as-received alloy and the ECAP processed billets. Samples were cut along their longitudinal cross-section, polished up to mirror finishing surface with silica colloidal suspension and, finally, etched using a solution of 10 ml H_2O, 10 ml acetic acid, 80 ml ethanol and 4.2 g picric acid. The microstructure was analyzed using a Leica DMRETM Optical Microscope (Leica microsystems, Wetzlar, Germany).

3.2.3. Mechanical characterization

The mechanical properties were characterized by means of uniaxial tensile tests and Vickers hardness measurements. The tensile tests were conducted on dogbone cylindrical samples having the gauge length of 20 mm and the diameter of 4 mm. The specimens were machined from the billets parallel to the ECAP direction. Each specimen was pulled to failure using an Instron 5969 testing machine (MA, USA) with a 50 kN load cell to obtain the load–displacement curves of the fabricated samples. A

strain rate of $3.5 \cdot 10^{-6}$ s^{-1} was used to conduct tensile tests under strain control mode. The reported results are averaged over three tests. The Vickers hardness tests were conducted on the plane perpendicular to the ECAP direction in accordance with ASTM E92 standard [48]. The surfaces of the sections were ground and mechanically polished to a mirror-like finish with silica colloidal suspension. The hardness tests were carried out at ambient temperature using a load of 100 g and a holding time of 15 s. The values of Vickers hardness (HV) were recorded using a Struers Duramin-A300 hardness tester equipped with a Vickers diamond indenter. An average over at least seven separate measurements taken at randomly selected points was used to measure the mean values of HV.

3.2.4. Corrosion performance evaluation

The corrosion performances of the as-received and of the ECAPed AZ31 alloy were measured by means of potentiodynamic polarization curves and hydrogen evolution experiments. In order to perform the former, small parallelepipeds with a thickness of 2 mm and a square face of 16 mm side were manufactured from the as-received bars and from the billets subjected to one, two and four passes of ECAP. The samples obtained this way were first polished with 2000 and then with 4000 grit silicon carbide papers and then cleaned with acetone and ethanol for five minutes in ultrasonic bath prior to testing. To perform the hydrogen evolution tests, the as-received bars and the billets subjected to one, two and four passes of ECAP were machined into small cubes with a 10 mm side, respectively. Again, prior to testing, the cubes were first polished with 2000 and then with 4000 grit silicon carbide papers and then cleaned with acetone and ethanol for five minutes in ultrasonic bath.

3.2.4.1. Potentiodynamic polarization curves

Potentiodynamic polarization tests were carried out on a Gamry Interface1000 potentiostat (Gamry Instruments, PA, USA) in order to compare the effects of the ECAP process on the corrosion resistance. Samples obtained from the as-received material and from the billets subjected to one, two and four passes of ECAP were tested. The electrochemical tests used three-electrode equipment with the as-received or the ECAPed samples as a working electrode, a Hg/Hg_2SO_4 electrode as a reference electrode, and a platinum plate electrode as a counter electrode. The samples were immersed in SBF solution (composition reported in Table 1). The temperature was set to 37±1°C to reproduce human body conditions. The potentiodynamic polarization curves were obtained applying a potential from ±2 V with respect to the open circuit potential (OCP), obtained after a stabilization period of 30 min. The scan rate of the potentiodynamic polarization test was 0.5 mV/s. The area of the samples exposed to SBF was 1 cm^2 and corrosion current density were determined using the Tafel extrapolation method, according to the ASTM G5-14 standard [49]. The tests were repeated three times for each condition.

Reagents	Amount
NaCl	8.035 g

$NaHCO_3$	0.355 g
KCl	0.225 g
$K_2HPO_4 \cdot 3H_2O$	0.231 g
$MgCl_2 \cdot 6H_2O$	0.311 g
1.0M-HCl	39 ml
$CaCl_2$	0.292 g
Na_2SO_4	0.072 g
Tris	6.118 g

Table 3.1: Reagents and their quantities for preparation of 1000 ml of the SBF solution according to [50].

3.2.4.2. Hydrogen evolution tests

The corrosion of one mole Mg leads to the evolution of one mole of hydrogen gas. This allows the measurement of Mg's corrosion rate through the collection of evolving hydrogen gas bubbles. Hence, hydrogen evolution tests were used to assess the effects of the ECAP process for improving corrosion resistance. The samples described in Section 2.4. were obtained from the as-received material and from the billets subjected to one, two and four passes of ECAP and were immersed individually in SBF at 37 °C for 96 hours. From each sample, the hydrogen bubbles were collected in a burette (Figure 3.2), according to an established protocol published elsewhere [51].

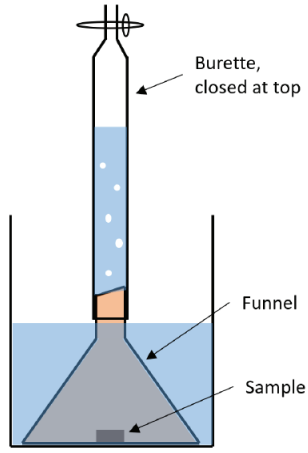

Figure 3.2: Schematic illustration of the set-up for the measurement of the evolved hydrogen volume.

3.2.5. Stress Corrosion Cracking (SCC) susceptibility

Slow strain rate tests are a common technique used for studying the combined effect of stress and corrosion/degradation process on the mechanical properties of a material, and

they have been used in this work to investigate the effect of ECAP on the SCC susceptibility. The SSRT experiments were carried out on the as-received and ECAPed dog-bone samples described in Section 2.3. at a strain rate of $3.5 \cdot 10^{-6}$ s^{-1} in SBF solution at body temperature (37 ± 1°C). The strain rate value was chosen according to [35] to render the AZ31 alloy susceptible to SCC. A schematic representation of the experimental set-up is shown in Figure 3.3. The sample was immersed for the whole duration of the test and the SBF solution was constantly changed by a pumping system. The SBF solution container was immersed in a water bath, which's temperature was constantly monitored with a thermometer. When the temperature was below its set value, a commercial resistance heating element placed inside the water bath automatically turned on until the desired temperature was reached again. In addition, while carrying out the SSRTs, the area of the specimen exposed to SBF was restricted to its gauge length using Teflon tapes wrapping the rest of the specimen, thus maintaining a constant area of exposure to the corrosive solution as well as avoiding the possibility of galvanic effects with other components of the testing set-up. For sake of comparability, the results obtained from the mechanical characterizations (Section 3.2.3.) were used as reference in air.

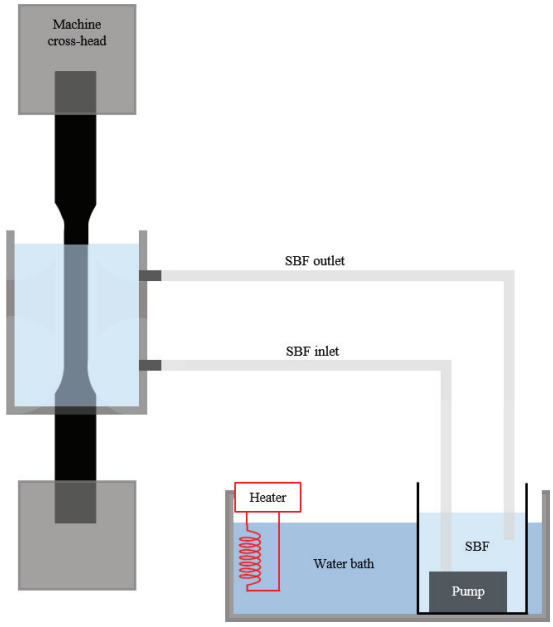

Figure 3.3: Schematic representation of the SSRT set-up.

The gauge length of the specimens were polished up to 4000 grit silicon carbide papers and then cleaned with ethanol prior to testing as suggested in other works [29,31,52]. SSRTs were repeated three times for reproducibility.
In order to quantify the AZ31 SCC sensitivity, the susceptibility indices I_{UTS} and I_{ε} were calculated according to Eq. (1) and Eq. (2) [36]:

$$I_{UTS} = \frac{UTS_{air} - UTS_{SBF}}{UTS_{air}} \quad (3.1)$$

and

$$I_{\varepsilon} = \frac{\varepsilon_{air} - \varepsilon_{SBF}}{\varepsilon_{air}} \quad (3.2)$$

where *UTS* is the Ultimate Tensile Strength and ε the elongation at failure, both evaluated during tests conducted in SBF solution and air. When the value of the susceptibility index approaches zero, the material is considered to be highly resistant to SCC, namely the greater the index the greater the susceptibility to SCC.

3.2.6. Fractography

The specimen fracture surfaces of the samples tested in air and in SBF were observed by means of a FEI Quanta 450 Scanning Electron Microscope (Thermo Fisher Scientific Inc., USA). Prior to fractographic evaluations, the samples tested in the corrosive environment were cleaned from the corrosion products by immersion for one minute in a solution prepared using 50 g chromium trioxide (CrO_3), 2.5 g silver nitrate ($AgNO_3$) and 5 g barium nitrate ($Ba(NO_3)_2$) in 250 ml distilled water, as suggested elsewhere [53]. Both the samples tested in air and in SBF were washed with distilled water and finally ultrasonically cleaned in acetone for 10 min before the fractographic evaluations.

3.3. Results

3.3.1. Microstructural observation

Figure 3.4 presents optical microstructures of the as-received material (a) and those of the material ECAPed by 1 pass (b), 2 passes (c) and 4 passes (d). Their equivalent diameter distributions determined by means of an image analysis software (Leica Application Software v.3.8, Leica Microsystems, Wetzlar, Germany) are reported in Figure 3.5 and in Table 3.2.

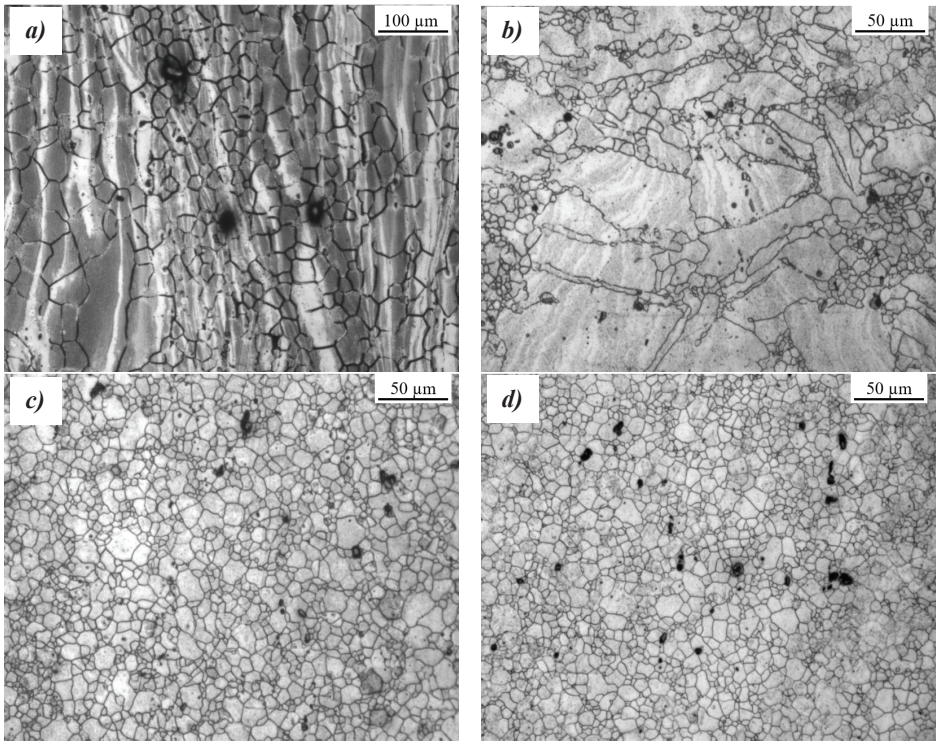

Figure 3.4: Micrograph of AZ31 alloy at the (a) as-received condition and after (b) 1 pass, (c) 2 passes and (d) 4 passes of ECAP; note the different scale bar in (a)

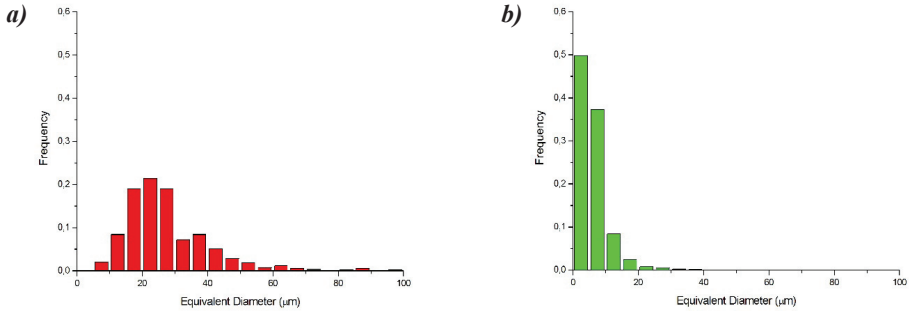

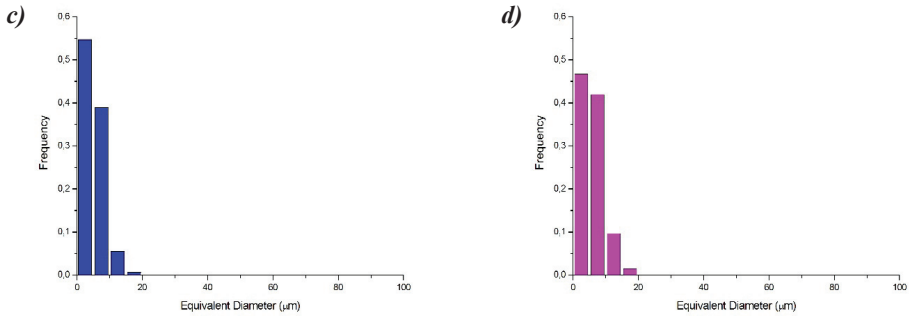

Figure 3.5: Equivalent diameter distribution of AZ31 alloy at the (a) as-received condition and after (b) 1 pass, (c) 2 passes and (d) 4 passes of ECAP

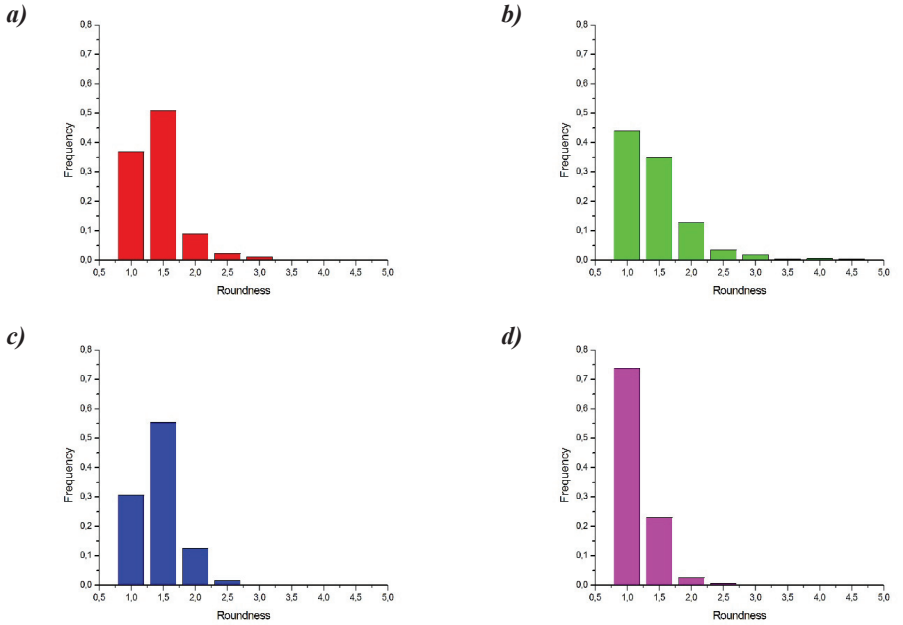

Figure 3.6: Grain roundness distribution of AZ31 alloy at the (a) as-received condition and after (b) 1 pass, (c) 2 passes and (d) 4 passes of ECAP

	As-received	ECAP		
		1 pass	2 passes	4 passes
Equivalent Diameter	27.5± 13.4	8.3 ± 5.2	6.8 ± 2.8	6.5 ± 3.1
Roundness	1.7± 0.3	1.9 ± 0.6	1.5 ± 0.3	1.4 ± 0.2

Table 3.2: Equivalent diameter and roundness from Figure 3.5 and 3.6

The as-received material exhibits large grains (Figure 3.4a) with a broad grain size distribution (Figure 3.5a) and an average grain diameter of 27.5 μm; moreover, the microstructure is characterized by almost equiaxed grains. After 1 pass, the material displays a heterogeneous microstructure (Figure 3.4b) so-called "bimodal" grain structure [54] consisting of coarse grains, that are reported to be the un-recrystallized grains from the initial state [55], surrounded by colonies of very fine grains, nucleated along the grain and twin boundaries through dynamic recrystallization (DRX) [56]. For this process condition, the average grain diameter decreases to 8.3 μm. In addition, the broad roundness distribution (Figure 3.6b) reveals that the grains are significantly distorted and elongated due to the plastic shear deformation after 1 pass. On the contrary, the microstructure of the material after 2 passes significantly changes and now comprises a uniform grain structure with fine equiaxed grains and an average diameter of 6.8 μm (Table 3.2). The grain structure after 4 passes is almost equivalent to the material after 2 passes: the average grain size is still 6.5 μm (Table 3.2) but the grain roundness distribution is narrower and more peaked close to the unit (Figure 3.6d). Therefore, even if processing the material by 4 ECAP passes at 250°C do not induce a further grain refinement of the alloy due to the grain nucleation stimulated by high temperature during strain accumulation [57], it produces a totally recrystallized and equiaxed microstructure.

3.3.2. Mechanical characterization

In Table 3.3, the Vickers hardness of the as-received and the 1, 2 and 4 ECAPed passed material is presented.

	As-received	**ECAP**		
		1 pass	**2 passes**	**4 passes**
HV	65.1± 5.1	69.2 ± 4.1	65.6 ± 5.7	57.9 ± 1.9

Table 3.3: Vickers hardness of the as-received and of the material ECAPed by 1 pass, 2 passes and 4 passes

The Vickers hardness value of AZ31 alloy slightly increases after 1 pass of ECAP, but 2 passes of ECAP leads to its reduction towards a value comparable to the as-received condition. Further ECAPing leads to a further reduction of the Vickers hardness.
The engineering stress-strain curves of the as-received and the 1, 2 and 4 passes ECAPed specimens are presented in Figure 3.7. In addition, Table 3.4 compares the yield strength (σ_y), the UTS and the elongation at failure obtained from the curves in Figure 3.7.

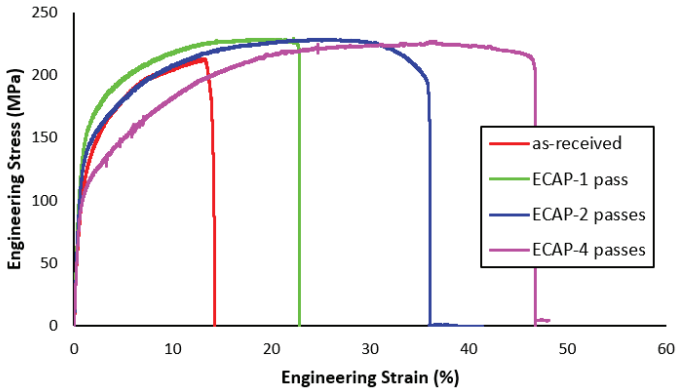

Figure 3.7: Engineering stress-strain curves of as-received AZ31 alloy (red) and ECAPed by 1 pass (green), 2 passes (blue) and 4 passes (fuchsia)

	As-received	ECAP		
		1 pass	2 passes	4 passes
σ_y (MPa)	97.7 ± 4.8	122.7 ± 5.3	109.5 ± 4.1	86.0 ± 3.7
UTS (MPa)	212.9 ± 5.6	229.1 ± 4.3	228.8 ± 2.5	227.2 ± 3.2
ε_f (%)	14.2 ± 1.9	22.8 ± 1.0	36.0 ± 0.7	46.8 ± 1.3

Table 3.4: Mechanical properties from Figure 3.7

The data demonstrated that both the yield and ultimate tensile strength and the elongation to failure increases after 1 pass of ECAP. However, further ECAP passes lead to a continuous decrease in the yield strength whereas to a continuous increase in ductility (the elongation to failure after 4 passes of ECAP is more than 3 times higher than the elongation to failure of the as-received material).

3.3.3. Corrosion performance evaluation

3.3.3.1. Potentiodynamic polarization curves

The potentiodynamic polarization curves of the AZ31 cylindrical samples in SBF plotted on a semi-logarithmic scale are shown in Figure 3.8. The related kinetic and thermodynamic corrosion electrochemical characteristics are reported in Table 3.5. The effect of ECAP on the corrosion resistance is of complex nature. One pass of ECAP leads to a reduced corrosion current density, and thus to an improved corrosion resistance since the corrosion current density is directly related to the corrosion rate, whereas further ECAP passes are found to worsen the corrosion resistance. It is worth to note that the corrosion current density of 2 and 4 ECAPed AZ31 alloy is even worse than that of the as-received material.

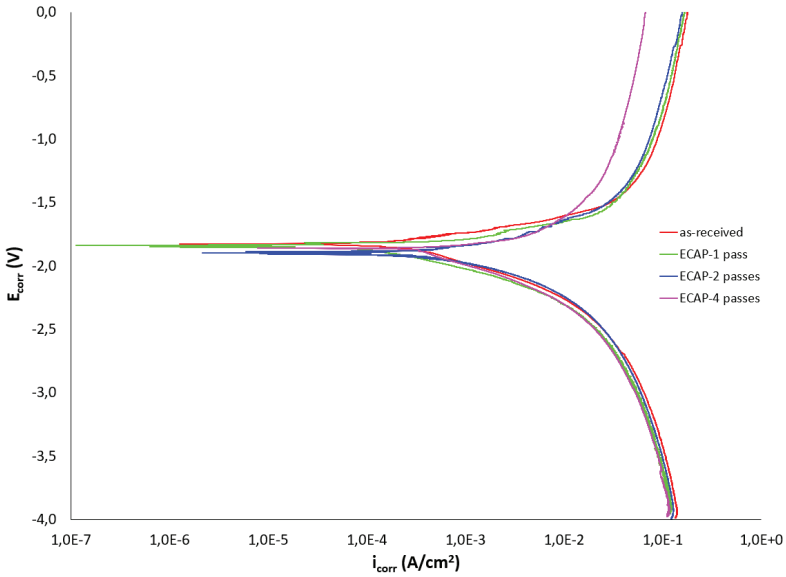

Figure 3.8: Potentiodynamic polarization curves for the as-received and ECAPed AZ31 samples in SBF solution at 37°C

	As-received	ECAP		
		1 pass	2 passes	4 passes
E_{corr} (V)	-1.83 ± 0.018	-1.84 ± 0.015	-1.90 ± 0.025	-1.86 ± 0.013
i_{corr} (μA/cm²)	215.6 ± 4.1	83.5 ± 10.6	286.5 ± 8.7	349.1 ± 13.8

Table 3.5: Electrochemical corrosion data extrapolated from Figure 3.8

3.3.3.2. Hydrogen evolution tests

The results from the hydrogen evolution tests are reported in Figure 3.9.

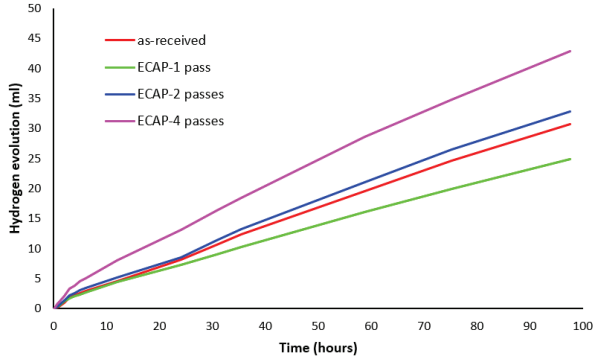

Figure 3.9: Hydrogen evolved from the as-received and ECAPed AZ31 alloy

The results from the hydrogen evolution tests agree with those obtained from potentiodynamic polarization curves. 1 pass of ECAP leads to a reduction in the amount of hydrogen evolved compared to the as-received material. However, 2 passes of ECAP lead to a deterioration in the corrosion resistance since the hydrogen evolved from the AZ31 alloy treated with 2 passes of ECAP is slightly higher than that of the as-received counterpart. Furthermore, further ECAP processing (4 passes) leads to a further increase of the amount of hydrogen evolved.

3.3.4. Stress Corrosion Cracking susceptibility

Figure 3.10 shows the engineering stress-strain curve of the as-received material (a) and that of the material ECAPed by 1 pass (b), 2 passes (c) and 4 passes (d) tested in SBF. For sake of comparison, the corresponding engineering stress-strain curves of the materials tested in air are reported. Finally, Figure 3.10e shows the comparison of the samples tested in SBF.

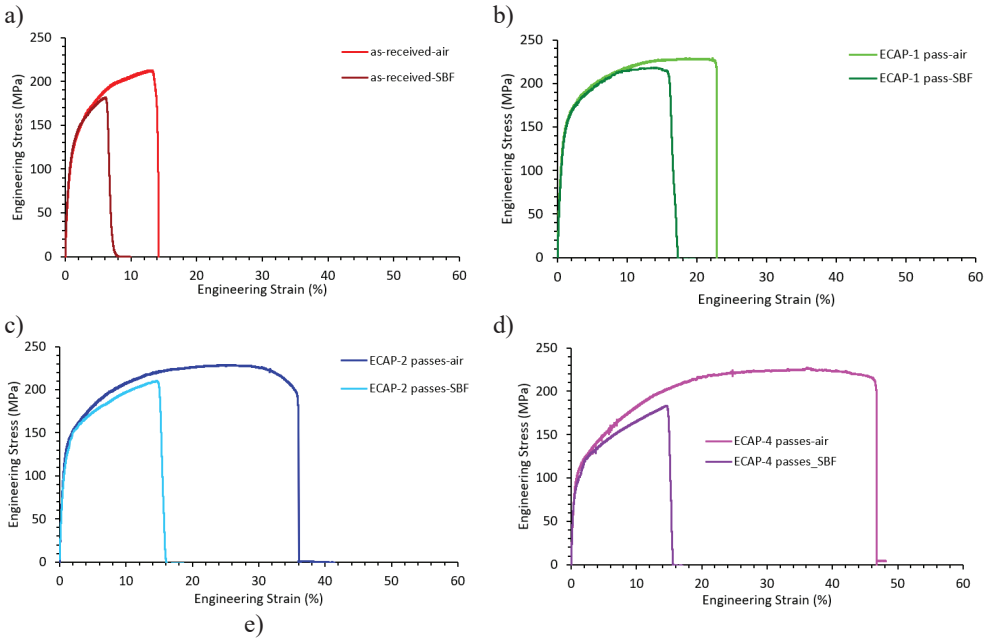

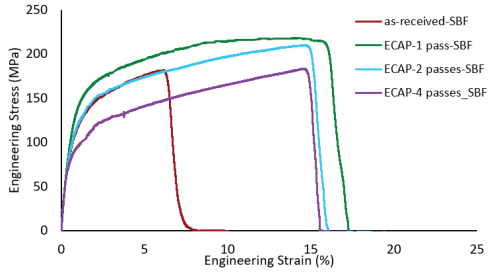

Figure 3.10: Engineering stress-strain curves of as-received AZ31 alloy (a) and ECAPed by 1 pass (b), 2 passes (c) and 4 passes (d) tested in SBF. For sake of comparison, the corresponding Engineering stress-strain curves of the samples tested in air are also reported; in Figure 10e the results of the samples tested in SBF are compared

In addition, Table 3.6 compares the UTS and the elongation to failure values obtained from the curves in Figure 3.10.

	As-received	**ECAP**		
		1 pass	**2 passes**	**4 passes**
UTS (MPa)	181.6 ± 8.2	218.0 ± 3.9	210.0 ± 5.4	183.3 ± 6.1
ε_f (%)	6.5 ± 1.6	16.2 ± 1.1	15.1 ± 2.1	14.9 ± 1.7

Table 3.6: Mechanical properties of the as-received material and of the material ECAPed tested in SBF

From the considerably reduced elongation at failure it can be seen that the alloy suffered embrittlement in SBF regardless the adoption of ECAP treatments. It is however worth noting that the introduction of ECAP processing led to an increased elongation at fracture.

To quantify the SCC susceptibility of the as-received and ECAPed material, the I_{UTS} and I_{ε} indices were evaluated and are reported in Figure 3.11.

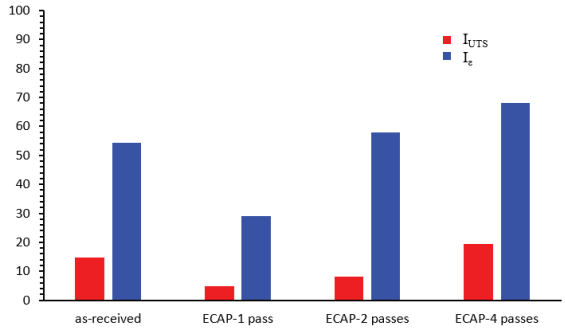

Figure 3.11: SCC susceptibility indexes for as-received material and for the ECAPed material

The SCC indexes reveals that after one pass of ECAP, the SCC susceptibility of the alloy was highly reduced, i.e. by 67% and 47% for I_{UTS} and the I_{ε}, respectively. However further ECAP treatments led to a worsening of the SCC indexes. In fact, I_{UTS} increased from 4.8% for 1 pass of ECAP to 8.2% and 19.3% for 2 and 4 passes, respectively, while I_{ε} increased from 28.9% to 58.1% and 68.2% for 2 and 4 passes, respectively. This suggests that the lowest SCC susceptibility indexes were obtained for the material treated with 1 pass of ECAP, that also leads to the highest UTS and elongation to failure when tested in SBF.

3.3.5. Fractography

3.3.5.1. Samples tested in air

The fracture surfaces of the samples tested in air are reported in Figure 3.12, and in particular the fractographies of the samples in the as-received condition are reported in Figures 3.12a and 3.12e, while those of the ECAPed samples are reported in Figures 3.12b and 3.12f, Figures 3.12c and 3.12g and Figures 3.12d and 13.2h for 1, 2 and 4 passes of ECAP, respectively.

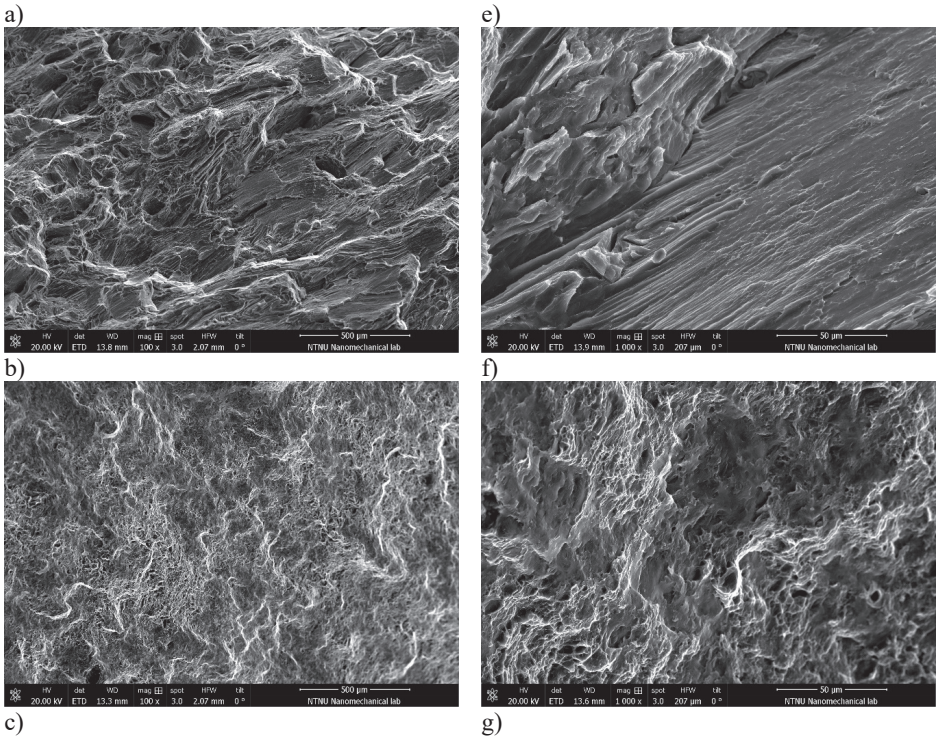

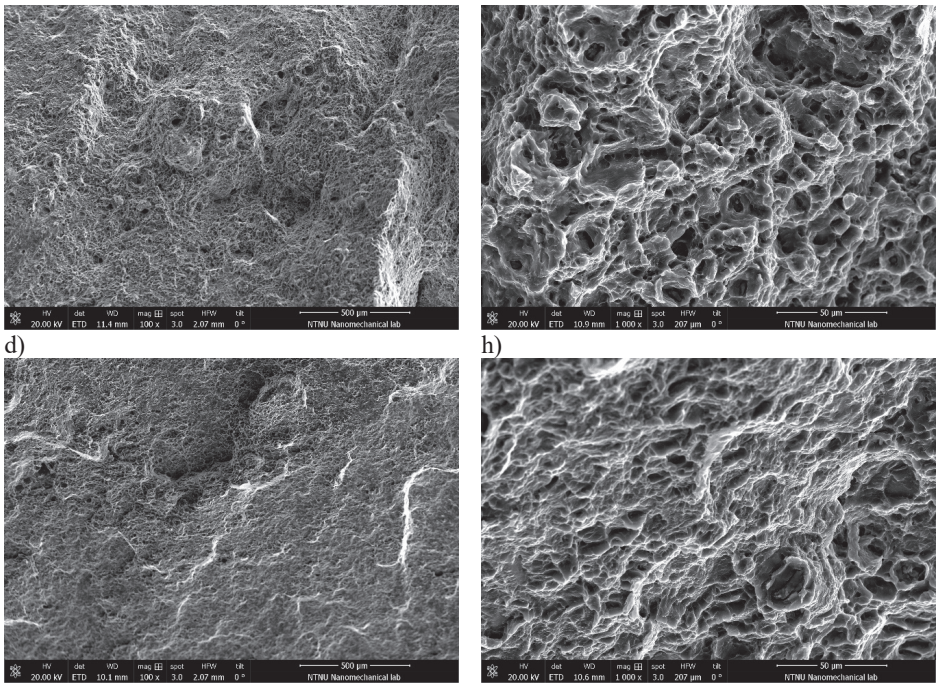

Figure 3.12: Fracture surfaces of the as received material (a and e) and of the material ECAPed by 1 pass (b and f), 2 passes (c and g) and 4 passes (d and h) tested in air

From the SEM pictures it can be seen that in the alloy in the as-received condition a predominant feature of the fracture surfaces is the occurrence of cleavage. This agrees with the reduced ductility shown by the mechanical tests in Figure 3.7 (red curve). After one pass of ECAP the fracture morphologies show a mixed fracture mode of ductile-brittle type with the typical combination of dimples and cleavage planes. This change in fracture morphology reveals an enhanced ductility, which is confirmed by the mechanical tests (green curve in Figure 3.7). Further ECAP processing leads to the transition from the mixed ductile-brittle fracture mode experienced by 1 pass ECAPed samples to the ductile markedly ductile fracture behavior of 2 and 4 passes ECAPed samples (Figures 3.12c and 3.12g and Figures 3.12d and 3.12h, respectively).

3.3.5.2. Samples tested in SBF

The fracture surfaces of the samples tested in SBF are reported in Figure 3.13, and in particular the fractographies of the samples in the as-received condition are reported in Figures 3.13a and 3.13e, while those of the ECAPed samples are reported in Figures 3.13b and 3.13f, Figures 3.13c and 3.13g and Figures 3.13d and 3.13h for 1, 2 and 4 passes of ECAP, respectively.

a) e)

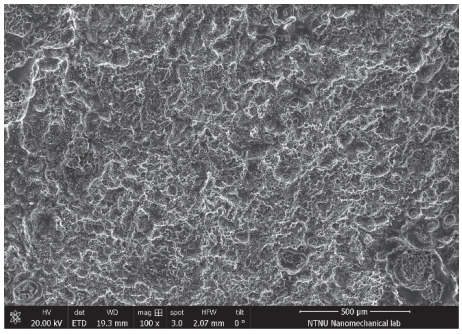
HV det WD mag spot HFW tilt
20.00 kV ETD 19.3 mm 100 x 3.0 2.07 mm 0 °
500 µm
NTNU Nanomechanical lab

b)

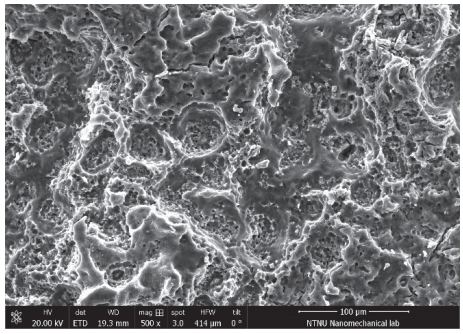
HV det WD mag spot HFW tilt
20.00 kV ETD 19.3 mm 500 x 3.0 414 µm 0 °
100 µm
NTNU Nanomechanical lab

f)

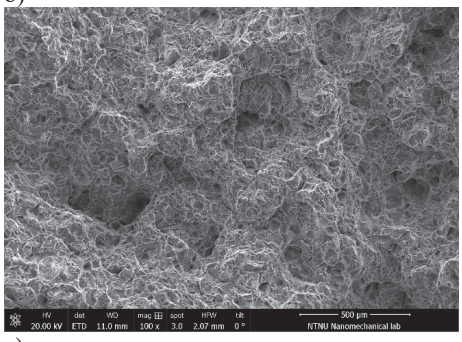
HV det WD mag spot HFW tilt
20.00 kV ETD 11.0 mm 100 x 3.0 2.07 mm 0 °
500 µm
NTNU Nanomechanical lab

c)

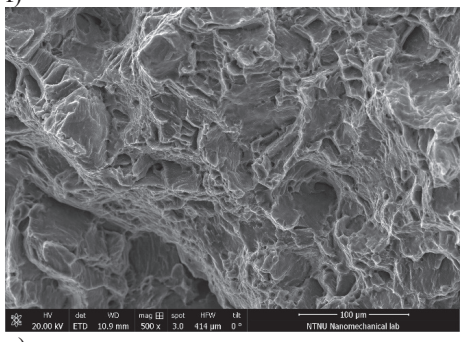
HV det WD mag spot HFW tilt
20.00 kV ETD 10.9 mm 500 x 3.0 414 µm 0 °
100 µm
NTNU Nanomechanical lab

g)

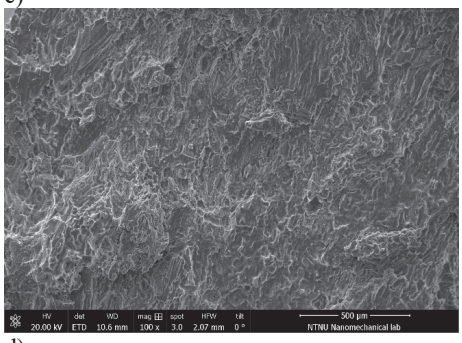
HV det WD mag spot HFW tilt
20.00 kV ETD 10.6 mm 100 x 3.0 2.07 mm 0 °
500 µm
NTNU Nanomechanical lab

d)

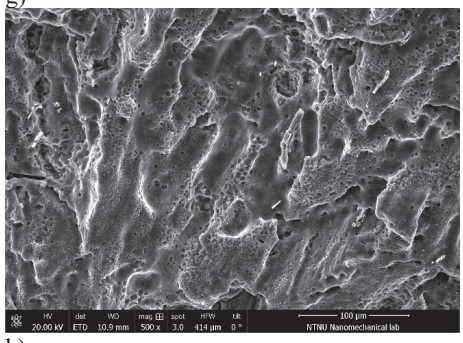
HV det WD mag spot HFW tilt
20.00 kV ETD 10.9 mm 500 x 3.0 414 µm 0 °
100 µm
NTNU Nanomechanical lab

h)

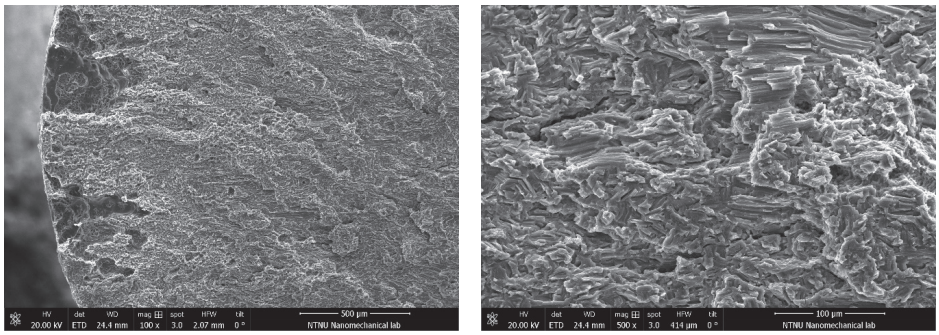

Figure 3.13: Fracture surfaces of the as received material (a and e) and of the material ECAPed by 1 pass (b and f), 2 passes (c and g) and 4 passes (d and h) tested in SBF

The surface fracture appearance of the samples tested in SBF are characterized by transgranular and intergranular cracks. The sample in the as-received condition shows a combination of the two crack typologies, while the sample subjected to 1 pass of ECAP shows a predominance of intergranular cracking. However, further increasing the number of ECAP passes are shown to change the failure mode from intergranular fracture of samples subjected to 1 pass of ECAP to a predominance of transgranular fracture of the samples subjected to 4 passes of ECAP.
In addition, the tilted views of the gauge section are reported in Figure 3.14. A small number of secondary cracks were shown by the sample in the as-received condition (Figure 3.14a). The effect of one pass of ECAP is shown to reduce the number of cracks, that were also less deep than in the as-received material (Figure 3.14b). However, denser and deeper secondary cracks were evident in the samples subjected to 2 passes of ECAP (Figure 3.14c), and even more visible in the samples subjected to 4 passes of ECAP, where corrosion pits are evident (Figure 3.14d).

a) b)

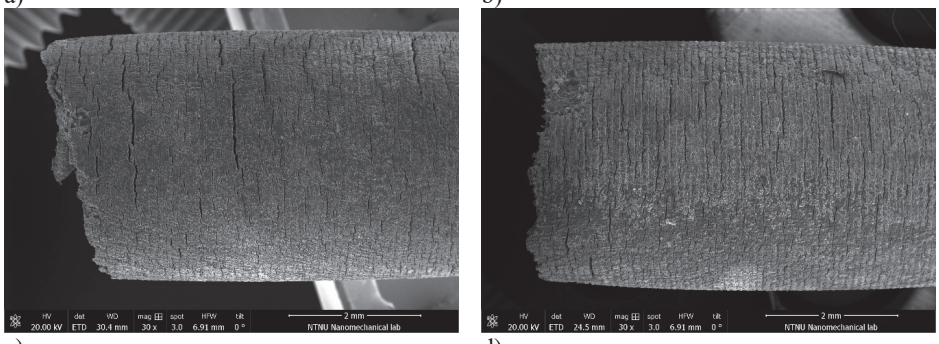

c) d)

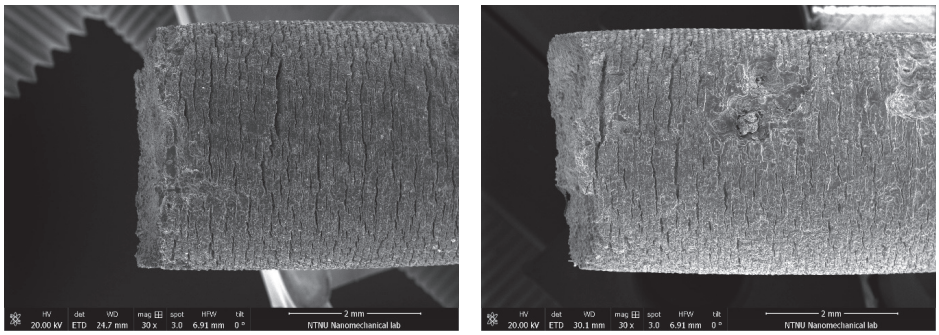

Figure 3.14: SEM fractographies of the gauge section of the as received material (a) and of the material ECAPed by 1 pass (b), 2 passes (c) and 4 passes (d) tested in SBF

3.4. Discussion

In this study, for the first time to the best of the authors' knowledge, the effect of ECAP on the SCC susceptibility has been investigated. To this aim, slow strain rate tests (SSRT) at a strain rate of $3.5 \cdot 10^{-6}$ s^{-1} have been carried out on one, two and four ECAPed AZ31 samples. From the experimental results (Figures 3.10 and 3.11) it can be seen that the application of one pass of ECAP has been proved to yield higher resistance to SCC in SBF compared to the material in the as-received conditions. The susceptibility indices I_{UTS} and I_{ε} of samples subjected to one pass of ECAP were in fact decreased up to approximately 67% and 47%, respectively, indicating a strengthened response to the combined application of mechanical load and corrosive environment. However, further ECAP processing led to an increased susceptibility to SCC, that, in the case of the samples subjected to 4 passes of ECAP, resulted to be even higher than the SCC susceptibility of the as-received material. These results can be linked to the different corrosion behavior of the material subject to different ECAP treatments.
SCC of Mg alloys is widely attributed to the combination of two mechanisms, namely the anodic dissolution and cleavage-like fracture due to hydrogen embrittlement [58]. The rupture of the protective $Mg(OH)_2$ film due to the anodic dissolution or due to mechanical loads allows the hydrogen evolved from the corrosion process to enter into the matrix and to embrittle the material, leading to a premature fracture [27]. Pitting is reported as main precursor for the initiation of SCC cracks [59,60]. The lower the tendency of a material to be subjected to pitting and to localized corrosion, the lower the corrosion rate and hence the SCC susceptibility. The increased resistance to pitting (Figure 3.14) and to corrosion (Figures 3.8 and 3.9) of samples subjected to 1 pass of ECAP reduced the SCC susceptibility of this material. The improved corrosion behavior can be linked to the reduced grain size compared to the as-received material (Figure 3.5). These results agree with those obtained by Minarik et al. [45] that reported the reduction of almost 15% in the corrosion rate after 12 passes of ECAP to be a consequence of the decrease in the grain size from 21 μm to 1.7 μm. This reduction in grain size hinders the corrosion due to three mechanisms. Firstly, the grain boundary acts as a physical corrosion barrier; smaller grain sizes yield an increased number of grain boundaries and hence a reduced corrosion rate [61]. Secondly, the geometrical mismatches between the MgO layer and the metallic substrate arising when the oxide

forms causes tensile stresses in the oxide, thereby increasing its propensity for cracking. A fine-grained microstructure is known to relieve these stresses [62]. This leads to a reduced degree of oxide cracking that provides a better surface coverage and hence an increased corrosion resistance [63]. Thirdly, the positive effect of small grain sizes on corrosion resistance can be attributed to the rapid formation of passivation oxide films at grain boundaries, which provides nucleation sites for passivating oxide films and the higher interfacial adherence of the passive film (MgO) at grain boundaries compared with the bulk [62,64] that provide a barrier to the corrosive fluid.
However, the results concerning the corrosion performances of the samples obtained with 2 and 4 passes of ECAP (Figures 3.8 and 3.9) are in contrast with what just stated. In fact, although the grain size is decreased, the corrosion resistance gets worse and becomes even lower than that of the as-received samples for the samples subjected to 4 passes of ECAP. The deterioration of the corrosion resistance despite the decrease of the grain size has been reported also elsewhere [65–67] and can be explained with the texture evolution within the material. ECAP is reported to modify the texture of the material due to the heavy shear strains imposed. The critical resolved shear stress (CRSS) for basal plane slip is 100 times lower than that for non-basal plane slip [68]. The basal plane hence rearranges to the shearing direction, which is inclined by 45° with respect to the "extrusion" direction. However, the basal plane is reported to be more corrosion resistance than the non-basal planes due to its high atomic density [69]. The activation energy required for the dissolution of an atom from a crystal is proportional to the atomic packing density of the crystallographic plane. As more and more basal planes will be rearranged at 45° from the "extrusion" direction with increasing number of ECAP passes, the corrosion resistance is reduced (Figures 3.8 and 3.9) and the susceptibility to pitting is increased (Figure 3.14), thus leading to enhanced SCC susceptibility (Figure 3.11). In addition, the arrangement of the basal planes along with the shearing direction (oriented at 45° to the stress axis) is of major importance from a mechanical point of view. Basal planes are in fact in positions favourable for basal slip, inducing an increased ductility with an increase of the number of passes (Figure 3.7 and Table 3.3) [70,71]. This affects also the yield strength. After one pass of ECAP the yield strength is increased by 30% due to the reduction in the grain size, 2 and 4 passes of ECAP reduces the yield strength while the grain size remains approximately constant. We hence hypothesize that this is due to the reduced strength necessary to activate the basal slip systems due to the rotation of the basal planes towards the shearing direction. This is in agreement with previous work [72], but has to be further investigated. Similarly, the effect of ECAP on the hardness measurements can also be related to the orientation of basal slip systems. After an increase in the hardness due to the reduced grain size after 1 pass of ECAP, the effect of the texture orientation becomes predominant and the arrangement of the basal planes towards the shearing direction becomes responsible for the drop in hardness. This is due to the basal grains that are characterized by a higher hardness than that their non-basal counterparts [73].

3.5. Conclusion

In this study, the effect of ECAP processing on the stress corrosion cracking (SCC) susceptibility of the AZ31 Mg alloy was assessed. SSRTs at a strain rate of $3.5 \cdot 10^{-6}$ s^{-1}

were carried out in SBF at 37°C. In addition, potentiodynamic polarization tests, hydrogen evolution tests, a mechanical characterization of the treated and un-treated alloy by means of tensile tests and hardness measurements and fracture surfaces analyses were carried out.
The main findings can be summarized as follows:

- Samples subjected to 1 pass of ECAP are characterized by the lowest susceptibility in SBF at body temperature (I_{UTS} and the I_{ε} were found to be 4.8% and 28.9%, respectively). This enhancement was attributed to the improved corrosion of the samples subjected to 1 pass of ECAP performances (i_{corr} is almost three times lower than that obtained for the as-received material and the evolved hydrogen is reduced of almost 20%) due to the reduced grain size that allows both a faster formation of the passivating surface oxide and a better surface coverage provided by this oxide layer as a consequence of a reduced degree of oxide cracking.
- Further ECAP processing (2 and 4 passes) are reported to deteriorate the SCC susceptibility (I_{UTS} and the I_{ε} were found to be 8.2% and 58.1% and 19.3% and 68.2% for 2 and 4 passes, respectively). Their SCC susceptibility becomes higher than that of the material in the as-received condition (I_{UTS} and the I_{ε} were found to be 14.7% and 54.2%, respectively). Although the grain size is slightly reduced compared to 1 pass of ECAP, we hypothesize that the deterioration in SCC susceptibility is due to the modified texture within the material. The alignments of basal planes with the shearing direction as a consequence of ECAP can explain the detrimental effects on the corrosion resistance shown by the potentiodynamic polarization curves (i_{corr} increases from 83.5 $\mu A/cm^2$ for 1 pass of ECAP to 286.5 and to 349.1 $\mu A/cm^2$ for 2 and 4 passes of ECAP, respectively) and by the hydrogen evolution tests (the hydrogen evolved from the as-received material increases by 7% and 39% for 2 and 4 passes of ECAP, respectively). Further evidences of the alignments of basal planes with the shearing direction are the results of the mechanical tests and of the hardness measurements.

It can be concluded that the ECAP process is an effective method to decrease the AZ31 sensitivity to SCC due to the great grain refinement that can be obtained. However, when the texture evolution becomes predominant over the grain refinement effect, ECAP processing results become detrimental to SCC susceptibility.

Bibliography Paper II

[1] Ginebra, M.P., Traykova, T., Planell, J.A. (2006). Calcium phosphate cements as bone drug delivery systems: A review, J. Control. Release, 113(2), pp. 102–10, Doi: 10.1016/j.jconrel.2006.04.007.

[2] (N.d.). http://share.iofbonehealth.org/EU-6-Material/Reports/IOF%20Report_EU.pdf. Available at: http://share.iofbonehealth.org/EU-6-Material/Reports/IOF Report_EU.pdf. [accessed November 20, 2019].

[3] Chen, Q., Thouas, G.A. (2015). Metallic implant biomaterials, Mater. Sci. Eng. R Reports, 87, pp. 1–57, Doi: 10.1016/J.MSER.2014.10.001.
[4] Hanawa, T. (2010).Overview of metals and applications. Metals for Biomedical Devices, Elsevier, pp. 3–24.
[5] Albrektsson, T., Brånemark, P.-I., Hansson, H.-A., Lindström, J. (1981). Osseointegrated Titanium Implants: *Requirements for Ensuring a Long-Lasting, Direct Bone-to-Implant Anchorage in Man*, Acta Orthop. Scand., 52(2), pp. 155–70, Doi: 10.3109/17453678108991776.
[6] Rossi, F., Lang, N.P., De Santis, E., Morelli, F., Favero, G., Botticelli, D. (2014). Bone-healing pattern at the surface of titanium implants: an experimental study in the dog, Clin. Oral Implants Res., 25(1), pp. 124–31, Doi: 10.1111/clr.12097.
[7] Bauer, T.W., Schils, J. (1999). The pathology of total joint arthroplasty.II. Mechanisms of implant failure., Skeletal Radiol., 28(9), pp. 483–97.
[8] Dujovne, A.R., Bobyn, J.D., Krygier, J.J., Miller, J.E., Brooks, C.E. (1993). Mechanical compatibility of noncemented hip prostheses with the human femur, J. Arthroplasty, 8(1), pp. 7–22, Doi: 10.1016/S0883-5403(06)80102-6.
[9] Engh, C.A., Bobyn, J.D. (1988). The influence of stem size and extent of porous coating on femoral bone resorption after primary cementless hip arthroplasty., Clin. Orthop. Relat. Res., (231), pp. 7–28.
[10] Kerner, J., Huiskes, R., van Lenthe, G.H., Weinans, H., van Rietbergen, B., Engh, C.A., Amis, A.A. (1999). Correlation between pre-operative periprosthetic bone density and post-operative bone loss in THA can be explained by strain-adaptive remodelling., J. Biomech., 32(7), pp. 695–703, Doi: 10.1016/S0021-9290(99)00041-X.
[11] Sumner, D.R., Galante, J.O. (1992). Determinants of stress shielding: design versus materials versus interface., Clin. Orthop. Relat. Res., (274), pp. 202–12.
[12] Turner, T.M., Sumner, D.R., Urban, R.M., Igloria, R., Galante, J.O. (1997). Maintenance of proximal cortical bone with use of a less stiff femoral component in hemiarthroplasty of the hip without cement. An investigation in a canine model at six months and two years., J. Bone Joint Surg. Am., 79(9), pp. 1381–90.
[13] Van Rietbergen, B., Huiskes, R., Weinans, H., Sumner, D.R., Turner, T.M., Galante, J.O. (1993). The mechanism of bone remodeling and resorption around press-fitted THA stems, J. Biomech., 26(4–5), pp. 369–82, Doi: 10.1016/0021-9290(93)90001-U.
[14] Wolff, J. (1986). The Law of Bone Remodelling, Berlin, Heidelberg, Springer Berlin Heidelberg.
[15] Pound, B.G. (2014). Corrosion behavior of metallic materials in biomedical applications . I . Ti and its alloys, 32, pp. 1–20, Doi: 10.1515/corrrev-2014-0007.
[16] Pound, B.G. (2014). Corrosion behavior of metallic materials in biomedical applications . II . Stainless steels and Co-Cr alloys, 32, pp. 21–41, Doi: 10.1515/corrrev-2014-0008.
[17] Jacobs, J.J., Gilbert, J.L., Urban, R.M. (1998). Corrosion of metal orthopaedic implants., J. Bone Joint Surg. Am., 80(2), pp. 268–82.
[18] Jacobs, J.J., Hallab, N.J., Skipor, A.K., Urban, R.M. (2003). Metal degradation products: a cause for concern in metal-metal bearings?, Clin. Orthop. Relat. Res., (417), pp. 139–47, Doi: 10.1097/01.blo.0000096810.78689.62.
[19] Beech, I.B., Sunner, J.A., Arciola, C.R., Cristiani, P. (2006). Microbially-

influenced corrosion: damage to prostheses, delight for bacteria., Int. J. Artif. Organs, 29(4), pp. 443–52.
[20] Peron, M., Torgersen, J., Berto, F. (2017). Mg and Its Alloys for Biomedical Applications: Exploring Corrosion and Its Interplay with Mechanical Failure, Metals (Basel)., 7(7), pp. 252, Doi: 10.3390/met7070252.
[21] Singh Raman, R.K., Jafari, S., Harandi, S.E. (2015). Corrosion fatigue fracture of magnesium alloys in bioimplant applications: A review, Eng. Fract. Mech., 137, pp. 97–108, Doi: 10.1016/j.engfracmech.2014.08.009.
[22] Staiger, M.P., Pietak, A.M., Huadmai, J., Dias, G. (2006). Magnesium and its alloys as orthopedic biomaterials: A review, Biomaterials, 27, pp. 1728–34, Doi: 10.1016/j.biomaterials.2005.10.003.
[23] Hänzi, A.C., Sologubenko, A.S., Uggowitzer, P.J. (2009). Design strategy for new biodegradable Mg–Y–Zn alloys for medical applications, ,.
[24] Song, G. (2007). Control of biodegradation of biocompatable magnesium alloys, Corros. Sci., 49(4), pp. 1696–701, Doi: 10.1016/J.CORSCI.2007.01.001.
[25] Teoh, S.. (2000). Fatigue of biomaterials: a review, Int. J. Fatigue, 22(10), pp. 825–37, Doi: 10.1016/S0142-1123(00)00052-9.
[26] Akahori, T., Niinomi, M., Fukunaga, K.-I., Inagaki, I. (2000). Effects of microstructure on the short fatigue crack initiation and propagation characteristics of biomedical α/β titanium alloys, Metall. Mater. Trans. A, 31(8), pp. 1949–58, Doi: 10.1007/s11661-000-0222-z.
[27] Jafari, S., Harandi, S.E., Singh Raman, R.K. (2015). A review of stress-corrosion cracking and corrosion fatigue of magnesium alloys for biodegradable implant applications, Jom, 67(5), pp. 1143–53, Doi: 10.1007/s11837-015-1366-z.
[28] Antunes, R.A., de Oliveira, M.C.L. (2012). Corrosion fatigue of biomedical metallic alloys: Mechanisms and mitigation, Acta Biomater., 8(3), pp. 937–62, Doi: 10.1016/j.actbio.2011.09.012.
[29] Jafari, S., Raman, R.K.S., Davies, C.H.J., Hofstetter, J., Uggowitzer, P.J., Löffler, J.F. (2017). Stress corrosion cracking and corrosion fatigue characterisation of MgZn1Ca0.3 (ZX10) in a simulated physiological environment, J. Mech. Behav. Biomed. Mater., 65, pp. 634–43, Doi: 10.1016/J.JMBBM.2016.09.033.
[30] Kannan, M.B., Raman, R.K.S. (2008). In vitro degradation and mechanical integrity of calcium-containing magnesium alloys in modified-simulated body fluid, Biomaterials, 29(15), pp. 2306–14, Doi: 10.1016/J.BIOMATERIALS.2008.02.003.
[31] Jafari, S., Raman, R.K.S., Davies, C.H.J. (2018). Stress corrosion cracking of an extruded magnesium alloy (ZK21) in a simulated body fluid, Eng. Fract. Mech., 201, pp. 47–55, Doi: 10.1016/J.ENGFRACMECH.2018.09.002.
[32] Mohajernia, S., Pour-Ali, S., Hejazi, S., Saremi, M., Kiani-Rashid, A.-R. (2018). Hydroxyapatite coating containing multi-walled carbon nanotubes on AZ31 magnesium: Mechanical-electrochemical degradation in a physiological environment, Ceram. Int., 44(7), pp. 8297–305, Doi: 10.1016/J.CERAMINT.2018.02.015.
[33] Chen, L., Sheng, Y., Zhou, H., Li, Z., Wang, X., Li, W. (2018). Influence of a MAO + PLGA coating on biocorrosion and stress corrosion cracking behavior of a magnesium alloy in a physiological environment, Corros. Sci., , Doi: 10.1016/J.CORSCI.2018.12.005.

[34] Gao, Y., Yerokhin, A., Matthews, A. (2015). Mechanical behaviour of cp-magnesium with duplex hydroxyapatite and PEO coatings, Mater. Sci. Eng. C, 49, pp. 190–200, Doi: 10.1016/J.MSEC.2014.12.081.
[35] Bobby Kannan, M., Dietzel, W., Blawert, C., Atrens, A., Lyon, P. (2008). Stress corrosion cracking of rare-earth containing magnesium alloys ZE41, QE22 and Elektron 21 (EV31A) compared with AZ80, Mater. Sci. Eng. A, 480(1–2), pp. 529–39, Doi: 10.1016/J.MSEA.2007.07.070.
[36] Choudhary, L., Singh Raman, R.K., Hofstetter, J., Uggowitzer, P.J. (2014). In-vitro characterization of stress corrosion cracking of aluminium-free magnesium alloys for temporary bio-implant applications, Mater. Sci. Eng. C, 42, pp. 629–36, Doi: 10.1016/J.MSEC.2014.06.018.
[37] Rim, K.T., Koo, K.H., Park, J.S. (2013). Toxicological Evaluations of Rare Earths and Their Health Impacts to Workers: A Literature Review, Saf. Health Work, 4(1), pp. 12–26, Doi: 10.5491/SHAW.2013.4.1.12.
[38] Bertolini, R., Bruschi, S., Ghiotti, A., Pezzato, L., Dabalà, M. (2017). The Effect of Cooling Strategies and Machining Feed Rate on the Corrosion Behavior and Wettability of AZ31 Alloy for Biomedical Applications, Procedia CIRP, 65, pp. 7–12, Doi: 10.1016/J.PROCIR.2017.03.168.
[39] Peron, M., Bertolini, R., Ghiotti, A., Torgersen, J., Bruschi, S., Berto, F. (2020). Enhancement of stress corrosion cracking of AZ31 magnesium alloy in simulated body fluid thanks to cryogenic machining, J. Mech. Behav. Biomed. Mater., 101, pp. 103429, Doi: 10.1016/J.JMBBM.2019.103429.
[40] Song, D., Li, C., Liang, N., Yang, F., Jiang, J., Sun, J., Wu, G., Ma, A., Ma, X. (2019). Simultaneously improving corrosion resistance and mechanical properties of a magnesium alloy via equal-channel angular pressing and post water annealing, Mater. Des., 166, Doi: 10.1016/j.matdes.2019.107621.
[41] Kutniy, K.V., Papirov, I.I., Tikhonovsky, M.A., Pikalov, A.I., Sivtzov, S.V., Pirozhenko, L.A., Shokurov, V.S., Shkuropatenko, V.A. (2009). Influence of grain size on mechanical and corrosion properties of magnesium alloy for medical implants, Materwiss. Werksttech., 40(4), pp. 242–6, Doi: 10.1002/mawe.200900434.
[42] Witecka, A., Bogucka, A., Yamamoto, A., Máthis, K., Krajňák, T., Jaroszewicz, J., Święszkowski, W. (2016). In vitro degradation of ZM21 magnesium alloy in simulated body fluids, Mater. Sci. Eng. C, 65, pp. 59–69, Doi: 10.1016/j.msec.2016.04.019.
[43] Wang, H., Estrin, Y., Zúberová, Z. (2008). Bio-corrosion of a magnesium alloy with different processing histories, Mater. Lett., 62(16), pp. 2476–9, Doi: 10.1016/J.MATLET.2007.12.052.
[44] Linderov, M., Vasilev, E., Merson, D., Markushev, M., Vinogradov, A. (2017). Corrosion Fatigue of Fine Grain Mg-Zn-Zr and Mg-Y-Zn Alloys, Metals (Basel)., 8(1), pp. 20, Doi: 10.3390/met8010020.
[45] Minárik, P., Jablonská, E., Král, R., Lipov, J., Ruml, T., Blawert, C., Hadzima, B., Chmelík, F. (2017). Effect of equal channel angular pressing on in vitro degradation of LAE442 magnesium alloy, Mater. Sci. Eng. C, 73, pp. 736–42, Doi: 10.1016/J.MSEC.2016.12.120.
[46] Ge, Q., Dellasega, D., Demir, A.G., Vedani, M. (2013). The processing of ultrafine-grained Mg tubes for biodegradable stents, Acta Biomater., 9(10), pp.

8604–10, Doi: 10.1016/j.actbio.2013.01.010.
[47] Segal, V.M. (1999). Equal channel angular extrusion: From macromechanics to structure formation, Mater. Sci. Eng. A, 271(1–2), pp. 322–33, Doi: 10.1016/s0921-5093(99)00248-8.
[48] ASTM E92. (2017). ASTM E92-17, Standard Test Methods for Vickers Hardness and Knoop Hardness of Metallic Materials, ASTM Int., , pp. 1–27, Doi: 10.1520/E0092-17.
[49] (N.d.). ASTM G5 - 14 Standard Reference Test Method for Making Potentiodynamic Anodic Polarization Measurements, ,.
[50] Kokubo, T., Takadama, H. (2006). How useful is SBF in predicting in vivo bone bioactivity?, Biomaterials, 27(15), pp. 2907–15, Doi: 10.1016/J.BIOMATERIALS.2006.01.017.
[51] Song, G., Atrens, A., StJohn, D. (2013).An Hydrogen Evolution Method for the Estimation of the Corrosion Rate of Magnesium Alloys. Magnesium Technology 2001, Hoboken, NJ, USA, John Wiley & Sons, Inc., pp. 254–62.
[52] Choudhary, L., Raman, R.K.S. (2011). Acta Biomaterialia Magnesium alloys as body implants : Fracture mechanism under dynamic and static loadings in a physiological environment, Acta Biomater., 8(2), pp. 916–23, Doi: 10.1016/j.actbio.2011.10.031.
[53] Thirumalaikumarasamy, D., Shanmugam, K., Balasubramanian, V. (2014). Comparison of the corrosion behaviour of AZ31B magnesium alloy under immersion test and potentiodynamic polarization test in NaCl solution, J. Magnes. Alloy., 2(1), pp. 36–49, Doi: 10.1016/J.JMA.2014.01.004.
[54] Xia, K., Wang, J.T., Wu, X., Chen, G., Gurvan, M. (2005). Equal channel angular pressing of magnesium alloy AZ31, Mater. Sci. Eng. A, 410–411, pp. 324–7, Doi: 10.1016/j.msea.2005.08.123.
[55] Gzyl, M., Rosochowski, A., Pesci, R., Olejnik, L., Yakushina, E., Wood, P. (2014). Mechanical properties and microstructure of az31b magnesium alloy processed by I-ECAP, Metall. Mater. Trans. A Phys. Metall. Mater. Sci., 45(3), pp. 1609–20, Doi: 10.1007/s11661-013-2094-z.
[56] Figueiredo, R.B., Langdon, T.G. (2010).Grain refinement and mechanical behavior of a magnesium alloy processed by ECAP. Journal of Materials Science, vol. 45, pp. 4827–36.
[57] Bryła, K., Dutkiewicz, J., Lityńska-dobrzyńska, L., Rokhlin, L.L., Kurtyka, P. (2012). Influence of number of ecap passes on microstructure and mechanical properties of az31 magnesium alloy, Arch. Metall. Mater., 57(3), pp. 711–7, Doi: 10.2478/v10172-012-0077-5.
[58] Winzer, N., Atrens, A., Song, G., Ghali, E., Dietzel, W., Kainer, K.U., Hort, N., Blawert, C. (2005). A critical review of the Stress Corrosion Cracking (SCC) of magnesium alloys, Adv. Eng. Mater., 7(8), pp. 659–93, Doi: 10.1002/adem.200500071.
[59] Stampella, R.S., Procter, R.P.M., Ashworth, V. (1984). Environmentally-induced cracking of magnesium, Corros. Sci., 24(4), pp. 325–41, Doi: 10.1016/0010-938X(84)90017-9.
[60] Raja, V.S., Padekar, B.S. (2013). Role of chlorides on pitting and hydrogen embrittlement of Mg–Mn wrought alloy, Corros. Sci., 75, pp. 176–83, Doi: 10.1016/J.CORSCI.2013.05.030.

[61] Aung, N.N., Zhou, W. (2010). Effect of grain size and twins on corrosion behaviour of AZ31B magnesium alloy, Corros. Sci., 52(2), pp. 589–94, Doi: 10.1016/J.CORSCI.2009.10.018.
[62] Birbilis, N., Ralston, K.D., Virtanen, S., Fraser, H.L., Davies, C.H.J. (2010). Grain character influences on corrosion of ECAPed pure magnesium, Corros. Eng. Sci. Technol., 45(3), pp. 224–30, Doi: 10.1179/147842209X12559428167805.
[63] Orlov, D., Ralston, K.D., Birbilis, N., Estrin, Y. (2011). Enhanced corrosion resistance of Mg alloy ZK60 after processing by integrated extrusion and equal channel angular pressing, Acta Mater., 59(15), pp. 6176–86, Doi: 10.1016/j.actamat.2011.06.033.
[64] Ralston, K.D., Birbilis, N., Davies, C.H.J. (2010). Revealing the relationship between grain size and corrosion rate of metals, Scr. Mater., 63(12), pp. 1201–4, Doi: 10.1016/J.SCRIPTAMAT.2010.08.035.
[65] Shahar, I.A., Hosaka, T., Yoshihara, S., MacDonald, B.J. (2017). Mechanical and Corrosion Properties of AZ31 Mg Alloy Processed by Equal-Channel Angular Pressing and Aging, Procedia Eng., 184, pp. 423–31, Doi: 10.1016/J.PROENG.2017.04.113.
[66] Song, D., Ma, A.B., Jiang, J.H., Lin, P.H., Yang, D.H., Fan, J.F. (2011). Corrosion behaviour of bulk ultra-fine grained AZ91D magnesium alloy fabricated by equal-channel angular pressing, Corros. Sci., 53(1), pp. 362–73, Doi: 10.1016/j.corsci.2010.09.044.
[67] Gu, X.N., Li, N., Zheng, Y.F., Kang, F., Wang, J.T., Ruan, L. (2011). In vitro study on equal channel angular pressing AZ31 magnesium alloy with and without back pressure, Mater. Sci. Eng. B, 176(20), pp. 1802–6, Doi: 10.1016/J.MSEB.2011.04.003.
[68] Mukai, T., Yamanoi, M., Watanabe, H., Higashi, K. (2001). Ductility enhancement in AZ31 magnesium alloy by controlling its grain structure, Scr. Mater., 45(1), pp. 89–94, Doi: 10.1016/S1359-6462(01)00996-4.
[69] Song, G.L. (2012). The effect of texture on the corrosion behavior of AZ31 Mg alloy, JOM, 64(6), pp. 671–9, Doi: 10.1007/s11837-012-0341-1.
[70] Gzyl, M., Rosochowski, A., Boczkal, S., Olejnik, L. (2015). The role of microstructure and texture in controlling mechanical properties of AZ31B magnesium alloy processed by I-ECAP, Mater. Sci. Eng. A, 638, pp. 20–9, Doi: 10.1016/j.msea.2015.04.055.
[71] Kim, W.J., Jeong, H.T. (2005). Grain-Size Strengthening in Equal-Channel-Angular-Pressing Processed AZ31 Mg Alloys with a Constant Texture, Mater. Trans., 46(2), pp. 251–8, Doi: 10.2320/matertrans.46.251.
[72] Agnew, S.R., Horton, J.A., Lillo, T.M., Brown, D.W. (2004). Enhanced ductility in strongly textured magnesium produced by equal channel angular processing, Scr. Mater., 50(3), pp. 377–81, Doi: 10.1016/j.scriptamat.2003.10.006.
[73] Sahoo, S.K., Sabat, R.K., Panda, S., Mishra, S.C., Suwas, S. (2015). Mechanical Property of Pure Magnesium: From Orientation Perspective Pertaining to Deviation from Basal Orientation, J. Mater. Eng. Perform., 24(6), pp. 2346–53, Doi: 10.1007/s11665-015-1522-1.

Chapter 4

On the effect of surface treatments obtained by means of mechanical processing on the SCC susceptibility of AZ31 alloy

Paper III: Enhancement of stress corrosion cracking of AZ31 magnesium alloy in simulated body fluid thanks to cryogenic machining

M. Peron [a,1], R. Bertolini [b], A. Ghiotti [b], J. Torgersen [a], S. Bruschi [b], F. Berto [a]

[a] *Department of Industrial and Mechanical Engineering, Norwegian University of Science and Technology, Richard Birkelands vei 2b, 7034 Trondheim, Norway*
[b] *Department of Industrial Engineering, University of Padova, Via Venezia 1, 35131, Padova, Italy*

Abstract[2]

Magnesium and its alloys have recently attracted great attention as potential materials for the manufacture of biodegradable implants. Unfortunately, their inadequate resistance to the simultaneous action of corrosion and mechanical stresses in the human body have hampered their use as implant materials. This work aims at evaluating the Stress Corrosion Cracking (SCC) susceptibility of the AZ31 Mg alloy after being machined under cryogenic cooling. The SCC behaviour was evaluated by means of Slow Strain Rate Tests (SSRTs) in Simulated Body Fluid (SBF) at 37 °C. Prior to testing, a full characterization of the machined surface integrity, including microstructural observations, residual stress, nano-hardness measurements and surface texture analysis was carried out together with the assessment of the corrosion properties through potentiodynamic polarization curves. In addition, the morphology of the fracture surfaces after SSRTs was analysed by means of 3D optical profiler and Scanning Electron Microscopy (SEM). The improved corrosion resistance due to the increased extension of the nano-surface layer and to the compressive residual stresses represents the reason of the reduced SCC susceptibility of cryogenically machined AZ31 samples as compared to dry machined ones.

Keywords: Stress corrosion cracking; cryogenic machining; simulated body fluid; AZ31; Magnesium alloy

4.1. Introduction

During the past years life expectancy has been continuously increasing, leading to an incessant growing number of people undergoing surgical procedures involving the implantation of medical devices [1]. Among these procedures, the orthopaedic sector experiences the highest growth. In Australia, for example, bone fractures represent about 54% of the injury hospitalisations [2]. The materials currently used in orthopaedic

[1] Corresponding author
[2] *Journal of the Mechanical Behavior of Biomedical Materials* 101 (2020) 103429

surgery are permanent metallic materials, such as stainless steel, titanium, and cobalt-chromium alloys [3]. Because of their high strength and good corrosion resistance, they have been widely used as load-bearing implants for bone healing and repair of damaged tissues [4–6]. The key problems with these permanent implants are however two-fold. Firstly, the great difference in elastic modulus of these materials compared to that of human bone results in the occurrence of the stress-shielding phenomenon. This is a consequence of stress distribution changes between the bone and the implant [7–13]: bones adapt to the reduced stress field according to the Wolff's law [14], resulting in the bone either becoming more porous (internal remodelling) or thinner (external remodelling), increasing the possibility of implant failure. Secondly, due to the arise of long-term complications [15–19], the permanent implant must be removed when the healing process is completed. However, the additional surgeries necessary to remove the implant cause an increase in costs to the health care system, as well as emotional stress to the patient. In order to solve these drawbacks, biodegradable metallic materials have been studied, in particular Mg and its alloys [20–22]. Mg has in fact low density and an elastic modulus in mechanical compatibility with natural bone, minimizing the risk of the stress shielding phenomenon [20]. In addition, Mg is highly abundant in the human body [23]. Indeed, it is essential for the metabolism in many biological mechanisms, being a cofactor for many enzymes [24], and Mg^{2+} ions resulting from the degradation process are reported to aid the healing process and the growth of tissue. Despite their highly attractive properties, Mg and its alloys have not yet been used as implant materials because of their high corrosion rates in physiological environments, which may result in a loss of mechanical integrity and in hydrogen evolution at a rate that is too fast for the bone tissue to accommodate. In addition, in orthopaedic applications, the implant must possess adequate resistance to failure when the corrosive human body fluid acts concurrently with the mechanical loading characteristics of the human body. Corrosion-assisted cracking phenomena, such as stress corrosion cracking (SCC) and corrosion fatigue (CF), were in fact reported to cause the failure of several traditional implants [25–28]. In particular, SCC is particularly dangerous because it leads to a sudden and catastrophic failure under mechanical loadings otherwise considered safe, and Mg and its alloys are particularly susceptible [29–31]. Therefore, it is important to develop Mg-based implants granting both strength and corrosion resistance in the human body without causing corrosion-assisted cracking phenomena.

Most studies focused on improving their electrochemical properties, whereas improving their resistance to corrosion-assisted cracking is overlooked. In fact, while different procedures have been applied in recent years to improve their corrosion resistance (alloying, surface modification, …), yet few of them have been assessed regarding their effects on the susceptibility to corrosion-assisted cracking phenomena. Mohajernia et al. [32] reported that hydroxyapatite coating containing multi-walled carbon nanotubes reduced the corrosion current density of AZ31 alloys by three orders of magnitude. In addition, they reported the elongation to failure of AZ31 samples subjected to slow strain rate tests (SSRT) in simulated body fluid (SBF) at 37 °C to be increased about 70% with the application of the coating. These results agree with those obtained by Chen et al. [33]. The authors coated Mg-4Zn-0.6Zr-0.4Sr with a composite coating consisting of a poly (lactic-co-glycolic acid) (PLGA) superimposed to a micro-arc oxidation (MAO) layer and they reported this composite coating to increase the elongation to failure of the bare alloy subjected to SSRT in modified simulated body

fluid (m-SBF) at 37 °C from 5% to 11%. Again, the corrosion rate was reduced by three orders of magnitude. However, when cyclic loading is applied, the presence of coatings might result to be detrimental for the fatigue life of the implants due to the formation of cracks in the coating (due to elastic modulus mismatch) that acts as stress concentrators and also due to the generally higher surface roughness of the coated samples compared to the polished uncoated counterparts [34]. Alternatively, alloying has been reported as a valuable solution to improve the corrosion resistance of Mg and to mitigate the corrosion-assisted cracking phenomena. For instance, Kannan et al. [35], compared the SCC susceptibility of three different rare earth (RE)-containing alloys, namely ZE41, QE22 and EV31A, with that of AZ80 alloy. They suggested that rare-earth elements in Mg alloys can improve the SCC resistance significantly, being EV31A alloy the most resistant to SCC compared to the other alloy. The beneficial effect of RE was found also by Choudhary et al. [36]. According to their findings, a lower SCC susceptibility was observed for RE-containing alloys, i.e. WZ21 and WE43 compared to Mg-Zn-Ca alloy (ZX50). However, some RE elements were reported to be toxic for the human body [37], and in general alloying may introduce elements that lead to adverse biological reactions. In recent years, mechanical processing inducing severe plastic deformation (SPD) have been investigated as an alternative to alloying and coating techniques. Again, broad attention was given to the effect of SPD techniques on the corrosion properties, whereas very few on the SCC susceptibility. Equal channel angular pressing (ECAP) has been extensively studied as method to reduce the corrosion rate due to its capability to induce a very fine and homogeneous microstructure. Sunil et al. [38] reported a better degradation behaviour of AZ31 alloy after four passes of ECAP compared to the annealed counterparts. These results agree with those obtained by Zhang et al. [39], where a decrease in the corrosion current density was obtained increasing the number of passes of ECAP. In addition, ECAP treated AZ61 alloys were reported to be characterized by an elongation to failure 30% higher than the as-cast material [40]. However, conventional SPD techniques such as ECAP require multiple deformation passes to accumulate large strain in the material, and suitable processing routes are also necessary to refine the material microstructure down to ultrafine grains [41]. Recently, machining has been studied as an effective method to achieve SPD. In fact, compared with the conventional SPD techniques, machining has been reported to impose higher level of strain into the workpiece material in just a single stage operation [42]. Furthermore, the use of liquid nitrogen as coolant during turning has recently shown to further improve the functional performance and product life [43]. Orthogonal cutting trials with different cutting tools with two edge radii were carried out under both dry and cryogenic conditions in [44]. Results showed that cryogenic machining using a large edge radius tool led to a thicker grain refinement layer, larger compressive residual stresses, and stronger intensity of basal texture compared to the dry machined condition. The effect of the improved surface integrity on corrosion resistance was evaluated by the same Authors in [45], in which optical inspection of the machined surfaces after immersion in saline solution was evaluated. It was stated that the degree of corrosion was correlated with the extension of the sub-surface featureless layer formed after turning: since cryogenic machining maximized the thickness of the layer, it led to the best corrosion behaviour. A step forward was made by Bruschi et al. [46], who investigated the effect of feed and cooling conditions on the corrosion resistance of the machined AZ31 Mg alloy. The corrosion resistance was measured through

potentiodynamic polarization curves in Simulated Body Fluid (SBF) at body temperature. A reduction up to an order of magnitude in the corrosion current density was found in the case of cryogenic machining regardless of the adopted feed. These improvements were associated to a wider nano-crystalline layer formed on the surface along with the generation of a more compressed surface.
These findings show that cryogenic machining is a viable path forward, but the mechanisms by which the SCC resistance improves, i.e. the microstructural reasoning behind such gains in performance, remain yet to be discovered. Here, AZ31 samples were machined under cryogenic cooling, and afterwards subjected to Slow Strain Rate Tests (SSRTs) at a strain rate of $3.5 \cdot 10^{-6}$ s^{-1}. The samples were immersed for the whole duration of the tests in SBF at 37 °C. The behaviour of dry machined samples was also investigated as a reference, reporting a higher SCC susceptibility. In support to a complete understanding of the different behaviour shown by dry and cryogenically machined samples, the authors carried out a full characterization of the surface integrity, including microstructural observations, residual stress, nano-hardness measurements and surface texture analysis, an evaluation of the corrosion behaviour through potentiodynamic polarization curves, and an analysis of the fracture surfaces after SSRTs with a Scanning Electron Microscope (SEM) and a 3D optical profiler.

4.2. Materials and methods

4.2.1. Material

AZ31 magnesium alloy was supplied in form of commercially available bars. The samples were cut and prepared for microstructural analysis using SiC papers for grinding and colloidal silica for final polishing. The grain structure was revealed by etching using a solution of alcohol (95 ml), picric acid (5 g), and acetic acid (10 ml) for 10 s. The microstructure was examined using a Leica DMRE™ Optical Microscope (OM).
The microstructure of the material in the as-received condition is shown in Figure 4.1 and consists of a quite homogeneous α matrix. The initial grain size was measured by linear intercept method and resulted equal to 24.1 ± 4 μm.

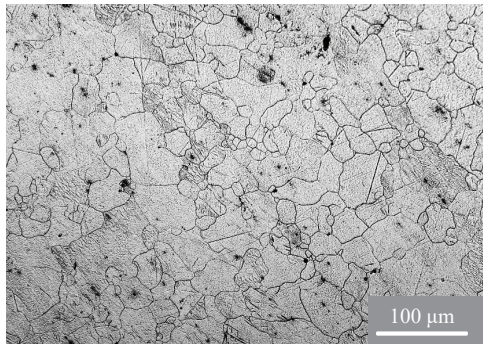

Figure 4.4: Microstructure of the AZ31 alloy in the as-received condition.

4.2.2. Machining tests

To carry out SSRTs, cylindrical dog-bone-shaped samples, whose dimensions are reported in Figure 4.2 , were used according to the standard [49]. The samples were machined on a Mori Seiki NL 1500™ CNC lathe equipped with an experimental setup devoted to the delivery of liquid nitrogen, specifically designed and described in detail in a previous work by the Authors [47], and herein reported in Figure 4.2b. To obtain the dog-bone shape of the samples, the machining operations were subdivided into two steps, namely a roughing and a finishing pass. For the roughing pass, the following machining parameters were employed: depth of cut (*d*) equal to 1 mm, cutting speed (*Vc*) of 80 m/min, and feed (*f*) equal to 0.2 mm/rev, whereas for the finishing pass the parameters were: depth of cut equal to 0.25 mm, a cutting speed of 100 m/min, and a feed equal to 0.1 mm/rev.
The surface integrity and corrosion performances after machining were evaluated on cylindrical samples manufactured using the same machining parameters applied for the realization of the dog-bone samples.
During all the machining operations, the workpiece was grabbed by the counter spindle of the lathe with a pressure of 1.30 kN to avoid vibrations.

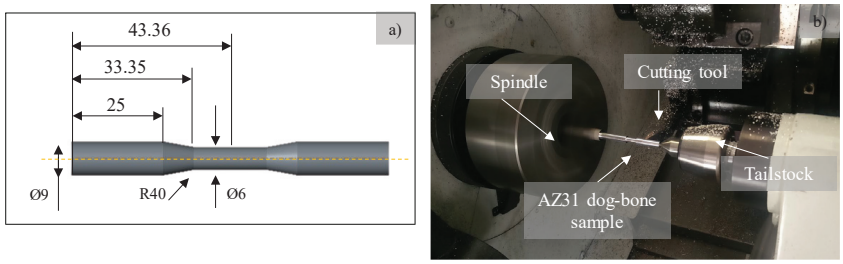

Figure 4.5: (a) Geometry and dimensions of the samples for SSRTs; (b) Experimental setup for the realization of the dog-bone samples in dry condition.

4.2.3. Surface integrity characterization

After machining, the cylindrical samples were cut along their section and prepared for microstructural characterization using the same procedure described in §4.2.1. The measurements of the machining-induced Severe Plastic Deformed (SPD) layers were carried every each 10 µm on three different OM images at 1000X magnification.
Samples were also extracted from the machined workpieces for Transmission Electron Microscopy (TEM) analysis and nano-hardness measurements. The cross-sectional TEM samples were prepared using a FEI™ Nova 200 dual-beam Focused Ion Beam (FIB) system. The TEM lamellas were then ion-milled with a 30 kV beam and finally polished at 5 kV. After reaching a thickness of ~100 nm, a Fischion™ NanoMill was used to further clean the FIB damaged surface at both sides. Selected Area Diffraction (SAD) and Bright Field (BF) TEM imaging were performed at 300 keV using a Hitachi™ HF3300 TEM.
The nano-hardness at the surface of the machined samples was measured with a diamond Berkovich indenter tip using the Hysitron™ TriboIndenter 800 load- and

depth-sensing nano-indenter system [8]. A minimum of 20 nano-indentations was performed for each sample with a maximum load of 5 mN and data acquisition frequency of 5 Hz.
The residual stresses were determined with CuKα-radiation using the (2,1,3) interference lines. The measurements were performed using a Spider^{TM} X GNR portable diffractometer working at 30 KV and 90 μA. The analysis was based on the sin2ψ-method for which the lattice spacings d were measured at five ψ-angles between −35° and +35°. For the calculation of residual stresses at the characterization site, Young's modulus and Poisson's ratio were assumed to be 45 GPa and 0.25, respectively. The counting time for each of the five measures at different ψ-angles was 500 s. The depth distribution of the residual stresses was determined by electrolytic removal of thin surface layers and subsequent X-ray measurements. For electrolytic polishing, we used a solution of 90 ml of water, 730 ml of ethanol, 100 ml of butoxyethanol and 78 ml of perchloric acid working at 18 V for 30 s at 20°C.
The machined surface textures were measured using a Sensofar™ Plu-Neox optical profiler with a 20x magnification Nikon™ confocal objective. To inspect surface defects, confocal images were acquired with the same objective.

4.2.4. Corrosion performances evaluation

Potentiodynamic polarization tests were carried out on an Amel^{TM} 2549 potentiostat, making use of a standard three-electrodes cell, where the machined cylindrical samples were the working electrode, a saturated Calomel electrode (SCE) the reference electrode, and a platinum electrode the counter electrode. The samples were immersed in SBF solution, whose composition is reported in Table 4.1. The temperature was set to 37±1°C to reproduce the human body conditions. The potentiodynamic polarization curves were obtained applying a potential from -2 V to -1.3 V at a scan rate of 0.5 mVs^{-1}. The corrosion potential and corrosion current density were determined using the Tafel extrapolation method, according to the ASTM G5-14 standard. The tests were repeated three times for each machining condition.

Reagents	Amount
NaCl	8.035 g
$NaHCO_3$	0.355 g
KCl	0.225 g
$K_2HPO_4 \cdot 3H_2O$	0.231 g
$MgCl_2 \cdot 6H_2O$	0.311 g
1.0M-HCl	39 ml
$CaCl_2$	0.292 g
Na_2SO_4	0.072 g
Tris	6.118 g

Table 4.1: Reagents and their quantities for preparation of 1000 ml of the SBF solution according to [48].

4.2.5. Slow strain rate tests (SSRT)

The SSRT experiments were carried out on the machined dog-bone samples at a strain rate of $3.5 \cdot 10^{-6}$ s^{-1} in SBF solution at body temperature (37 ± 1°C). The strain rate value was chosen in order to make the AZ31 alloy susceptible to SCC according to [35]. A schematic representation of the experimental set-up is shown in Figure 4.3. The sample was immersed for the whole duration of the test and the SBF solution was constantly changed by means of a pumping system. The SBF solution container was immersed in a water bath, whose temperature was constantly monitored by a thermometer. When the temperature was below its set value, a commercial resistance heating element placed inside the water bath automatically turned on until the desired temperature was reached again. In addition, while carrying out the SSRTs, the area of the specimen exposed to SBF was restricted to its gauge length using Teflon tapes wrapping the rest of the specimen, thus maintaining a constant area of exposure to the corrosive solution as well as avoiding the possibility of galvanic effect with other components of the testing set-up. For sake of comparison, also SSRTs in air were carried out.

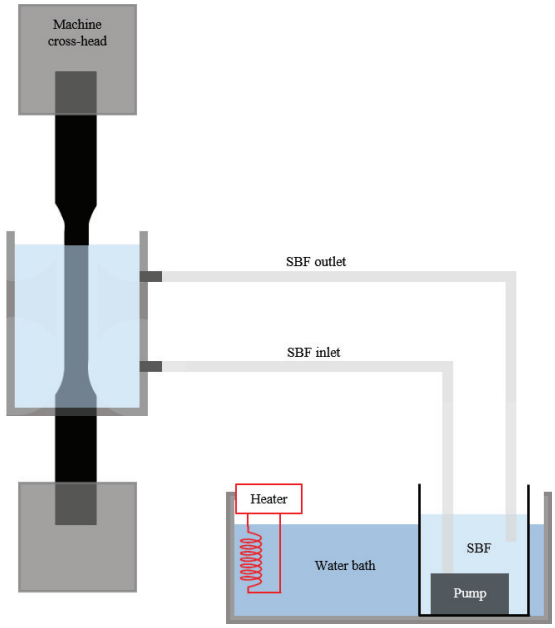

Figure 4.3: Schematic representation of the SSRT set-up.

The samples were cleaned with ethanol prior to testing. It is worth noting that, differently from other works on this field [29,31,49], the gauge length of the specimen was not grounded prior to testing, in order to avoid the removal of the surface features induced by the cryogenic machining. SSRTs were repeated three times for reproducibility.

In order to quantify the AZ31 SCC sensitivity, the susceptibility indices I_{UTS} and I_{ε} were calculated according to Eq. (4.1) and Eq. (4.2) [36]:

$$I_{UTS} = \frac{UTS_{air} - UTS_{SBF}}{UTS_{air}} \quad (4.1)$$

and

$$I_{\varepsilon} = \frac{\varepsilon_{air} - \varepsilon_{SBF}}{\varepsilon_{air}} \quad (4.2)$$

where *UTS* is the Ultimate Tensile Strength and ε the elongation at failure, both evaluated during tests conducted in SBF solution and air. When the value of the susceptibility index approaches zero, the material is considered to be highly resistant to SCC, namely the greater the index the greater the susceptibility to SCC.

4.2.6. Characterization after SSRT

The specimen fracture surfaces after SSRTs were cleaned by immersion for one minute in a solution prepared using 50 g chromium trioxide (CrO_3), 2.5 g silver nitrate ($AgNO_3$) and 5 g barium nitrate ($Ba(NO_3)_2$) in 250 ml distilled water, as suggested by [50]. The specimens were then washed with distilled water and finally ultrasonically cleaned in acetone for 10 min. The fracture surfaces were observed by means of a FEI™ QUANTA 450 SEM in Secondary Electron (SE) mode. The topography of the surface fractures was also measured using a Sensofar Plu Neox™ with a confocal 20X objective.
Finally, the fractured specimens were cut along their longitudinal section. The microstructure was observed by using the same experimental approach described in § 4.2.1.

4.3. Results

4.3.1. Surface integrity

Figures 4.4a and 4.4b show the micrographs of the samples machined under dry and cryogenic conditions, respectively. From these images, it can be seen that machining introduced an SPD layer close to the surface irrespective of the cutting conditions. Such layers consisted of ultrafine grains highly deformed along the cutting direction, characterized also by the presence of slip bands. The extension of the SPD layer increased by 24% with cryogenic cooling compared to dry cutting.

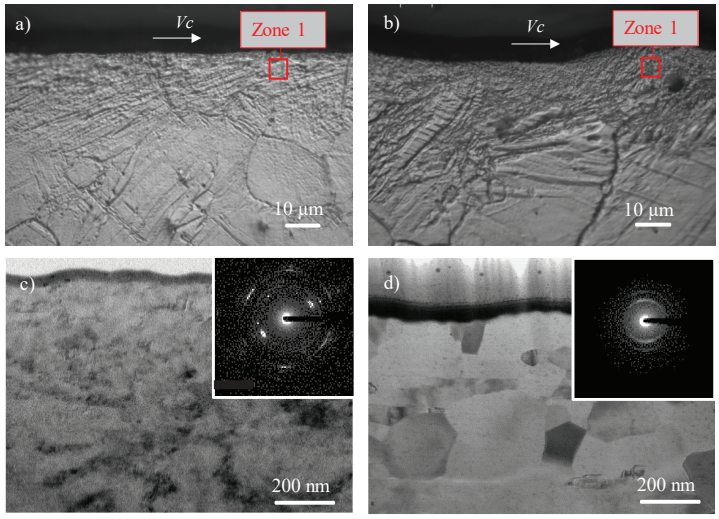

SPD layer extension (µm)	Nano-crystalline layer extension (µm)	SPD layer extension (µm)	Nano-crystalline layer extension (µm)
24 ± 2	1 ± 0.5	29.3 ± 3	4.5 ± 0.5

Figure 4.4: Optical images (a and b), BF TEM micrographs and SAD patterns (c and d) of the dry (on the left) and cryogenic (on the right) machined samples.

To further characterize the SPD layers, high-magnification TEM bright field images were captured on Zone 1 of Figure 4.4a and b and shown in Figure 4.4c and d.
In both cases, a grain refinement upon a nanoscale was achieved, but its extension depended heavily on the cooling condition. In the case of cryogenic machined samples, the nanoscale layer was almost five times thicker than in the dry cut samples. In fact, the SAD pattern of the dry cut samples revealed the presence of micrometre sized grains just below the nanolayer. On the contrary, the SAD pattern of the cryogenic cooled samples assumed a ring-like shape since the nanoscale layer was much wider.
As a consequence of the different microstructural features close to the machined surface, the mechanical properties of the material were altered. The nano-hardness values measured at the machined surface showed a very significant increase compared to the bulk value (1.35 GPa), achieving the values of 2.09 ± 0.5 GPa for the dry samples and 2.12 ± 0.2 for the cryogenic cooled ones. Coherently, no sensible differences in nano-hardness were found between the dry and cryogenic cooled samples since both showed the presence of the nanoscale layer at the machined surface (see Figure 4.4).
Figure 4.5 reports the axial residual stresses as a function of the distance from the machined surface. A totally compressive residual stress was found in the case of cryogenic cooling condition, while a tensile residual stress state was found in the case of dry cutting. Actually, the peak of residual stress was 270 MPa (tensile) in dry condition, and decreased to -143 MPa (compressive) in cryogenic condition. After approximately

200 μm from the machined surface, a null state of stress was achieved regardless of the adopted cooling condition.

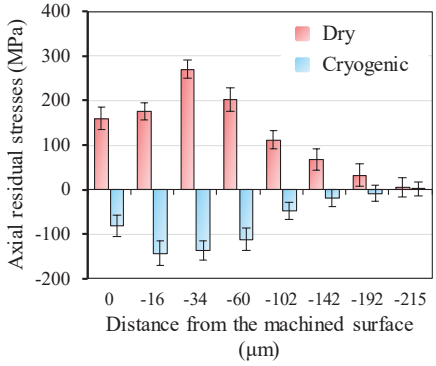

Figure 4.5: Axial residual stresses as a function of the cooling strategy.

Figure 4.6 shows the confocal images of the two surfaces machined using the two adopted strategies: no relevant differences can be seen in terms of average surface roughness *Sa* as a consequence of the application of liquid nitrogen during cutting. However, the density of tears was drastically increased in the case of dry cutting. It is worth nothing that the presence of defects is usually not revealed by surface roughness measurements [51].

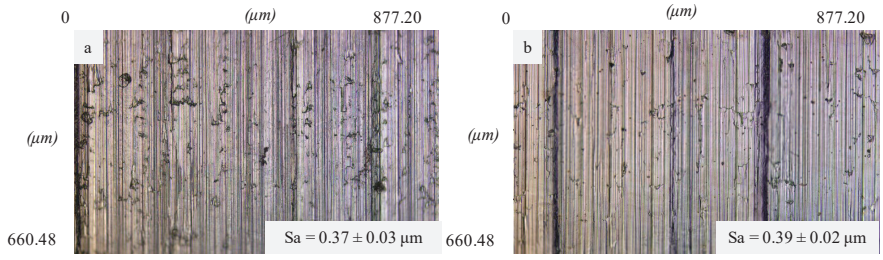

Figure 4.6: Machined surfaces images and relative surface roughness.

4.3.2. Corrosion behaviour

The potentiodynamic polarization curves of the AZ31 cylindrical samples plotted on a semi-logarithmic scale are shown in Figure 4.7. The related kinetic and thermodynamic corrosion electrochemical characteristics are reported in Table 4.2. Compared to the dry condition, cryogenically machined samples showed an improved corrosion resistance, namely an ennoblement of corrosion potential E_{corr} and a reduction of corrosion current density i_{corr} of an order of magnitude. It is worth noting that the corrosion current density is directly related to the corrosion rate by the Faraday's law, which expresses the material loss of the implant during its permanence into the human body. This

implies that the application of liquid nitrogen during cutting leads to a reduced corrosion rate.

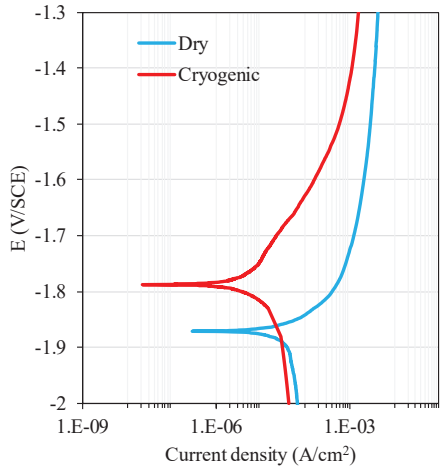

Figure 4.7: Potentiodynamic polarization curves for the AZ31 cylindrical samples in SBF solution at 37°C.

	Ecorr (V/SCE)	Icorr (μA/cm²)
Dry	-1.87 ± 0.015	10 ± 4
Cryogenic	-1.79 ± 0.025	2 ± 0.5

Table 4.2: Electrochemical corrosion data extrapolated from Figure 4.7.

4.3.3. Stress corrosion cracking behaviour

The engineering stress-strain curves for the dry and cryogenic machined AZ31 samples tested in air and in SBF are reported in Figure 4.8a and b, respectively. In addition, Table 4.3 compares the UTS and elongation at failure values obtained from the curves in Figure 4.8.

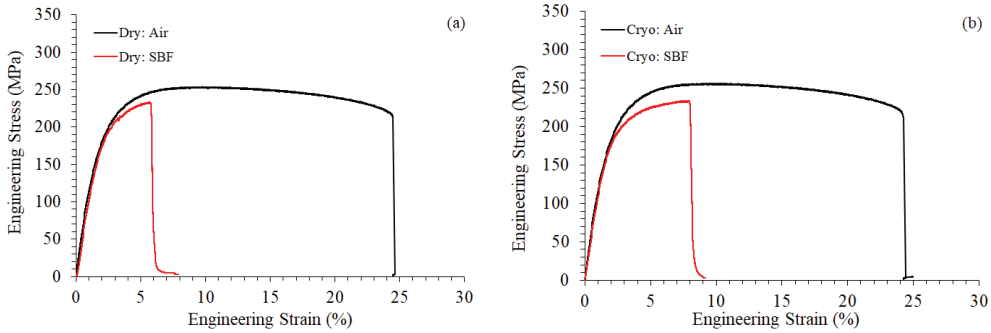

Figure 4.8: Engineering stress-strain curves of dry (a) and cryogenic (b) machined AZ31 samples tested in air and SBF at 37°C and strain rate of $3.5 \cdot 10^{-6}$ s^{-1}.

Manufacturing strategy	In Air		In SBF	
	UTS (MPa)	Elongation at failure (%)	UTS (MPa)	Elongation at failure (%)
Dry	256.3± 8.7	24.5 ± 0.7	233.3 ± 1.9	6.1 ± 0.3
Cryogenic	253.6± 5.6	24.2 ± 0.5	235.3 ± 1.0	7.8 ± 0.2

Table 4.3: Mechanical properties from Figure 4.8.

The machining cooling strategy did not influence the AZ31 mechanical properties when tested in air, since the mechanical behaviour of both dry and cryogenic machined samples is characterized by an elasto-plastic behaviour which resemble the one found by [52]. On the other hand, the considerably reduced elongation at failure when testing in SBF indicates that the alloy suffered embrittlement in SBF regardless of the adopted cooling strategy during cutting. It is however worth noting that cryogenic cooling led to a less pronounced reduction of elongation at fracture compared to the case of dry cutting.

To quantify the SCC susceptibility of the dry and cryogenic-machined samples, the I_{UTS} and I_{ε} indices were evaluated and are reported in Figure 4.9.

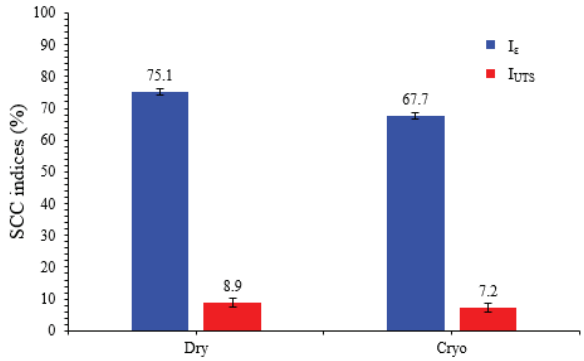

Figure 4.9: SCC indices for the dry and cryogenic machined samples.

The SCC indices of the cryogenic machined sample are, in general, lower than the ones of the dry machined sample. However, the I_{UTS} and the I_{ε} values for the dry machined sample are almost 23% and 11% higher than those of the cryogenic machined sample, respectively. This suggests that a higher resistance to SCC in SBF is provided when AZ31 is machined under cryogenic cooling which will be further analysed in section 4.4.

4.3.4. Fracture surfaces

Figure 4.10 shows the macroscopic appearance of the cryogenic machined samples after SSRTs. Clearly, the fracture in air exhibits rougher features typical of a ductile fracture;

on the contrary, the samples tested in SBF appear smooth and characterized by secondary cracked zones.

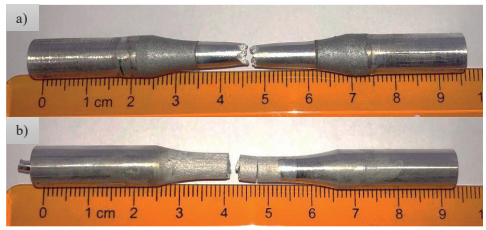

Figure 4.10: Photos of the cryogenic machined samples after SSRTs in: a) air; b) SBF at body temperature.

A more detailed investigation is given in Figure 4.11, which reports the surface topographies and SEM images of the samples of Figure 4.10. The overall view of the fracture surface confirms the ductile nature of the failure in the case of air testing, characterized by a significant amount of dimples, while the sample tested in SBF shows mix mode fracture features, namely ductile and brittle fracture characteristics. An additional confirmation of that is given by the z-range of the height of the surface texture shown in Figure 4.11a and d, which is considerably higher in the case of air testing, in relation to a more ductile behaviour.
Finally, the surface fracture appearance is completely different: in the case of SBF condition, both transgranular and intergranular cracks are evident, which are absent in the case of air testing (compare Figure 4.11f with Fig. 4.11c).
It is worth underlining that these considerations about the fracture features after testing in air and SBF are true irrespective of the adopted cooling conditions and, for the sake of brevity, the outcomes from the dry machined samples are not reported here.

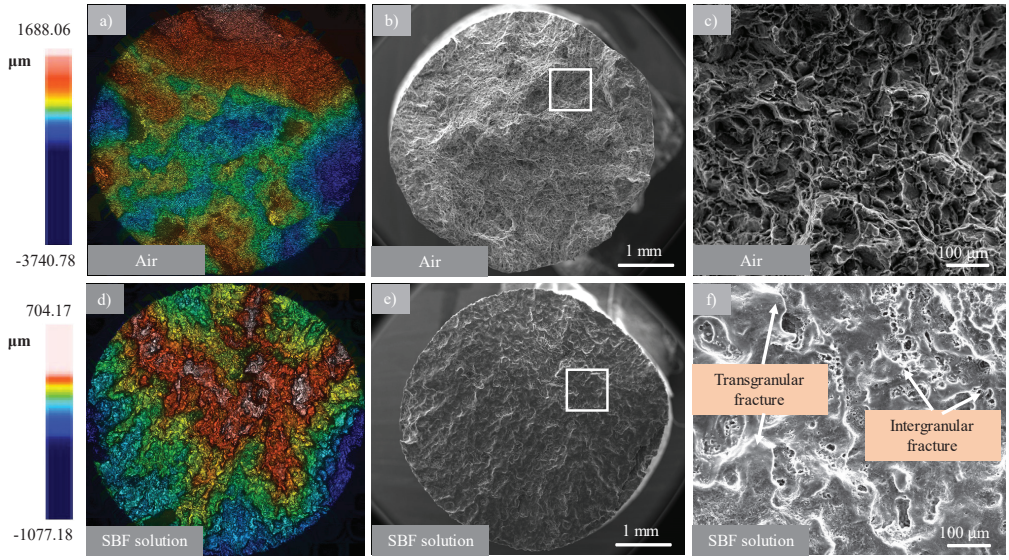

Figure 4.11: AZ31 samples after cryogenic machining and SSRT in air and SBF: (a) and (d) topographies of the overall fracture surface; (b) and (e) SEM images of the overall fracture surface; (c) and (f) magnified images of the zones highlighted in (b) and (e).

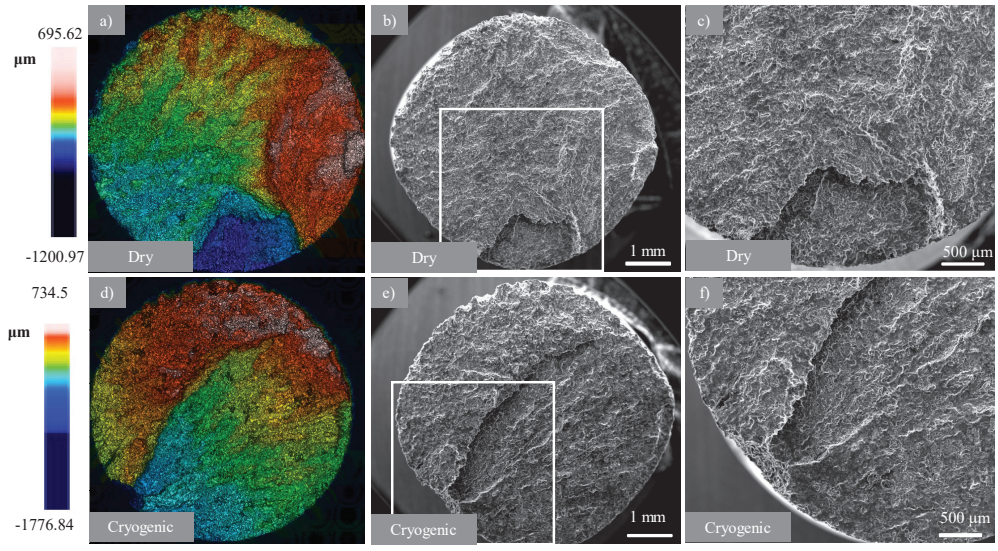

Figure 4.12: AZ31 samples after dry and cryogenic machining and SSRT in SBF at 37°C: (a) and (d) topographies of the overall fracture surface; (b) and (e) SEM images of the overall fracture surface; (c) and (f) magnified images of the zones highlighted in (b) and (e).

Figure 4.12 shows the comparison between the fracture surfaces after SSRT in SBF as a function of the machining cooling strategy. The topographies of the overall fracture surface (Figure 4.12 a and d) clearly demonstrated the sequence of the rupture. The large crack observed on the circumferential areas of the samples contributed considerably to the fracture: this crack propagated and, finally, when a critical SCC crack length was achieved, mechanical overloading took over, leading to the fracture of the sample. At a higher magnification (Figure 4.12 c and f), cleavage-like features and grain boundary cracking were observed, with a predominance of the former. Evidence of this is reported in Figure 4.13, where optical micrographs of the fractured specimens are reported.

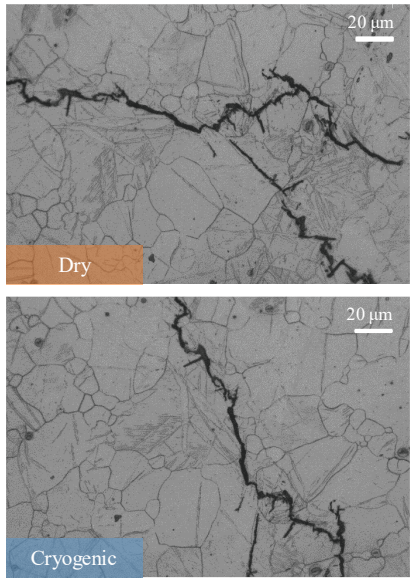

Figure 4.13: Optical micrographs of the AZ31 magnesium alloy after SSRTs in: a) dry; b) cryogenic conditions.

The fractographies of the specimens machined with different cooling strategies were similar, indicating that the susceptibility to SCC was independent of the application of liquid nitrogen. However, the tendency to pitting and localized corrosion at the sample circumference of the dry machined sample is considerably greater than that of the cryogenic machined one, as it can be seen from the tilted views of the gauge section of the samples reported in Figure 4.14. In fact, in the case of the dry sample, denser and deeper secondary cracks were evident, which contribute to a faster mechanical failure of the sample acting as stress concentrators.

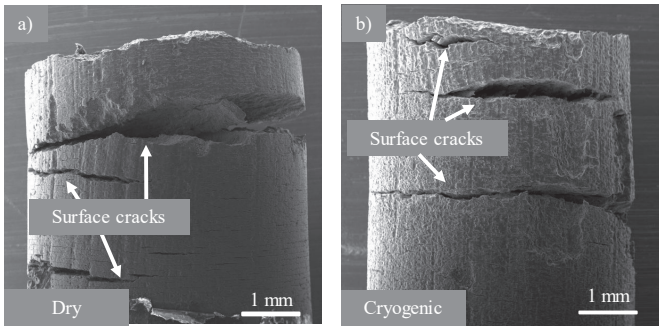

Figure 4.14: SEM fractographies of the gauge section of (a) dry and (b) cryogenic machined AZ31 samples after SSRTs in SBF.

4.4. Discussion

In this study, cryogenically machined samples have been proved to yield higher resistance to SCC in SBF compared to dry machined ones. The susceptibility indices I_{UTS} and I_{ε} of cryogenic machined samples were in fact decreased up to approximately 23% and 11%, respectively, compared to those of dry machined, indicating a strengthened response to the synergistic application of mechanical load and corrosive environment. The examination of the fracture surfaces after SCCTs revealed that this improvement was not due to a different mechanism for corrosion crack propagation. The failure mechanisms of both dry and cryogenically machined samples are in fact a combination of transgranular and intergranular cracking, with a predominance of the former (Figures 4.11 and 4.13). The reasons of this improvement are instead based on the increase in corrosion resistance because of cryogenic machining. SCC of Mg alloys is widely attributed to the combination of two mechanisms, namely the anodic dissolution and cleavage-like fracture due to hydrogen embrittlement [53]. The rupture of the protective $Mg(OH)_2$ film due to the anodic dissolution or to mechanical loads allows the hydrogen evolved from the corrosion process to enter into the matrix and to embrittle the material, leading to a premature fracture [27]. In particular, pitting was reported as main precursor for the initiation of SCC cracks [54,55]. The reduced tendency to pitting and localized corrosion of the cryogenically machined samples (Figure 4.14) thus represents one of the reasons for the reduced SCC susceptibility, together with a lower corrosion rate (Figure 4.7). As the subsequent SCC crack propagation is governed by hydrogen embrittlement, and since hydrogen evolution is intimately associated with Mg dissolution (the dissolution of one Mg atom generates one hydrogen gas molecule [20]), a lower corrosion rate leads to a reduction of material embrittlement, and thus to a higher resistance to SCC.

The modified material corrosion performances are related to the machining-induced surface integrity changes. TEM analyses gathered in Figure 4.4 reported that the cryogenic treatment provides a surface nanolayer almost five times thicker than that after dry machining. These results agree with those obtained by Pu et al. reporting a wider nanocrystalline region in cryogenically machined AZ31B alloy than in the dry machined counterparts [45]. The wider extension of both the SPD and nano-crystalline layer in the case of cryogenic cooling can be explained as follows: during machining,

the material is subjected to high strain at very high strain rate inducing the fragmentation of original grains by dislocation movements [56]. With the application of liquid nitrogen, this effect is emphasized since the temperature is greatly reduced. From a corrosion perspective, the thicker the nanocrystalline region, the lower the corrosion rate as nanoscale-sized grains reduce the corrosion rate [57,58] due to an accelerated formation of a passivating oxide film at grain boundaries [59]. An improved passive film renders the surface more electrochemically stable with a higher Electron Work Function (EWF), and the higher the EWF, the lower the corrosion rate.

The wider surface nanolayer induced by the cryogenic machining is not the only important variable that improves the corrosion resistance. As it can be seen from Figure 4.5, cryogenic machining induces a compressive state of stress, contrarily to what happened in dry machining. Residual stresses can usually be divided into the sum of two parts, one mechanically induced, and one thermally induced. During cutting, the material removal process itself is responsible for generating a compressive state on the workpiece, whereas the friction yields a tensile state of stress. However, the application of cryogenic cooling allows minimizing the tensile part of the residual stresses, leading to a compressive stress distribution at the machined surface. It is widely known that a tensile state of stress facilitates nucleation of micro-cracks as soon as corrosion is triggered [60,61], whereas compressive residual stresses are reported to increase the corrosion resistance. In particular, Denkena and Lucas reported the corrosion rate of a Mg-Ca alloy to be improved by a factor of approximately 100 [62]. The presence of a compressive state leads also to the formation and growth of a strengthened passive film since it narrows the interatomic distance of atoms, making the formation, growth and maintenance of the passive film easier [63]. Therefore, due to surface compressive residual stresses, the cryogenic machined samples showed lower corrosion current densities than the dry machined counterparts, leading to a superior ability to resist to the action of a mechanical loading in a corrosive environment.

Another reason for the improved corrosion resistance is surface texture. Although cryogenic machining was found to have no sensible influence on the surface roughness (Figure 4.6), a different effect was reported on the presence of surface defects. The density of tears in fact drastically increased in the case of the dry condition. Tears are machining defects usually attributed to the entrapment of chip particles or material coming from the wear of the insert [64]. During cutting, these particles are dragged along the surface, causing scratches. In the case of cryogenic cooling, the wear of the tool is sensibly decreased due to the inhibition of the tool wear adhesion phenomena, a thermally activated mechanism. In addition, friction is reduced due to the increase of hardness of the mating interfaces compared to the dry condition [65]. This leads to a lower generation of particles coming from the wear of the tool, and therefore, less surface defects strengthening the resistance of the surface to corrosive attacks and reducing the SCC susceptibility.

4.5. Conclusions

In this study, the effect of cryogenic cooling during machining on the stress corrosion cracking (SCC) susceptibility of the AZ31 Mg alloy was assessed. SSRTs at a strain rate of $3.5 \cdot 10^{-6}$ s^{-1} were carried out in SBF at 37°C. In addition, potentiodynamic

polarization tests, a full characterization of the surface integrity prior to testing and fracture surfaces analyses were carried out.
The main findings can be summarized as follows:

- Cryogenic machined samples were characterized by lower SCC susceptibility in SBF at body temperature than dry cut samples. This enhancement was attributed to the improved corrosion performances of the cryogenic machined samples due to the presence of a wider nanocrystalline layer, resulting in a faster formation of passivating surface oxides, and to the presence of compressive residual stresses instead of tensile.
- The analysis of the morphologies of the fracture surfaces after SSRTs proved that the use of liquid nitrogen during machining did not alter the AZ31 response mechanisms to SCC, being the fracture characterized by the presence of both intergranular and transgranular cracks, with the predominance of the latter. However, the analysis of both the fracture surface and the gauge section evidenced that cryogenic machined samples were less prone to pitting and localized corrosion, decreasing the SCC susceptibility.

It can be concluded that the cryogenic machining is an effective method to decrease the AZ31 sensitivity to SCC, and, therefore, can be considered a viable pathway for the fabrication of biodegradable implants with a prolonged durability inside the human body.

References

[1] Ginebra, M.P., Traykova, T., Planell, J.A. (2006). Calcium phosphate cements as bone drug delivery systems: A review, J. Control. Release, 113(2), pp. 102–10, Doi: 10.1016/j.jconrel.2006.04.007.

[2] Bradley, C., Harrison, J.E. (2004). Descriptive epidemiology of traumatic fractures in Australia, Australian Institute of Health and Welfare.

[3] Chen, Q., Thouas, G.A. (2015). Metallic implant biomaterials, Mater. Sci. Eng. R Reports, 87, pp. 1–57, Doi: 10.1016/J.MSER.2014.10.001.

[4] Hanawa, T. (2010).Overview of metals and applications. Metals for Biomedical Devices, Elsevier, pp. 3–24.

[5] Albrektsson, T., Brånemark, P.-I., Hansson, H.-A., Lindström, J. (1981). Osseointegrated Titanium Implants: *Requirements for Ensuring a Long-Lasting, Direct Bone-to-Implant Anchorage in Man*, Acta Orthop. Scand., 52(2), pp. 155–70, Doi: 10.3109/17453678108991776.

[6] Rossi, F., Lang, N.P., De Santis, E., Morelli, F., Favero, G., Botticelli, D. (2014). Bone-healing pattern at the surface of titanium implants: an experimental study in the dog, Clin. Oral Implants Res., 25(1), pp. 124–31, Doi: 10.1111/clr.12097.

[7] Bauer, T.W., Schils, J. (1999). The pathology of total joint arthroplasty.II. Mechanisms of implant failure., Skeletal Radiol., 28(9), pp. 483–97.

[8] Dujovne, A.R., Bobyn, J.D., Krygier, J.J., Miller, J.E., Brooks, C.E. (1993). Mechanical compatibility of noncemented hip prostheses with the human femur, J. Arthroplasty, 8(1), pp. 7–22, Doi: 10.1016/S0883-5403(06)80102-6.

[9] Engh, C.A., Bobyn, J.D. (1988). The influence of stem size and extent of porous

coating on femoral bone resorption after primary cementless hip arthroplasty., Clin. Orthop. Relat. Res., (231), pp. 7–28.
[10] Kerner, J., Huiskes, R., van Lenthe, G.H., Weinans, H., van Rietbergen, B., Engh, C.A., Amis, A.A. (1999). Correlation between pre-operative periprosthetic bone density and post-operative bone loss in THA can be explained by strain-adaptive remodelling., J. Biomech., 32(7), pp. 695–703, Doi: 10.1016/S0021-9290(99)00041-X.
[11] Sumner, D.R., Galante, J.O. (1992). Determinants of stress shielding: design versus materials versus interface., Clin. Orthop. Relat. Res., (274), pp. 202–12.
[12] Turner, T.M., Sumner, D.R., Urban, R.M., Igloria, R., Galante, J.O. (1997). Maintenance of proximal cortical bone with use of a less stiff femoral component in hemiarthroplasty of the hip without cement. An investigation in a canine model at six months and two years., J. Bone Joint Surg. Am., 79(9), pp. 1381–90.
[13] Van Rietbergen, B., Huiskes, R., Weinans, H., Sumner, D.R., Turner, T.M., Galante, J.O. (1993). The mechanism of bone remodeling and resorption around press-fitted THA stems, J. Biomech., 26(4–5), pp. 369–82, Doi: 10.1016/0021-9290(93)90001-U.
[14] Wolff, J. (1986). The Law of Bone Remodelling, Berlin, Heidelberg, Springer Berlin Heidelberg.
[15] Pound, B.G. (2014). Corrosion behavior of metallic materials in biomedical applications . I . Ti and its alloys, 32, pp. 1–20, Doi: 10.1515/corrrev-2014-0007.
[16] Pound, B.G. (2014). Corrosion behavior of metallic materials in biomedical applications . II . Stainless steels and Co-Cr alloys, 32, pp. 21–41, Doi: 10.1515/corrrev-2014-0008.
[17] Jacobs, J.J., Gilbert, J.L., Urban, R.M. (1998). Corrosion of metal orthopaedic implants., J. Bone Joint Surg. Am., 80(2), pp. 268–82.
[18] Jacobs, J.J., Hallab, N.J., Skipor, A.K., Urban, R.M. (2003). Metal degradation products: a cause for concern in metal-metal bearings?, Clin. Orthop. Relat. Res., (417), pp. 139–47, Doi: 10.1097/01.blo.0000096810.78689.62.
[19] Beech, I.B., Sunner, J.A., Arciola, C.R., Cristiani, P. (2006). Microbially-influenced corrosion: damage to prostheses, delight for bacteria., Int. J. Artif. Organs, 29(4), pp. 443–52.
[20] Peron, M., Torgersen, J., Berto, F. (2017). Mg and Its Alloys for Biomedical Applications: Exploring Corrosion and Its Interplay with Mechanical Failure, Metals (Basel)., 7(7), pp. 252, Doi: 10.3390/met7070252.
[21] Li, N., Zheng, Y. (2013). Novel Magnesium Alloys Developed for Biomedical Application: A Review, J. Mater. Sci. Technol., 29(6), pp. 489–502, Doi: 10.1016/J.JMST.2013.02.005.
[22] Singh Raman, R.K., Jafari, S., Harandi, S.E. (2015). Corrosion fatigue fracture of magnesium alloys in bioimplant applications: A review, Eng. Fract. Mech., 137, pp. 97–108, Doi: 10.1016/j.engfracmech.2014.08.009.
[23] Staiger, M.P., Pietak, A.M., Huadmai, J., Dias, G. (2006). Magnesium and its alloys as orthopedic biomaterials: A review, Biomaterials, 27, pp. 1728–34, Doi: 10.1016/j.biomaterials.2005.10.003.
[24] Hänzi, A.C., Sologubenko, A.S., Uggowitzer, P.J. (2009). Design strategy for new biodegradable Mg–Y–Zn alloys for medical applications, ,.
[25] Teoh, S.. (2000). Fatigue of biomaterials: a review, Int. J. Fatigue, 22(10), pp.

825–37, Doi: 10.1016/S0142-1123(00)00052-9.
[26] Akahori, T., Niinomi, M., Fukunaga, K.-I., Inagaki, I. (2000). Effects of microstructure on the short fatigue crack initiation and propagation characteristics of biomedical α/β titanium alloys, Metall. Mater. Trans. A, 31(8), pp. 1949–58, Doi: 10.1007/s11661-000-0222-z.
[27] Jafari, S., Harandi, S.E., Singh Raman, R.K. (2015). A review of stress-corrosion cracking and corrosion fatigue of magnesium alloys for biodegradable implant applications, Jom, 67(5), pp. 1143–53, Doi: 10.1007/s11837-015-1366-z.
[28] Antunes, R.A., de Oliveira, M.C.L. (2012). Corrosion fatigue of biomedical metallic alloys: Mechanisms and mitigation, Acta Biomater., 8(3), pp. 937–62, Doi: 10.1016/j.actbio.2011.09.012.
[29] Jafari, S., Raman, R.K.S., Davies, C.H.J., Hofstetter, J., Uggowitzer, P.J., Löffler, J.F. (2017). Stress corrosion cracking and corrosion fatigue characterisation of MgZn1Ca0.3 (ZX10) in a simulated physiological environment, J. Mech. Behav. Biomed. Mater., 65, pp. 634–43, Doi: 10.1016/J.JMBBM.2016.09.033.
[30] Kannan, M.B., Raman, R.K.S. (2008). In vitro degradation and mechanical integrity of calcium-containing magnesium alloys in modified-simulated body fluid, Biomaterials, 29(15), pp. 2306–14, Doi: 10.1016/J.BIOMATERIALS.2008.02.003.
[31] Jafari, S., Raman, R.K.S., Davies, C.H.J. (2018). Stress corrosion cracking of an extruded magnesium alloy (ZK21) in a simulated body fluid, Eng. Fract. Mech., 201, pp. 47–55, Doi: 10.1016/J.ENGFRACMECH.2018.09.002.
[32] Mohajernia, S., Pour-Ali, S., Hejazi, S., Saremi, M., Kiani-Rashid, A.-R. (2018). Hydroxyapatite coating containing multi-walled carbon nanotubes on AZ31 magnesium: Mechanical-electrochemical degradation in a physiological environment, Ceram. Int., 44(7), pp. 8297–305, Doi: 10.1016/J.CERAMINT.2018.02.015.
[33] Chen, L., Sheng, Y., Zhou, H., Li, Z., Wang, X., Li, W. (2018). Influence of a MAO + PLGA coating on biocorrosion and stress corrosion cracking behavior of a magnesium alloy in a physiological environment, Corros. Sci., , Doi: 10.1016/J.CORSCI.2018.12.005.
[34] Gao, Y., Yerokhin, A., Matthews, A. (2015). Mechanical behaviour of cp-magnesium with duplex hydroxyapatite and PEO coatings, Mater. Sci. Eng. C, 49, pp. 190–200, Doi: 10.1016/J.MSEC.2014.12.081.
[35] Bobby Kannan, M., Dietzel, W., Blawert, C., Atrens, A., Lyon, P. (2008). Stress corrosion cracking of rare-earth containing magnesium alloys ZE41, QE22 and Elektron 21 (EV31A) compared with AZ80, Mater. Sci. Eng. A, 480(1–2), pp. 529–39, Doi: 10.1016/J.MSEA.2007.07.070.
[36] Choudhary, L., Singh Raman, R.K., Hofstetter, J., Uggowitzer, P.J. (2014). In-vitro characterization of stress corrosion cracking of aluminium-free magnesium alloys for temporary bio-implant applications, Mater. Sci. Eng. C, 42, pp. 629–36, Doi: 10.1016/J.MSEC.2014.06.018.
[37] Rim, K.T., Koo, K.H., Park, J.S. (2013). Toxicological Evaluations of Rare Earths and Their Health Impacts to Workers: A Literature Review, Saf. Health Work, 4(1), pp. 12–26, Doi: 10.5491/SHAW.2013.4.1.12.
[38] Ratna Sunil, B., Sampath Kumar, T.S., Chakkingal, U., Nandakumar, V., Doble, M., Devi Prasad, V., Raghunath, M. (2016). In vitro and in vivo studies of

biodegradable fine grained AZ31 magnesium alloy produced by equal channel angular pressing, Mater. Sci. Eng. C, 59, pp. 356–67, Doi: 10.1016/J.MSEC.2015.10.028.
[39] Zhang, F., Ma, A., Jiang, J., Xu, H., Song, D., Lu, F., Nishida, Y. (2013). Enhanced biodegradation behavior of ultrafine-grained ZE41A magnesium alloy in Hank's solution, Prog. Nat. Sci. Mater. Int., 23(4), pp. 420–4, Doi: 10.1016/J.PNSC.2013.06.003.
[40] Xie, Q., Ma, A., Jiang, J., Cheng, Z., Song, D., Yuan, Y., Liu, H., Xie, Q., Ma, A., Jiang, J., Cheng, Z., Song, D., Yuan, Y., Liu, H. (2017). Stress Corrosion Cracking Behavior of Fine-Grained AZ61 Magnesium Alloys Processed by Equal-Channel Angular Pressing, Metals (Basel)., 7(9), pp. 343, Doi: 10.3390/met7090343.
[41] Mostaed, E., Fabrizi, A., Dellasega, D., Bonollo, F., Vedani, M. (2015). Microstructure, mechanical behavior and low temperature superplasticity of ECAP processed ZM21 Mg alloy, J. Alloys Compd., 638, pp. 267–76, Doi: 10.1016/J.JALLCOM.2015.03.029.
[42] Bertolini, R., Bruschi, S., Ghiotti, A. (2018). Large Strain Extrusion Machining under Cryogenic Cooling to Enhance Corrosion Resistance of Magnesium Alloys for Biomedical Applications, Procedia Manuf., 26, pp. 217–27, Doi: 10.1016/J.PROMFG.2018.07.030.
[43] Pu, Z., Outeiro, J.C., Batista, A.C., Dillon, O.W., Puleo, D.A., Jawahir, I.S. (2011). Surface Integrity in Dry and Cryogenic Machining of AZ31B Mg Alloy with Varying Cutting Edge Radius Tools, Procedia Eng., 19, pp. 282–7, Doi: 10.1016/J.PROENG.2011.11.113.
[44] Jawahir, I.S., Puleo, D.A., Schoop, J. (2016). Cryogenic Machining of Biomedical Implant Materials for Improved Functional Performance, Life and Sustainability, Procedia CIRP, 46, pp. 7–14, Doi: 10.1016/J.PROCIR.2016.04.133.
[45] Pu, Z., Dillon, O.W., Puelo, D.A., Jawahir, I.S. (2015). Cryogenic machining and burnishing of magnesium alloys to improve in vivo corrosion resistance, Surf. Modif. Magnes. Its Alloy. Biomed. Appl., , pp. 103–33, Doi: 10.1016/B978-1-78242-078-1.00005-0.
[46] Bruschi, S., Bertolini, R., Ghiotti, A., Savio, E., Guo, W., Shivpuri, R. (2018). Machining-induced surface transformations of magnesium alloys to enhance corrosion resistance in human-like environment, CIRP Ann., 67(1), pp. 579–82, Doi: 10.1016/J.CIRP.2018.04.040.
[47] Bertolini, R., Bruschi, S., Ghiotti, A., Pezzato, L., Dabalà, M. (2017). The Effect of Cooling Strategies and Machining Feed Rate on the Corrosion Behavior and Wettability of AZ31 Alloy for Biomedical Applications, Procedia CIRP, 65, pp. 7–12, Doi: 10.1016/J.PROCIR.2017.03.168.
[48] Kokubo, T., Takadama, H. (2006). How useful is SBF in predicting in vivo bone bioactivity?, Biomaterials, 27(15), pp. 2907–15, Doi: 10.1016/J.BIOMATERIALS.2006.01.017.
[49] Choudhary, L., Raman, R.K.S. (2011). Acta Biomaterialia Magnesium alloys as body implants : Fracture mechanism under dynamic and static loadings in a physiological environment, Acta Biomater., 8(2), pp. 916–23, Doi: 10.1016/j.actbio.2011.10.031.

[50] Thirumalaikumarasamy, D., Shanmugam, K., Balasubramanian, V. (2014). Comparison of the corrosion behaviour of AZ31B magnesium alloy under immersion test and potentiodynamic polarization test in NaCl solution, J. Magnes. Alloy., 2(1), pp. 36–49, Doi: 10.1016/J.JMA.2014.01.004.
[51] Bruschi, S., Pezzato, L., Ghiotti, A., Dabalà, M., Bertolini, R. (2019). Effectiveness of using low-temperature coolants in machining to enhance durability of AISI 316L stainless steel for reusable biomedical devices, J. Manuf. Process., 39, pp. 295–304, Doi: 10.1016/J.JMAPRO.2019.02.003.
[52] Şerban, D.A., Marsavina, L., Rusu, L., Negru, R. (2019). Numerical study of the behavior of magnesium alloy AM50 in tensile and torsional loadings, Arch. Appl. Mech., 89(5), pp. 911–7, Doi: 10.1007/s00419-018-1492-5.
[53] Winzer, N., Atrens, A., Song, G., Ghali, E., Dietzel, W., Kainer, K.U., Hort, N., Blawert, C. (2005). A critical review of the Stress Corrosion Cracking (SCC) of magnesium alloys, Adv. Eng. Mater., 7(8), pp. 659–93, Doi: 10.1002/adem.200500071.
[54] Stampella, R.S., Procter, R.P.M., Ashworth, V. (1984). Environmentally-induced cracking of magnesium, Corros. Sci., 24(4), pp. 325–41, Doi: 10.1016/0010-938X(84)90017-9.
[55] Raja, V.S., Padekar, B.S. (2013). Role of chlorides on pitting and hydrogen embrittlement of Mg–Mn wrought alloy, Corros. Sci., 75, pp. 176–83, Doi: 10.1016/J.CORSCI.2013.05.030.
[56] Shen, N., Ding, H., Pu, Z., Jawahir, I.S., Jia, T. (2017). Enhanced Surface Integrity From Cryogenic Machining of AZ31B Mg Alloy: A Physics-Based Analysis With Microstructure Prediction, J. Manuf. Sci. Eng., 139(6), pp. 061012, Doi: 10.1115/1.4034279.
[57] Hamu, G. Ben., Eliezer, D., Wagner, L. (2009). The relation between severe plastic deformation microstructure and corrosion behavior of AZ31 magnesium alloy, J. Alloys Compd., 468(1–2), pp. 222–9, Doi: 10.1016/J.JALLCOM.2008.01.084.
[58] Liu, Y., Liu, D., You, C., Chen, M. (2015). Effects of grain size on the corrosion resistance of pure magnesium by cooling rate-controlled solidification, Front. Mater. Sci., 9(3), pp. 247–53, Doi: 10.1007/s11706-015-0299-3.
[59] Witte, F., Hort, N., Vogt, C., Cohen, S., Kainer, K.U., Willumeit, R., Feyerabend, F. (2008). Degradable biomaterials based on magnesium corrosion, Curr. Opin. Solid State Mater. Sci., 12(5), pp. 63–72, Doi: 10.1016/j.cossms.2009.04.001.
[60] Sano, Y., Obata, M., Kubo, T., Mukai, N., Yoda, M., Masaki, K., Ochi, Y. (2006). Retardation of crack initiation and growth in austenitic stainless steels by laser peening without protective coating, Mater. Sci. Eng. A, 417(1–2), pp. 334–40, Doi: 10.1016/J.MSEA.2005.11.017.
[61] Brinksmeier, E., Cammett, J.T., König, W., Leskovar, P., Peters, J., Tönshoff, H.K. (1982). Residual Stresses — Measurement and Causes in Machining Processes, CIRP Ann., 31(2), pp. 491–510, Doi: 10.1016/S0007-8506(07)60172-3.
[62] Denkena, B., Lucas, A. (2007). Biocompatible Magnesium Alloys as Absorbable Implant Materials – Adjusted Surface and Subsurface Properties by Machining Processes, CIRP Ann., 56(1), pp. 113–6, Doi: 10.1016/J.CIRP.2007.05.029.
[63] Liu, X., Frankel, G.S. (2006). Effects of compressive stress on localized

corrosion in AA2024-T3, Corros. Sci., 48(10), pp. 3309–29, Doi: 10.1016/J.CORSCI.2005.12.003.
[64] Ginting, A., Nouari, M. (2009). Surface integrity of dry machined titanium alloys, Int. J. Mach. Tools Manuf., 49(3–4), pp. 325–32, Doi: 10.1016/J.IJMACHTOOLS.2008.10.011.
[65] Bordin, A., Bruschi, S., Ghiotti, A., Bariani, P.F. (2015). Analysis of tool wear in cryogenic machining of additive manufactured Ti6Al4V alloy, Wear, 328–329, pp. 89–99, Doi: 10.1016/J.WEAR.2015.01.030.

Chapter 5

Evaluating the corrosion and biological performances of Atomic Layer Deposition technique

5.1. Paper IV: On the comparison between the corrosion performances of sputtered and ALDed TiO2 thin layer with different substrate roughness and topology

M. Peron[1], A. Bin Afif, A. Dadlani, F. Berto, J. Torgersen

Department of Mechanical and Industrial Engineering, Norwegian University of Science and Technology, Richard Birkelands vei 2b, 7034 Trondheim, Norway

Abstract[2]

The reduction of corrosion of an AZ31 alloy in Simulated Body Fluid (SBF) was assessed when coated with a 40 nm TiO_2 obtained by the sputter technique and compared to a similar coating made by the recently developed Atomic Layer Deposition (ALD). Corrosion experiments were performed on samples with different surface roughness and topologies, and ALD has been found to better perform compared to sputter due to a higher surface integrity and adhesion strength. In addition, in porous 3D structures, ALDed samples emit 68% less hydrogen than their sputter coated counterparts due to the sputter coating's line of sight problem.

Keywords: Atomic Layer Deposition (ALD); sputter; corrosion resistance; Magnesium; TiO_2 coating

5.1.1. Introduction

Due to the increasing average age and obesity of our society, the demand for orthopedic interventions requiring the implantation of medical devices is continuously increasing [1,2]. To be used in orthopaedic surgery, a material has to be characterized by high strength and good corrosion resistance. Permanent metallic materials, such as stainless steel, titanium, and cobalt-chromium alloys, meet these requirements [3–5], and have therefore been used [6]. However, two key issues arise with such materials. Firstly, the vast difference in elastic modulus compared to human bone results in the occurrence of stress-shielding: a consequence of stress distribution changes between the bone and the implant [7–13]. Bones adapt to the reduced stress field according to the Wolff's law [14] resulting either in the increase of bone porosity (internal remodeling) or in its thinning (external remodeling). Secondly, to avoid possible long-term complications such as local inflammations [15–19], the implant shall ideally vanish when the healing process is completed. However common metallic implants are permanent and thus remain in the body. When complications arise, additional surgeries are required to

[1] Corresponding author
[2] *Surface and Coatings Technology* (submitted paper)

remove the implant causing an increase in costs to the health care system, as well as emotional stress to the patient.

Biodegradable metallic materials may resolve these issues. Here, Mg and its alloys stand out [20–22] due to their low density and an elastic modulus compatible with natural bone that minimize the risk of stress shielding [20]. In addition, Mg is highly abundant in the human body [23]; it is essential for the metabolism in many biological systems, is a cofactor for many enzymes [24], aids the healing process, and the growth of tissue via Mg^{2+} ions that are products of the degradation process. Despite their highly attractive properties, Mg and its alloys have not yet been used as implant materials because of their high corrosion rates in physiological environments, which may result in a loss of mechanical integrity and in hydrogen evolution beyond what bone tissue is able to accommodate. The high corrosion rate is further enhanced by the designed porosity and surface roughness of today's implants sought to enhance the osseointegration and cell adhesion [25–27].

In the last years, several procedures have been explored to improve the corrosion resistance of Mg and its alloys, including mechanical processing inducing severe plastic deformation (SPD). SPD techniques, such as equal channel angular pressing (ECAP), induce high plastic deformations within the material that lead to a dynamic recrystallization characterized by the nucleation and growth of new and finer grains, These methods have been extensively studied since fine grains are known to improve the overall corrosion resistance [28–31]. However, conventional SPD techniques such as ECAP require multiple deformation passes to accumulate large strain in the material, and suitable processing routes are also necessary to refine the material microstructure down to ultrafine grains [32]. Recently, machining has been studied as an effective method to achieve SPD. In fact, compared with the conventional SPD techniques, machining has been reported to impose higher level of strain into the workpiece material in just a single stage operation [33]. Furthermore, the use of liquid nitrogen as coolant during machining has recently shown to further improve the functional performance and product life [34]. Peron et al. [35], reported a reduction of up to an order of magnitude in the corrosion current density when AZ31 Mg alloys were cryogenically machined. These improvements were associated with the formation of a nano-crystalline and compressed surface layer. However, once the nano-crystalline surface layer dissolves, the machining induced corrosion resistance disappears.

A potential Mg implant may need surface texture and porosity to enhance ingrowth of cells and tissue at the patient specific site of interest [36,37]. In such a scenario, cryogenic machining, despite its benefits in initial corrosion resistance, might not be applicable as (1) intricate features are difficult to be made and (2) the resulting surfaces are smooth without texture. Hence an alternative, surface confined approach might be required that allows the control of surface texture. Coatings have thus emerged as an effective way to preserve designed macroscopic porosity and surface roughness tailored for osseointegration and to match mechanical characteristics [38][39]. Particularly sputtering has been studied due to the possibility to carry out the deposition at low temperatures, making the coating relatively insensitive to thermodynamic phenomena [40]. Jin et al. reported that the application of a 600 nm thick TaN layer on WE43 alloy reduced the corrosion current density in Simulated Body Fluid (SBF) by two orders of magnitude [41]. A similar improvement was also reported in Ref. [42] for a 30 nm TiN coated WE43 alloy. However, the effectiveness of sputtering can be limited since it is

subject to the line-of-sight. When considering implants, their complex shapes such as notches, pores and undercuts cannot be entirely coated due to this limitation, which renders corrosion to be most severe at places that are not accessible to the process.
To overcome this issue, Chemical Vapor Deposition (CVD) techniques might be a solution. CVD is the collective name for a number of processes where the substrate surface is exposed to one or more volatile precursors, which react and/or decompose on the substrate surface to produce the desired deposit [43]. Among CVD techniques, Atomic Layer Deposition (ALD) stands out in terms of conformality, film density and possibility for compositional control due to its self-limiting surface-gas phase reactions that have recently found application in corrosion protection [44,45]. Liu et al. reported a three orders of magnitude decrease in the corrosion current density of an AZ31 Mg alloy that was coated with a 10 nm thick ZrO_2 layer [44], while Yang et al. reported a 40 nm layer of ZrO_2 to reduce the corrosion current density of MgSr alloy by two orders of magnitude [46].
This suggests that ALD coatings would promise a significant enhancement of the corrosion resistance in Mg alloys, a research field that is yet underexplored. Here we aim to provide new insight inside into the corrosion performance of ALD coated Mg alloys and to compare it to sputter coating films employing samples of different surface roughness and topologies that shall resemble a more realistic condition of an implant surface. To do so, an AZ31 alloy has been machined into flat discs with two different roughness and into small cubes with pass-through holes to resemble the induced porosity in real implants [47,48]. All these different geometries have been coated with a 40 nm layer of TiO_2 obtained by means of sputter and ALD and their corrosion properties in SBF have been evaluated by means of potentiodynamic polarization curves tests and hydrogen evolution experiments. The behavior of bare samples has also been investigated as a reference.
To evaluate the different performances of ALD and sputtering, the chemical composition of the layer obtained by the two techniques has been assessed by means of XPS analyses before and after 24 hours of corrosion in SBF. In addition, the surface integrity of rough and polished samples coated with the two techniques has been assessed by means of Scanning Electron Microscope (SEM) analyses.

5.1.2. Materials and methods

5.1.2.1. Sample preparation

AZ31 magnesium alloy was supplied in form of commercially available bars (Dynamic Metals Ltd, Bedfordshire, UK). The microstructure was analyzed using a Leica DMRETM Optical Microscope (Leica microsystems, Wetzlar, Germany) after polishing the surface and etching it using a solution of alcohol (95 ml), picric acid (5 g), and acetic acid (10 ml). The microstructure is shown in Figure 5.1.1 and consists of a quite homogeneous α matrix. The initial grain size was measured by linear intercept method and resulted equal to 14.8 ± 8 μm.

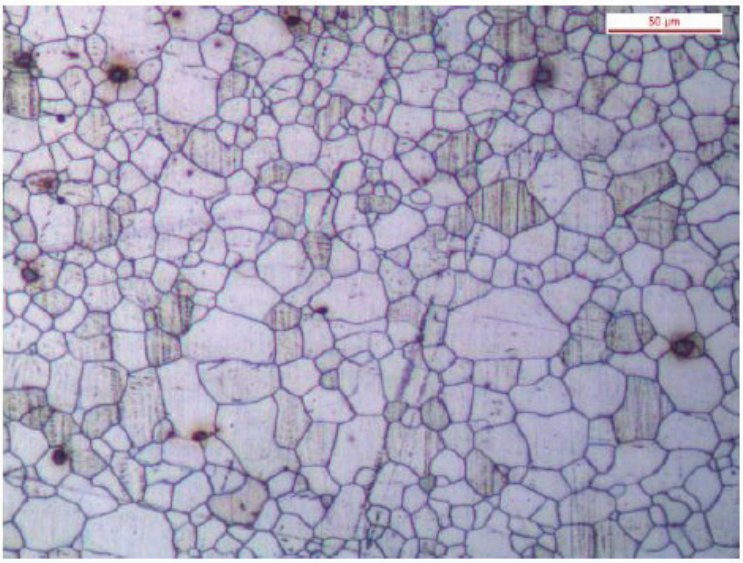

Figure 5.1.6: Microstructure of the AZ31 alloy in the as-received condition.

To simulate different biologically relevant conditions, flat discs (for potentiodynamic polarization curves) and plates (for hydrogen evolution experiments) with two different roughness and small cubes (for hydrogen evolution experiments) with pass-through holes to resemble the induced porosity in real implants have been machined. Discs with a diameter of 29 mm and a thickness of 2 mm (Figure 5.1.2a) and 2 mm thick plates (60 mm long and 25 mm wide, Figure 5.1.2b) were manufactured from the bars. The discs and the plates were then grounded either using 40 grit silicon carbide papers to obtain a rough surface and up to 4000 grit silicon carbide papers to obtain a smooth surface. In the following, we will refer to the former group as "grounded", while to the latter as "polished". Both the typologies of samples were cleaned with acetone and ethanol for five minutes in ultrasonic bath and then coated with a 40 nm TiO_2 layer using sputtering and ALD, respectively.

The induced porosity of real implants has instead been resembled by manufacturing cubic samples of side 10 mm with six rows and six columns of equally spaced pass-through holes (φ = 1 mm) on each side (Figure 5.1.2c) obtained by means of a CNC milling machine.

a) b) c)

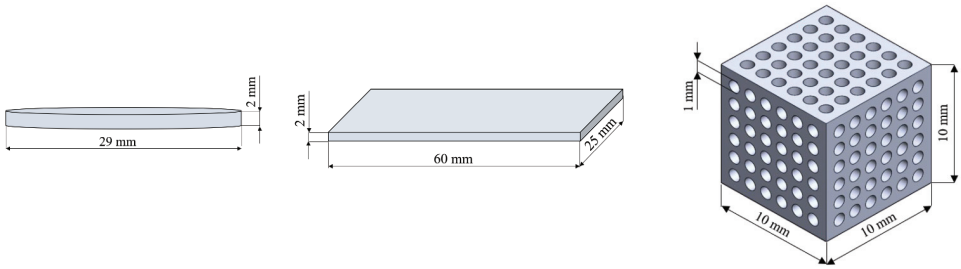

Figure 5.1.2: Representation of the discs (a), plates (b) and 3D structures (c) used in the hydrogen evolution experiments

5.1.2.2. Sputtering

Thin film of TiO_2 is deposited using an AJA ATC-2200V magnetron sputtering tool (AJA International Inc, MA, USA). The source used is 99.99% pure 2″ TiO_2 target. The sputtering chamber is pumped down to base pressure below 2e-7 torr. Deposition is carried out with RF power of 63W, at a pressure of 3mtorr with an Argon gas flow rate of 63 sccm. Initial depositions are conducted to determine the deposition rate, which is found to be 0.21nm/min.

5.1.2.3. ALD

The ALD growth of TiO_2 thin film was conducted on Savannah S200 system (Ultratech/Cambridge NanoTech, MA, USA), operating on thermal mode at reactor temperature of 160˚C. The metal organic precursor used was Tetrakis (dimethyl amido) titanium (IV) or TDMA-Ti, supplied by Sigma-Aldrich (Merck Life Sciences AS, Norway), heated at 75˚C and with deionized water as an oxidizer. Nitrogen was flown as a carrier gas at a constant flow rate of 20 sccm. The oxidant and precursor were pulsed in the following sequence, Water pulse 0.015 s, purge 5 sec, TDMA-Ti precursor pulse 0.1 s and purge 5 s. SiO_2 witness wafers were also coated to determine the growth rate using a spectroscopic ellipsometry (Woollam M2000, J.A. Woollam, NE, USA). The growth rate was found to be 0.5 A˚/cycle.

5.1.2.4. Surface characterization

The roughness values of bare polished and grounded discs were measured using a Dektak 150 Profilometer (Veeco, AZ, USA). A linear scan was conducted in a hills and value mode. For calculating the Roughness average (R_a), an assessment length of 300µm was defined, where an arithmetic average deviation from the mean line is calculated. Measurements were carried out on multiple points in the sample and an average value was calculated.
In addition, the surface integrity (amount and length of cracks) of sputtered and ALD polished and grounded coated discs was analyzed using FEI Quanta 450 Scanning electron Microscope (Thermo Fisher Scientific Inc., USA) with an acceleration voltage

of 10 kV at a working distance of about 10 mm. Three samples for each condition, respectively, were assessed for reproducibility.
Finally, X-ray photoluminescence (XPS) measurements were conducted to evaluate the chemical composition of the sputter and ALD coated samples. In addition, the chemical composition of the polished samples coated by ALD and sputter, respectively, after 24 hours of immersion in SBF was also assessed. Kratos Analytical XPS Microprobe (Kratos Analytical Ltd, Manchester, UK) which uses Al (Kα) radiation of 1486 eV in a vacuum environment of $5*10^{-9}$ Torr was used. CasaXPS software was used to analyze the XPS data.

5.1.2.5. Potentiodynamic polarization curves

Discs with a diameter of 29 mm and a thickness of 2 mm were manufactured as reported in Section 5.1.2.1. Potentiodynamic polarization tests were carried out on a Gamry Interface1000 potentiostat (Gamry Instruments, PA, USA) in order to compare the effectiveness of sputtered and ALD coatings in improving the corrosion resistance with different surface roughness. Bare samples were also tested as reference. The electrochemical tests used three-electrode equipment with the bare or coated samples as a working electrode, a Hg/Hg_2SO_4 electrode as a reference electrode, and a platinum plate electrode as a counter electrode. The samples were immersed in SBF solution (composition reported in Table 5.1.1). The temperature was set to 37±1°C to reproduce human body conditions. The potentiodynamic polarization curves were obtained applying a potential from ±1 V with respect to the open circuit potential (OCP), obtained after a stabilization period of 30 min. The scan rate of the potentiodynamic polarization test was 0.5 mV/s. The area of the samples exposed to SBF was 1 cm^2 disregarding the surface roughness and the corrosion potential and corrosion current density was determined using the Tafel extrapolation method, according to the ASTM G5-14 standard [49]. The tests were repeated three times for each surface roughness.

Reagents	Amount
NaCl	8.035 g
$NaHCO_3$	0.355 g
KCl	0.225 g
$K_2HPO_4 \cdot 3H_2O$	0.231 g
$MgCl_2 \cdot 6H_2O$	0.311 g
1.0_M-HCl	39 ml
$CaCl_2$	0.292 g
Na_2SO_4	0.072 g
Tris	6.118 g

Table 5.1.1: Reagents and their quantities for preparation of 1000 ml of the SBF solution according to [50].

5.1.2.6. Hydrogen evolution experiments

The corrosion of one mole Mg leads to the evolution of one mole of hydrogen gas which allows the measurement of Mg's corrosion rate through the collection of

evolving hydrogen bubbles. Hence, hydrogen evolution tests were used to compare the protection of sputter- and ALD- coated samples considering two different surface conditions each. To do so, the commercially available bars were manufactured into 2 mm thick plates (60 mm long and 25 mm wide) as described in Section 5.1.2.1. The samples were then immersed individually in SBF at 37 °C for 72 hours and the hydrogen bubbles were collected into a burette from each sample (Figure 5.1.3), as suggested in Ref. [51]. Bare "grounded" and "polished" samples were also tested as reference, respectively.

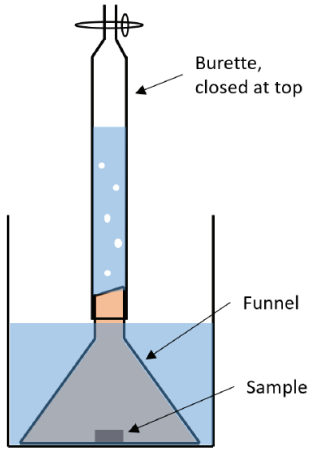

Figure 5.1.3: Schematic illustration of the set-up for measurement of the volume of hydrogen evolved.

In addition, hydrogen evolution tests were carried out on the cubic samples described in Section 5.1.2.1. These samples were used to compare the performances of sputter and ALD in the case of 3D structures that resemble the induced porosity in real implants. Bare samples were also tested as reference.

5.1.2.7. Degradation behavior

Bare and coated cylindrical and cubic samples, prepared as described in Section 5.1.2.5. and Section 5.1.2.1., respectively, were soaked for one day in SBF at 37 °C to carry out macro- and micro-morphological characterizations before and after corrosion. All samples were ultrasonically cleaned for 5 minutes in acetone and ethanol, dried in the air, and then observed by means of Canon EOS 4000D (Canon, Tokyo, Japan) and FEI Quanta 450 Scanning Electron Microscope (Thermo Fisher Scientific Inc., USA) for macro- and micro-morphological characterizations, respectively. In addition, 3D samples after corrosion have been sliced to show the corroded aspect of the undercuts for bare, sputter coated and ALD coated samples.

5.1.3. Results

5.1.3.1. Surface characterization

5.1.3.1.1. Surface integrity

The presence of cracks on ALD and sputter polished and grounded discs have been assessed by means of SEM analyses and the representative images have been reported in Figure 5.1.4. In addition, the average length and numerosity are reported in Table 5.1.2.

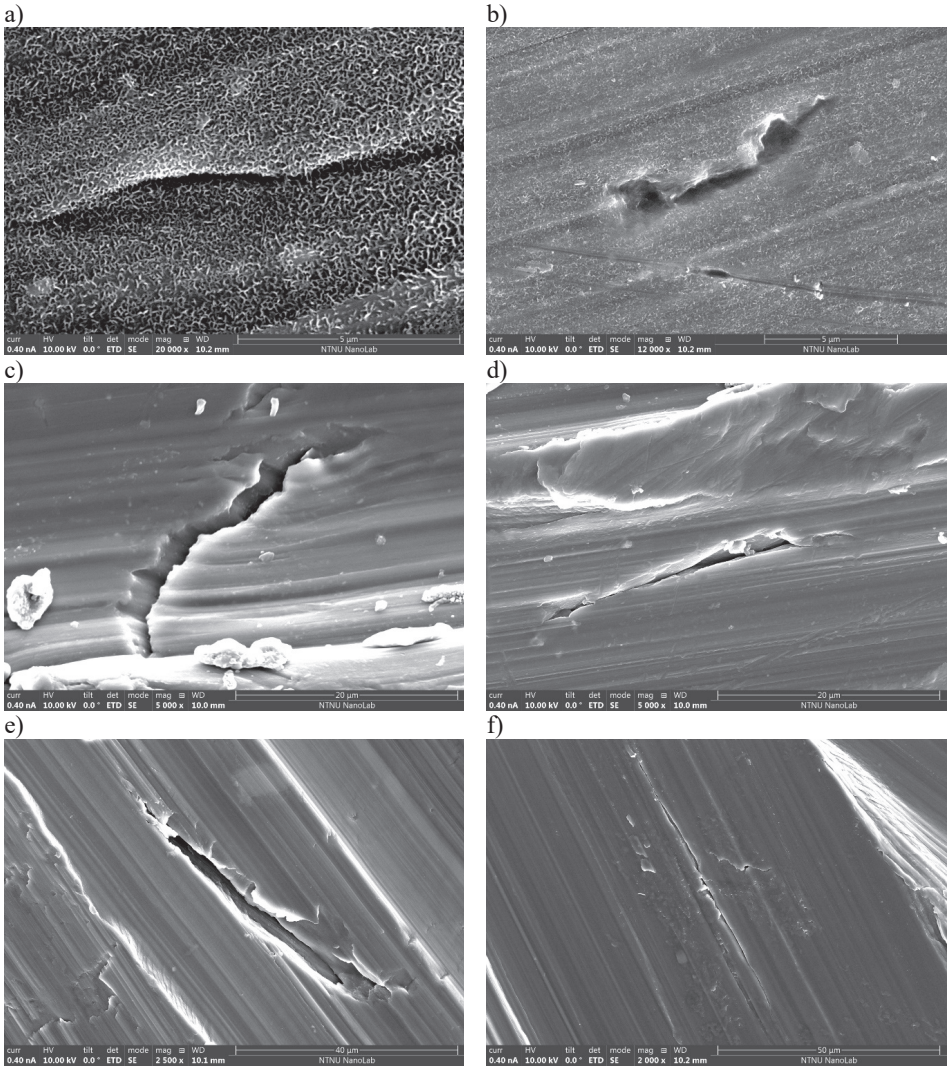

Figure 5.1.4: SEM images of representative cracks formed on polished sputter (a and b), grounded ALD (c and d) and grounded sputter (e and f) discs. On polished ALD samples no cracks were observed. Being the size of cracks different for each condition, the scale bars differ from picture to picture

	Polished ALD	Polished sputter	Grounded ALD	Grounded sputter
Crack length (µm)	-	8.04 ± 2.48	23.59 ± 3.96	58.12 ± 7.25
Density (n° cracks/cm^2)	-	1.21 ± 0.37	3.18 ± 0.62	5.3 ± 0.78

Table 5.1.2: Average crack length and density (meant as number of cracks per square centimetre) of the cracks detected for the different conditions. On polished ALD samples no cracks were observed

ALD polished discs are not shown since no cracks were observed, while cracks were observed for all the other conditions. It can be noted that the number of cracks (crack density in Table 5.1.2) and the length of the cracks increased moving from polished to grounded samples. In addition, under the same conditions, sputter coated samples are shown to be characterized by more and longer cracks.

5.1.3.1.2. Roughness evaluation

The average surface roughness of the polished bare samples was 118.6 ± 5.1 nm, while that of the grounded bare samples was 4794.3 ± 49.4 nm.

5.1.3.1.3. XPS

5.1.3.1.3.1. XPS before corrosion

XPS was conducted to determine the chemical composition of the ALD and sputter deposited TiO_2. The measurements were carried out on thin films deposited on Si wafer. To start with, etching was conducted on the surface to remove the effect of environmental contamination and surface oxidation. Surface was etched for 180 seconds with an ion beam energy of 2 KeV. Regional scans for the elements, titanium, O and C were carried out at high resolution. Negligible amounts of C were observed in the regional scan, thus indicating an ideal deposition without any process contamination. Figure 5.1.5a and Figure 5.1.5c are regional scans of titanium deposited using ALD and Sputter deposition techniques, respectively. The peaks are found to be very similar in both the deposition techniques. Peaks corresponding to the core level binding energies, 459 eV and 464 eV of Ti $2p_{3/2}$ and Ti $2p_{1/2}$ are observed, which is due to Ti^{4+} oxidation state in TiO_2 [52]. The shoulder at lower energy around 456 eV is due to the presence of Ti^{3+} caused by the argon etching step [53]. Figure 5.1.5b and Figure 5.1.5d are regional scans of the oxygen peak in ALD coated and sputter coated samples, respectively. The peak at 531 eV is due to oxygen atoms in TiO_2 phase [54], while the small shoulder at higher energy is due to O in -OH groups present in the form of impurities.

Stoichiometric TiO_2 thin films should have Ti and oxygen in 1:2 ratio i.e. 66.7% O and 33.3% Ti, but in our case, we have found the composition to be around 60% for O and 40% Ti indicating an O deficient deposition in both cases.

Deposition Mode	O 1s	Ti 2p
ALD	60%	40%
Sputtering	61%	39%

Table 5.1.3: Chemical composition of ALD and Sputter deposited TiO_2

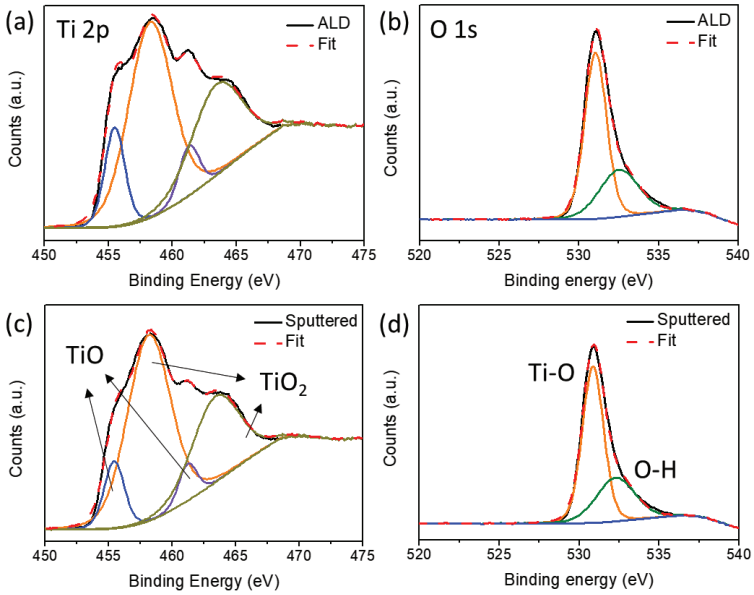

Figure 5.1.5: XPS spectra for ALD deposited TiO_2 (a) Ti 2p (b) O 1s and Sputter deposited TiO_2 (c) Ti 2p (d) O 1s

5.1.3.1.3.2. XPS after corrosion

The chemical composition of sputter and ALD coated polished discs after 24 h of corrosion in SBF (Figure 5.1.6) was evaluated using XPS and reported in Table 5.1.4. In this case, the main interest was on the amount of chemical elements, and thus the binding energies were not assessed. Etching was conducted on the surface to remove the effect of environmental contamination and surface oxidation. The surface was etched for 180 seconds with an ion beam energy of 2 KeV. Regional scans for Mg, Ti and O were carried out at high resolution. In addition, Ca and P have also been assessed since Mg and its alloys are reported to form Mg (Ca) phosphates [55].

a) b)

Figure 5.1.6: Images of ALD (a) and sputter (b) coated polished samples after 24 hours of immersion in SBF

Element	Concentration (%) before corrosion		Concentration (%) after corrosion	
	ALD	Sputter	ALD	Sputter
Mg	9	11	9	8
Ti	21	22	3	11
O	69	66	73	69
Ca	1	1	6	7
P	0	0	9	5

Table 5.1.4: Chemical composition of ALD and sputter polished discs before and after 24 h of immersion in SBF

5.1.3.2. Potentiodynamic polarization tests

The potentiodynamic polarization curves of the AZ31 cylindrical "grounded" and "polished" samples plotted on a semi-logarithmic scale are shown in Figures 5.17 and 5.1.8, respectively. Bare, sputter coated and ALD coated curves are reported in black, blue and red lines, respectively. The related kinetic and thermodynamic corrosion electrochemical characteristics are reported in Tables 5.1.5 and 5.1.6.

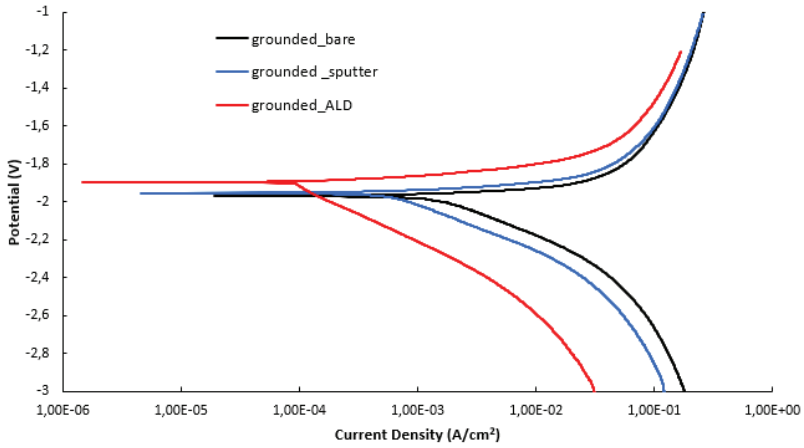

Figure 5.1.7: Potentiodynamic polarization curves of grounded samples.

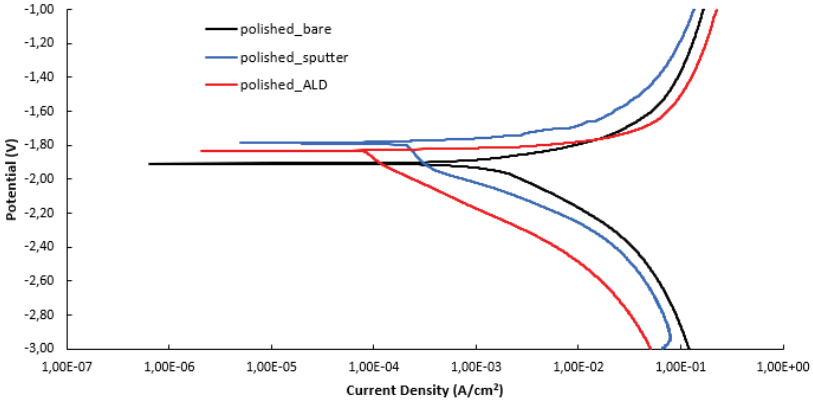

Figure 5.1.8: Potentiodynamic polarization curves of polished samples.

	Ecorr (V)	icorr (μA/cm^2)
Bare	-1.97 ± 0.025	1500 ± 40
Sputter coated	-1.95 ± 0.035	600 ± 10
ALD coated	-1.90 ± 0.015	102 ± 4

Table 5.1.5: Electrochemical corrosion data extrapolated from Figure 5.1.7.

	Ecorr (V)	icorr (μA/cm^2)
Bare	-1.91 ± 0.02	1400 ± 25
Sputter coated	-1.79 ± 0.033	220 ± 15
ALD coated	-1.83 ± 0.016	84 ± 6

Table 5.1.6: Electrochemical corrosion data extrapolated from Figure 5.1.8.

Considering both grounded and polished samples, the presence of TiO_2 coatings led to an improvement in corrosion resistance, namely an ennoblement of corrosion potential E_{corr} and a reduction of corrosion current density i_{corr} of more than one order of magnitude. It is worth noting that the corrosion current density is directly related to the corrosion rate by the Faraday's law, which expresses the material loss of the implant during its permanence into the human body. This implies that the application of coatings leads to a reduced corrosion rate. ALD coatings are shown to be more effective in the protection from corrosion, especially when a high surface roughness is considered.

5.1.3.3. Hydrogen evolution tests

The hydrogen evolution of grounded and polished plates is reported in Figures 5.1.9 and 5.1.10, respectively. Bare, sputter coated and ALD coated hydrogen evolution are reported in black, blue and red lines, respectively.

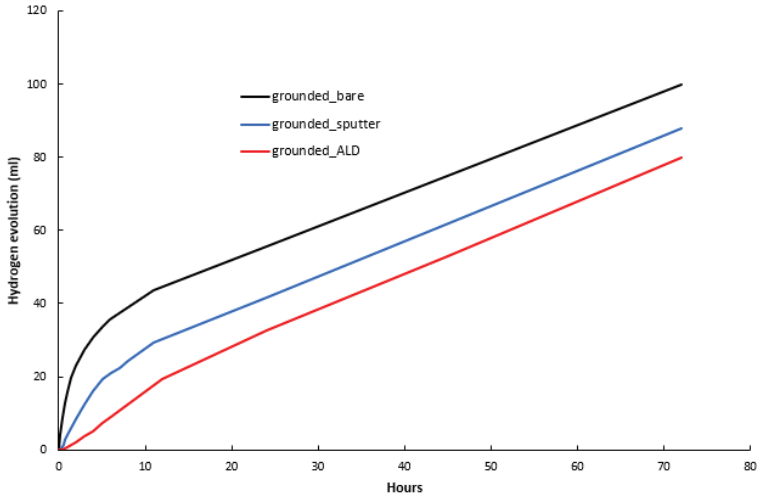

Figure 5.1.9: Hydrogen evolution of grounded samples

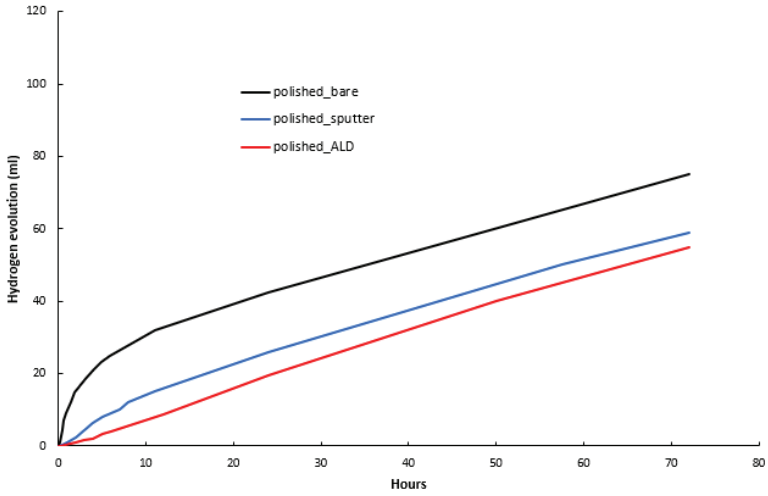

Figure 5.1.10: Hydrogen evolution of polished samples

The results of the hydrogen evolution tests are in line with the potentiodynamic polarization curves, i.e. the application of the coating decelerates the corrosion process, irrespective of the considered surface roughness. In addition, the difference in the efficiency of the sputter and ALD coatings is more visible in the grounded samples, again in agreement with the potentiodynamic polarization curves.
The better performances of ALD compared to sputtering in reducing corrosion is further confirmed by the hydrogen evolution tests carried out on 3D structures reported in Figure 5.1.11.

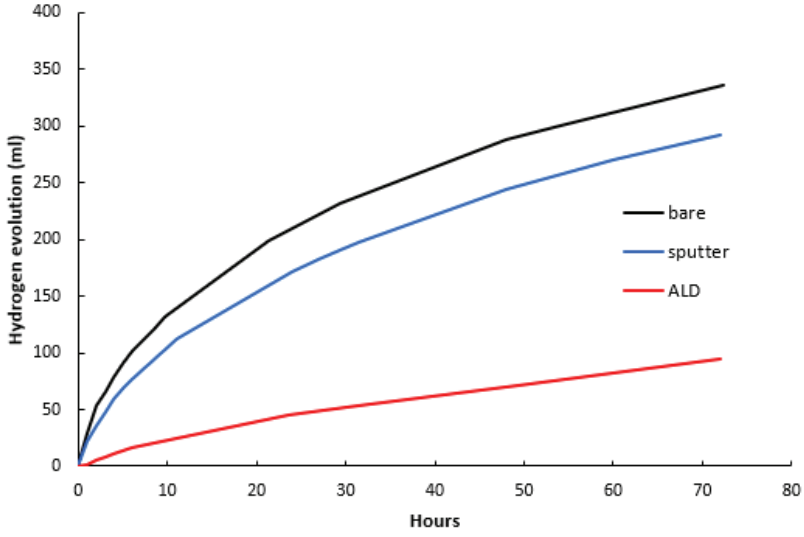

Figure 5.1.11: Hydrogen evolution of the 3D structures reported in Figure 5.1.2

5.1.3.4. Degradation behavior

5.1.3.4.1. Cylindrical samples

Figures 5.1.12 and 5.1.13 display the macro-morphologies of sputter and ALD coated cylindrical samples before and after one day of corrosion in SBF for polished and grounded samples, respectively. The bare AZ31 polished and grounded samples were taken as control.

	Bare	Sputter	ALD
Before corrosion		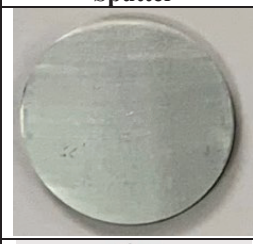	
After corrosion			

Figure 5.1.12: Macro-morphologies of polished bare, sputter and ALD TiO_2 coated samples before and after corrosion

	Bare	Sputter	ALD
Before corrosion	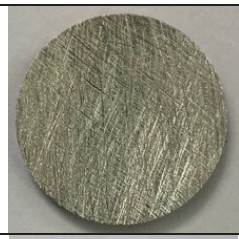	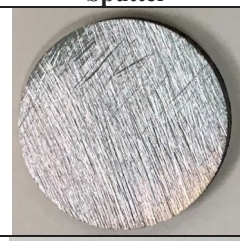	
After corrosion			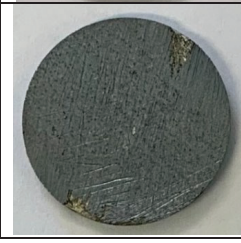

Figure 5.1.13: Macro-morphologies of grounded bare, sputter and ALD TiO_2 coated samples before and after corrosion

From the macro-morphologies it can be clearly seen that the degree of corrosion damage decreased with the application of coatings for both polished and grounded samples. In particular, the protectiveness of the ALD coating is shown to be higher since most of the TiO_2 coating is still present both in the polished and grounded samples, whereas several spots exposing the Mg substrate are visible on the sputter coated samples, particularly regarding the grounded specimen. The higher protectiveness of the ALD coating are further confirmed by the micro-morphologies after corrosion of polished and grounded cylindrical samples, gathered in Figures 5.1.14 and 5.1.15, respectively.

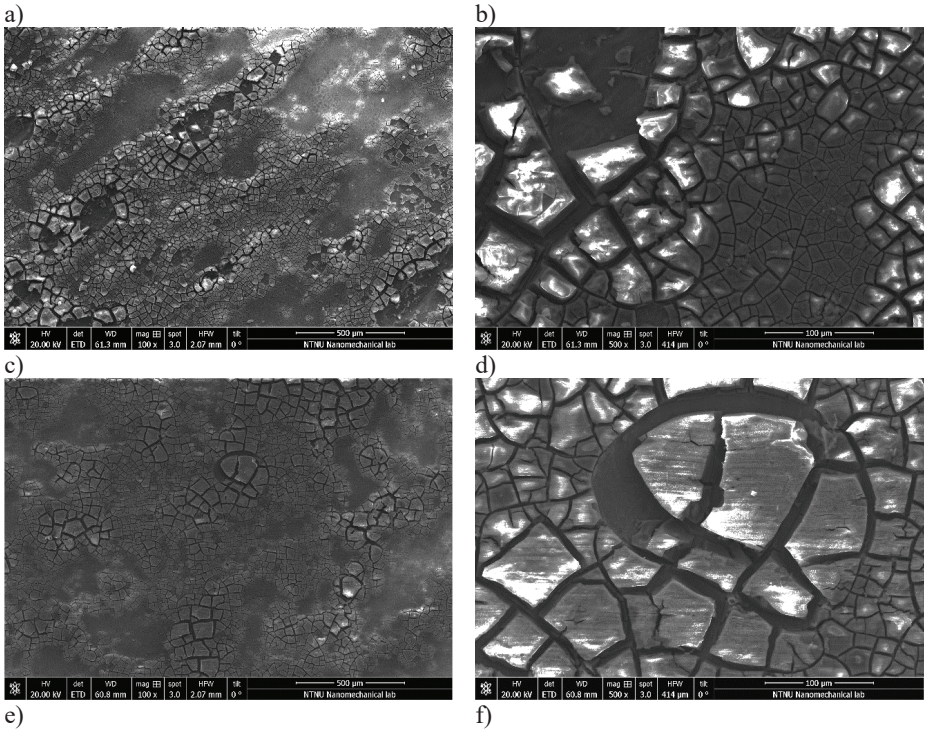

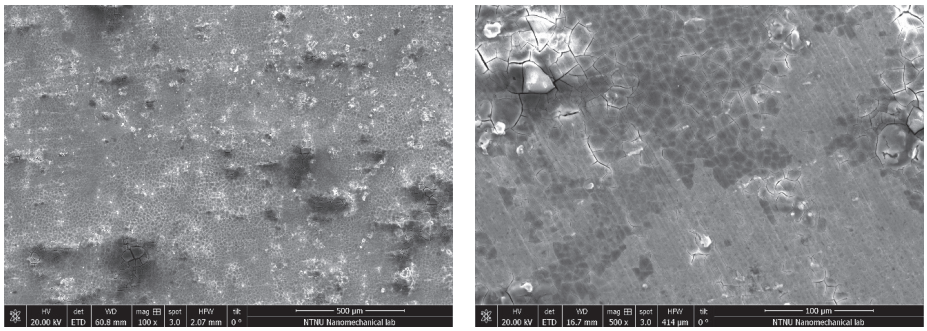

Figure 5.1.14: Micro-morphologies of bare (a and b), sputter (c and d) and ALD (e and f) coated cylindrical polished samples after corrosion

a) b)

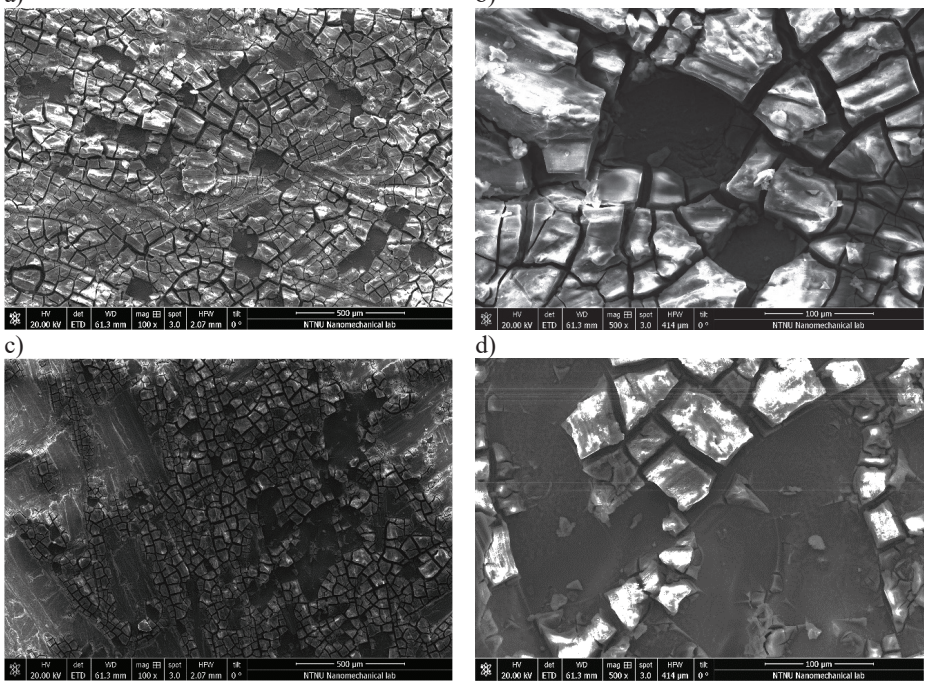

c) d)

e) f)

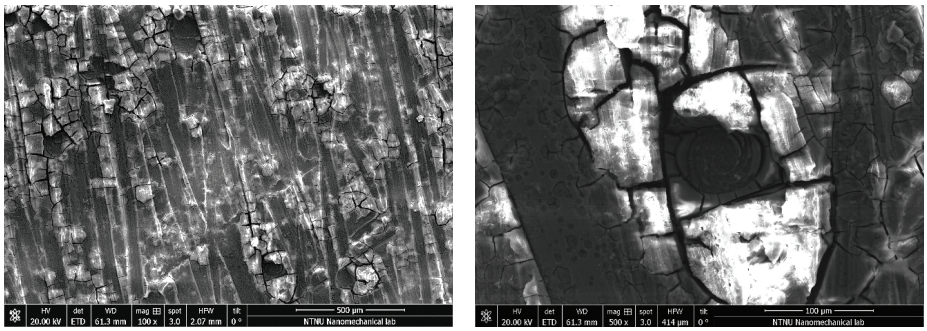

Figure 5.1.15: Micro-morphologies of bare (a and b), sputter (c and d) and ALD (e and f) coated cylindrical grounded samples after corrosion

In the micro-morphologies of ALD coated samples, wider un-corroded areas are visible compared to sputter coated and especially bare samples. This is even more evident when polished samples are considered. For all the samples, the corroded areas have numerous cracks dividing the surface into a network structure, where the delamination and the flaking off of the protective film can be observed.

5.1.3.4.2. 3D samples

The macro-morphologies of 3D bare, sputter coated and ALD coated samples before and after one day of corrosion in SBF are reported in Figure 5.1.16.

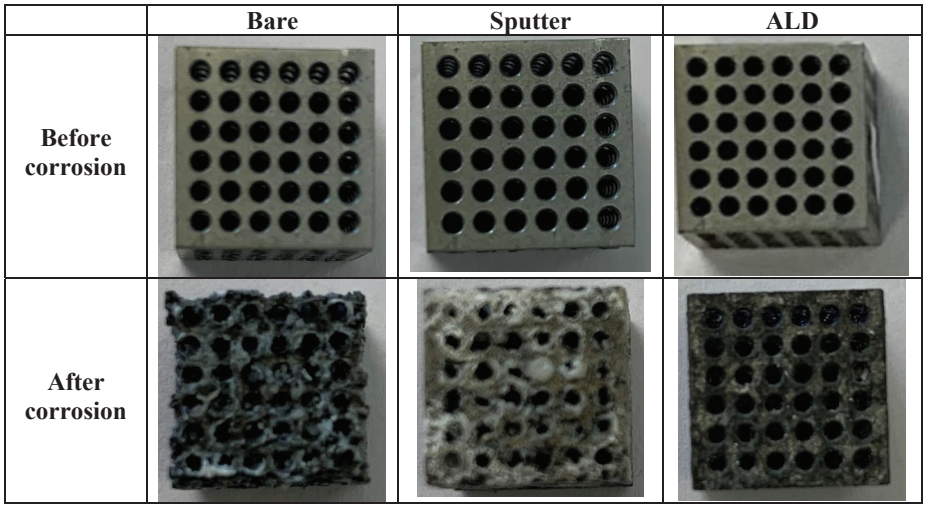

Figure 5.1.16: Macro-morphologies of polished bare, sputter and ALD TiO_2 coated samples before and after corrosion

The bare samples are highly corroded, rendering it difficult to recognize the original shape. A reduction in corrosion is obtained by the application of coatings, particularly in

the case of ALD coated samples. This is confirmed by the micro-morphologies of the corroded samples (Figure 5.1.17). In fact, while for bare samples the structure is fully covered by corrosion products (Figure 5.1.17a) and the original structure can be barely detected in some locations (in particular within the holes that are obstructed by the corrosion products (Figure 5.1.17b)), the sputter coated samples are characterized by a lower amount of corrosion products (Figure 5.1.17c) and the original structure can still be recognized retaining visible un-corroded areas (Figure 5.1.17d). An even lower corrosion is detected in the ALD coated samples (Figures 5.1.17e and 5.1.17f).

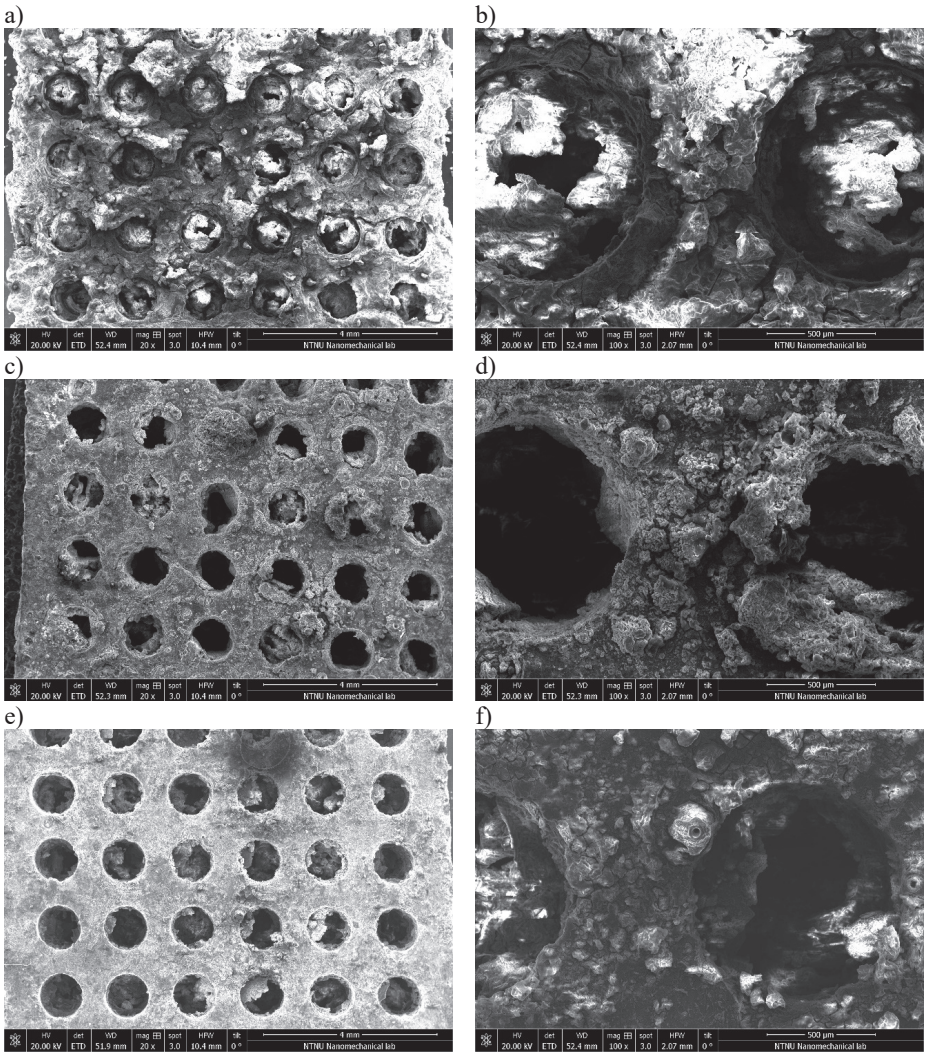

Figure 5.1.17: Micro-morphologies of bare (a and b), sputter (c and d) and ALD (e and f) coated 3D samples after corrosion

However, the improvement in corrosion resistance of sputter coated samples with respect to bare samples is not obvious when looking at the micro-morphology of the corroded sample's sliced cross-section (Figure 5.1.18). The micro-morphologies of the corroded sputter 3D samples (Figure 5.1.18b) are comparable to those of the bare counterparts (Figure 5.1.18a). In ALD samples (Figure 5.1.18c), in contrast, the corrosion seems consistently lower, which we attribute to the nature of the coating process providing effective barriers also within a given 3D aspect, independent from its topological and surface complexity.

a)

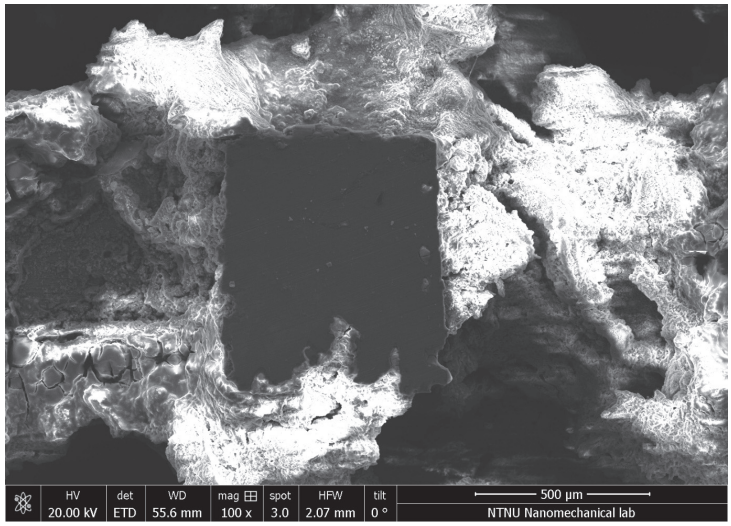

b)

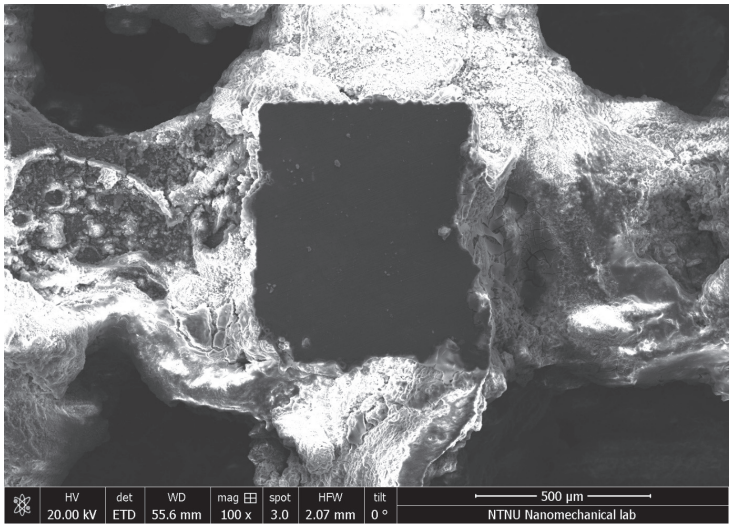

c)

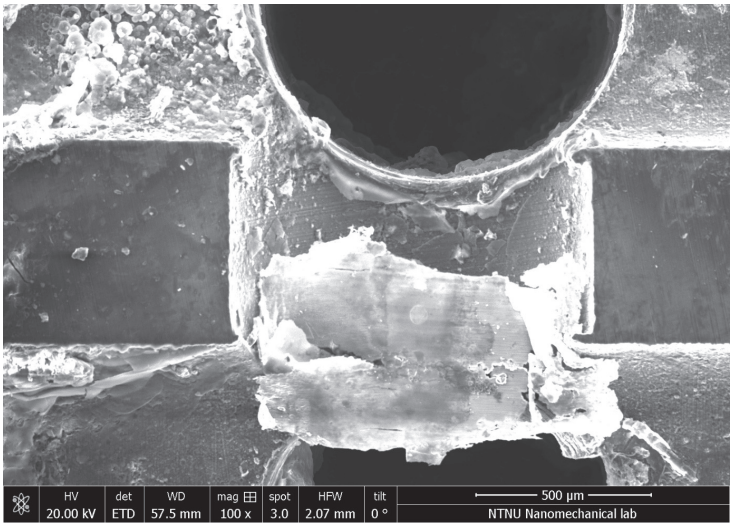

Figure 5.1.18: Micro-morphology of the bare (a), sputter coated (b) and ALD coated (c) corroded sample's sliced cross-section

5.1.4. Discussions

The corrosion performances of ALD and sputter coating techniques were herein assessed on different surface roughness and on an induced porosity that resemble a designed porosity of an implant surface [47,48]. Porosity has in fact been shown to assist the ingrowth of cell [56,57]. To do so, potentiodynamic polarization curves and hydrogen evolution tests have been carried out. Although both sputter and ALD TiO_2 40 nm coatings are shown to improve the corrosion resistance, the performance of ALD and sputter coatings differ, where deviations increase with surface and topological complexity (roughness and porosity). Whereas the corrosion current density (i_{corr}) of ALD coated polished samples differs by a factor of three compared to sputter coated counterparts, the i_{corr} is six times lower on ALD coated grounded samples. These results are corroborated by hydrogen evolution experiments. After 72 hours of exposure to SBF, the amount of evolved hydrogen from polished samples coated with ALD is 6.8% lower than on sputter coated samples, while the difference is as high as 10% on grounded samples.

The reduced effectiveness of sputtered coatings on rough surfaces is in agreement with the results of Munemasa and Kumakiri [58]. They reported that the corrosion protection of sputter coated carbon steel decreases with the increase in substrate roughness. They related this effect to an increased amount of uncovered surface area in the case of rougher substrates. Sputter is a line-of-sight technique and this represents a limitation when seeking complete surface coverage of areas that are shadowed by surface features of a rough substrate. This limitation becomes particularly problematic on 3D aspects, such as cell scaffolds than naturally have to comprise a 3D topology to provide anchoring points and topological cues for cells [59,60]. In an attempt to mimic such a

scenario, we performed hydrogen evolution experiments on simple 3D porous structures. Here, several macroscopic undercuts and shadowed areas are present. The ALD coating performs significantly better in such a scenario; the respective specimens are characterized by a 68% reduced hydrogen evolution compared to sputter coated counterparts. Regarding the micro-morphologies of the undercuts and shadowed areas of the sliced 3D structures reported in Figure 5.1.18, it can be seen that the sputter coated samples (Figure 5.1.18b) possesses a morphology similar to bare samples (Figure 5.1.18a), indicating that these areas have not or only barely been covered in the first place. ALD, instead, is a conformal process, and thus it is able to coat the inner areas as shown by the micro-morphologies of the sliced 3D samples (Figure 5.1.18c) leading to significant effects in the structure's appearance after its exposure to SBF.

However, the better performance of ALD compared to sputter coatings cannot be ascribed to the line-of-sight limitation only, but also to defects in the coating. It is clear that defects such as cracks and pores provide access for the media to attack the underlying substrate thereby reducing the coating's effectiveness. If the coatings deposited were perfectly conformal, dense and defect-free, their corrosion rate would ideally match the literature reported values for pure TiO_2 in SBF. However, the corrosion rate of the sputter and ALD coated samples (measured by means of the Faraday's law [61] after normalization by the surface area) differs significantly from that of pure TiO_2 ($0.37 \cdot 10^{-6}$ mm/year) [62]. In fact, polished samples (characterized by a Sdr[1] of 0.06) have corrosion rates $1.8 \cdot 10^{-3}$ and $6.8 \cdot 10^{-4}$ mm/year for sputter and ALD coated samples, respectively, while grounded samples (characterized by a Sdr of 0.1), yield $4.7 \cdot 10^{-3}$ and $8.1 \cdot 10^{-4}$ mm/year, respectively. The higher difference reported between the corrosion rate of sputter coated AZ31 samples and that of pure TiO_2 compared to that for ALD coated indicates a higher amount of defect in the sputter TiO_2 coating, as confirmed by the surface integrity assessments reported in Figure 5.1.4 and Table 5.1.2. In particular, the higher amount of cracks shown for grounded samples further increases the difference in corrosion rate from pure and defect-free TiO_2.

These cracks usually form as a consequence of the induced residual stresses on the coating due to the difference in the thermal expansion coefficient between the coating and the substrate [63,64]. The thermal expansion coefficient of Mg is reported to be $27 \cdot 10^{-6}$ °C^{-1} [64], while that of TiO_2 is $7 \cdot 10^{-6}$ °C^{-1} [65,66]. The higher amount of cracks in the sputter coating may be attributed to the higher process temperature during sputtering (260 °C) compared to ALD (160 °C) [67]. In addition, the higher the substrate roughness, the higher the residual stresses induced during the coating deposition [68,69] leading to a higher number and longer cracks [70], which is clearly visible on our grounded samples (Figure 5.1.4 and Table 5.1.2). Finally, such cracks are reported to reduce the adhesion strength [71]. This is confirmed by the images of ALD and sputter coated polished samples after 24 hours of immersion in SBF (Figure 5.1.6). The ALD samples are characterized by a more uniform corrosion mode, indicative of a stronger film adhesion. This is also shown by the corresponding XPS measurements. ALD films have a lower concentration of titanium after corrosion (3%, as compared to 11% in the sputter coated samples). This, in combination with the fact that the amount of Mg is unchanged in ALD samples while it decreases in sputter samples, suggests that

[1] Area roughness parameter, describes the additional area provided by texture with respect to the planar area [72]

after 24 hours of immersion, the Mg substrate coated by ALD, has barely been affected with the SBF having mainly attacked the TiO_2 layer. Contrarily, in the sputter coated samples, the corrosion is less uniform. A higher amount of Ti prevails after corrosion whereas Mg is reduced, indicative of an attack on the underlying substrate.
We conclude that both coatings can be considered viable for the fabrication of biodegradable implants with a prolonged durability inside the human body. However, the choice of the coating technique has to be taken based on the specific scenario. Surface integrity of the coatings and an effective barrier in undercuts and shadowed areas render ALD superior in our study, which may have an impact on the choice of coating techniques for Mg based biomedical implants.

5.1.5. Conclusions

In this work, we aimed to provide new insight into the corrosion performances of ALD coated AZ31 Mg alloy and provide a comparison in corrosion protection performances of ALD and sputtered biocompatible TiO_2 coatings. We compared different surface roughness and topologies in order to resemble the topology and the appearance of an implant designed for cell adhesion and ingrowth. An AZ31 alloy has been machined into samples with two different roughness and into small cubes with pass-through holes to resemble an induced porosity. All these different geometries have been coated with a 40 nm layer of TiO_2 obtained by means of sputter and ALD and their corrosion properties have been evaluated by means of potentiodynamic polarization curves tests and hydrogen evolution experiments. In addition, a characterization of the surface integrity prior to testing and of the chemical composition before and after testing have been carried out.
The main findings can be summarized as follows:

- The ALD technique has been shown to provide the better corrosion protection both for smooth and rough surfaces. Dealing with the former, the corrosion current density of bare samples has been reduced from 1400 $\mu A/cm^2$ to 220 $\mu A/cm^2$ and 84 $\mu A/cm^2$ using sputtering and ALD, respectively, while for rough samples, the corrosion current density of the bare material was reduced from 1500 $\mu A/cm^2$ to 600 $\mu A/cm^2$ and 102 $\mu A/cm^2$ using sputtering and ALD, respectively.
- A similar trend was obtained in hydrogen evolution tests. The hydrogen evolved from bare polished samples was reduced by 21% and 27% with sputter and ALD, respectively. Dealing with rough samples, the hydrogen evolved from the bare material was instead reduced by 12% and 20% considering sputter and ALD, respectively.
- The line-of-sight limitation of sputtering is particularly evident in the case of 3D porous structures, where the hydrogen evolved from the bare samples are reduced only by 13% when sputtered coatings are considered, while ALD coatings lead to a reduction of 72%.
- The improved corrosion performances of ALD compared to sputtering is not only due to the line-of-sight limitation, but also to the increased surface integrity of the former. In fact, under the same conditions, sputter coatings are characterized by more and longer cracks. No difference in the chemical

composition of the coating prior to corrosion was found, while the amount of Ti and Mg differs after 24 hours of corrosion, indicating a more uniform corrosion of the ALD samples, as confirmed also by the pictures of the samples.

It can be concluded that both sputtering and ALD are effective methods to increase the corrosion resistance of AZ31 alloy, but ALD has been shown to provide the best corrosion performances regardless the surface conditions (roughness and topology). Therefore, it can be considered a viable pathway for the fabrication of biodegradable implants with a prolonged durability inside the human body.

Acknowledgement

Abdulla Bin Afif was supported by NTNU's Enabling technologies: Nanotechnology. The Research Council of Norway is acknowledged for the support to the Norwegian Micro- and Nano-Fabrication Facility, NorFab, project number 245963/F50. Anup Dadlani was funded by the Norwegian Research Council under project number 274459 Translate.

Bibliography Paper IV

[1] M.P. Ginebra, T. Traykova, J.A. Planell, Calcium phosphate cements as bone drug delivery systems: A review, J. Control. Release. 113 (2006) 102–110. https://doi.org/10.1016/j.jconrel.2006.04.007.

[2] http://share.iofbonehealth.org/EU-6-Material/Reports/IOF%20Report_EU.pdf, (n.d.). http://share.iofbonehealth.org/EU-6-Material/Reports/IOF Report_EU.pdf (accessed November 20, 2019).

[3] T. Hanawa, Overview of metals and applications, in: Met. Biomed. Devices, Elsevier, 2010: pp. 3–24. https://doi.org/10.1533/9781845699246.1.3.

[4] T. Albrektsson, P.-I. Brånemark, H.-A. Hansson, J. Lindström, Osseointegrated Titanium Implants: *Requirements for Ensuring a Long-Lasting, Direct Bone-to-Implant Anchorage in Man*, Acta Orthop. Scand. 52 (1981) 155–170. https://doi.org/10.3109/17453678108991776.

[5] F. Rossi, N.P. Lang, E. De Santis, F. Morelli, G. Favero, D. Botticelli, Bone-healing pattern at the surface of titanium implants: an experimental study in the dog, Clin. Oral Implants Res. 25 (2014) 124–131. https://doi.org/10.1111/clr.12097.

[6] Q. Chen, G.A. Thouas, Metallic implant biomaterials, Mater. Sci. Eng. R Reports. 87 (2015) 1–57. https://doi.org/10.1016/J.MSER.2014.10.001.

[7] T.W. Bauer, J. Schils, The pathology of total joint arthroplasty.II. Mechanisms of implant failure., Skeletal Radiol. 28 (1999) 483–97. http://www.ncbi.nlm.nih.gov/pubmed/10525792 (accessed March 31, 2017).

[8] A.R. Dujovne, J.D. Bobyn, J.J. Krygier, J.E. Miller, C.E. Brooks, Mechanical compatibility of noncemented hip prostheses with the human femur, J. Arthroplasty. 8 (1993) 7–22. https://doi.org/10.1016/S0883-5403(06)80102-6.

[9] C.A. Engh, J.D. Bobyn, The influence of stem size and extent of porous coating on femoral bone resorption after primary cementless hip arthroplasty., Clin. Orthop. Relat. Res. (1988) 7–28. http://www.ncbi.nlm.nih.gov/pubmed/3370887 (accessed March 31, 2017).

[10] J. Kerner, R. Huiskes, G.H. van Lenthe, H. Weinans, B. van Rietbergen, C.A. Engh, A.A. Amis, Correlation between pre-operative periprosthetic bone density and post-operative bone loss in THA can be explained by strain-adaptive remodelling., J. Biomech. 32 (1999) 695–703. https://doi.org/10.1016/S0021-9290(99)00041-X.
[11] D.R. Sumner, J.O. Galante, Determinants of stress shielding: design versus materials versus interface., Clin. Orthop. Relat. Res. (1992) 202–12. http://www.ncbi.nlm.nih.gov/pubmed/1729005 (accessed March 31, 2017).
[12] T.M. Turner, D.R. Sumner, R.M. Urban, R. Igloria, J.O. Galante, Maintenance of proximal cortical bone with use of a less stiff femoral component in hemiarthroplasty of the hip without cement. An investigation in a canine model at six months and two years., J. Bone Joint Surg. Am. 79 (1997) 1381–90. http://www.ncbi.nlm.nih.gov/pubmed/9314401 (accessed March 31, 2017).
[13] B. Van Rietbergen, R. Huiskes, H. Weinans, D.R. Sumner, T.M. Turner, J.O. Galante, The mechanism of bone remodeling and resorption around press-fitted THA stems, J. Biomech. 26 (1993) 369–382. https://doi.org/10.1016/0021-9290(93)90001-U.
[14] J. Wolff, The Law of Bone Remodelling, Springer Berlin Heidelberg, Berlin, Heidelberg, 1986. https://doi.org/10.1007/978-3-642-71031-5.
[15] B.G. Pound, Corrosion behavior of metallic materials in biomedical applications . I . Ti and its alloys, 32 (2014) 1–20. https://doi.org/10.1515/corrrev-2014-0007.
[16] B.G. Pound, Corrosion behavior of metallic materials in biomedical applications . II . Stainless steels and Co-Cr alloys, 32 (2014) 21–41. https://doi.org/10.1515/corrrev-2014-0008.
[17] J.J. Jacobs, J.L. Gilbert, R.M. Urban, Corrosion of metal orthopaedic implants., J. Bone Joint Surg. Am. 80 (1998) 268–82. http://www.ncbi.nlm.nih.gov/pubmed/9486734 (accessed March 31, 2017).
[18] J.J. Jacobs, N.J. Hallab, A.K. Skipor, R.M. Urban, Metal degradation products: a cause for concern in metal-metal bearings?, Clin. Orthop. Relat. Res. (2003) 139–47. https://doi.org/10.1097/01.blo.0000096810.78689.62.
[19] I.B. Beech, J.A. Sunner, C.R. Arciola, P. Cristiani, Microbially-influenced corrosion: damage to prostheses, delight for bacteria., Int. J. Artif. Organs. 29 (2006) 443–52. http://www.ncbi.nlm.nih.gov/pubmed/16705614 (accessed June 20, 2017).
[20] M. Peron, J. Torgersen, F. Berto, Mg and Its Alloys for Biomedical Applications: Exploring Corrosion and Its Interplay with Mechanical Failure, Metals (Basel). 7 (2017) 252. https://doi.org/10.3390/met7070252.
[21] N. Li, Y. Zheng, Novel Magnesium Alloys Developed for Biomedical Application: A Review, J. Mater. Sci. Technol. 29 (2013) 489–502. https://doi.org/10.1016/J.JMST.2013.02.005.
[22] R.K. Singh Raman, S. Jafari, S.E. Harandi, Corrosion fatigue fracture of magnesium alloys in bioimplant applications: A review, Eng. Fract. Mech. 137 (2015) 97–108. https://doi.org/10.1016/j.engfracmech.2014.08.009.
[23] M.P. Staiger, A.M. Pietak, J. Huadmai, G. Dias, Magnesium and its alloys as orthopedic biomaterials: A review, Biomaterials. 27 (2006) 1728–1734. https://doi.org/10.1016/j.biomaterials.2005.10.003.
[24] A.C. Hänzi, A.S. Sologubenko, P.J. Uggowitzer, Design strategy for new

biodegradable Mg–Y–Zn alloys for medical applications, Int. J. Mater. Res. 100 (2009) 1127–1136. https://doi.org/10.3139/146.110157.
[25] M. Fraldi, · L Esposito, G. Perrella, A. Cutolo, S.C. Cowin, L. Esposito, Topological optimization in hip prosthesis design, Biomech Model Mechanobiol. 9 (2010) 389–402. https://doi.org/10.1007/s10237-009-0183-0.
[26] L. E Murr, S. M Gaytan, E. Martinez, F.R. Medina, R.B. Wicker, Fabricating Functional Ti-Alloy Biomedical Implants by Additive Manufacturing Using Electron Beam Melting, J. Biotechnol. Biomater. 02 (2012). https://doi.org/10.4172/2155-952X.1000131.
[27] A.-F. Obaton, J. Fain, M. Djemaï, D. Meinel, F. Léonard, E. Mahé, B. Lécuelle, J.-J. Fouchet, G. Bruno, In vivo XCT bone characterization of lattice structured implants fabricated by additive manufacturing, Heliyon. 3 (2017). https://doi.org/10.1016/J.HELIYON.2017.E00374.
[28] K.D. Ralston, N. Birbilis, C.H.J. Davies, Revealing the relationship between grain size and corrosion rate of metals, Scr. Mater. 63 (2010) 1201–1204. https://doi.org/10.1016/J.SCRIPTAMAT.2010.08.035.
[29] N. Birbilis, K.D. Ralston, S. Virtanen, H.L. Fraser, C.H.J. Davies, Grain character influences on corrosion of ECAPed pure magnesium, Corros. Eng. Sci. Technol. 45 (2010) 224–230. https://doi.org/10.1179/147842209X12559428167805.
[30] B. Ratna Sunil, T.S. Sampath Kumar, U. Chakkingal, V. Nandakumar, M. Doble, V. Devi Prasad, M. Raghunath, In vitro and in vivo studies of biodegradable fine grained AZ31 magnesium alloy produced by equal channel angular pressing, Mater. Sci. Eng. C. 59 (2016) 356–367. https://doi.org/10.1016/J.MSEC.2015.10.028.
[31] F. Zhang, A. Ma, J. Jiang, H. Xu, D. Song, F. Lu, Y. Nishida, Enhanced biodegradation behavior of ultrafine-grained ZE41A magnesium alloy in Hank's solution, Prog. Nat. Sci. Mater. Int. 23 (2013) 420–424. https://doi.org/10.1016/J.PNSC.2013.06.003.
[32] E. Mostaed, A. Fabrizi, D. Dellasega, F. Bonollo, M. Vedani, Microstructure, mechanical behavior and low temperature superplasticity of ECAP processed ZM21 Mg alloy, J. Alloys Compd. 638 (2015) 267–276. https://doi.org/10.1016/J.JALLCOM.2015.03.029.
[33] R. Bertolini, S. Bruschi, A. Ghiotti, Large Strain Extrusion Machining under Cryogenic Cooling to Enhance Corrosion Resistance of Magnesium Alloys for Biomedical Applications, Procedia Manuf. 26 (2018) 217–227. https://doi.org/10.1016/J.PROMFG.2018.07.030.
[34] Z. Pu, J.C. Outeiro, A.C. Batista, O.W. Dillon, D.A. Puleo, I.S. Jawahir, Surface Integrity in Dry and Cryogenic Machining of AZ31B Mg Alloy with Varying Cutting Edge Radius Tools, Procedia Eng. 19 (2011) 282–287. https://doi.org/10.1016/J.PROENG.2011.11.113.
[35] M. Peron, R. Bertolini, A. Ghiotti, J. Torgersen, S. Bruschi, F. Berto, Enhancement of stress corrosion cracking of AZ31 magnesium alloy in simulated body fluid thanks to cryogenic machining, J. Mech. Behav. Biomed. Mater. 101 (2020) 103429. https://doi.org/10.1016/J.JMBBM.2019.103429.
[36] R. Smeets, B. Stadlinger, F. Schwarz, B. Beck-Broichsitter, O. Jung, C. Precht, F. Kloss, A. Gröbe, M. Heiland, T. Ebker, T. Ebker, Impact of Dental Implant

Surface Modifications on Osseointegration, Biomed Res. Int. 2016 (2016) 1–16. https://doi.org/10.1155/2016/6285620.
[37] T. Albrektsson, A. Wennerberg, Oral implant surfaces: Part 1--review focusing on topographic and chemical properties of different surfaces and in vivo responses to them., Int. J. Prosthodont. 17 (n.d.) 536–43. http://www.ncbi.nlm.nih.gov/pubmed/15543910 (accessed October 30, 2017).
[38] J. M.Rúa, A.A. Zuleta, J. Ramírez, P. Fernández-Morales, Micro-arc oxidation coating on porous magnesium foam and its potential biomedical applications, Surf. Coatings Technol. 360 (2019) 213–221. https://doi.org/10.1016/j.surfcoat.2018.12.106.
[39] Z. Chen, X. Mao, L. Tan, T. Friis, C. Wu, R. Crawford, Y. Xiao, Osteoimmunomodulatory properties of magnesium scaffolds coated with β-tricalcium phosphate, Biomaterials. 35 (2014) 8553–8565. https://doi.org/10.1016/j.biomaterials.2014.06.038.
[40] I.S. Abela, Physical vapour deposition on Mg alloys for biomedical applications, in: Surf. Modif. Magnes. Its Alloy. Biomed. Appl., Elsevier Inc., 2015: pp. 81–100. https://doi.org/10.1016/B978-1-78242-078-1.00004-9.
[41] W. Jin, G. Wang, X. Peng, W. Li, A.M. Qasim, P.K. Chu, Tantalum nitride films for corrosion protection of biomedical Mg-Y-RE alloy, J. Alloys Compd. 764 (2018) 947–958. https://doi.org/10.1016/J.JALLCOM.2018.06.151.
[42] W. Jin, G. Wang, A.M. Qasim, S. Mo, Q. Ruan, H. Zhou, W. Li, P.K. Chu, Corrosion protection and enhanced biocompatibility of biomedical Mg-Y-RE alloy coated with tin dioxide, Surf. Coatings Technol. 357 (2019) 78–82. https://doi.org/10.1016/j.surfcoat.2018.10.005.
[43] P. O'Brien, Chemical Vapor Deposition, in: Encycl. Mater. Sci. Technol., Elsevier, 2001: pp. 1173–1176. https://doi.org/10.1016/B0-08-043152-6/00219-9.
[44] X. Liu, Q. Yang, Z. Li, W. Yuan, Y. Zheng, Z. Cui, X. Yang, K.W.K. Yeung, S. Wu, A combined coating strategy based on atomic layer deposition for enhancement of corrosion resistance of AZ31 magnesium alloy, Appl. Surf. Sci. 434 (2018) 1101–1111. https://doi.org/10.1016/J.APSUSC.2017.11.032.
[45] E. Marin, A. Lanzutti, L. Guzman, L. Fedrizzi, Chemical and electrochemical characterization of TiO2/Al2O3 atomic layer depositions on AZ-31 magnesium alloy, J. Coatings Technol. Res. 9 (2012) 347–355. https://doi.org/10.1007/s11998-011-9372-8.
[46] Q. Yang, W. Yuan, X. Liu, Y. Zheng, Z. Cui, X. Yang, H. Pan, S. Wu, Atomic layer deposited ZrO2 nanofilm on Mg-Sr alloy for enhanced corrosion resistance and biocompatibility, Acta Biomater. 58 (2017) 515–526. https://doi.org/10.1016/J.ACTBIO.2017.06.015.
[47] J.P. Long, S.J. Hollister, S.A. Goldstein, A paradigm for the development and evaluation of novel implant topologies for bone fixation: In vivo evaluation, J. Biomech. 45 (2012) 2651–2657. https://doi.org/10.1016/j.jbiomech.2012.08.011.
[48] D. Mahmoud, M. Elbestawi, Lattice Structures and Functionally Graded Materials Applications in Additive Manufacturing of Orthopedic Implants: A Review, J. Manuf. Mater. Process. 1 (2017) 13. https://doi.org/10.3390/jmmp1020013.
[49] ASTM G5 - 14 Standard Reference Test Method for Making Potentiodynamic

Anodic Polarization Measurements, (n.d.). https://compass.astm.org/Standards/HISTORICAL/G5-14.htm (accessed December 3, 2019).
[50] T. Kokubo, H. Takadama, How useful is SBF in predicting in vivo bone bioactivity?, Biomaterials. 27 (2006) 2907–2915. https://doi.org/10.1016/J.BIOMATERIALS.2006.01.017.
[51] G. Song, A. Atrens, D. StJohn, An Hydrogen Evolution Method for the Estimation of the Corrosion Rate of Magnesium Alloys, in: Magnes. Technol. 2001, John Wiley & Sons, Inc., Hoboken, NJ, USA, 2013: pp. 254–262. https://doi.org/10.1002/9781118805497.ch44.
[52] S. Nezar, N. Saoula, S. Sali, M. Faiz, M. Mekki, N.A. Laoufi, N. Tabet, Properties of TiO 2 thin films deposited by rf reactive magnetron sputtering on biased substrates, Appl. Surf. Sci. 395 (2017) 172–179. https://doi.org/10.1016/j.apsusc.2016.08.125.
[53] J.H. Kim, S. Lee, H.S. Im, Effect of target density and its morphology on TiO2 thin films grown on Si(100) by PLD, Appl. Surf. Sci. 151 (1999) 6–16. https://doi.org/10.1016/S0169-4332(99)00269-X.
[54] J. Yu, X. Zhao, J. Du, W. Chen, Preparation, microstructure and photocatalytic activity of the porous TiO2 anatase coating by sol-gel processing, J. Sol-Gel Sci. Technol. 17 (2000) 163–171. https://doi.org/10.1023/A:1008703719929.
[55] Y. Xin, K. Huo, T. Hu, G. Tang, P.K. Chu, Corrosion products on biomedical magnesium alloy soaked in simulated body fluids, J. Mater. Res. 24 (2009) 2711–2719. https://doi.org/10.1557/jmr.2009.0323.
[56] Q. Zhang, Y. Jiang, Y. Zhang, Z. Ye, W. Tan, M. Lang, Effect of porosity on long-term degradation of poly (ε-caprolactone) scaffolds and their cellular response, Polym. Degrad. Stab. 98 (2013) 209–218. https://doi.org/10.1016/j.polymdegradstab.2012.10.008.
[57] C. Hadjicharalambous, O. Prymak, K. Loza, A. Buyakov, S. Kulkov, M. Chatzinikolaidou, Effect of Porosity of Alumina and Zirconia Ceramics toward Pre-Osteoblast Response, Front. Bioeng. Biotechnol. 3 (2015) 175. https://doi.org/10.3389/fbioe.2015.00175.
[58] J. Munemasa, T. Kumakiri, Effect of the surface roughness of substrates on the corrosion properties of films coated by physical vapour deposition, Surf. Coatings Technol. 49 (1991) 496–499. https://doi.org/10.1016/0257-8972(91)90106-7.
[59] V. Karageorgiou, D. Kaplan, Porosity of 3D biomaterial scaffolds and osteogenesis, Biomaterials. 26 (2005) 5474–5491. https://doi.org/10.1016/j.biomaterials.2005.02.002.
[60] F.J. O'Brien, B.A. Harley, M.A. Waller, I. V. Yannas, L.J. Gibson, P.J. Prendergast, The effect of pore size on permeability and cell attachment in collagen scaffolds for tissue engineering, in: Technol. Heal. Care, IOS Press, 2007: pp. 3–17. https://doi.org/10.3233/thc-2007-15102.
[61] A. Pardo, S. Feliu, M.C. Merino, R. Arrabal, E. Matykina, Electrochemical estimation of the corrosion rate of magnesium/aluminium alloys, Int. J. Corros. 2010 (2010). https://doi.org/10.1155/2010/953850.
[62] M. Lorenzetti, E. Pellicer, J. Sort, M.D. Baró, J. Kovač, S. Novak, S. Kobe, Improvement to the corrosion resistance of Ti-based implants using

hydrothermally synthesized nanostructured anatase coatings, Materials (Basel). 7 (2014) 180–194. https://doi.org/10.3390/ma7010180.
[63] S. Il Pyun, Y.G. Yoon, E. Lugscheider, R. Mathesius, Relationship between interfacial reaction and adhesion at PVD TiO2 film-metal (Ti or Al) interfaces, Surf. Coatings Technol. 61 (1993) 233–237. https://doi.org/10.1016/0257-8972(93)90231-C.
[64] C. (Christoph) Leyens, M. (Manfred) Peters, John Wiley & Sons., Wiley InterScience (Online service), Titanium and titanium alloys : fundamentals and applications, Wiley-VCH, 2003.
[65] H. Hayashi, T. Saitou, N. Maruyama, H. Inaba, K. Kawamura, M. Mori, Thermal expansion coefficient of yttria stabilized zirconia for various yttria contents, Solid State Ionics. 176 (2005) 613–619. https://doi.org/10.1016/j.ssi.2004.08.021.
[66] D.R. Hummer, P.J. Heaney, J.E. Post, Thermal expansion of anatase and rutile between 300 and 575 K using synchrotron powder X-ray diffraction, Powder Diffr. 22 (2007) 352–357. https://doi.org/10.1154/1.2790965.
[67] Y. Xu, Y. Zhang, T. He, K. Ding, X. Huang, H. Li, J. Shi, Y. Guo, J. Zhang, The Effects of Thermal and Atmospheric Pressure Radio Frequency Plasma Annealing in the Crystallization of TiO2 Thin Films, Coatings. 9 (2019) 357. https://doi.org/10.3390/coatings9060357.
[68] N. Kumar, T.M. Wilkinson, C.E. Packard, M. Kumar, Design of low surface roughness-low residual stress-high optoelectronic merit a-IZO thin films for flexible OLEDs ARTICLES YOU MAY BE INTERESTED IN, J. Appl. Phys. 119 (2016) 225303. https://doi.org/10.1063/1.4953212.
[69] P. Yáñez-Contreras, J.D.O. Barceinas-Sánchez, C.A. Poblano-Salas, J.M. Medina-Flores, A.L. García-García, I. Domínguez-López, Estudio de la evolución del perfil de esfuerzos residuales en recubrimientos barrera térmica depositados sobre acero inoxidable AISI 304, DYNA. 83 (2016) 160–166. https://doi.org/10.15446/dyna.v83n197.51150.
[70] H.J. Moon, Development of thin film inorganic membranes for oxygen separation, Forschungszentrum Jülich, 2012.
[71] R.B. (Robert B. Heimann, H.D. Lehmann, Bioceramic coatings for medical implants : trends and techniques, n.d.
[72] ISO - ISO 25178-2:2012 - Geometrical product specifications (GPS) — Surface texture: Areal — Part 2: Terms, definitions and surface texture parameters, (n.d.). https://www.iso.org/standard/42785.html (accessed February 7, 2020).

5.2. Paper V: On the evaluation of ALD TiO_2, ZrO_2 and HfO_2 coatings on corrosion and cytotoxicity performances

M. Peron[a1], S. Cogo[b], M. Bjelland[a], A. Bin Afif[a], A. Dadlani[a], E. Greggio[b], F. Berto[a], J. Torgersen[a]

[a] *Department of Industrial and Mechanical Engineering, Norwegian University of Science and Technology, Richard Birkelands vei 2b, 7034 Trondheim, Norway*
[b] *Department of Biology, University of Padova, Via Ugo Bassi 58/b, 35131, Padova, Italy*

Abstract[2]

In the last years, magnesium and its alloys have been widely studied as materials for temporary implant devices. However, one of their main limitations is their high corrosion rate. Coatings have been proven to provide an effective barrier. Though only little explored in the field, Atomic Layer Deposition (ALD) stands out as a coating technology due to the outstanding film conformality and density achievable. Here, we provide first insights into the corrosion behavior and the induced biological response of 100 nm thick ALD TiO_2, HfO_2 and ZrO_2 coatings on AZ31 alloy by means of potentiodynamic polarization curves, electrochemical impedance spectroscopy (EIS), hydrogen evolution experiments and MTS colorimetric assays with L929 cells. Whereas all three coatings improve the corrosion behavior and cytotoxicity of the alloy, HfO_2, in particular, reduces the evolved hydrogen by 95% and increases the cell viability by 588% (after 5 days of culture) with respect to the uncoated AZ31 counterpart. ZrO_2 coatings show a similar tendency with slightly worse performance. TiO_2 was characterized by the lowest corrosion improvements and, though generally considered a biocompatible coating, was found to be characterized by grade 3 cytotoxicity after 5 days of culture, which does not meet the demands for cellular applications. These results indicate the strong link between biocompatibility and corrosion protection and signify the need of considering the latter when choosing a biocompatible coating to protect temporary Mg based alloys before implantation.

Keywords: Atomic Layer Deposition (ALD); coatings; corrosion resistance; cytocompatibility; Magnesium

5.2.1. Introduction

[1] Corresponding author
[2] *Acta Biomaterialia* (submitted paper)

As ageing and obesity increases the demand for the implantation of medical devices [1], medical technology advances, with an increased interest in the use of metallic materials for implantable devices to assist with tissue repair or replacement. Implantable devices can be divided into permanent and temporary. For the latter, where implants are only required to stay inside the human body until the tissue heals sufficiently to regain load bearing capacity and integrity, biodegradable materials are desired and Magnesium (Mg) stands out [2–4] due to its attractive features; (1) an elastic modulus compatible with natural bone minimizing the risk of stress shielding [2] and (2) the ability to degrade *in vivo* without releasing toxic products [5–7]. Accelerated corrosion of pure Mg hampers its usability in clinical applications as mechanical failure of the implant is prone to occur before the tissue has recovered. During corrosion, hydrogen gas gets produced at rates beyond what bone tissue is able to accommodate ultimately causing severe host tissue damage [8,9].

To tailor the corrosion rate of Mg, different strategies have been developed. Alloying is an effective way to tune the corrosion rate [10,11], but may introduce elements causing adverse biological reactions [12]. Therefore, in recent years, mechanical processing inducing severe plastic deformation (SPD) has been investigated as viable alternative not requiring chemical changes to the base material. SPD techniques cause a dynamic recrystallization characterized by the nucleation and growth of new and finer grains and Equal Channel Angular Pressing (ECAP) is one such technique [13,14]. Sunil et al. [15], for example, reported the fourfold reduction of the corrosion current density of an AZ31 alloy with respect to the annealed counterpart after they underwent four passes of ECAP and an increased L6 cells adhesion with the number of passes. They correlated the improved cell proliferation on fine grained ECAPed samples to the higher wettability and lower degradation rate of ECAPed samples. Whereas SPD is a viable pathway to increase both corrosion resistance and cell viability, SPD techniques such as ECAP require multiple deformation passes to accumulate large strain in the to refine the material microstructure down to ultrafine grains [16]. Machining is another effective method to achieve surface confined SPD not requiring large plastic deformations of the entire material. Compared to conventional SPD, it induces higher strain levels into the workpiece in just a single stage operation [17]. In addition, the use of liquid nitrogen as coolant during machining further improves the functional performance and product life [18]. We reported a reduction of up to an order of magnitude in the corrosion current density when AZ31 Mg alloys were cryogenically machined [19]. These improvements were associated with the formation of a nano-crystalline and compressed surface layer. However, once the nano-crystalline surface layer dissolves, the machining induced corrosion resistance disappears. In addition, a potential Mg implant may need surface texture and porosity to enhance ingrowth of cells and tissue at the patient specific site of interest [20,21]. In such a scenario, cryogenic machining, despite its benefits in initial corrosion resistance, might not be applicable as intricate features and textured surfaces are difficult to be made [22].

Hence, an alternative, surface confined approach allowing the control of surface texture might be required. Coatings have thus emerged as an effective way to preserve designed macroscopic porosity and surface roughness tailored for osseointegration and to match mechanical characteristics. Several coatings techniques, such as anodizing, fluoride conversion coating, sol-gel techniques and physical vapor deposition techniques, have been developed in the last years to increase the corrosion resistance [23]. However, all

these techniques are characterized by some drawbacks that limit their use, mainly low control of the thickness and high porosity and cracking [24–26]. In addition, the effectiveness of physical vapor deposition techniques, such as sputtering, may be limited due to the inherent line-of-sight deposition process [27]. To overcome this issue, Chemical Vapor Deposition (CVD) is employed. In this class of processes, the substrate surface is exposed to one or more volatile precursors that react and/or decompose to produce the desired surface deposit. Among CVD techniques, Atomic Layer Deposition (ALD) stands out in terms of conformality, film density and possibility for compositional control due to its self-limiting surface-gas phase reactions and it has recently found application in corrosion protection of biomedical implants [28,29]. In this field, researchers have mainly focused on the effect of biocompatible coatings deposited by means of ALD on the corrosion resistance of metallic implant materials [30,31]. In particular, their interest has fallen on TiO_2 and ZrO_2. TiO_2 is in fact known to be biocompatible since it can induce *in vitro* bone-like apatite formation and can stimulate osteoconductivity *in vivo* [32–34], along with the ability to bond directly and reliably to living bone in a short period after implantation [35], while ZrO_2 is an important biomaterial widely used in applications such as dental implants where osteointegration is of minor importance compared to the requirements of corrosion and wear resistance [36] and of a reduced bacterial colonization [37,38]. Dealing with Mg and its alloys, although limited data are available, the application of both ALDed TiO_2 and ZrO_2 has been shown to promisingly improve the corrosion resistance. Marin et al. [29] reported that a 100 nm thick TiO_2 layer reduced the corrosion current density of a commercial AZ31 Mg alloy from 10^{-4} A/cm^2 to 10^{-6} A/cm^2, while Liu et al. reported a three order of magnitude decrease in the corrosion current density of an AZ31 Mg alloy that was coated with a 10 nm thick ZrO_2 layer [28], agreeing with the results obtained by the authors for a 100 nm thick ZrO_2 layer [39,40]. However, in the development of reliable Mg-based implants, and more in general of temporary implants, the corrosion resistance of a material is fundamental also because it can affect the cell response: degradation products evolving during the corrosion process may in fact cause adverse effect on the surrounding (the vicinity of the implant). Considering Mg, from the corrosion process, H_2 evolves, influencing the pH around the implant, and it is widely known that a high pH has harmful effects on the cell viability, migration and proliferation [41]: a pH higher than 8.5 was in fact reported to inhibit the proliferation of hBMSCs [42]. Nevertheless, to the best of the authors' knowledge, the cytotoxicity of ALD TiO_2 and ZrO_2 coatings has never been evaluated. In this work we thus aim to fill this gap and to provide further insight in the corrosion performances of ALD TiO_2 and ZrO_2 coatings in a physiologically relevant environment. To do so, potentiodynamic polarization curves, electrochemical impedance spectroscopy (EIS) and hydrogen evolution tests have been carried out on 100 nm thick TiO_2 and ZrO_2 coated AZ31 samples to assess the corrosion performances and cytotoxicity studies by MTS colorimetric assay using L929 cells were carried out to investigate the possible effect of TiO_2 and ZrO_2 ALD coatings on cell viability in the vicinity of the implant. To substantiate the importance of high corrosion resistance to the viability of the cells surrounding an implant, we compare the results obtained on TiO_2 and ZrO_2 coated AZ31 substrates with those obtained on HfO_2 coated counterparts, considered also biocompatible [43,44]. In this perspective, 100nm thick ALD HfO_2 layer has been herein coated on an AZ31 substrate and potentiodynamic polarization curves,

electrochemical impedance spectroscopy (EIS) and hydrogen evolution tests have been carried out to assess the corrosion performances. In addition, cytotoxicity studies by MTS colorimetric assay using L929 cells has also been carried out.

5.2.2. Materials and methods

5.2.2.1. Materials and environment

AZ31 Mg alloy was supplied in form of commercially available bars. The microstructure of the material in the as-received condition is shown in Figure 5.2.1 and consists of a quite homogeneous α matrix. The initial grain size was measured by linear intercept method and resulted equal to 13.2 ± 8 μm.

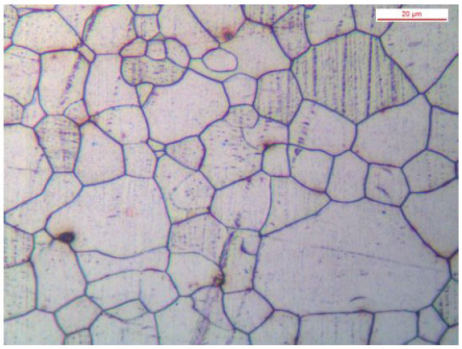

Figure 5.2.1: Microstructure of the AZ31 alloy in the as-received condition.

The test medium was a simulated body fluid (SBF) prepared according to Ref. [45] for the corrosion tests and Dulbecco's Modified Eagle Medium (DMEM – Life Technologies Corp, California, USA) supplemented with 10%v/v fetal bovine serum (FBS), 100U/ml penicillin and 100μg/ml streptomycin for the cytotoxicity tests.

5.2.2.2. Atomic Layer Deposition

The deposition of the ALD coatings was carried out in a commercial ALD reactor (Savannah S200, Veeco Instruments Inc., Massachusetts, USA) through successive cyclic reactions. Dealing with ZrO_2, 926 successive cyclic reactions between Tetrakis (dimethylamino) zirconium (TDMAZ) and deionized water (H_2O) at 160 °C were carried out to obtain a total thickness of 100 nm. Each cycle was composed of two parts. The first part consisted of a 250-ms TDMAZ precursor pulse and a 10-s Hi-purity N_2 purge with a flow rate of 20 sccm to remove residual reactants and by-products from the chamber so as to prevent any additional chemical vapor deposition reactions. The second part comprised a 150-ms H_2O precursor pulse and a 15-ms Hi-purity N_2 purge. In the process of deposition, the TDMAZ precursor, H_2O precursor, and delivery lines were heated to 75 °C, 25 °C, and 160 °C, respectively. During the deposition process, the ZrO_2 layer deposition rate was of approximately 1.08 Å/cycle. Concerning TiO_2, the metal organic precursor used was Tetrakis (dimethylamido) titanium (IV) or TDMA-Ti heated at 75˚C. Each cycle was again composed of two parts. The first part consisted of

a 0.1 s TDMA-Ti precursor pulse and a 5 s Hi-purity N_2 purge with a flow rate of 20 sccm. The second part comprised a 0.015 s H_2O precursor pulse and a 5 s Hi-purity N_2 purge. The deposition rate was found to be 0.5 A˚/cycle. Finally, the deposition of HfO_2 was carried out through successive cyclic reactions between Tetrakis (dimethylamino) Hafnium (TDMAH) and deionized water (H_2O) at 160 °C. Each cycle was composed of two parts. The first part consisted of a 200-ms TDMAZ precursor pulse and a 10-s Hi-purity N_2 purge with a flow rate of 20 sccm to remove residual reactants and by-products from the chamber to prevent any additional chemical vapor deposition reactions. The second part comprised a 150-ms H_2O precursor pulse and a 10 s Hi-purity N_2 purge. In the process of deposition, the TDMAH precursor, H_2O precursor, and delivery lines were heated to 75 °C, 25 °C, and 160 °C, respectively. The deposition rate was measured at 1.3 Å/cycle.

5.2.2.3. Coating characterization

X-ray photoluminescence (XPS) measurements were conducted to assess the chemical composition of the TiO_2, ZrO_2 and HfO_2 ALD coatings. Kratos Analytical XPS Microprobe (Kratos Analytical Ltd, Manchester, UK) which uses Al (Kα) radiation of 1486 eV in a vacuum environment of $5*10^{-9}$ Torr was used. CasaXPS software was used to analyze the XPS data.

5.2.2.4. Potentiodynamic polarization curves

Discs with a diameter of 29 mm and a thickness of 2 mm were manufactured from the commercially available bars using a lathe. The samples were then grounded up to 2000 grit silicon carbide papers and cleaned with acetone and ethanol for five minutes in ultrasonic bath. Some of these samples were then coated as described in Section 2.2. Potentiodynamic polarization curves of bare and coated samples were carried out in simulated body fluid (SBF) with a pH of 7.4 on the Gamry Reference 600+ potentiostat. The electrochemical tests used three-electrode equipment with the bare or coated samples as a working electrode, a Hg/Hg_2SO_4 electrode as a reference electrode, and a platinum plate electrode as a counter electrode. The area of the samples exposed to SBF was 1 cm^2. The potentiodynamic polarization test was conducted at a stable open-circuit potential after a stabilization period of 30 min. The scan rate of the potentiodynamic polarization test was 0.5 mV/s.

5.2.2.5. Electrochemical impedance spectroscopy

Electrochemical impedance spectroscopy was carried out using the same three-electrode configuration and the same potentiostat as described in the previous Section. Additionally, the electrochemical cell was placed inside a Faraday's cage to avoid noise in the results. To fit the results, the software Gamry Echem Analyst (Gamry Instruments, Warminster, PA, USA) was used. The signal amplitude during EIS was 10 mV relative to the open circuit potential (OCP) at a frequency range of 10^{-2} to 10^5 Hz, and the samples were kept in SBF for half an hour before measurements to stabilize and measure OCP.

5.2.2.6. Hydrogen evolution tests

During the immersion tests, the chemical reaction between Mg and electrolyte occurs as shown in the following equation [2]:

$$Mg + 2H_2O \rightarrow Mg(OH)_2 + H_2 \quad (5.2.1)$$

From the above equation it can be easily understood that the dissolution of one magnesium atom generates one hydrogen gas molecule. In other words, the evolution of one mole of hydrogen gas corresponds to the dissolution of one mole of magnesium. Therefore, measuring the volume of hydrogen evolved allows to assess the corrosion rate of Mg and its alloys in a way that permits to overcome the drawbacks of the weight loss method and of the electrochemical techniques [46]. To do so, cubic samples of side 5 mm were obtained from the as-received material and they were grounded up to 2000 grit silicon carbide papers and cleaned with acetone and ethanol for five minutes in ultrasonic bath. Some of these samples were then coated as described in Section 5.2.2.2. The immersion tests were carried out in SBF at 37 °C for 7 days individually to monitor the hydrogen evolution. Hydrogen bubbles were collected into a burette from each sample as suggested in [46].

5.2.2.7. Degradation behavior

Cylindrical samples prepared as described in Section 5.2.2.4. were soaked for one day in SBF at 37 °C to carry out macro- and micro-morphological characterizations before and after corrosion. All samples were ultrasonically cleaned for 5 minutes in acetone and ethanol, dried in the air, and then observed by means of Canon EOS 4000D (Canon, Tokyo, Japan) and FEI Quanta 450 Scanning Electron Microscope (Thermo Fisher Scientific Inc., USA) for macro- and micro-morphological characterizations, respectively.

5.2.2.8. Cytotoxicity testing

Cytotoxicity was assessed via the MTS cell proliferation assay (Promega) in L929 murine fibroblasts as per manufacturer's recommendations. To compare the cytocompatibility of the different coatings, extracts were prepared by incubating the samples in complete Dulbecco's Modified Eagle Medium (DMEM), supplemented with 10%v/v fetal bovine serum (FBS), 100U/ml penicillin and 100µg/ml streptomycin with 1.25ml/cm^2 extraction ratio for 72 hours at 37°C in a humidified atmosphere with 5% CO_2 [47,48]. The supernatants were collected and centrifuged, and 100% extracts were employed for the cell proliferation assay. Briefly, 3x10^3 cells/well were seeded on 96-well plates and incubated for 24 hours to allow attachment. Starting from the following day, 100µl of the different extracts were added to each well. Complete DMEM was applied as a negative control. The effect of the extracts on cell viability was assessed after 1, 3 and 5 days of treatment. The generation of colored formazan by reduction of the MTS tetrazolium compound was monitored by measuring absorbance at 490nm on a VICTOR™X3 plate reader (Perkin Elmer, Massachusetts, USA).

In addition, another set of samples was incubated as just described to assess the pH evolution of the extracts with a pH meter Inolab 730 (WTW, Weilheim, Germany).

5.2.3. Results

5.2.3.1. Coating characterization

XPS was conducted to determine the chemical composition of the ALD deposited TiO_2, ZrO_2 and HfO_2. In order to have minimum effect of the underlying substrate, the measurements were carried out on thin film deposited on Si wafer. Prior to chemical characterization, the effect of environmental contamination and surface oxidation were removed by etching the surface for 180 seconds with an energy of 2 KeV. Dealing with titania, regional scans for titanium, oxygen and carbon were carried out at high resolution. Negligible amounts of carbon were observed in the regional scan of carbon, thus indicating an ideal deposition without any process contamination. Figure 5.2.2 (a) and (b) are regional scan of titanium and oxygen, respectively. For titanium, peaks corresponding to the core level binding energies, 459 eV and 464 eV of Ti $2p_{3/2}$ and Ti $2p_{1/2}$ are observed, which is due to Ti^{4+} oxidation state in TiO_2 [49]. The shoulder at lower energy around 456 eV is due to the presence of Ti^{3+} caused due to the argon etching step [50]. Dealing with oxygen, the peak at 531 eV is due to oxygen atoms in TiO_2 phase [51], while the small shoulder at higher energy is due to oxygen in hydroxyl groups present in the form impurities. Stoichiometric TiO_2 thin films should have Ti and oxygen in 1:2 ratio i.e. 66.7% oxygen and 33.3% titanium, but in our case, we have found the composition to be around 60% for oxygen and 40% titanium, thus indicating an oxygen deficient deposition.

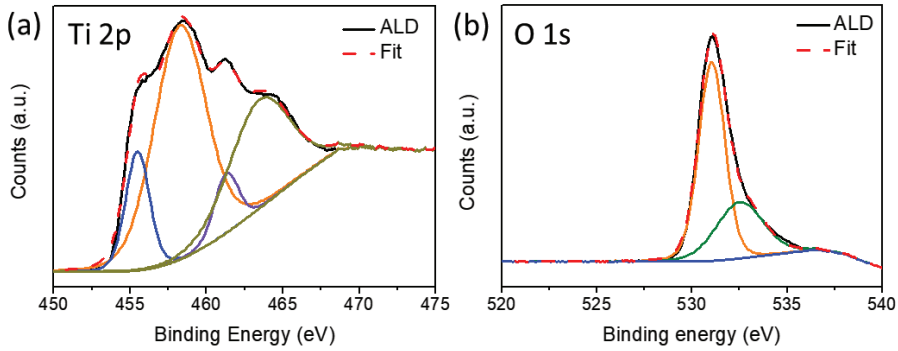

Figure 5.2.2: XPS spectra for ALD deposited TiO_2 (a) Ti 2p (b) O 1s

Dealing with zirconia, regional scans zirconium, oxygen and carbon were also carried out at high resolution. No peak was observed in the high resolution scan for element carbon, thus showing a near carbon free ALD deposition. The high resolution spectra (Figure 5.2.3a) of Zr 3d shows two peaks at binding energy 182 eV and 184 eV, which correspond to Zr $3d_{5/2}$ and Zr $3d_{3/2}$ respectively. The scan conducted for O 1s (Figure 5.2.3b) showed a peak at 530 eV which belongs to ZrO_2 and the shoulder on the higher energy side is due to the oxidation of metal in air forming ZrO. The quantification

calculation using CASAXPS software showed a composition as 40 % Zr and 60% O. Thus indicating an oxygen deficient zirconia thin film.

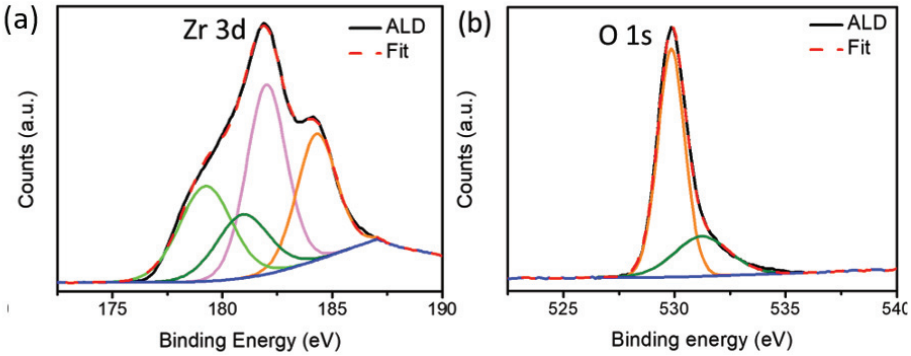

Figure 5.2.3: XPS spectra for ALD deposited ZrO_2 (a) Zr 3d (b) O 1s

Finally, dealing with hafnia, regional scans for the elements, hafnium, oxygen and carbon were again carried out at high resolution. Negligible amounts of carbon were observed in the regional scan of carbon, thus indicating an ideal deposition without any process contamination. Figure 5.2.4b shows the core level spectra of O 1s associated with HfO_2 [52]. The region at higher energy above the peak at 531 eV shows a shoulder due to presence of a small amount of contamination due to carbon or moisture. In the regional scan of element Hf 4f, peak positions at 18.5 eV and 20.7 eV, correspond to Hf $4f_{7/2}$ and Hf $4f_{5/2}$ in HfO_2 [53]. The shoulders at lower energies below 18.5 eV are due Hf interstitials and oxygen vacancies [54]. Stoichiometric HfO_2 thin films should have Hf and Oxygen in 1:2 ratio i.e. 66.7% oxygen and 33.3% hafnium, but in our case, we have found the composition to be around 63% oxygen and 37% hafnium, thus indicating a slightly oxygen deficient deposition.

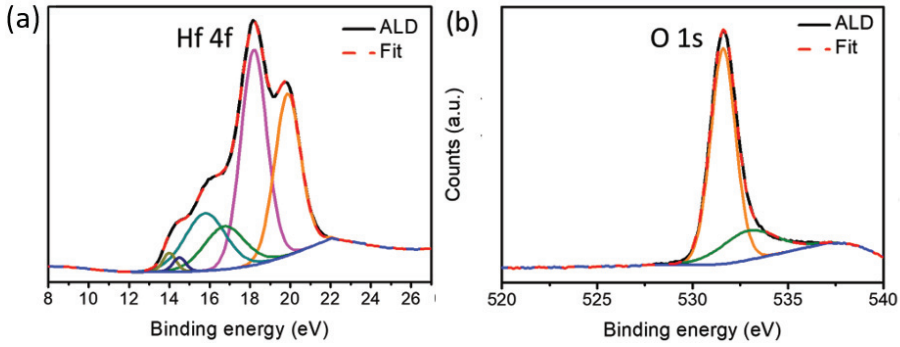

Figure 5.2.4: XPS depth profile spectra of ALD deposited HfO_2 (a) Hf 4f and (b) O 1s

5.2.3.2. Potentiodynamic polarization curves

The potentiodynamic polarization curves of the coated and bare samples are shown in Figure 5.2.5 and the results of the corrosion potentials (E_{corr}) and of the corrosion

current densities (i_{corr}) are shown in Table 5.2.1. In general, the potentiodynamic polarization test is used to investigate the corrosion properties of materials. The corrosion current density and free corrosion potential in the Tafel curve are closely related to the corrosion situation of the sample, i.e., a lower corrosion current density corresponds to a smaller corrosion rate and a higher free corrosion potential corresponds to a minor corrosion trend. Compared with the uncoated alloy, the corrosion current densities of the coated samples display declining trends (Figure 5.2.5 and Table 5.2.1). In particular, the HfO_2 coating is reported to provide the lowest corrosion current density, that is half of that provided by ZrO_2 and 40 times lower than that of TiO_2.

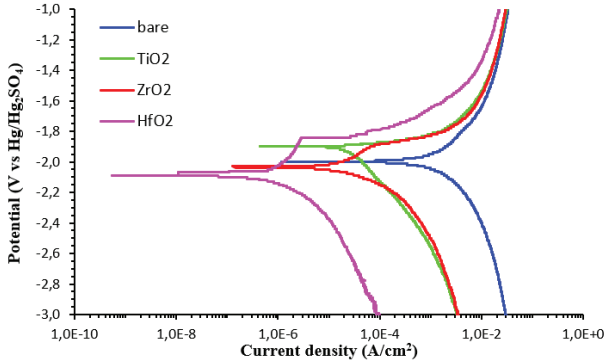

Figure 5.2.5: Potentiodynamic polarization curves of bare (blue), TiO_2 (green), ZrO_2 (red) and HfO_2 (fuchsia) AZ31 alloy in SBF.

	Bare	**TiO_2 coating**	**ZrO_2 coating**	**HfO_2 coating**
E_{corr} (V)	-2.0	-1.90	-2.02	-2.09
i_{corr} (A/cm^2)	$3.0\ 10^{-3}$	$24.9\ 10^{-6}$	$1.2\ 10^{-6}$	$0.6\ 10^{-6}$

Table 5.2.1: Results of the corrosion potentials (E_{corr}) and corrosion cuttent densities (i_{corr}) for bare and coated AZ31 samples in SBF.

5.2.3.3. Electrochemical impedance spectroscopy

The Nyquist-plots of bare and TiO_2, ZrO_2, and HfO_2 are shown in Figure 5.2.6a, 5.2.6b, 5.2.6c and 5.2.6d, respectively. In the Nyquist plots, the bare and the coated samples are characterized by three time constants being the capacitive loop in the high and medium frequency range and the inductive loop in the low-frequency range [55,56]. Being the capacity loop connected to the transfer process between the coating and the substrate, a larger capacitive loop means better corrosion resistance [57]. Due to the larger diameter of the capacitive loops of the coated samples compared to the bare sample, the treated samples show much better performance in corrosion resistance. The capacitive loops and hence the corrosion performance is ranked HfO_2 > ZrO_2 > TiO_2 > bare, confirming the results of the potentiodynamic polarization curves. There is a large difference in impedance among the different samples, as can be seen by inspecting the order of magnitudes on the axes.

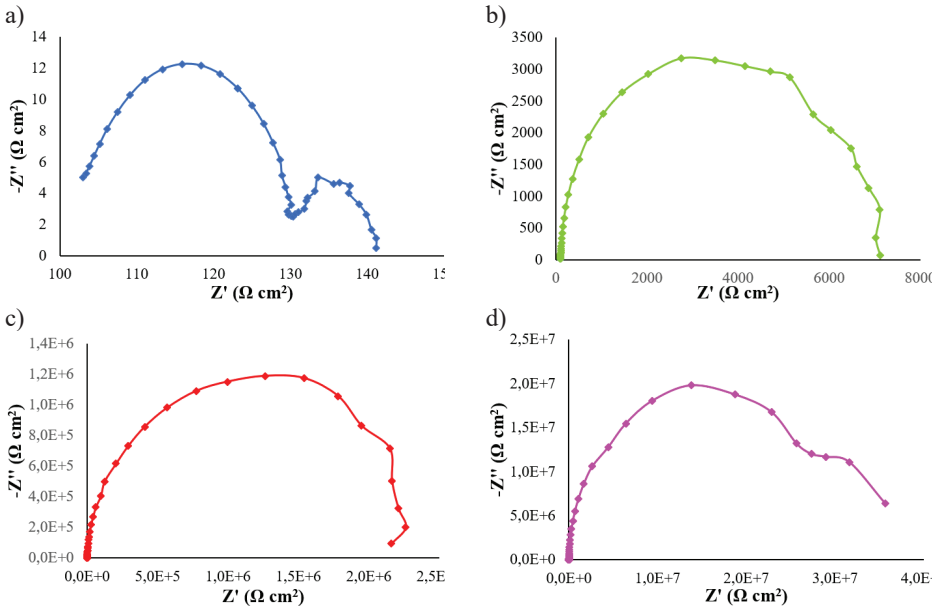

Figure 5.2.6: Nyquist plots of bare (a), TiO_2 (b), ZrO_2 (c) and HfO_2 (d) coated AZ31 alloy in SBF.

The Bode plots of bare and TiO_2, ZrO_2, and HfO_2 are shown in Figure 5.2.7a, 5.2.7b, 5.2.7c and 5.2.7d, respectively. The Bode plots also help to investigate the corrosion resistance as a higher value of $|Z|_{f\to 0}$ means greater corrosion resistance [58,59]. The $|Z|_{f\to 0}$ value for the bare, TiO_2, ZrO_2 and HfO_2 coated samples is $1.4 \cdot 10^2\ \Omega \cdot cm^2$, $4.5 \cdot 10^3\ \Omega \cdot cm^2$, $2.1 \cdot 10^6\ \Omega \cdot cm^2$ and $4 \cdot 10^7\ \Omega \cdot cm^2$, respectively, confirming the results found in the Nyquist plots.

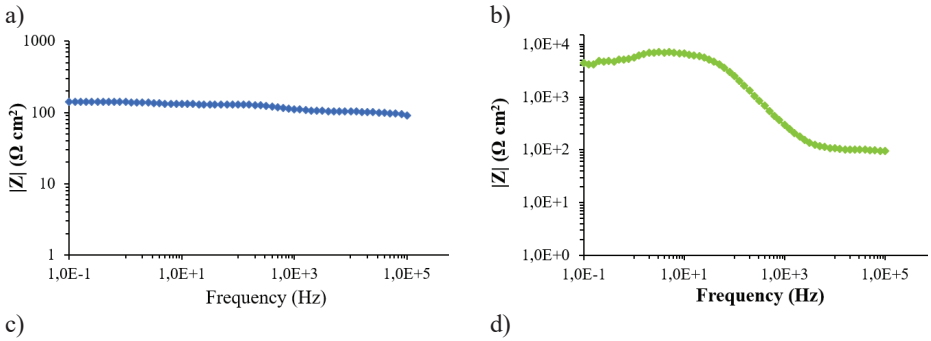

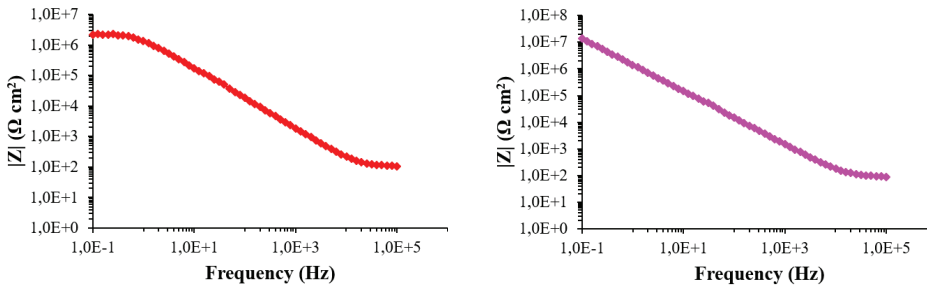

Figure 5.2.7: Bode plots of bare (a), TiO_2 (b), ZrO_2 (c) and HfO_2 (d) coated AZ31 alloy in SBF.

5.2.3.4. Hydrogen evolution tests

The hydrogen evolution curves of bare and coated samples are reported in Figure 5.2.8, and the results further suggest that the application of the coatings can prevent the degradation of AZ31 alloy. In particular, after 7 days, the hydrogen evolved from the bare samples is reduced by 52% if 100 nm of ALD TiO_2 is considered. Higher improvements are obtained if ZrO_2 and, above all, HfO_2 are employed: the former leads to a reduction in the hydrogen evolved by 92.5%, while the latter to a reduction by 95%.

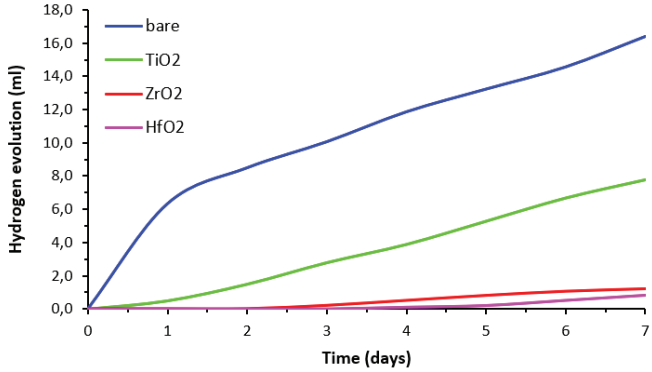

Figure 5.2.8: Hydrogen evolved from the immersion of bare and coated AZ31 alloy in SBF.

5.2.3.5. Degradation behaviour

Figure 5.2.9 displays the macro-morphologies of TiO_2, ZrO_2 and HfO_2 coated samples before and after one day of corrosion in SBF. The bare AZ31 sample was taken as control.

	Bare	TiO_2	ZrO_2	HfO_2
Before corrosion			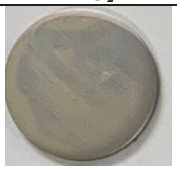	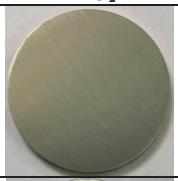
After corrosion				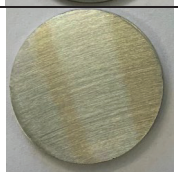

Figure 5.2.9: Macro-morphologies of bare, TiO_2, ZrO_2 and HfO_2 coated samples before and after corrosion

It can be clearly seen that the degree of corrosion damage decreased with the application of coatings, until it became negligible for HfO_2 coated samples. In particular, the extensively corroded surface of bare samples, characterized by pits, was reduced by applying a TiO_2 layer, where un-corroded areas were accompanied by corroded areas characterized by a filiform corrosion. Barely any corrosion apart from the small area at the edge of the sample was observable from the macro-morphologies of ZrO_2 coated samples. However, the micro-morphologies revealed some small corroded area in the center of the ZrO_2 coated samples (Figures 5.2.10e and 5.2.10f). In addition, although the macro-morphologies of HfO_2 coated samples did not reveal any corrosion, the micro-morphologies showed the presence of some small areas where the early stage of the corrosion products formation can be seen, together with the onset of filiform corrosion (Figures 5.2.10g and 5.2.10h). TiO_2 coated samples and bare samples are characterized by a large number of cracks dividing the surface into network structure (Figures 5.2.10a and 5.2.10b and Figures 5.2.10c and 5.2.10d for bare and TiO_2 coated samples, respectively). In addition, in the bare samples, the surface film layer began to delaminate and flake off (Figures 5.2.10a and 5.2.10b).

a)

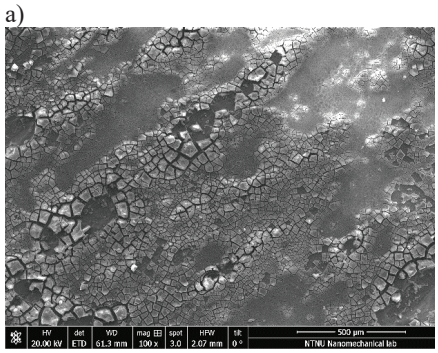

b)

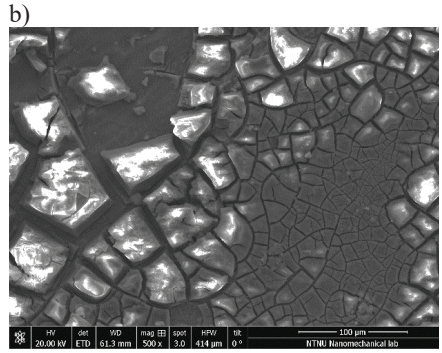

c)

d)

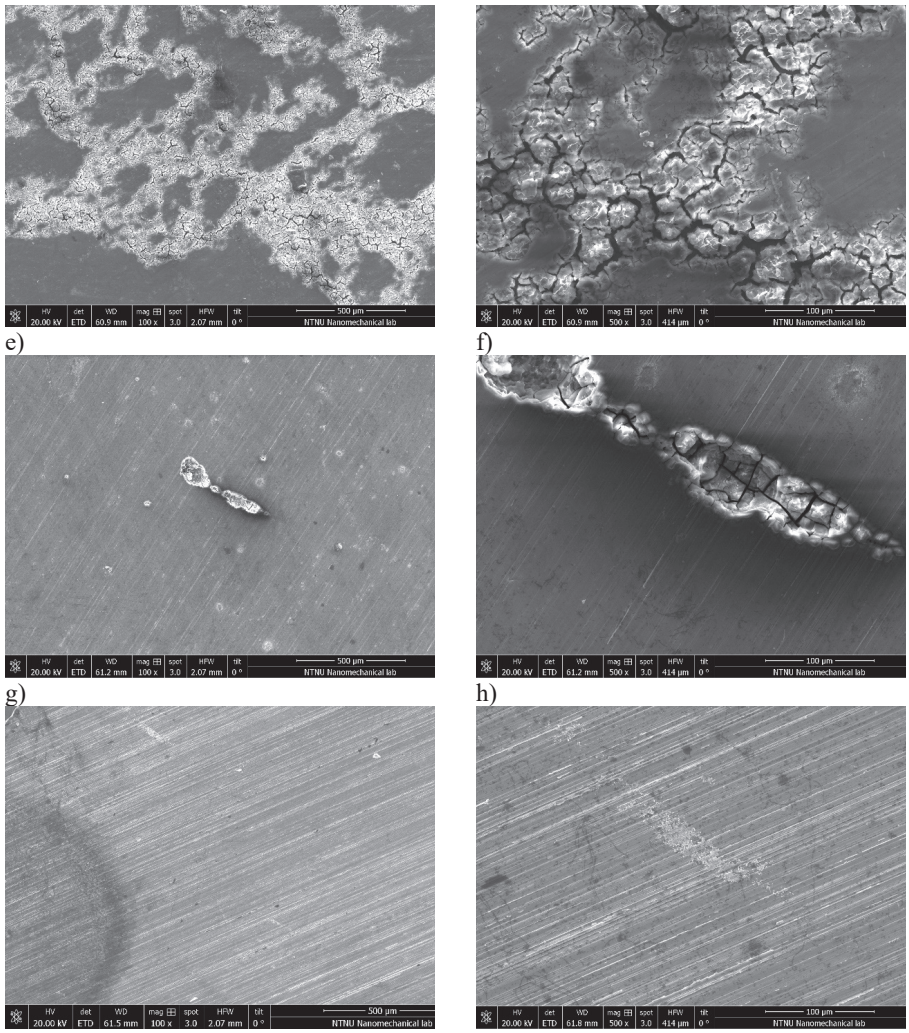

Figure 5.2.10: Micro-morphologies of bare (a and b), TiO_2 (c and d), ZrO_2 (e and f) and HfO_2 (g and h) coated samples before and after corrosion

5.2.3.6. Cytotoxicity testing

The L929 murine cell line and the MTS assay were employed to determine the cytotoxicity of the different ALD coatings. Figure 5.2.11 shows the viability of L929 cells after exposure to extracts of the AZ31 alloy and coated samples after 1, 3 and 5 days' culture.

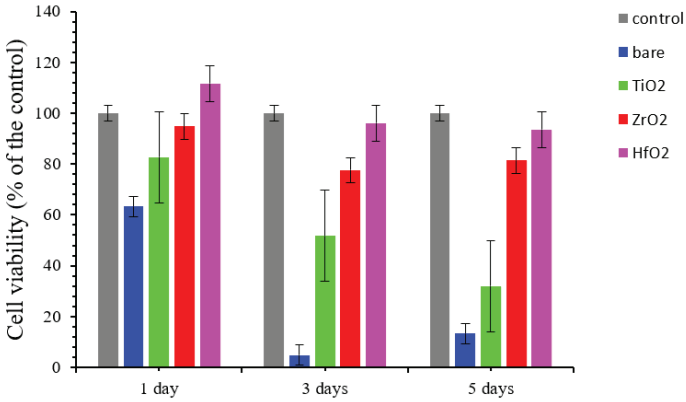

Figure 5.2.11: Cell viability of L-929 cultured in extracts from bare and coated AZ31 substrates after culture for 1, 3 and 5 days. Error bars represent means ± SEM for n=3

Finally, Figure 5.2.12 reports the pH evolution during the preparation of the extracts.

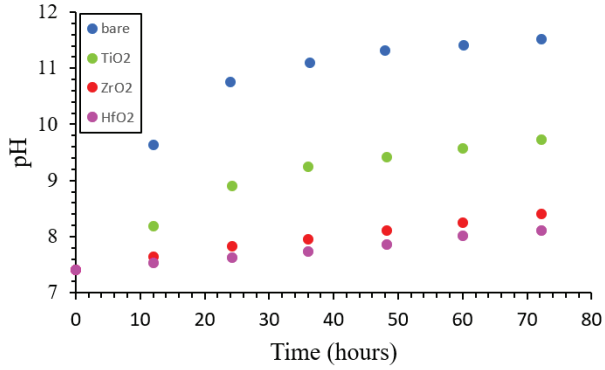

Figure 5.2.12. pH evolution of bare and coated samples in DMEM supplemented with 10% FBS

As it can be seen, the application of the coatings is shown to reduce the increase in pH produced by the bare alloy. In particular, the pH is reduced by 15.5% if 100 nm of ALD TiO_2 is considered. Higher improvements are obtained if ZrO_2 and, above all, HfO_2 are employed: the former leads to a reduction in the hydrogen evolved by 27.1%, while the latter to a reduction by 29.7%.

5.2.4. Discussion

In recent years, ALD has emerged as a promising coating technique for biomedical materials due to the high conformality and density of its films. Dealing with biodegradable materials, and in particular with Mg and its alloys, researchers have focused on assessing their corrosion resistance after the deposition of biocompatible coatings, mainly TiO_2 and ZrO_2, obtained by ALD. However, the literature in the field is still limited and in this work we have thus provided further insights in the corrosion

performances in SBF of three different biocompatible materials (TiO_2, ZrO_2 and HfO_2) obtained by means of ALD. In addition, in a temporary implant that is made to disappear over time, the impact of the corrosion products to the immediate surrounding of the implant becomes important and is an additional factor to consider in addition to cell attachment. From the corrosion process of Mg and its alloys, for example, H_2 evolves, influencing the pH, and it is widely known that a high pH has harmful effects on the cell viability, migration and proliferation [41]. However, the effects of ALDed coatings on the cytotoxicity of Mg and its alloys have not been studied yet to the best of the authors' knowledge. Thus, the effects of the three biocompatible materials mentioned above deposited by means of ALD on the cytotoxicity of AZ31 alloy have been investigated here and correlated to the corrosion properties of the coatings, aiming to assess whether biocompatibility issues may arise when materials considered biocompatible when the cells are in direct contact are used as coatings for biodegradable materials such as Mg and its alloys.
From the MTS assay results reported in Figure 5.2.11, it can be seen that the application of coatings increases the cell viability of the bare AZ31 alloy. However, according to the evaluation of cytotoxicity listed in Table 5.2.2, not all the coatings lead to Grade 1 cytotoxicity, that represents the threshold above which a material is considered to meet the demands for cellular applications [60].

Cell viability	≥100	75-99	50-74	25-49	1-24	<1
Grade	0	1	2	3	4	5

Table 5.2.2: The standard evaluation of cytotoxicity (%)

In fact, Grade 1 cytotoxicity was constantly found only for ZrO_2 and HfO_2, with the latter to be the only one showing Grade 0 cytotoxicity. TiO_2 coatings is instead characterized by Grade 1 cytotoxicity only at 1 day of culture, after that the viability decreases down to Grade 2. Considering bare samples, they are always characterized by a too low viability to meet the demands for cellular applications.
These results can be related to the corrosion performances of the coatings. In fact, from the corrosion process of Mg and its alloys, Mg^{2+} ions and H_2 evolve. The former are reported to exert an adverse effect on the attachment and proliferation of cells when their local concentration is high since cell proliferation is delayed in hyper-osmotic solutions [61]. Wong et al. reported that a magnesium ion concentration of 200 ppm caused the down-regulation of osteogenesis-related genes [62]. The hydrogen released, instead, increases the pH eventually leading to cell death: a pH higher than 8.5 was in fact reported to inhibit the proliferation of hBMSCs [42]. Therefore, the higher the corrosion rate, the worse the cell viability, and this is confirmed by the results herein obtained. In fact, from the potentiodynamic polarization curves, the EIS results and the hydrogen evolution tests, it can be seen that the corrosion resistance follow the following trend $HfO_2 > ZrO_2 > TiO_2 >$ bare, leading to the consequent pH evolution reported in Figure 5.2.12 that explains the cytotoxicity results: Grade 1 cytotoxicity was found only for ZrO_2 and HfO_2, that are the coatings that best performed dealing with corrosion and that lead to a lower increase in the pH. In particular, HfO_2 coating is the only one showing Grade 0 cytotoxicity as a consequence of the lowest increase in pH. Grade 3 and 4 were instead found for the TiO_2 coating and, particularly, for the bare samples.

The different corrosion performances provided by the different materials can be related to the integrity of the coatings and to their electrochemical properties. Dealing with the former, the presence of defects such as cracks and pores are known to affect the corrosion behavior inducing filiform corrosion (Figure 5.2.10) and to reduce the protectiveness of the coating allowing a path to the fluid to enter the material [63]. Cracks are known to form as a consequence of the induced residual stresses on the coating due to the difference in the thermal expansion coefficient between the coating and the substrate [64,65]. The thermal expansion coefficient of Mg is reported to be $27 \cdot 10^{-6}$ °C^{-1} [66], while those of TiO_2, ZrO_2 and HfO_2 are $7 \cdot 10^{-6}$ °C^{-1}, $11 \cdot 10^{-6}$ °C^{-1} and $10 \cdot 10^{-6}$ °C^{-1}, respectively [67–69]. The mismatch between the substrate and the coating is lower with ZrO_2 and higher with TiO_2. This would suggest ZrO_2 coating to provide the highest corrosion resistance among the considered materials. However, the results herein reported showed that the highest improvements in terms of corrosion resistance were provided by the HfO_2 coatings. This can be linked to the lower porosity of the HfO_2 compared to ZrO_2 and, even more, to TiO_2. Elsener et al. [70] proposed an electrochemical method to estimate the porosity of thin films based on the following Equation:

$$Porosity = \left(\frac{R_{p,s}}{R_p} \right) \cdot 10^{\frac{\Delta E_{corr}}{b_a}} \quad (5.2.2)$$

Where $R_{p,s}$ and R_p are the polarization resistance of the bare and coated material in Ωcm^2, respectively, ΔE_{corr} is the change of the corrosion potential caused by the presence of the coating layer in mV and b_a is the anodic Tafel slope of the bare substrate in mV/decade. The polarization resistances,corresponding to the diameter of the capacitive loop in the Nyquist plots, are reported in Table 5.2.3, the ΔE_{corr} can be measured from the results of the potentiodynamic polarization curves reported in Table 1 and the anodic Tafel slope of the bare substrate was measured equal to 442 mV/decade from the potentiodynamic polarization curves. The corresponding porosity was found to be 0.36%, 0.0016% and 0,00007% for TiO_2, ZrO_2 and HfO_2, respectively.

	Bare	**TiO_2**	**ZrO_2**	**HfO_2**
Polarization Resistance (Ω cm^2)	42.9	$7.0\ 10^3$	$2.3\ 10^6$	$3.8\ 10^8$

Table 5.2.3: Polarization resistance of bare and coated samples

Another reason for the better corrosion resistance of HfO_2 is the difference in cohesive energies [71]. In fact, the higher the cohesive energy, the more electrochemically stable is the material and thus, the lower its corrosion. The cohesive energy of HfO_2 is the highest among the three materials herein studied, while TiO_2 is the lowest [72]; the cohesive energy of ZrO_2 is instead slightly lower than that of HfO_2 and this could explain the different corrosion behavior observed. Finally, the lower wettability of HfO_2 compared to ZrO_2 and TiO_2 further explain the herein reported corrosion behavior [73–75] and hence the cell viability results.

It is worth mentioning that for the biocompatibility of TiO_2, the results herein reported differ from what is reported in literature. In fact, TiO_2 is widely known as one of the

most biocompatible materials since it induces fast deposition of apatite from SBF *in vitro* and stimulates the adhesion and proliferation of cells [76,77]. However, although the biocompatibility of TiO_2 remains undisputed when the cells are in direct contact, biocompatibility issues may arise when TiO_2 is used as coating material for Mg and its alloys and it is not effective in reducing the corrosion rate of the magnesium substrate leading to an environment that reveals to be toxic for the cells due to the increase in the pH and to the high concentration of Mg^{2+} ions.
Therefore, in the choice of a coating material for degradable Mg alloys used as implant material, it is important to consider its cohesive energy, wettability, porosity and thermal expansion coefficient to provide an effective reduction of the corrosion rate of the Mg substrate that otherwise would affect the biocompatibility of the coating itself creating an lethal environment for the cell.

5.2.5. Conclusions

In this study, the effect of a 100 nm thick TiO_2, ZrO_2 and HfO_2 ALD coating on the corrosion behavior and on the cytotoxicity of the AZ31 Mg alloy was assessed. To this regard, potentiodynamic polarization curves, EIS and hydrogen evolution experiments have been carried out to assess the former, while MTS colorimetric assay using L929 cells to assess the latter. Whereas the presence of TiO2 coatings is reported to improve the corrosion performances with respect to the bare AZ31 alloys, ZrO_2 and, above all, HfO_2 ALD coatings provide a significant higher corrosion resistance. This can be reasoned by their lower wettability and their higher electrochemical stability and surface integrity (in terms of cracks and pores). This improved corrosion resistance has effects on the cytotoxicity of AZ31 alloy. Indeed, the reduced corrosion provided by the coatings leads to a lower increase in the pH and in the concentration of Mg^{2+} ions, inducing the cytotoxicity Grade to move from Grade 4 for bare AZ31 alloy to Grade 2 for TiO_2 coating and to Grade 1 for ZrO_2 and HfO_2 coatings. In particular, HfO_2 coating was also found to report a Grade 0 cytotoxicity considering the extracts assessed at 1 day of culture. As a grade 1 toxicity is the minimum requirement for FDA approval, the choice of the coating has to include a cytotoxicity benchmark of its corrosion products and cannot be linked to cell attachment to the biomaterial surface only.

Bibliography Paper V

[1] M.P. Ginebra, T. Traykova, J.A. Planell, Calcium phosphate cements as bone drug delivery systems: A review, J. Control. Release. 113 (2006) 102–110. https://doi.org/10.1016/j.jconrel.2006.04.007.

[2] M. Peron, J. Torgersen, F. Berto, Mg and Its Alloys for Biomedical Applications: Exploring Corrosion and Its Interplay with Mechanical Failure, Metals (Basel). 7 (2017) 252. https://doi.org/10.3390/met7070252.

[3] N. Li, Y. Zheng, Novel Magnesium Alloys Developed for Biomedical Application: A Review, J. Mater. Sci. Technol. 29 (2013) 489–502. https://doi.org/10.1016/J.JMST.2013.02.005.

[4] R.K. Singh Raman, S. Jafari, S.E. Harandi, Corrosion fatigue fracture of magnesium alloys in bioimplant applications: A review, Eng. Fract. Mech. 137 (2015) 97–108.

https://doi.org/10.1016/j.engfracmech.2014.08.009.

[5] M.P. Staiger, A.M. Pietak, J. Huadmai, G. Dias, Magnesium and its alloys as orthopedic biomaterials: A review, Biomaterials. 27 (2006) 1728–1734. https://doi.org/10.1016/j.biomaterials.2005.10.003.

[6] A.C. Hänzi, A.S. Sologubenko, P.J. Uggowitzer, Design strategy for new biodegradable Mg–Y–Zn alloys for medical applications, Int. J. Mater. Res. 100 (2009) 1127–1136. https://doi.org/10.3139/146.110157.

[7] Y. Sasaki, G.A. Sathi, O. Yamamoto, Wound healing effect of bioactive ion released from Mg-smectite, Mater. Sci. Eng. C. 77 (2017) 52–57. https://doi.org/10.1016/j.msec.2017.03.236.

[8] F. Witte, V. Kaese, H. Haferkamp, E. Switzer, A. Meyer-Lindenberg, C.J. Wirth, H. Windhagen, In vivo corrosion of four magnesium alloys and the associated bone response, Biomaterials. 26 (2005) 3557–3563. https://doi.org/10.1016/j.biomaterials.2004.09.049.

[9] B. Zberg, P.J. Uggowitzer, J.F. Löffler, MgZnCa glasses without clinically observable hydrogen evolution for biodegradable implants, Nat. Mater. 8 (2009) 887–891. https://doi.org/10.1038/nmat2542.

[10] M. Bobby Kannan, W. Dietzel, C. Blawert, A. Atrens, P. Lyon, Stress corrosion cracking of rare-earth containing magnesium alloys ZE41, QE22 and Elektron 21 (EV31A) compared with AZ80, Mater. Sci. Eng. A. 480 (2008) 529–539. https://doi.org/10.1016/J.MSEA.2007.07.070.

[11] L. Choudhary, R.K. Singh Raman, J. Hofstetter, P.J. Uggowitzer, In-vitro characterization of stress corrosion cracking of aluminium-free magnesium alloys for temporary bio-implant applications, Mater. Sci. Eng. C. 42 (2014) 629–636. https://doi.org/10.1016/J.MSEC.2014.06.018.

[12] K.T. Rim, K.H. Koo, J.S. Park, Toxicological Evaluations of Rare Earths and Their Health Impacts to Workers: A Literature Review, Saf. Health Work. 4 (2013) 12–26. https://doi.org/10.5491/SHAW.2013.4.1.12.

[13] K.D. Ralston, N. Birbilis, C.H.J. Davies, Revealing the relationship between grain size and corrosion rate of metals, Scr. Mater. 63 (2010) 1201–1204. https://doi.org/10.1016/J.SCRIPTAMAT.2010.08.035.

[14] N. Birbilis, K.D. Ralston, S. Virtanen, H.L. Fraser, C.H.J. Davies, Grain character influences on corrosion of ECAPed pure magnesium, Corros. Eng. Sci. Technol. 45 (2010) 224–230. https://doi.org/10.1179/147842209X12559428167805.

[15] B. Ratna Sunil, T.S. Sampath Kumar, U. Chakkingal, V. Nandakumar, M. Doble, V. Devi Prasad, M. Raghunath, In vitro and in vivo studies of biodegradable fine grained AZ31 magnesium alloy produced by equal channel angular pressing, Mater. Sci. Eng. C. 59 (2016) 356–367. https://doi.org/10.1016/J.MSEC.2015.10.028.

[16] E. Mostaed, A. Fabrizi, D. Dellasega, F. Bonollo, M. Vedani, Microstructure, mechanical behavior and low temperature superplasticity of ECAP processed ZM21 Mg alloy, J. Alloys Compd. 638 (2015) 267–276. https://doi.org/10.1016/J.JALLCOM.2015.03.029.

[17] R. Bertolini, S. Bruschi, A. Ghiotti, Large Strain Extrusion Machining under Cryogenic

Cooling to Enhance Corrosion Resistance of Magnesium Alloys for Biomedical Applications, Procedia Manuf. 26 (2018) 217–227. https://doi.org/10.1016/J.PROMFG.2018.07.030.

[18] Z. Pu, J.C. Outeiro, A.C. Batista, O.W. Dillon, D.A. Puleo, I.S. Jawahir, Surface Integrity in Dry and Cryogenic Machining of AZ31B Mg Alloy with Varying Cutting Edge Radius Tools, Procedia Eng. 19 (2011) 282–287. https://doi.org/10.1016/J.PROENG.2011.11.113.

[19] M. Peron, R. Bertolini, A. Ghiotti, J. Torgersen, S. Bruschi, F. Berto, Enhancement of stress corrosion cracking of AZ31 magnesium alloy in simulated body fluid thanks to cryogenic machining, J. Mech. Behav. Biomed. Mater. 101 (2020) 103429. https://doi.org/10.1016/J.JMBBM.2019.103429.

[20] R. Smeets, B. Stadlinger, F. Schwarz, B. Beck-Broichsitter, O. Jung, C. Precht, F. Kloss, A. Gröbe, M. Heiland, T. Ebker, T. Ebker, Impact of Dental Implant Surface Modifications on Osseointegration, Biomed Res. Int. 2016 (2016) 1–16. https://doi.org/10.1155/2016/6285620.

[21] T. Albrektsson, A. Wennerberg, Oral implant surfaces: Part 1--review focusing on topographic and chemical properties of different surfaces and in vivo responses to them., Int. J. Prosthodont. 17 (n.d.) 536–43. http://www.ncbi.nlm.nih.gov/pubmed/15543910 (accessed October 30, 2017).

[22] R. Bertolini, S. Bruschi, A. Ghiotti, L. Pezzato, M. Dabalà, The Effect of Cooling Strategies and Machining Feed Rate on the Corrosion Behavior and Wettability of AZ31 Alloy for Biomedical Applications, Procedia CIRP. 65 (2017) 7–12. https://doi.org/10.1016/J.PROCIR.2017.03.168.

[23] T.S.N. Sankara Narayanan, I.-S. Park, M.H. Lee, Surface modification of magnesium and its alloys for biomedical applications. Volume 2, Modification and coating techniques, n.d.

[24] T. Lei, Anodic electrodeposition of MgO coatings to improve corrosion resistance in vivo, in: Surf. Modif. Magnes. Its Alloy. Biomed. Appl., Elsevier Inc., 2015: pp. 135–150. https://doi.org/10.1016/B978-1-78242-078-1.00006-2.

[25] T.F. da Conceição, N. Scharnagl, Fluoride conversion coatings for magnesium and its alloys for the biological environment, in: Surf. Modif. Magnes. Its Alloy. Biomed. Appl., Elsevier Inc., 2015: pp. 3–21. https://doi.org/10.1016/B978-1-78242-078-1.00001-3.

[26] Q. Li, Sol-gel coatings to improve the corrosion resistance of magnesium (Mg) alloys, in: Corros. Prev. Magnes. Alloy. A Vol. Woodhead Publ. Ser. Met. Surf. Eng., Elsevier Ltd, 2013: pp. 469–485. https://doi.org/10.1533/9780857098962.3.469.

[27] I.S. Abela, Physical vapour deposition on Mg alloys for biomedical applications, in: Surf. Modif. Magnes. Its Alloy. Biomed. Appl., Elsevier Inc., 2015: pp. 81–100. https://doi.org/10.1016/B978-1-78242-078-1.00004-9.

[28] X. Liu, Q. Yang, Z. Li, W. Yuan, Y. Zheng, Z. Cui, X. Yang, K.W.K. Yeung, S. Wu, A combined coating strategy based on atomic layer deposition for enhancement of corrosion resistance of AZ31 magnesium alloy, Appl. Surf. Sci. 434 (2018) 1101–1111. https://doi.org/10.1016/J.APSUSC.2017.11.032.

[29] E. Marin, A. Lanzutti, L. Guzman, L. Fedrizzi, Chemical and electrochemical characterization of TiO2/Al2O3 atomic layer depositions on AZ-31 magnesium alloy, J.

Coatings Technol. Res. 9 (2012) 347–355. https://doi.org/10.1007/s11998-011-9372-8.

[30] E. Marin, A. Lanzutti, L. Paussa, L. Guzman, L. Fedrizzi, Long term performance of atomic layer deposition coatings for corrosion protection of stainless steel, Mater. Corros. 66 (2015) 907–914. https://doi.org/10.1002/maco.201408012.

[31] C.X. Shan, X. Hou, K.L. Choy, Corrosion resistance of TiO2 films grown on stainless steel by atomic layer deposition, Surf. Coatings Technol. 202 (2008) 2399–2402. https://doi.org/10.1016/j.surfcoat.2007.08.066.

[32] T. Kasuga, H. Kondo, M. Nogami, Apatite formation on TiO2 in simulated body fluid, J. Cryst. Growth. 235 (2002) 235–240. https://doi.org/10.1016/S0022-0248(01)01782-1.

[33] X.X. Wang, S. Hayakawa, K. Tsuru, A. Osaka, Bioactive titania gel layers formed by chemical treatment of Ti substrate with a H2O2/HCl solution, Biomaterials. 23 (2002) 1353–1357. https://doi.org/10.1016/S0142-9612(01)00254-X.

[34] M. Uchida, H.-M. Kim, T. Kokubo, T. Nakamura, APATITE-FORMING ABILITY OF TITANIA GELS WITH DIFFERENT STRUCTURES, in: Bioceramics, WORLD SCIENTIFIC, 1999: pp. 149–152. https://doi.org/10.1142/9789814291064_0036.

[35] J.-M. Wu, S. Hayakawa, K. Tsuru, A. Osaka, Low-Temperature Preparation of Anatase and Rutile Layers on Titanium Substrates and Their Ability To Induce in Vitro Apatite Deposition, J. Am. Ceram. Soc. 87 (2004) 1635–1642. https://doi.org/10.1111/j.1551-2916.2004.01635.x.

[36] R. Osman, M. Swain, A Critical Review of Dental Implant Materials with an Emphasis on Titanium versus Zirconia, Materials (Basel). 8 (2015) 932–958. https://doi.org/10.3390/ma8030932.

[37] H. Harianawala, M. Kheur, S. Kheur, T. Sethi, A. Bal, M. Burhanpurwala, F. Sayed, Biocompatibility of Zirconia, n.d.

[38] L. Rimondini, L. Cerroni, A. Carrassi, P. Torricelli, Bacterial colonization of zirconia ceramic surfaces: an in vitro and in vivo study., Int. J. Oral Maxillofac. Implants. 17 (n.d.) 793–8. http://www.ncbi.nlm.nih.gov/pubmed/12507238 (accessed January 23, 2020).

[39] M. Peron, F. Berto, J. Torgersen, Stress corrosion cracking behavior of zirconia ALD–coated AZ31 alloy in simulated body fluid, Mater. Des. Process. Commun. (2019) mdp2.126. https://doi.org/10.1002/mdp2.126.

[40] M. Peron, J. Torgersen, F. Berto, Effect of Zirconia ALD coating on stress corrosion cracking of AZ31 alloy in simulated body fluid, in: Procedia Struct. Integr., Elsevier B.V., 2019: pp. 538–548. https://doi.org/10.1016/j.prostr.2019.08.198.

[41] C.R. Kruse, M. Singh, S. Targosinski, I. Sinha, J.A. Sørensen, E. Eriksson, K. Nuutila, The effect of pH on cell viability, cell migration, cell proliferation, wound closure, and wound reepithelialization: In vitro and in vivo study, Wound Repair Regen. 25 (2017) 260–269. https://doi.org/10.1111/wrr.12526.

[42] L.-E. Monfoulet, P. Becquart, D. Marchat, K. Vandamme, M. Bourguignon, E. Pacard, V. Viateau, H. Petite, D. Logeart-Avramoglou, The pH in the Microenvironment of Human Mesenchymal Stem Cells Is a Critical Factor for Optimal Osteogenesis in Tissue-Engineered Constructs, Tissue Eng. Part A. 20 (2014) 1827–1840. https://doi.org/10.1089/ten.tea.2013.0500.

[43] J.A. Field, A. Luna-Velasco, S.A. Boitano, F. Shadman, B.D. Ratner, C. Barnes, R. Sierra-Alvarez, Cytotoxicity and physicochemical properties of hafnium oxide nanoparticles, Chemosphere. 84 (2011) 1401–1407. https://doi.org/10.1016/j.chemosphere.2011.04.067.

[44] S. Mohammadi, M. Esposito, M. Cucu, L.E. Ericson, P. Thomsen, Tissue response to hafnium, J. Mater. Sci. Mater. Med. 12 (2001) 603–611. https://doi.org/10.1023/A:1011237610299.

[45] T. Kokubo, H. Takadama, How useful is SBF in predicting in vivo bone bioactivity?, Biomaterials. 27 (2006) 2907–2915. https://doi.org/10.1016/J.BIOMATERIALS.2006.01.017.

[46] G. Song, A. Atrens, D. StJohn, An Hydrogen Evolution Method for the Estimation of the Corrosion Rate of Magnesium Alloys, in: Magnes. Technol. 2001, John Wiley & Sons, Inc., Hoboken, NJ, USA, 2013: pp. 254–262. https://doi.org/10.1002/9781118805497.ch44.

[47] ISO 10993-12:2012 - Biological evaluation of medical devices -- Part 12: Sample preparation and reference materials, (n.d.). https://www.iso.org/standard/53468.html (accessed December 26, 2018).

[48] ISO 10993-5:2009 - Biological evaluation of medical devices -- Part 5: Tests for in vitro cytotoxicity, (n.d.). https://www.iso.org/standard/36406.html (accessed December 26, 2018).

[49] S. Nezar, N. Saoula, S. Sali, M. Faiz, M. Mekki, N.A. Laoufi, N. Tabet, Properties of TiO 2 thin films deposited by rf reactive magnetron sputtering on biased substrates, Appl. Surf. Sci. 395 (2017) 172–179. https://doi.org/10.1016/j.apsusc.2016.08.125.

[50] J.H. Kim, S. Lee, H.S. Im, Effect of target density and its morphology on TiO2 thin films grown on Si(100) by PLD, Appl. Surf. Sci. 151 (1999) 6–16. https://doi.org/10.1016/S0169-4332(99)00269-X.

[51] J. Yu, X. Zhao, J. Du, W. Chen, Preparation, microstructure and photocatalytic activity of the porous TiO2 anatase coating by sol-gel processing, J. Sol-Gel Sci. Technol. 17 (2000) 163–171. https://doi.org/10.1023/A:1008703719929.

[52] A.R. Chourasia, J.L. Hickman, R.L. Miller, G.A. Nixon, M.A. Seabolt, X-Ray Photoemission Study of the Oxidation of Hafnium, Int. J. Spectrosc. 2009 (2009) 1–6. https://doi.org/10.1155/2009/439065.

[53] H. Hernández-Arriaga, E. López-Luna, E. Martínez-Guerra, M.M. Turrubiartes, A.G. Rodríguez, M.A. Vidal, Growth of HfO2/TiO2 nanolaminates by atomic layer deposition and HfO2-TiO2 by atomic partial layer deposition, J. Appl. Phys. 121 (2017). https://doi.org/10.1063/1.4975676.

[54] C. Morant, L. Galán, J.M. Sanz, An XPS study of the initial stages of oxidation of hafnium, Surf. Interface Anal. 16 (1990) 304–308. https://doi.org/10.1002/sia.740160163.

[55] T.S. Lim, H.S. Ryu, S.H. Hong, Electrochemical corrosion properties of CeO 2-containing coatings on AZ31 magnesium alloys prepared by plasma electrolytic oxidation, Corros. Sci. 62 (2012) 104–111. https://doi.org/10.1016/j.corsci.2012.04.043.

[56] G. Song, A. Atrens, D. St. John, X. Wu, J. Nairn, The anodic dissolution of magnesium

in chloride and sulphate solutions, Corros. Sci. 39 (1997) 1981–2004. https://doi.org/10.1016/S0010-938X(97)00090-5.

[57] Q. Yang, W. Yuan, X. Liu, Y. Zheng, Z. Cui, X. Yang, H. Pan, S. Wu, Atomic layer deposited ZrO 2 nanofilm on Mg-Sr alloy for enhanced corrosion resistance and biocompatibility, Acta Biomater. 58 (2017) 515–526. https://doi.org/10.1016/j.actbio.2017.06.015.

[58] Y. Liu, Z. Yu, S. Zhou, L. Wu, Self-assembled monolayers on magnesium alloy surfaces from carboxylate ions, Appl. Surf. Sci. 252 (2006) 3818–3827. https://doi.org/10.1016/j.apsusc.2005.05.072.

[59] J. Zhao, X. Xie, C. Zhang, Effect of the graphene oxide additive on the corrosion resistance of the plasma electrolytic oxidation coating of the AZ31 magnesium alloy, Corros. Sci. 114 (2017) 146–155. https://doi.org/10.1016/j.corsci.2016.11.007.

[60] H. Yang, K. Xia, T. Wang, J. Niu, Y. Song, Z. Xiong, K. Zheng, S. Wei, W. Lu, Growth, in vitro biodegradation and cytocompatibility properties of nano-hydroxyapatite coatings on biodegradable magnesium alloys, J. Alloys Compd. 672 (2016) 366–373. https://doi.org/10.1016/J.JALLCOM.2016.02.156.

[61] F. Lang, M. Föller, K. Lang, P. Lang, M. Ritter, A. Vereninov, I. Szabo, S.M. Huber, E. Gulbins, Cell Volume Regulatory Ion Channels in Cell Proliferation and Cell Death, Methods Enzymol. 428 (2007) 209–225. https://doi.org/10.1016/S0076-6879(07)28011-5.

[62] H.M. Wong, S. Wu, P.K. Chu, S.H. Cheng, K.D.K. Luk, K.M.C. Cheung, K.W.K. Yeung, Low-modulus Mg/PCL hybrid bone substitute for osteoporotic fracture fixation, Biomaterials. 34 (2013) 7016–7032. https://doi.org/10.1016/J.BIOMATERIALS.2013.05.062.

[63] A.S. Hamdy Makhlouf, Intelligent Stannate-Based Coatings of Self-Healing Functionality for Magnesium Alloys, in: Intell. Coatings Corros. Control, Elsevier Inc., 2015: pp. 537–555. https://doi.org/10.1016/B978-0-12-411467-8.00015-5.

[64] S. Il Pyun, Y.G. Yoon, E. Lugscheider, R. Mathesius, Relationship between interfacial reaction and adhesion at PVD TiO2 film-metal (Ti or Al) interfaces, Surf. Coatings Technol. 61 (1993) 233–237. https://doi.org/10.1016/0257-8972(93)90231-C.

[65] C. (Christoph) Leyens, M. (Manfred) Peters, John Wiley & Sons., Wiley InterScience (Online service), Titanium and titanium alloys : fundamentals and applications, Wiley-VCH, 2003.

[66] H. Yang, L. Huang, M. Zh, Hot Forming Characteristics of Magnesium Alloy AZ31 and Three-Dimensional FE Modeling and Simulation of the Hot Splitting Spinning Process, in: Magnes. Alloy. - Des. Process. Prop., InTech, 2011. https://doi.org/10.5772/13778.

[67] H. Hayashi, T. Saitou, N. Maruyama, H. Inaba, K. Kawamura, M. Mori, Thermal expansion coefficient of yttria stabilized zirconia for various yttria contents, Solid State Ionics. 176 (2005) 613–619. https://doi.org/10.1016/j.ssi.2004.08.021.

[68] D.R. Hummer, P.J. Heaney, J.E. Post, Thermal expansion of anatase and rutile between 300 and 575 K using synchrotron powder X-ray diffraction, Powder Diffr. 22 (2007) 352–357. https://doi.org/10.1154/1.2790965.

[69] R.P. Haggerty, P. Sarin, Z.D. Apostolov, P.E. Driemeyer, W.M. Kriven, Thermal

Expansion of HfO_2 and ZrO_2, J. Am. Ceram. Soc. 97 (2014) 2213–2222. https://doi.org/10.1111/jace.12975.

[70] B. Elsener, A. Rota, H. Böhni, Impedance Study on the Corrosion of PVD and CVD Titanium Nitride Coatings, Mater. Sci. Forum. 44–45 (1991) 29–38. https://doi.org/10.4028/www.scientific.net/msf.44-45.29.

[71] W. Li, D.Y. Li, Influence of surface morphology on corrosion and electronic behavior, Acta Mater. 54 (2006) 445–452. https://doi.org/10.1016/j.actamat.2005.09.017.

[72] M.A. Turchanin, P.G. Agraval, Cohesive energy, properties, and formation energy of transition metal alloys, Powder Metall. Met. Ceram. 47 (2008) 26–39. https://doi.org/10.1007/s11106-008-0006-3.

[73] M.L. González-Martín, L. Labajos-Broncano, B. Jańczuk, J.M. Bruque, Wettability and surface free energy of zirconia ceramics and their constituents, J. Mater. Sci. 34 (1999) 5923–5926. https://doi.org/10.1023/A:1004767914895.

[74] F. Zhang, B.W. Robinson, H. De Villiers-Lovelock, R.J.K. Wood, S.C. Wang, Wettability of hierarchically-textured ceramic coatings produced by suspension HVOF spraying, J. Mater. Chem. A. 3 (2015) 13864–13873. https://doi.org/10.1039/c5ta02130h.

[75] A. Wiatrowski, A. Obstarczyk, M. Mazur, D. Kaczmarek, D. Wojcieszak, Characterization of HfO2 optical coatings deposited by MF magnetron sputtering, Coatings. 9 (2019). https://doi.org/10.3390/COATINGS9020106.

[76] H. Li, Q. Cui, B. Feng, J. Wang, X. Lu, J. Weng, Antibacterial activity of TiO_2 nanotubes: Influence of crystal phase, morphology and Ag deposition, Appl. Surf. Sci. 284 (2013) 179–183. https://doi.org/10.1016/j.apsusc.2013.07.076.

[77] T. Sun, M. Wang, Low-temperature biomimetic formation of apatite/TiO_2 composite coatings on Ti and NiTi shape memory alloy and their characterization, Appl. Surf. Sci. 255 (2008) 396–400. https://doi.org/10.1016/j.apsusc.2008.06.123.

Chapter 6

Atomic Layer Deposited thin films: on their effect on the SCC susceptibility of AZ31 alloy

Paper VI: Effect of titania and zirconia ALD coating on stress corrosion cracking susceptibility of AZ31 alloy in simulated body fluid

M. Peron[1], A. Bin Afif, A. Dadlani, F. Berto, J. Torgersen

Department of Industrial and Mechanical Engineering, Norwegian University of Science and Technology, Richard Birkelands vei 2b, 7034 Trondheim, Norway

Abstract[2]

Recently, magnesium and its alloys have been widely studied as materials for temporary implant devices. However, one of the main limitations hampering their use in these applications is the occurrence of corrosion-assisted cracking phenomena, such as stress corrosion cracking (SCC) and corrosion fatigue (CF). This work aims to provide insights and performance improvements regarding the SCC of AZ31 alloy coated with 100 nm thick layers of titania and zirconia produced by atomic layer deposition (ALD). Slow strain rate tests have been carried out in SBF at 37 °C with an applied strain rate equal to 2.6 10^{-6} s^{-1}. The presence of the coating provided a reduction in the SCC susceptibility, measured by means of the UTS and elongation to failure susceptibility indices (I_{UTS} and I_{ε}). In particular, the I_{UTS} is reduced by 6% and 70% and the I_{ε} is reduced by more than 40% and 76% with a titania and zirconia layer, respectively. We assess the underlying mechanisms leading to this drastic change in properties discussing potentiodynamic polarization, hydrogen evolution and fracture behavior. The presented results can be useful making Mg a more commonplace implant material, where the conformality and quality of ALD coatings may advance the field.

Keywords: Atomic Layer Deposition (ALD); titania (TiO_2); zirconia (ZrO_2); magnesium; Stress Corrosion Cracking (SCC)

6.1. Introduction

In the last years, orthopedic surgeries are becoming more and more common [1,2]. The materials currently used in orthopedic surgery are permanent metallic materials, such as stainless steel, titanium, and cobalt-chromium alloys [3]. However, their implementations in biomedical applications are coupled with two main drawbacks, such as the arising of the stress-shielding phenomenon as a consequence of the great difference in elastic modulus of these materials compared to that of human bone [4–11] and the need of secondary surgical intervention due to the risk of long-term complications [12–16]. To solve these drawbacks, biodegradable materials have gained

[1] Corresponding author
[2] *Materials & Design* (submitted paper)

wide interest [17]. In particular, Magnesium (Mg) is one of the most attractive candidates for biodegradable applications due to its excellent bio-mechanical compatibility with the human physiology, particularly its mechanical compatibility to bones [17–20]. However, despite their highly attractive properties, Mg and its alloys have not yet been used as implants materials because of their high corrosion rates, especially in the human body fluid containing chlorides. The latter gives rise to an immature drop in mechanical integrity of the device before accomplishing its defined mission [21]. Even more severe than the corrosion rate are the critical hydrogen gas bubbles and the alkalization resulting from an accelerated corrosion of Mg in human body. This leads to the accumulation of hydrogen bubbles in the form of gas pockets next to the implant, which, consequently, causes the necrosis of tissues. If the corrosion rate of a Mg implant could be adequately tailored, hydrogen evolution may be suppressed decelerating the formation of critical subcutaneous bubbles. This may reduce the alkalization effect to a level that can be easily balanced by metabolic mechanisms. However, the challenge is not only of chemical origin. The implant must also possess adequate resistance to cracking under the simultaneous action of the corrosive environment and the mechanical load it is subject to in the human body. As such, corrosion-assisted cracking phenomena, such as stress corrosion cracking (SCC) and corrosion fatigue (CF) were reported to cause the failure of several traditional implants [22–25]. SCC is particularly dangerous as it leads to a sudden and catastrophic failure under mechanical loading conditions otherwise considered to be safe. Mg and its alloys have been reported to be susceptible to SCC in simulated physiological conditions [26–28]. It is thus important to develop Mg-based implants that confer a combination of strength and corrosion resistance in human body fluid.

A plethora of studies focus on corrosion mitigation strategies all the way from alloying to surface modifications [29–31]. Yet, the literature on improving their resistance to corrosion-assisted cracking is limited. Mohajernia et al. [32] reported that hydroxyapatite coatings containing multi-walled carbon nanotubes reduced the corrosion current density of AZ31 alloy by three order of magnitude when the specimens were exposed to simulated body fluid (SBF) at 37 °C. The authors performed elongation to failure experiments, reporting the application of the coating to increase of the elongation to failure of AZ31 samples about 70% when subjected to slow strain rate tests (SSRT) in the same environment. Chen et al. [33] coated Mg-4Zn-0.6Zr-0.4Sr with a composite coating consisting of a poly (lactic-co-glycolic acid) (PLGA) superimposed to a micro-arc oxidation (MAO) layer and reported an increase in the elongation to failure in modified simulated body fluid of about 120% as compared to the bare alloy. However, the aforementioned coating technologies have limitations in line of sight, conformality, density and biocompatibility as well as limited controllability of the thickness. Recently, a new coating technique has been introduced. Atomic Layer Deposition (ALD) is a coating technique based on chemical vapor deposition (CVD) which prepares thin films with high conformality offering thickness control on the atomic level [34]. The obtained films are dense and pin-hole free. In fact, since ALD is based on chemical reactions and not physical depositions, it provides superior film uniformity [35]. TiO_2 and ZrO_2 layers deposited by this technique have been shown to provide an efficient improvement in the corrosion resistance of Mg alloys. Marin et al. [36] reported that a 100 nm thick ALD TiO_2 reduced the corrosion current density of a commercial AZ31 Mg alloy from 10^{-4} A/cm^2 to 10^{-6} A/cm^2. Liu et al. reported that a 10

nm ALD ZrO_2 coating reduced the corrosion current density of a commercial AZ31 Mg alloy from 5.1 10^{-4} A/cm^2 to 2.7 10^{-7} A/cm^2 [37]. Also Yang et al. [38] reported a decrease of three orders of magnitude in the corrosion current density after the application of a 40 nm thick ALD ZrO_2 coating on a Mg-1Sr alloy. However, the assessment of the effect of ALD coatings on the SCC susceptibility is still limited. Some preliminary results have been published by the authors showing promising results of the application of 100 nm thick ZrO_2 layer on AZ31 Mg alloy [39,40], but, to the best of our knowledge, no thorough investigation on the SCC susceptibility has been performed. In this work, we aim to fill this gap, investigating the SCC susceptibility of AZ31 alloy coated with a 100 nm thick ZrO_2 ALD layer. In addition, the SCC susceptibility of AZ31 alloy coated with 100 nm thick TiO_2 ALD layer is shown. Slow Strain Rate Tests (SSRTs) at strain rate equal to 2.6 10^{-6} s^{-1} have been carried out, and the samples were immersed in simulated body fluid at 37 °C for the whole duration of the tests. The behavior of bare samples was investigated as a reference. To elaborate on the different behavior shown by bare and TiO_2 and ZrO_2 coated samples, the authors evaluated the corrosion behavior through potentiodynamic polarization curves and hydrogen evolution experiments and analyzed the fracture surfaces after SSRTs with a Scanning Electron Microscope (SEM).

6.2. Materials and methods

6.2.1. Materials and environment

AZ31 Mg alloy was supplied in the form of commercially available bars. The microstructure of the material in the as-received condition is shown in Figure 6.1 and consists of a quite homogeneous α matrix. The initial grain size was measured by the linear intercept method resulting in sizes of 13.2 ± 8 μm.

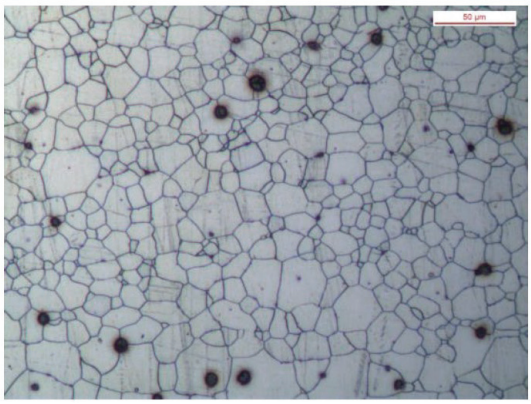

Figure 6.1: Microstructure of the AZ31 alloy in the as-received condition.

The test medium was a simulated body fluid (SBF) prepared according to Ref. [41].

6.2.2. Atomic Layer Deposition

The deposition of the ALD coatings was performed in a commercial ALD reactor (Savannah S200, Veeco Instruments Inc., Massachusetts, USA) through successive cyclic reactions. 926 successive cycles of ZrO_2 utilizing Tetrakis (dimethylamino) zirconium (TDMAZ) and deionized water (H_2O) as reactants were carried out at 160 °C to obtain a total thickness of 100 nm. Each cycle was composed of two parts. The first part consisted of a 250-ms TDMAZ precursor pulse and a 10-s Hi-purity N_2 purge (semiconductor grade) with a flow rate of 20 sccm to remove residual reactants and by-products from the chamber to separate the chemical vapor deposition reactions. The second part comprised a 150-ms H_2O precursor pulse and a 15-ms High-purity N_2 purge. In the process of deposition, the TDMAZ precursor and delivery lines were heated to 75 °C and 160 °C, respectively, while the H_2O precursor was kept at room temperature. During the deposition process, the ZrO_2 layer deposition rate was of approximately 1.08 Å/cycle. Concerning TiO_2, the metal organic precursor used was Tetrakis (dimethylamido) titanium (IV) (TDMA-Ti) heated to 75˚C. Each cycle was again composed of two parts. The first part consisted of a 0.1 s TDMA-Ti precursor pulse and a 5 s High-purity N_2 purge with a flow rate of 20 sccm. The second part comprised a 0.015 s H_2O precursor pulse and a 5 s High-purity N_2 purge. The deposition rate was found to be 0.5 A˚/cycle.

6.2.3. Coating characterization

X-ray photoluminescence (XPS) measurements were conducted to assess the chemical composition of the TiO_2, and ZrO_2 coating. Kratos Analytical XPS Microprobe (Kratos Analytical Ltd, Manchester, UK) which uses Al (Kα) radiation of 1486 eV in a vacuum environment of $5*10^{-9}$ Torr was used. CasaXPS software was used to analyze the XPS data.

6.2.4. Potentiodynamic polarization curves

Discs with a diameter of 29 mm and a thickness of 2 mm were manufacturing using a lathe from the commercially available bars. The samples were then grounded with 2000 grit silicon carbide papers and cleaned with acetone and ethanol for five minutes in ultrasonic bath. Some of these samples were then coated as described in Section 2.2. Potentiodynamic polarization curves of bare and coated samples were carried out in simulated body fluid (SBF) with a pH of 7.4 on a Gamry Reference 600+ potentiostat. The electrochemical tests used a three-electrode equipment with the bare or coated samples as a working electrode, a Hg/Hg_2SO_4 electrode as a reference electrode, and a platinum plate as counter electrode. The area of the samples exposed to SBF was 1 cm^2 (excluding roughness induced area deviations). The potentiodynamic polarization tests were conducted at a stable open-circuit potential after a stabilization period of 30 min. The scan rate of the potentiodynamic polarization test was 0.5 mV/s.

6.2.5. Hydrogen evolution tests

During the immersion tests, the chemical reaction between Mg and electrolyte occurs as shown in the following equation [17]:

$$Mg + 2H_2O \rightarrow Mg(OH)_2 + H_2 \quad (6.1)$$

From the above equation it can be easily understood that the dissolution of one Mg atom generates one H_2 gas molecule. In other words, the evolution of one mole of H_2 gas corresponds to the dissolution of one mole of Mg. Therefore, measuring the volume of hydrogen evolved allows to assess the corrosion rate of Mg and its alloys in a way that allows to overcome the drawbacks of the weight loss method and of the electrochemical techniques [42]. To do so, cubic samples of 5 mm side lengths were obtained from the as-received material and they were grounded with 2000 grit silicon carbide papers and cleaned with acetone and ethanol for five minutes in ultrasonic bath. Some of these samples were then coated as described in Section 2.2. The immersion tests were carried out in SBF at 37 °C for 7 days individually to monitor the hydrogen evolution. Hydrogen bubbles were collected into a burette from each sample as suggested in [42].

6.2.6. Slow Strain Rate Tests (SSRT)

Cylindrical dog-bone-shaped samples, with dimensions reported in Figure 6.2, were tested according to a standard [43]. The sample were machined from the received bars using a lathe.

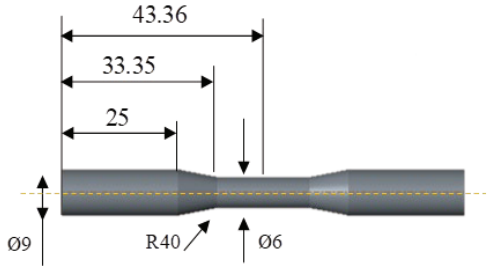

Figure 6.2: Geometry and dimensions of the samples for SSRTs

The samples were then grounded with 2000 grit silicon carbide papers and cleaned with acetone and ethanol for five minutes in ultrasonic bath. Some of these samples were then coated as described in Section 6.2.2.
The SSRTs were carried out both on bare, TiO_2 and ZrO_2 coated samples, respectively at a strain rate of $3.5 \cdot 10^{-6}$ s^{-1} in SBF solution held at body temperature (37 ± 1°C). The strain rate value was chosen in order to render the Mg alloy susceptible to SCC [44]. A schematic representation of the experimental set-up is shown in Figure 6.2.3. The sample was immersed for the whole duration of the test and the SBF was constantly changed with a pumping system. The SBF container was immersed in a water bath. A thermometer monitored its temperature. When the temperature was below its set value, a commercial resistance heating element placed inside the water bath automatically turned on until the desired temperature was reached again. In addition, while carrying out the SSRTs, the area of the specimen exposed to SBF was restricted to its gauge length by using Teflon tapes wrapped around the rest of the specimen thereby

maintaining a constant area of exposure to the corrosive solution as well as avoiding the possibility of galvanic effects with other components of the testing set-up.

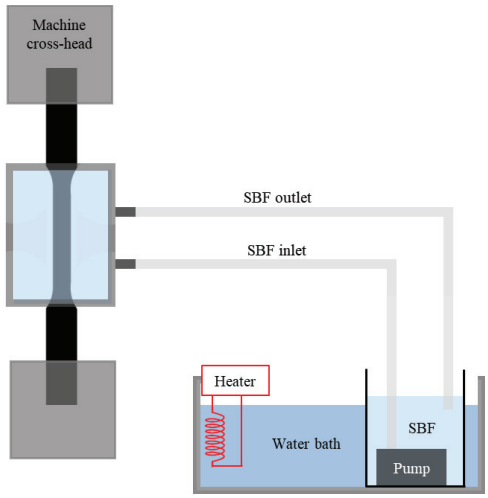

Figure 6.3: Schematic representation of the SSRT set-up.

In order to quantify the AZ31 SCC sensitivity, the susceptibility indices I_{UTS} and I_{ε} were calculated according to Eq. (6.2) and Eq. (6.3) [45]:

$$I_{UTS} = \frac{UTS_{air} - UTS_{SBF}}{UTS_{air}} \tag{6.2}$$

$$I_{\varepsilon} = \frac{\varepsilon_{air} - \varepsilon_{SBF}}{\varepsilon_{air}} \tag{6.3}$$

where *UTS* is the Ultimate Tensile Strength and ε the elongation at failure both evaluated during tests conducted in SBF and air. When the value of the susceptibility index approaches zero, the material is considered to be highly resistant to SCC, namely the greater the index the greater the susceptibility to SCC.

6.2.7. Fractography

The specimen fracture surfaces after SSRTs were cleaned by immersion for one minute in a solution prepared using 50 g chromium trioxide (CrO_3), 2.5 g silver nitrate ($AgNO_3$) and 5 g barium nitrate ($Ba(NO_3)_2$) in 250 ml distilled water, as suggested by [46]. The specimens were then washed with distilled water and finally ultrasonically cleaned in acetone for 10 min. The fracture surfaces were observed by means of a FEI™ QUANTA 450 SEM (Thermo Fisher Scientific Inc., USA).

6.3. Results

6.3.1. Coating characterization

XPS was conducted to determine the chemical composition of the ALD deposited TiO_2 and ZrO_2. The measurements were carried out on thin films deposited on p-doped <100> 500µm thick, 2 inch Si wafers, in order to have minimum effect of the underlying substrate. To start with, etching was conducted on the surface to remove the effect of environmental contamination and surface oxidation. Surface was etched for 180 seconds with an energy of 2 KeV. On TiO_2 substrates, regional scans for Ti, O and C were carried out at high resolution. Negligible amounts of C were observed in the regional scan indicating an ideal deposition without any process contamination. Figure 6.4 (a) and (b) are regional scan of Ti and O, respectively. For Ti, peaks corresponding to the core level binding energies, 459 eV and 464 eV of Ti $2p_{3/2}$ and Ti $2p_{1/2}$ are observed, which is due to Ti^{4+} oxidation state in TiO_2 [47]. The shoulder at lower energy around 456 eV is due to the presence of Ti^{3+} caused by the argon etching step [48]. The O peak at 531 eV is related to O atoms in TiO_2 phase [49], while the small shoulder at higher energy is due to O in OH groups present in the form impurities. Stoichiometric TiO_2 thin films should have Ti and O in 1:2 ratio i.e. 66.7% oxygen and 33.3% titanium, but in our case, we have found the composition to be around 60% for oxygen and 40% titanium, thus indicating an oxygen deficient deposition.

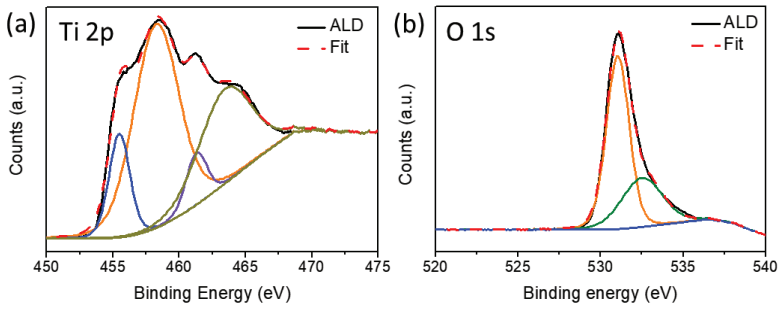

Figure 6.4: XPS spectra for ALD deposited TiO_2 (a) Ti 2p (b) O 1s

Regional scans of Zr, O and C were also carried out for ZrO_2 coated samples at high resolution. No peak was observed in the high-resolution scan for elemental carbon indicating a carbon free ALD deposition. The high resolution spectra (Figure 6.5a) of Zr 3d shows two peaks at binding energy 182 eV and 184 eV, which correspond to Zr $3d_{5/2}$ and Zr $3d_{3/2}$, respectively. The scan conducted for O 1s (Figure 6.5b) showed a peak at 530 eV which belongs to ZrO_2 and the shoulder on the higher energy side is due to the oxidation of metal in air forming ZrO. The quantification calculation using CASA XPS software showed a composition as 40 % Zr and 60% O. This indicates an oxygen deficient ZrO_2 thin film.

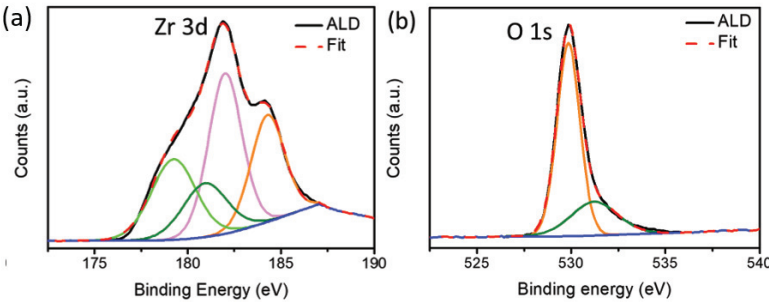

Figure 6.5: XPS spectra for ALD deposited ZrO_2 (a) Zr 3d (b) O 1s

6.3.2. Potentiodynamic polarization curves

The potentiodynamic polarization curves of the TiO_2 and ZrO_2 coated and bare samples are shown in Figure 6.6 and the results of the corrosion potentials (E_{corr}) and of the corrosion current densities (i_{corr}) are shown in Table 6.1. Compared to the uncoated alloy, the corrosion current densities of the coated samples display declining trends (Figure 6.6 and Table 6.1). Since a lower corrosion current density corresponds to a smaller corrosion rate, this suggests that the application of coatings protects Mg alloys from corrosion, which is consistent with previous reports [37,38,50]. In particular, the ZrO_2 coating is shown to provide a higher reduction of the corrosion current density compared to the TiO_2 coating.

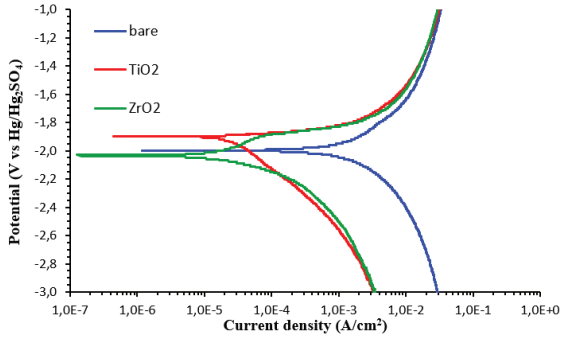

Figure 6.6: Potentiodynamic polarization curves of bare (blue), TiO_2 coated (red) and ZrO_2 coated (green) AZ31 alloy in SBF.

	Bare	TiO_2 coating	ZrO_2 coating
E_{corr} (V)	-2.0	-1.90	-2.02
i_{corr} (A/cm^2)	3.0 10^{-3}	2.5 10^{-5}	1.2 10^{-6}

Table 6.1: The results of corrosion potentials (E_{corr}) and corrosion current densities (i_{corr}) for bare and coated AZ31 samples in SBF.

6.3.3. Hydrogen evolution tests

The hydrogen evolution curves of bare and coated samples are reported in Figure 6.7, and the results further suggest that the application of coatings can prevent the degradation of AZ31 alloy. In particular, the 100 nm thick ZrO_2 coating provides a better protection than the TiO_2 coating. The hydrogen evolved from the bare sample is in fact reduced by 93% with a ZrO_2 coating and by 52% with a TiO_2 coating, respectively.

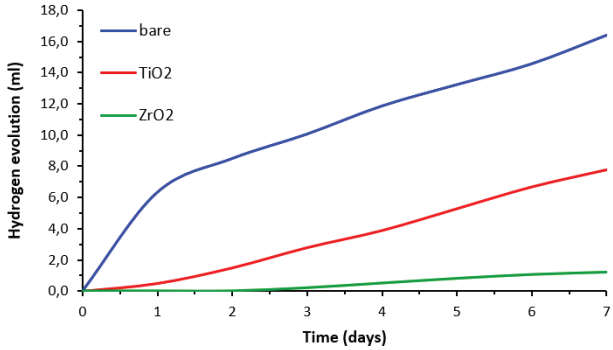

Figure 6.7: Hydrogen evolved from the immersion of bare (blue), TiO_2 coated (red) and ZrO_2 coated (green) AZ31 alloy in SBF.

6.3.4. Slow Strain Rate tests (SSRT)

The engineering stress-strain curves for the bare, TiO_2 coated and ZrO_2 coated AZ31 samples tested in air and in SBF are reported in Figure 6.8 a, b and c respectively. In addition, Table 6.2 compares the UTS and elongation at failure values obtained from the curves in Figure 6.8.

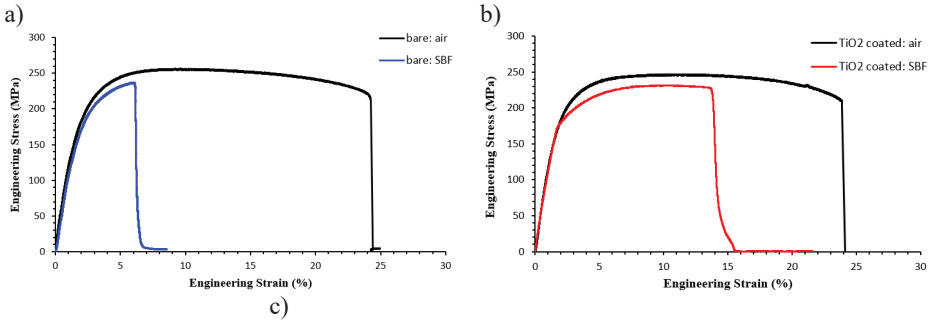

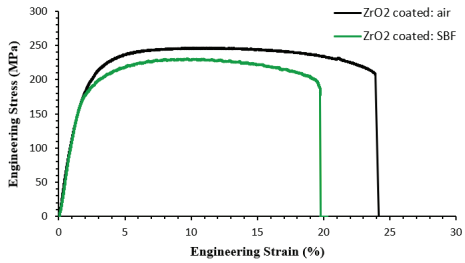

Figure 6.8: Engineering stress-strain curves of bare (a) and coated (b) AZ31 samples tested in air and SBF at 37°C and strain rate of $3.5 \cdot 10^{-6}$ s^{-1}

Surface	In Air		In SBF	
	UTS (MPa)	Elongation at failure (%)	UTS (MPa)	Elongation at failure (%)
Bare	256.3± 8.7	24.5 ± 0.7	233.3 ± 1.9	6.1 ± 0.3
TiO_2 Coated	252.7± 5.2	24.3 ± 0.6	231.4 ± 5.1	13.8 ± 0.4
ZrO_2 Coated	253.6± 5.6	24.1 ± 0.5	246.8± 1.0	19.7 ± 0.2

Table 6.2: Mechanical properties of bare and coated samples from Figure 6.8

The surface characteristics did not influence the AZ31 mechanical properties when tested in air. Both the bare and the coated samples are characterized by an excellent and comparable combination of strength and ductility. On the other hand, the coated samples were characterized by a considerably higher elongation to failure than the bare counterparts when tested in SBF, indicating a lower tendency to suffer from embrittlement in SBF. In particular, the elongation to failure of the bare samples tested in SBF was increased by 126% with the application of the TiO_2 coating and by 223% with the ZrO_2 coating.

To quantify the SCC susceptibility of the bare and coated samples, the I_{UTS} and I_{ε} indices were evaluated and are reported in Figure 6.9.

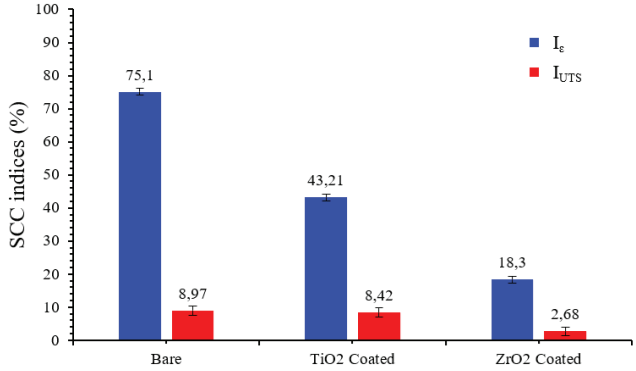

Figure 6.9: SCC indices for the bare and coated AZ31 samples

The application of 100 nm thick ZrO_2 coating is shown to be more effective in reducing the SCC susceptibility than the TiO_2 counterpart. In fact, the I_{ε} is reduced from 75.1 to

43.2 and to 18.3 applying the TiO_2 and ZrO_2 coating, respectively, while the I_{UTS} is reduced from 8.97 to 8.42 and 2.68 applying the TiO_2 and ZrO_2 coating, respectively. It is interesting to note that the impact on UTS is very low when applying the TiO_2 coating, whereas the impact on elongation is significant.

6.3.5. Fractography

Fracture surfaces of the bare samples tested in air and in SBF are reported in Figures 6.10a and 6.10b and Figure 6.10c and 6.10d, respectively. The overall view of the fracture surface confirms the ductile nature of the failure in the case of testing in air. Here, the fracture surface is characterized by a significant amount of dimples (Figures 6.10a and 6.10b), while the sample tested in SBF shows mixed mode fracture features, namely ductile and brittle fracture characteristics. In addition, the surface fracture appearance is completely different: in the case of SBF condition, both transgranular and intergranular cracks are evident, with a predominance of the former, which are absent in the case of air testing (compare Figure 6.10d with Figure 6.10b). The application of the coatings did not alter the AZ31 response mechanisms to SCC, being the fracture characterized by both a ductile and brittle zone, with the latter characterized by the presence of both intergranular and transgranular cracks. However, the application of the TiO_2 coating leads to the change of the fracture appearance in the brittle zone due to the reduced embrittlement of the material as a consequence of the reduced corrosion: in fact, while in the bare samples, the transgranular fracture was predominant, the TiO_2 coated samples show intergranular cracking as the main mechanism (Figure 6.10f). Finally, the application of the ZrO_2 coating leads to a failure that is predominantly ductile (Figure 6.10g). This is particularly apparent in the center of the sample, with the mixed mode fracture features close to the sample edges appearing to have experienced transgranular and intergranular cracking (Figure 6.10h).

a)

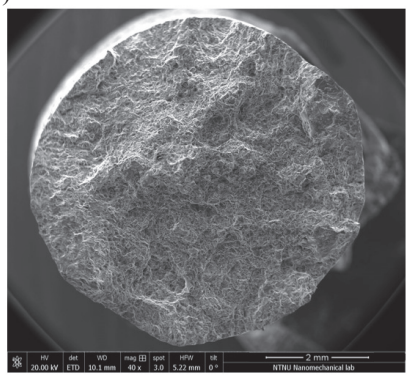

b)

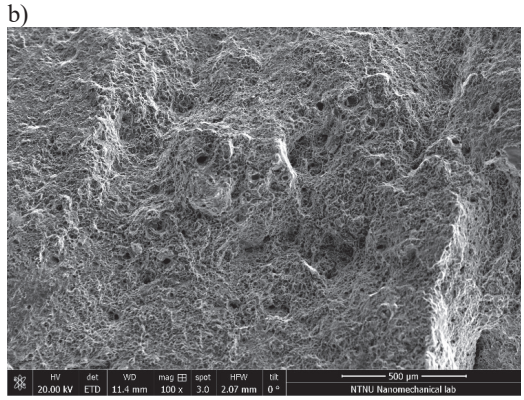

c)

d)

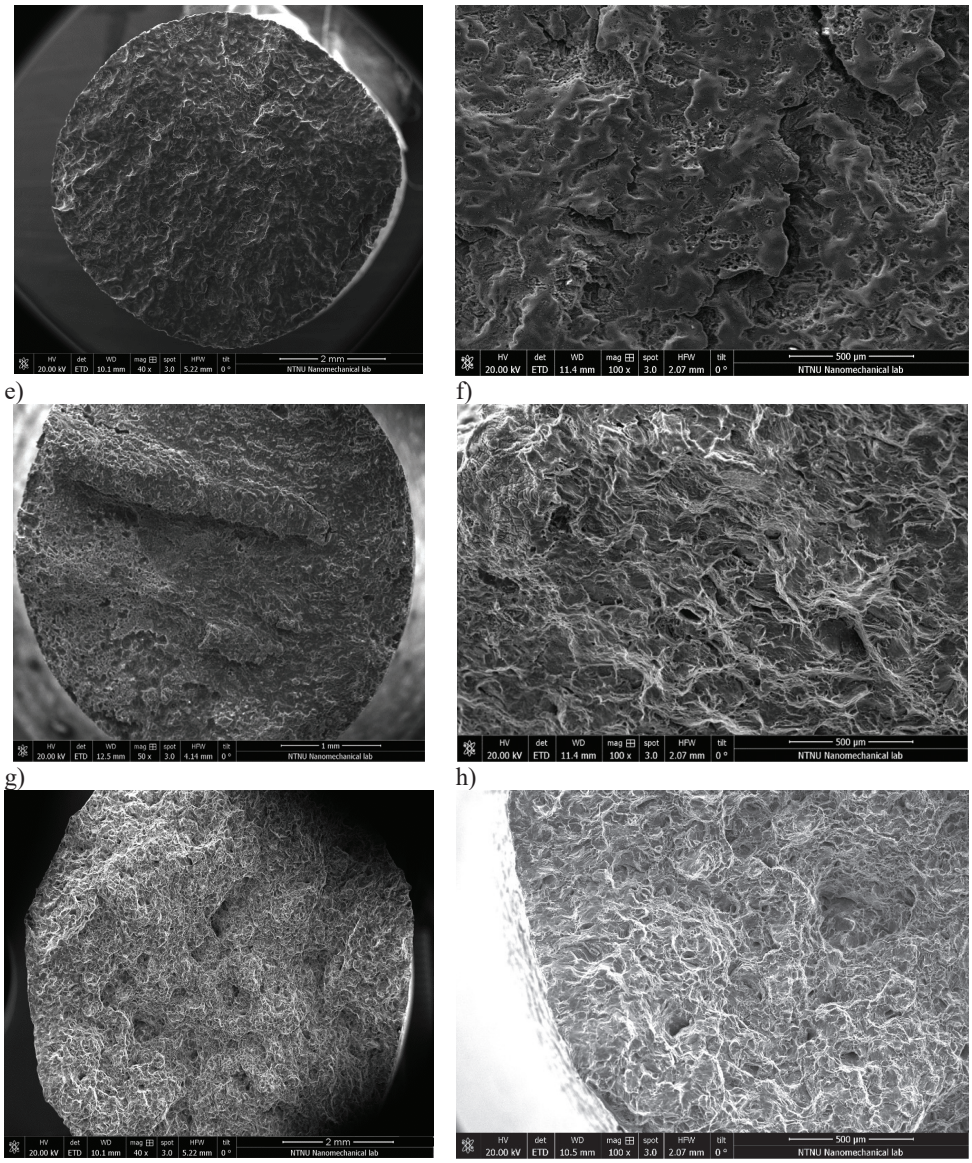

Figure 6.10: Fracture surfaces of bare samples tested in air (a and b) and in SBF (c and d), of TiO_2 coated samples tested in SBF (e and f) and of ZrO_2 coated samples tested in SBF (g and h)

The reduced corrosion of the coated samples tested in SBF with respect to the bare sample is also confirmed by the tilted views of the gauge section (compare Figure 6.11b and c with Figure 6.11a), where deep secondary cracks and some pits can be observed

in the bare samples, while no deep secondary cracks and no pits are present in the coated sample. In addition, necking can also be observed in the ZrO_2 coated samples confirming the increased ductility (Figures 6.10g and 6.10h).

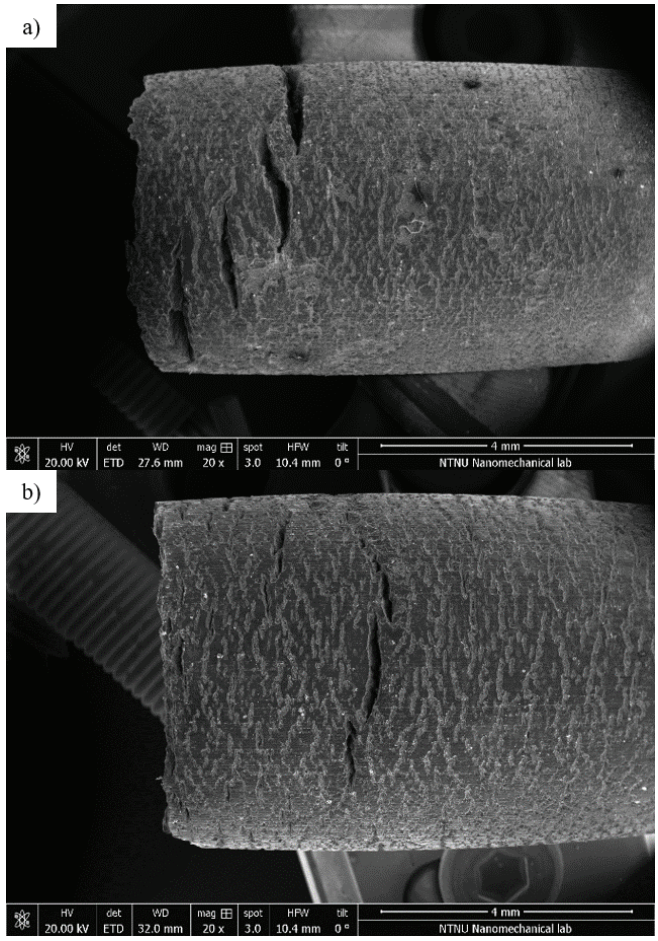

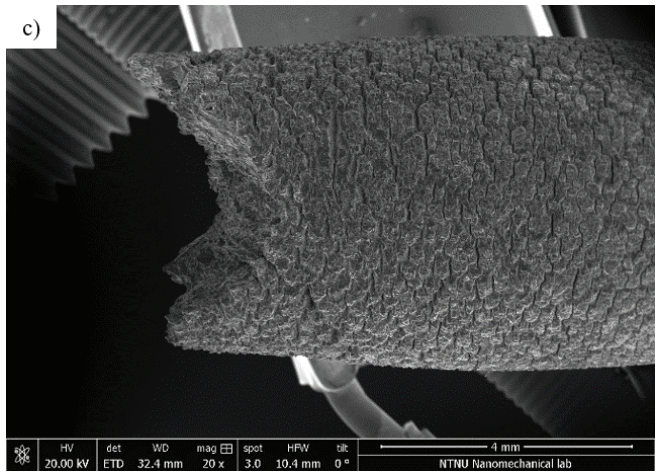

Figure 6.11: SEM fractographies of the gauge section of bare (a), of TiO_2 coated (b) and of ZrO_2 coated (c) AZ31 samples after SSRTs in SBF.

6.4. Discussions

From the experimental results reported in Figure 6.8 and from the I_{SCC} indices in Figure 6.9, the presence of both coatings yielded an increase in the mechanical performances in presence of a corrosive environment. However, the improvements provided by the TiO_2 and ZrO_2 coatings were consistently different. In fact, while the former reduced the I_{UTS} and the I_ε of 6% and 40%, respectively, the latter provided a much higher reduction in the SCC susceptibility of the AZ31 alloy. The I_{UTS} and the I_ε were reduced by 70% and 76%, respectively. This can be explained by the general SCC behavior of Mg alloys that is widely attributed to the combination of two mechanisms; (1) the anodic dissolution and (2) the cleavage-like fracture due to hydrogen embrittlement [51]. The rupture of the protective $Mg(OH)_2$ film due to the anodic dissolution or through mechanical loads allows the hydrogen evolved from the corrosion process to enter into the matrix and to embrittle the material, which ultimately leads to a premature fracture [24]. Altering the corrosion rate hence affects the SCC susceptibility directly. In particular, the lower the corrosion rate, the lower the SCC susceptibility due to a reduced effect of the anodic dissolution and of the hydrogen embrittlement phenomenon. Therefore, the reduced SCC susceptibility of the coated samples can be explained by the corrosion performances of the coatings (Figures 6.6 and 6.7). The corrosion current density of the bare samples is in fact reduced by two and three orders of magnitude with the TiO_2 and ZrO_2 coatings, respectively. In addition, the hydrogen evolved from the bare samples is reduced by 52% and 93% for TiO_2 and ZrO_2 coatings, respectively. The reduced amount of evolved hydrogen is consistently linked with the lower embrittlement of the material, shown by the mechanical tests (Figure 6.8), the fractographies of the samples tested in SBF (Figure 6.10) and by the tilted view of the gauge section (Figure 6.11). The TiO_2 coated samples are characterized by a brittle fracture zone, where the intergranular fracture, characteristic of the anodic dissolution, is predominant. This is different from the bare samples, where the transgranular fracture related to the HE

phenomenon is predominant. We can thus conclude that a lower amount of hydrogen entering the material with the application of the coating decreases its SCC susceptibility. Further improvements are achieved applying ZrO_2 coatings. The fracture behavior changes from predominantly cleavage facets towards a mixed brittle-ductile behavior where cleavage facets and dimple-like morphologies are present. The increased ductility is confirmed by the tilted views of the gauge section of ZrO_2 coated samples (Figure 6.11c), where necking can be observed. In addition, pitting was reported as main precursor for the initiation of SCC cracks [52,53]. The reduced tendency to pitting and localized corrosion of the coated samples (Figures 6.11b and 6.11c) thus represents another reason for the reduced SCC susceptibility.

The different corrosion performances of the TiO_2 and ZrO_2 coatings can be explained considering their electrochemical stabilities. ZrO_2 is electrochemically more stable than TiO_2 due its higher cohesive energy [54]. In fact, the higher the cohesive energy, the more electrochemically stable is the material and, thus, the lower the corrosion [55]. Moreover, TiO_2 is reported to be more hydrophilic than ZrO_2 [56,57] thus promoting corrosion [58]. In addition, the integrity of the coating represents another important aspect to be considered. The presence of defects such as pores and cracks provides a path for the fluid to access the substrate bypassing the protective nature of the coating, reducing its effectiveness. The underlying hypothesis of limited conformality and defects leading to the reduced protection of the underlying substrate can be formulated looking at the corrosion rate of the respective coating materials alone. Considering Faraday's law [59], TiO_2 and ZrO_2 are $0.37 \cdot 10^{-6}$ and $0.87 \cdot 10^{-7}$ mm/year, respectively [60,61], when considering their exposure to simulated body fluid at 37 °C. However, we experience a corrosion rate of $2.11 \cdot 10^{-4}$ and $1.14 \cdot 10^{-5}$ mm/year, respectively. These rates are higher by 3 and 2 orders of magnitude, respectively. The defects are usually cracks formed as a consequence of the induced residual stresses on the coating due to the difference in the thermal expansion coefficient between the coating and the substrate [62,63]. The lower number of defects in ZrO_2 with respect to that of TiO_2 coating may be attributed to the closer match of the coefficient of thermal expansion with that of AZ31 alloys. The coefficient of thermal expansion of Mg is $27 \cdot 10^{-6}$ $°C^{-1}$ [64]. ZrO_2's coefficient of thermal expansion is $11 \cdot 10^{-6}$ $°C^{-1}$, whereas that of TiO_2 is $7 \cdot 10^{-6}$ $°C^{-1}$[65,66], the mismatch between the substrate and the coating is hence lower for ZrO_2.

Finally, the reduced SCC susceptibility of the ZrO_2 coated AZ31 samples with respect to the TiO_2 counterparts may also be linked to the difference in their mechanical properties. ZrO_2 has a higher UTS and higher elongation to failure compared to TiO_2, eventually resulting in a higher protectiveness of the film under strain [67,68]. We hypothesize that the longer the coating layer resists to the applied stresses, the longer the barrier effect of the coating will last, thus increasing the resistance to SCC.

Therefore, in the choice of a coating material a multitude of factors has to be taken into account. These include the cohesive energy, the wettability and the thermal expansion mismatch of the coating to the substrate. This study also discusses the fundamental role of the mechanical characteristics of the protective layer. In particular, a high elongation to failure might guarantee the coating's integrity when strained.

6.5. Conclusion

In this study, the effect of a 100 nm thick TiO_2 and ZrO_2 coatings on the SCC susceptibility of the AZ31 Mg alloy was assessed. To this regard, SSRTs at a strain rate of $3.5 \cdot 10^{-6}$ s^{-1} were carried out in SBF at 37 °C on bare and coated samples, respectively. In addition, potentiodynamic polarization tests, hydrogen evolution tests and fracture surfaces analyses were carried out.
The main findings can be summarized as follows:

- The coated samples were shown to reduce the SCC susceptibility of AZ31 alloy. In particular, TiO_2 reduced the I_{UTS} and the I_ε of 6% and 40%, respectively, while ZrO_2 of 70% and 76%, respectively. The reduced SCC susceptibility provided by the coatings was evidenced also by the fracture surface analyses that showed a transition from a mixed mode fracture where the brittle zone was predominantly transgranular in the bare samples, to a predominance of intergranular failures in the TiO_2 coated samples and to a predominantly ductile failure for ZrO_2 coated samples.
- The different SCC susceptibility was attributed to the improved corrosion of the coated samples. The difference in the corrosion behavior between TiO_2 and ZrO_2 coated samples was related to the four main aspects, i.e. different cohesive energies, different wettability, different defect densities and sizes and different mechanical properties. ZrO_2 coatings have comparably higher cohesive energy that leads to a more electrochemically stable material. It is thus less prone to corrosion and has a lower wettability. Moreover, the lower mismatch between the coefficient of thermal expansion of ZrO_2 and magnesium with respect to that between TiO_2 and magnesium leads to a reduced amount of cracks and thus a more protective barrier to the fluid. Finally, the higher mechanical properties of ZrO_2 (higher UTS and higher elongation to failure) compared to those of TiO_2 increases the stability of the coatings in presence of mechanical stresses, and, in this way, hinders the fluid's access to the base material.

It can be concluded that the application of TiO_2 and ZrO_2 coatings are both effective methods to decrease the AZ31 sensitivity to SCC due to the increased corrosion resistance. In the choice of an appropriate coating, this work shows that cohesive energy, wettability, thermal expansion and elongation at break of the coating are important parameters to be optimized in order to provide an effective barrier.

Acknowledgement

Abdulla Bin Afif was supported by NTNU's Enabling technologies: Nanotechnology. The Research Council of Norway is acknowledged for the support to the Norwegian Micro- and Nano-Fabrication Facility, NorFab, project number 245963/F50. Anup Dadlani was funded by the Norwegian Research Council under project number 274459 Translate.

Data availability

The raw/processed data required to reproduce these findings cannot be shared at this time as the data also forms part of an ongoing study.

Bibliography Paper VI

[1] M.P. Ginebra, T. Traykova, J.A. Planell, Calcium phosphate cements as bone drug delivery systems: A review, J. Control. Release. 113 (2006) 102–110. https://doi.org/10.1016/j.jconrel.2006.04.007.

[2] http://share.iofbonehealth.org/EU-6-Material/Reports/IOF%20Report_EU.pdf, (n.d.). http://share.iofbonehealth.org/EU-6-Material/Reports/IOF Report_EU.pdf (accessed November 20, 2019).

[3] Q. Chen, G.A. Thouas, Metallic implant biomaterials, Mater. Sci. Eng. R Reports. 87 (2015) 1–57. https://doi.org/10.1016/J.MSER.2014.10.001.

[4] T.W. Bauer, J. Schils, The pathology of total joint arthroplasty.II. Mechanisms of implant failure., Skeletal Radiol. 28 (1999) 483–97. http://www.ncbi.nlm.nih.gov/pubmed/10525792 (accessed March 31, 2017).

[5] A.R. Dujovne, J.D. Bobyn, J.J. Krygier, J.E. Miller, C.E. Brooks, Mechanical compatibility of noncemented hip prostheses with the human femur, J. Arthroplasty. 8 (1993) 7–22. https://doi.org/10.1016/S0883-5403(06)80102-6.

[6] C.A. Engh, J.D. Bobyn, The influence of stem size and extent of porous coating on femoral bone resorption after primary cementless hip arthroplasty., Clin. Orthop. Relat. Res. (1988) 7–28. http://www.ncbi.nlm.nih.gov/pubmed/3370887 (accessed March 31, 2017).

[7] J. Kerner, R. Huiskes, G.H. van Lenthe, H. Weinans, B. van Rietbergen, C.A. Engh, A.A. Amis, Correlation between pre-operative periprosthetic bone density and post-operative bone loss in THA can be explained by strain-adaptive remodelling., J. Biomech. 32 (1999) 695–703. https://doi.org/10.1016/S0021-9290(99)00041-X.

[8] D.R. Sumner, J.O. Galante, Determinants of stress shielding: design versus materials versus interface., Clin. Orthop. Relat. Res. (1992) 202–12. http://www.ncbi.nlm.nih.gov/pubmed/1729005 (accessed March 31, 2017).

[9] T.M. Turner, D.R. Sumner, R.M. Urban, R. Igloria, J.O. Galante, Maintenance of proximal cortical bone with use of a less stiff femoral component in hemiarthroplasty of the hip without cement. An investigation in a canine model at six months and two years., J. Bone Joint Surg. Am. 79 (1997) 1381–90. http://www.ncbi.nlm.nih.gov/pubmed/9314401 (accessed March 31, 2017).

[10] B. Van Rietbergen, R. Huiskes, H. Weinans, D.R. Sumner, T.M. Turner, J.O. Galante, The mechanism of bone remodeling and resorption around press-fitted THA stems, J. Biomech. 26 (1993) 369–382. https://doi.org/10.1016/0021-9290(93)90001-U.

[11] J. Wolff, The Law of Bone Remodelling, Springer Berlin Heidelberg, Berlin, Heidelberg, 1986. https://doi.org/10.1007/978-3-642-71031-5.

[12] B.G. Pound, Corrosion behavior of metallic materials in biomedical applications . I . Ti and its alloys, 32 (2014) 1–20. https://doi.org/10.1515/corrrev-2014-0007.

[13] B.G. Pound, Corrosion behavior of metallic materials in biomedical applications . II . Stainless steels and Co-Cr alloys, 32 (2014) 21–41. https://doi.org/10.1515/corrrev-2014-0008.

[14] J.J. Jacobs, J.L. Gilbert, R.M. Urban, Corrosion of metal orthopaedic implants., J. Bone Joint Surg. Am. 80 (1998) 268–82. http://www.ncbi.nlm.nih.gov/pubmed/9486734 (accessed March 31, 2017).
[15] J.J. Jacobs, N.J. Hallab, A.K. Skipor, R.M. Urban, Metal degradation products: a cause for concern in metal-metal bearings?, Clin. Orthop. Relat. Res. (2003) 139–47. https://doi.org/10.1097/01.blo.0000096810.78689.62.
[16] I.B. Beech, J.A. Sunner, C.R. Arciola, P. Cristiani, Microbially-influenced corrosion: damage to prostheses, delight for bacteria., Int. J. Artif. Organs. 29 (2006) 443–52. http://www.ncbi.nlm.nih.gov/pubmed/16705614 (accessed June 20, 2017).
[17] M. Peron, J. Torgersen, F. Berto, Mg and Its Alloys for Biomedical Applications: Exploring Corrosion and Its Interplay with Mechanical Failure, Metals (Basel). 7 (2017) 252. https://doi.org/10.3390/met7070252.
[18] R.K. Singh Raman, S. Jafari, S.E. Harandi, Corrosion fatigue fracture of magnesium alloys in bioimplant applications: A review, Eng. Fract. Mech. 137 (2015) 97–108. https://doi.org/10.1016/j.engfracmech.2014.08.009.
[19] M.P. Staiger, A.M. Pietak, J. Huadmai, G. Dias, Magnesium and its alloys as orthopedic biomaterials: A review, Biomaterials. 27 (2006) 1728–1734. https://doi.org/10.1016/j.biomaterials.2005.10.003.
[20] A.C. Hänzi, A.S. Sologubenko, P.J. Uggowitzer, Design strategy for new biodegradable Mg–Y–Zn alloys for medical applications, Int. J. Mater. Res. 100 (2009) 1127–1136. https://doi.org/10.3139/146.110157.
[21] G. Song, Control of biodegradation of biocompatable magnesium alloys, Corros. Sci. 49 (2007) 1696–1701. https://doi.org/10.1016/J.CORSCI.2007.01.001.
[22] S.. Teoh, Fatigue of biomaterials: a review, Int. J. Fatigue. 22 (2000) 825–837. https://doi.org/10.1016/S0142-1123(00)00052-9.
[23] T. Akahori, M. Niinomi, K.-I. Fukunaga, I. Inagaki, Effects of microstructure on the short fatigue crack initiation and propagation characteristics of biomedical α/β titanium alloys, Metall. Mater. Trans. A. 31 (2000) 1949–1958. https://doi.org/10.1007/s11661-000-0222-z.
[24] S. Jafari, S.E. Harandi, R.K. Singh Raman, A review of stress-corrosion cracking and corrosion fatigue of magnesium alloys for biodegradable implant applications, Jom. 67 (2015) 1143–1153. https://doi.org/10.1007/s11837-015-1366-z.
[25] R.A. Antunes, M.C.L. de Oliveira, Corrosion fatigue of biomedical metallic alloys: Mechanisms and mitigation, Acta Biomater. 8 (2012) 937–962. https://doi.org/10.1016/j.actbio.2011.09.012.
[26] S. Jafari, R.K.S. Raman, C.H.J. Davies, J. Hofstetter, P.J. Uggowitzer, J.F. Löffler, Stress corrosion cracking and corrosion fatigue characterisation of MgZn1Ca0.3 (ZX10) in a simulated physiological environment, J. Mech. Behav. Biomed. Mater. 65 (2017) 634–643. https://doi.org/10.1016/J.JMBBM.2016.09.033.
[27] M.B. Kannan, R.K.S. Raman, In vitro degradation and mechanical integrity of calcium-containing magnesium alloys in modified-simulated body fluid, Biomaterials. 29 (2008) 2306–2314. https://doi.org/10.1016/J.BIOMATERIALS.2008.02.003.
[28] S. Jafari, R.K.S. Raman, C.H.J. Davies, Stress corrosion cracking of an extruded

magnesium alloy (ZK21) in a simulated body fluid, Eng. Fract. Mech. 201 (2018) 47–55. https://doi.org/10.1016/J.ENGFRACMECH.2018.09.002.
[29] Z.-R. Qi, Q. Zhang, L.-L. Tan, X. Lin, Y. Yin, X.-L. Wang, K. Yang, Y. Wang, Comparison of degradation behavior and the associated bone response of ZK60 and PLLA in vivo, J. Biomed. Mater. Res. Part A. 102 (2014) 1255–1263. https://doi.org/10.1002/jbm.a.34795.
[30] Z. Zhen, T. Xi, Y. Zheng, L. Li, L. Li, In Vitro Study on Mg–Sn–Mn Alloy as Biodegradable Metals, J. Mater. Sci. Technol. 30 (2014) 675–685. https://doi.org/10.1016/J.JMST.2014.04.005.
[31] S.S. Hou, R.R. Zhang, S.K. Guan, C.X. Ren, J.H. Gao, Q.B. Lu, X.Z. Cui, In vitro corrosion behavior of Ti-O film deposited on fluoride-treated Mg–Zn–Y–Nd alloy, Appl. Surf. Sci. 258 (2012) 3571–3577. https://doi.org/10.1016/J.APSUSC.2011.11.116.
[32] S. Mohajernia, S. Pour-Ali, S. Hejazi, M. Saremi, A.-R. Kiani-Rashid, Hydroxyapatite coating containing multi-walled carbon nanotubes on AZ31 magnesium: Mechanical-electrochemical degradation in a physiological environment, Ceram. Int. 44 (2018) 8297–8305. https://doi.org/10.1016/J.CERAMINT.2018.02.015.
[33] L. Chen, Y. Sheng, H. Zhou, Z. Li, X. Wang, W. Li, Influence of a MAO + PLGA coating on biocorrosion and stress corrosion cracking behavior of a magnesium alloy in a physiological environment, Corros. Sci. (2018). https://doi.org/10.1016/J.CORSCI.2018.12.005.
[34] O. Graniel, M. Weber, S. Balme, P. Miele, M. Bechelany, Atomic layer deposition for biosensing applications, Biosens. Bioelectron. 122 (2018) 147–159. https://doi.org/10.1016/J.BIOS.2018.09.038.
[35] P.R. Chalker, Photochemical atomic layer deposition and etching, Surf. Coatings Technol. 291 (2016) 258–263. https://doi.org/10.1016/j.surfcoat.2016.02.046.
[36] E. Marin, A. Lanzutti, L. Guzman, L. Fedrizzi, Chemical and electrochemical characterization of TiO2/Al2O3 atomic layer depositions on AZ-31 magnesium alloy, J. Coatings Technol. Res. 9 (2012) 347–355. https://doi.org/10.1007/s11998-011-9372-8.
[37] X. Liu, Q. Yang, Z. Li, W. Yuan, Y. Zheng, Z. Cui, X. Yang, K.W.K. Yeung, S. Wu, A combined coating strategy based on atomic layer deposition for enhancement of corrosion resistance of AZ31 magnesium alloy, Appl. Surf. Sci. 434 (2018) 1101–1111. https://doi.org/10.1016/J.APSUSC.2017.11.032.
[38] Q. Yang, W. Yuan, X. Liu, Y. Zheng, Z. Cui, X. Yang, H. Pan, S. Wu, Atomic layer deposited ZrO2 nanofilm on Mg-Sr alloy for enhanced corrosion resistance and biocompatibility, Acta Biomater. 58 (2017) 515–526. https://doi.org/10.1016/J.ACTBIO.2017.06.015.
[39] M. Peron, J. Torgersen, F. Berto, Effect of Zirconia ALD coating on stress corrosion cracking of AZ31 alloy in simulated body fluid, in: Procedia Struct. Integr., Elsevier B.V., 2019: pp. 538–548. https://doi.org/10.1016/j.prostr.2019.08.198.
[40] M. Peron, F. Berto, J. Torgersen, Stress corrosion cracking behavior of zirconia ALD–coated AZ31 alloy in simulated body fluid, Mater. Des. Process. Commun. (2019) mdp2.126. https://doi.org/10.1002/mdp2.126.
[41] T. Kokubo, H. Takadama, How useful is SBF in predicting in vivo bone

bioactivity?, Biomaterials. 27 (2006) 2907–2915. https://doi.org/10.1016/J.BIOMATERIALS.2006.01.017.
[42] G. Song, A. Atrens, D. StJohn, An Hydrogen Evolution Method for the Estimation of the Corrosion Rate of Magnesium Alloys, in: Magnes. Technol. 2001, John Wiley & Sons, Inc., Hoboken, NJ, USA, 2013: pp. 254–262. https://doi.org/10.1002/9781118805497.ch44.
[43] ASTM International, ASTM-E466-96. Standard Practice for Slow Strain Rate Testing to Evaluate the Susceptibility of Metallic Materials to Environmentally Assisted Cracking, (n.d.). https://doi.org/10.1520/G0129-00R13.
[44] M. Bobby Kannan, W. Dietzel, C. Blawert, A. Atrens, P. Lyon, Stress corrosion cracking of rare-earth containing magnesium alloys ZE41, QE22 and Elektron 21 (EV31A) compared with AZ80, Mater. Sci. Eng. A. 480 (2008) 529–539. https://doi.org/10.1016/J.MSEA.2007.07.070.
[45] L. Choudhary, R.K. Singh Raman, J. Hofstetter, P.J. Uggowitzer, In-vitro characterization of stress corrosion cracking of aluminium-free magnesium alloys for temporary bio-implant applications, Mater. Sci. Eng. C. 42 (2014) 629–636. https://doi.org/10.1016/J.MSEC.2014.06.018.
[46] D. Thirumalaikumarasamy, K. Shanmugam, V. Balasubramanian, Comparison of the corrosion behaviour of AZ31B magnesium alloy under immersion test and potentiodynamic polarization test in NaCl solution, J. Magnes. Alloy. 2 (2014) 36–49. https://doi.org/10.1016/J.JMA.2014.01.004.
[47] S. Nezar, N. Saoula, S. Sali, M. Faiz, M. Mekki, N.A. Laoufi, N. Tabet, Properties of TiO 2 thin films deposited by rf reactive magnetron sputtering on biased substrates, Appl. Surf. Sci. 395 (2017) 172–179. https://doi.org/10.1016/j.apsusc.2016.08.125.
[48] J.H. Kim, S. Lee, H.S. Im, Effect of target density and its morphology on TiO2 thin films grown on Si(100) by PLD, Appl. Surf. Sci. 151 (1999) 6–16. https://doi.org/10.1016/S0169-4332(99)00269-X.
[49] J. Yu, X. Zhao, J. Du, W. Chen, Preparation, microstructure and photocatalytic activity of the porous TiO2 anatase coating by sol-gel processing, J. Sol-Gel Sci. Technol. 17 (2000) 163–171. https://doi.org/10.1023/A:1008703719929.
[50] F. Liu, D. Shan, Y. Song, E.-H. Han, W. Ke, Corrosion behavior of the composite ceramic coating containing zirconium oxides on AM30 magnesium alloy by plasma electrolytic oxidation, Corros. Sci. 53 (2011) 3845–3852. https://doi.org/10.1016/J.CORSCI.2011.07.037.
[51] N. Winzer, A. Atrens, G. Song, E. Ghali, W. Dietzel, K.U. Kainer, N. Hort, C. Blawert, A critical review of the Stress Corrosion Cracking (SCC) of magnesium alloys, Adv. Eng. Mater. 7 (2005) 659–693. https://doi.org/10.1002/adem.200500071.
[52] R.S. Stampella, R.P.M. Procter, V. Ashworth, Environmentally-induced cracking of magnesium, Corros. Sci. 24 (1984) 325–341. https://doi.org/10.1016/0010-938X(84)90017-9.
[53] V.S. Raja, B.S. Padekar, Role of chlorides on pitting and hydrogen embrittlement of Mg–Mn wrought alloy, Corros. Sci. 75 (2013) 176–183. https://doi.org/10.1016/J.CORSCI.2013.05.030.
[54] M.A. Turchanin, P.G. Agraval, Cohesive energy, properties, and formation energy of transition metal alloys, Powder Metall. Met. Ceram. 47 (2008) 26–39.

https://doi.org/10.1007/s11106-008-0006-3.
[55] W. Li, D.Y. Li, Influence of surface morphology on corrosion and electronic behavior, Acta Mater. 54 (2006) 445–452. https://doi.org/10.1016/j.actamat.2005.09.017.
[56] M.L. González-Martín, L. Labajos-Broncano, B. Jańczuk, J.M. Bruque, Wettability and surface free energy of zirconia ceramics and their constituents, J. Mater. Sci. 34 (1999) 5923–5926. https://doi.org/10.1023/A:1004767914895.
[57] F. Zhang, B.W. Robinson, H. De Villiers-Lovelock, R.J.K. Wood, S.C. Wang, Wettability of hierarchically-textured ceramic coatings produced by suspension HVOF spraying, J. Mater. Chem. A. 3 (2015) 13864–13873. https://doi.org/10.1039/c5ta02130h.
[58] Y. Akaltun, M. Aslan, T.Yetim, T.Çayir, A. Çelik, The effect of wettability on corrosion resistance of oxide films produced by SILAR method on magnesium, aluminum and copper substrates, Surf. Coatings Technol. 292 (2016) 121–131. https://doi.org/10.1016/j.surfcoat.2016.03.011.
[59] A. Pardo, S. Feliu, M.C. Merino, R. Arrabal, E. Matykina, Electrochemical estimation of the corrosion rate of magnesium/aluminium alloys, Int. J. Corros. 2010 (2010). https://doi.org/10.1155/2010/953850.
[60] M. Lorenzetti, E. Pellicer, J. Sort, M.D. Baró, J. Kovač, S. Novak, S. Kobe, Improvement to the corrosion resistance of Ti-based implants using hydrothermally synthesized nanostructured anatase coatings, Materials (Basel). 7 (2014) 180–194. https://doi.org/10.3390/ma7010180.
[61] M. Sowa, D. Łastówka, A.I. Kukharenko, D.M. Korotin, E.Z. Kurmaev, S.O. Cholakh, W. Simka, Characterisation of anodic oxide films on zirconium formed in sulphuric acid: XPS and corrosion resistance investigations, J. Solid State Electrochem. 21 (2017) 203–210. https://doi.org/10.1007/s10008-016-3369-2.
[62] S. Il Pyun, Y.G. Yoon, E. Lugscheider, R. Mathesius, Relationship between interfacial reaction and adhesion at PVD TiO2 film-metal (Ti or Al) interfaces, Surf. Coatings Technol. 61 (1993) 233–237. https://doi.org/10.1016/0257-8972(93)90231-C.
[63] C. (Christoph) Leyens, M. (Manfred) Peters, John Wiley & Sons., Wiley InterScience (Online service), Titanium and titanium alloys : fundamentals and applications, Wiley-VCH, 2003.
[64] H. Yang, L. Huang, M. Zh, Hot Forming Characteristics of Magnesium Alloy AZ31 and Three-Dimensional FE Modeling and Simulation of the Hot Splitting Spinning Process, in: Magnes. Alloy. - Des. Process. Prop., InTech, 2011. https://doi.org/10.5772/13778.
[65] H. Hayashi, T. Saitou, N. Maruyama, H. Inaba, K. Kawamura, M. Mori, Thermal expansion coefficient of yttria stabilized zirconia for various yttria contents, Solid State Ionics. 176 (2005) 613–619. https://doi.org/10.1016/j.ssi.2004.08.021.
[66] D.R. Hummer, P.J. Heaney, J.E. Post, Thermal expansion of anatase and rutile between 300 and 575 K using synchrotron powder X-ray diffraction, Powder Diffr. 22 (2007) 352–357. https://doi.org/10.1154/1.2790965.
[67] C.M. Cristache, M. Burlibasa, G. Cristache, S. Drafta, I.A. Popovici, A.A. Iliescu, S. Zisi, L. Burlibasa, Zirconia and its biomedical applications, Metal. Int. XVI (2011) 18–23. https://www.researchgate.net/publication/286038141_Zirconia_and_its_biomedic

al_applications (accessed January 20, 2020).
[68] Titanium Dioxide - online catalogue source - supplier of research materials in small quantities - Goodfellow, (n.d.). http://www.goodfellow.com/E/Titanium-Dioxide.html (accessed January 20, 2020).

Chapter 7

Conclusion and recommendation

7.1. Conclusion

Throughout the thesis, the relation between microstructural and surface properties and the SCC susceptibility have been investigated. The modification of the bulk has been obtained by means of ECAP, while that of the surface by means of cryogenic machining and deposition of different coatings. The main goal of the study was to assess how selected procedures initially studied for improving the corrosion resistance of Mg and its alloys impact the SCC susceptibility of AZ31 alloys in Simulated Body Fluid (SBF) at 37 °C and to provide new insight into the development of SCC-resistant implants. The main contribution of this thesis to the literature are as follows:

- Extensive bibliographical analysis of the different Mg alloys studied as biomaterials with particular interest in their corrosion, mechanical and biological properties and their interplay with corrosion-assisted cracking phenomena

- Studying the effect of ECAP, cryogenic machining and ALD coatings on the SCC susceptibility of an AZ31 alloy.

- Comparable evaluation of the corrosion properties of ALD and sputter on samples characterized by different roughness and topologies.

- Comparable evaluation of the corrosion and biological properties of three different coatings produced by means of ALD

The summary of the findings is given below separately for each chapter of the thesis.

Chapter 2 (paper I and book)

In the second chapter, the main mechanisms governing the SCC phenomenon and the different techniques used to improve the mechanical strength and the corrosion resistance of Mg and their effect on the biocompatibility have been reviewed. In particular, to gain a deep understanding of the different Mg alloys so far studied as biomaterials and the different techniques used to improve their corrosion, mechanical and biological properties, more than 1200 papers have been reviewed, providing the following main conclusions:

- SCC of Mg and its alloys is widely attributed to the combination of two mechanisms, i.e. (1) the anodic dissolution and (2) the cleavage-like fracture due to hydrogen embrittlement

- The main approaches studied to improve the corrosion resistance of Mg and its alloys can be divided into two main groups, one characterized by the modification of the bulk (mainly obtained by means of SPD techniques) and the other by the modification of the surface (obtained by mechanical processing or by the deposition of coatings)

- Mg-Zn based alloy are found to be the alloy characterized by the best compromise between corrosion, mechanical and biological properties

Chapter 3 (Paper II)

The third chapter evaluates the effect of the bulk modification of an AZ31 alloy obtained by means of ECAP on the SCC susceptibility. Different number of passes of ECAP passes were applied on AZ31 alloy and SSRT were carried out to assess the SCC susceptibility of the differently processed alloy. To provide a better understanding of the different failure mechanisms shown by the different ECAP-treated samples, corrosion experiments and fracture surface analyses were carried out. The main conclusions of the paper are as following:

- Samples after 1 pass of ECAP were characterized by the lowest SCC susceptibility, and further ECAP processing led to an increase in the SCC susceptibility, such that samples after 4 passes of ECAP showed a SCC susceptibility higher than that of the samples in the as-received conditions.

- The enhancement reported in the samples subjected to 1 pass of ECAP was attributed to its improved corrosion resistance due to the reduced grain size that allows both a faster formation of the passivating surface oxide and a better surface coverage provided by this oxide layer as a consequence of a reduced degree of oxide cracking.

- We hypothesize that the deterioration of the SCC resistance observed with 2 and 4 passes of ECAP was due to the modified texture within the material. In fact, although the grain size is slightly reduced compared to 1 pass of ECAP, the alignments of basal planes with the shearing direction as a consequence of ECAP can explain the detrimental effects on the corrosion resistance that led to the increased SCC susceptibility

Chapter 4 (Paper III)

In the fourth chapter of the thesis the effect of surface treatments obtained by means of mechanical processing on the SCC susceptibility of AZ31 alloy has been evaluated. In particular, cryogenic machining has been considered. A full characterization of the machined surface integrity, including microstructural observations, residual stress, nano-hardness measurements and surface texture analyses were carried out together with the assessment of the corrosion properties to explain the SCC susceptibility obtained carrying out SSRT. The main conclusions of the paper are as following:

- Cryogenic machined samples were characterized by a slightly lower SCC susceptibility in SBF at body temperature than dry cut samples

- This enhancement was attributed to the improved corrosion performances of the cryogenic machined samples due to the presence of a wider nanocrystalline layer, resulting in a faster formation of passivating surface oxides, and to the presence of compressive residual stresses instead of tensile.

- The reduced SCC susceptibility of cryogenic machined samples was also attributed to their reduced tendency to pitting and localized corrosion evidenced by the analyses of both the fracture surface and the gauge section.

Chapter 5 (Papers IV and V)

The fifth chapter presents the evaluation of the recently developed ALD technique for biomedical applications. The corrosion and the biological properties of AlDed coatings were evaluated. Dealing with the former, the corrosion performances of ALD coated Mg alloys were compared to those of sputter coating films employing samples of different surface roughness and topologies that shall resemble a more realistic condition of an implant surface. The biological properties of three different coatings (TiO_2, ZrO_2 and HfO_2) obtained by means of ALD were evaluated using MTS assay using L929 cells to complete the evaluation of the applicability of ALD as a coating technique for biomedical applications. The main conclusions of the papers are as following:

- The ALD technique has been shown to provide a better corrosion protection than sputter technique both for smooth and rough surfaces as a consequence of its increased surface integrity. SEM analyses reveals in fact that under the same conditions sputter coatings are characterized by more and longer cracks than ALDed coatings.

- In the case of 3D porous structures, the improvements provided by ALD were even more evident due to the line-of-sight limitation of sputtering, evidenced by the micro-morphologies of the undercuts and shadowed areas of the sliced 3D structures.

- The MTS assays reported HfO_2 coatings to be characterized by the highest cell viability as a consequence of their highest corrosion resistance that leads to a lower increase in the pH and in the concentration of Mg^{2+} ions.

- The improved corrosion resistance of HfO_2 coatings are reasoned by their lower wettability and their higher electrochemical stability and surface integrity (in terms of cracks and pores) compared to ZrO_2 and, above all, TiO_2 coatings.

- Although the biocompatibility of TiO_2 remains undisputed when the cells are in direct contact, biocompatibility issues may arise when TiO_2 is used as coating

material for Mg and its alloys and it is not effective in reducing the corrosion rate of the magnesium substrate leading to an environment that reveals to be toxic for the cells due to the increase in the pH and to the high concentration of Mg^{2+} ions.

Chapter 6 (paper VI)

In the sixth chapter, the effects of TiO_2 and ZrO_2 ALD coatings on the SCC susceptibility of AZ31 alloy were assessed. Potentiodynamic polarization curves and hydrogen evolution experiments together with the fracture surface analyses have been carried out to understand the different SCC susceptibilities obtained by means of SSRT. The main conclusions of the papers are as following:

- The application of coatings was shown to reduce the SCC susceptibility of AZ31 alloy. In particular ZrO_2 coatings better performed compared to TiO_2. The different SCC susceptibility was evidenced also by the fracture surface analyses that showed a transition from a mixed mode fracture where the brittle zone was predominantly transgranular in the bare samples, to a predominance of intergranular failures in the TiO_2 coated samples and to a predominantly ductile failure for ZrO_2 coated samples.

- The different SCC susceptibility was attributed to the improved corrosion of the coated samples. The difference in the corrosion behavior between TiO_2 and ZrO_2 coated samples was related to the four main aspects, i.e. different cohesive energies, different wettability, different defect densities and sizes and different mechanical properties.

7.2. Recommendations

There are several topics that should be considered in the future studies:

- The SCC susceptibility of HfO_2 ALD coating can be assessed.

- An optimized ECAP treated AZ31 alloy can be combined with ZrO_2 coating to further improve the SCC resistance.

- Corrosion Fatigue of cryogenically machined, ECAP treated and ALD coated AZ31 samples need to be investigated.

- Further improvements in the field can be achieved by substituting the AZ31 alloy with a more biocompatible Mg alloy such as ZK60 or WE43.

ISBN 978-82-326-4642-5 (printed ver.)
ISBN 978-82-326-4643-2 (electronic ver.)
ISSN 1503-8181

NTNU
Norwegian University of
Science and Technology